Self-Assembly at Ionic Liquid-Based Interfaces:

Fundamentals and Applications

by

Denzil Frost

A Dissertation Presented in Partial Fulfillment
of the Requirements for the Degree
Doctor of Philosophy

Approved June 2013 by the
Graduate Supervisory Committee:

Lenore Dai, Chair
Cesar Torres
David Nielsen
Kyle Squires
Kaushal Rege

ARIZONA STATE UNIVERSITY

August 2013

ABSTRACT

Liquid-liquid interfaces serve as ideal 2-D templates on which solid particles can self-assemble into various structures. These self-assembly processes are important in fabrication of micron-sized devices and emulsion formulation. At oil/water interfaces, these structures can range from close-packed aggregates to ordered lattices. By incorporating an ionic liquid (IL) at the interface, new self-assembly phenomena emerge. ILs are ionic compounds that are liquid at room temperature (essentially molten salts at ambient conditions) that have remarkable properties such as negligible volatility and high chemical stability and can be optimized for nearly any application. The nature of IL-fluid interfaces has not yet been studied in depth. Consequently, the corresponding self-assembly phenomena have not yet been explored.

We demonstrate how the unique molecular nature of ILs allows for new self-assembly phenomena to take place at their interfaces. These phenomena include droplet bridging (the self-assembly of both particles and emulsion droplets), spontaneous particle transport through the liquid-liquid interface, and various gelation behaviors. In droplet bridging, self-assembled monolayers of particles effectively “glue” emulsion droplets to one another, allowing the droplets to self-assembly into large networks. With particle transport, it is experimentally demonstrated the ILs overcome the strong adhesive nature of the liquid-liquid interface and extract solid particles from the bulk phase without the aid of external forces. These phenomena are quantified and corresponding mechanisms are proposed.

The experimental investigations are supported by molecular dynamics (MD) simulations, which allow for a molecular view of the self-assembly process. In particular,

we show that particle self-assembly depends primarily on the surface chemistry of the particles and the non-IL fluid at the interface. Free energy calculations show that the attractive forces between nanoparticles and the liquid-liquid interface are unusually long-ranged, due to capillary waves. Furthermore, IL cations can exhibit molecular ordering at the IL-oil interface, resulting in a slight residual charge at this interface. We also explore the transient IL-IL interface, revealing molecular interactions responsible for the unusually slow mixing dynamics between two ILs. This dissertation, therefore, contributes to both experimental and theoretical understanding of particle self-assembly at IL based interfaces.

ACKNOWLEDGMENTS

I am pleased to acknowledge those who have played key roles in helping me complete this dissertation. First, I would like to express my appreciation for my advisor and mentor, Dr. Lenore Dai. Because of her encouragement and guidance, my graduate studies have become the most fulfilling phase of my education. The skills and advice she has passed on to me are invaluable. I would also like to thank Drs. David Nielsen, Kaushal Rege, Kyle Squires, and Cesar Torres for serving on my graduate committee and offering their time and knowledge to guide and expand my research. Dr. Veronica Burrows taught most of my core ChE classes and I am grateful to her for providing me with a reliable foundation in these subjects, but most especially research methods.

Thanks to all of those who kept the lab running and made it a great place to work. Mr. Fred Pena was always there to fix things or answer safety questions (and share a hunting story or two) and Mr. Al Thompson kept my computer performing optimally. I am very grateful for outstanding graduate, undergraduate, and high school students surpassed so many expectations and really helped my experiments along. In no particular order, these are Elizabeth Nofen, Jared Schoepf, Harrison Phelan, Brian Perea, Michael Machas, Miranda Ngan, Mariela Robledo, Nathaniel Kroeger, and Ankita Thakur. Thanks to Prithwish Chatterjee for help with the DSC, Haobo Chen for the FTIR measurements, Jin Zou for her collaboration on the gelation project, and Mingmeng Zhang for help measuring zeta potential. I would also like to thank Stella Nickerson for her excellent work on the surface tension calculations and Dr. Yanmei Song for getting me started on molecular dynamics simulations when I first arrived at ASU. I am grateful to Drs. Calvin Bartholomew, William Hecker, and Ken Solen at Brigham Young

University who were my undergraduate research advisors that inspired me to pursue this doctorate degree.

An important thanks goes to my parents, Rick and Cathie Frost, who encouraged me to do my very best in everything and documented my first scientific inquiry, the waterfall-maker. My most heartfelt thanks goes to my wife, Crystal, for her patience, support, and abundant praise. After proofreading my papers, listening to my presentations, and hearing me talk about my studies (all while taking care of our two children), she should probably get a PhD too. Since I mentioned them, thanks to my children, Brianna and Denzil, for being there to come home to.

For financial support of this research, I would like to thank the National Science Foundation, NASA, Science Foundation Arizona, Achievement Rewards for College Scientists, the ASU Graduate College, and the ASU High Performance Computing Initiative.

TABLE OF CONTENTS

Page

LIST OF TABLES

LIST OF FIGURES

CHAPTER 1

INTRODUCTION

Liquid-liquid interfaces are able to provide 2D templates for self-assembly of small particles. By the virtue of inter-particle interactions alone, intricate patterns and structures spontaneously form and may be fused together to maintain their morphology in the absence of the interfacial template. Flat liquid-liquid interfaces can be used to make membrane-like structures whereas spherical interfaces (i.e. emulsion droplets) can be used to make capsule-like structures. Such micro- and nano-structures may have high-impact applications in medical, food, and petroleum fields. In addition, this phenomenon has already seen wide applications in another form: Pickering emulsions. Emulsions are stable mixtures of immiscible liquids, one liquid being dispersed as droplets in the other, and are encountered regularly in the food, medical, and petroleum industries. To stabilize against coalescence and eventual separation, Pickering emulsion droplets are armored with solid particles. In contrast to traditional emulsions stabilized by surfactants, Pickering emulsions offer decreased toxicity, easier handling, enhanced stability, and options of functionalization. These unique qualities have made them excellent candidates for medical [1], catalysis [2, 3], and food [4, 5] applications.

So far, particle self-assembly has been studied primarily at oil/water interfaces. Ionic liquids (ILs) are a novel class of liquids with an unfathomed wealth of useful properties that can greatly enhance the applicability and tunability of self-assembly processes. Room temperature ILs are ionic materials that melt below 100^{o}C, many of them being liquid at room temperature. The remarkable advantage of ILs is that their properties can be tuned for virtually any application simply by judicious choice of the

constituent ions. Consequently, they are also called “designer solvents.” Such tunability would greatly enhance the field of particle self-assembly. For example, self-assembly at liquid-liquid interfaces is usually governed by properties of the solid particles, which sometimes requires expensive functionalization. If, instead, this process could be tuned by the solvent, the cost of continuous production of self-assembled structures could be greatly reduced because there would be no need to repeatedly functionalize particles. Pickering emulsions already have wide applications and with the incorporation of ILs, their properties may be optimized for specific tasks. Particle behavior at IL-based liquid-liquid interfaces, however, has not yet been investigated. It is the objective of this study to pioneer a fundamental understanding of this phenomenon in comparison to oil/water interfaces and provide reference examples of particle self-assembly using this new class of liquids. The corresponding presentation is organized as follows.

Chapter 2 is divided into two sections which provide background information on the two components of this study: particle self-assembly and ILs. The first section discusses theories and applications of particle self-assembly at liquid-liquid interface with an emphasis on how this phenomenon is tuned. The second section contains a brief history and relevant theory of ILs and lists some of the major IL-based technological developments.

Chapter 3 discusses our experimental and computational work on some unique characteristics of liquid-liquid interfaces containing ILs including interfacial tension, molecular ordering, and unusually prolonged dynamics. Particularly, the interface between two miscible ILs is investigated with the purpose of determining the molecular interactions responsible for the remarkably slow mixing and, consequently, long-lived

interface. In the subsequent section, a new phenomenon is discussed in which solid particles were spontaneously transported across IL-fluid interfaces, despite the large adhesion energy particles feel at the interface. ILs possess unique qualities to facilitate this process and a proposed mechanism is discussed. In addition to this process, ILs also exhibit unique morphologies when incorporated in Pickering emulsions. The third section of Chapter 3 discusses an oil-in-IL Pickering emulsion system in which droplets were bridged by solid particles: essentially the self-assembly of both particles and droplets. After discussing the emulsion formulation, general morphology and stability characteristics of this emulsion are discussed in comparison to oil/water emulsions. Characterization of the bridging morphology with respect to particle concentration, particle size, and droplet phase composition are also discussed as well as insight into possible causes behind the formation of this unique morphology. In light of these features, we then discuss how the transport, stability, and morphologies of these IL-based Pickering emulsions could be manipulated using an organogelator. Gelation characteristics of the pure IL, IL-in-water emulsions, and oil-in-IL emulsions are discussed with emphasis on enhancements in stability and control of self-assembly processes. To complete this study of IL-based Pickering emulsions, the last section presents studies of particle self-assembly in IL-in-IL Pickering emulsions. Many of the morphologies and transport phenomena unique to IL-based Pickering emulsions were observed in these systems and their dependence on particle surface chemistry, droplet phase, and continuous phase provide additional insight into these phenomena.

Chapter 4 extends our fundamental studies of particle self-assembly at IL-based interfaces, specifically the IL/water and IL/hexane interfaces. Fundamental studies

consist of equilibrium molecular dynamics (MD) simulations and potential of mean force (PMF) calculations. The MD simulations provided an unparalleled molecular view of the self-assembly process at these interfaces while the PMF studies allowed us to examine the free energy of the particle-interface interaction. Following an explanation of the simulation techniques, the self-assembly of hydrophobic nanoparticles at the IL/water and IL/hexane interfaces is analyzed and discussed. The effect of surface charge on this phenomenon is also analyzed particle desorption energies are compared to macroscopic models. In the subsequent section, hydrophilic particles are introduced and their self-assembly behaviors are compared to those of the hydrophobic particles. This section focuses particularly on the molecular behavior of the IL as it interacted with particles of different surface chemistries. IL solvation layers around each particle are analyzed according to their structure and dynamics. It is shown that the unique binary nature of ILs allows high adaptability to a variety of surface chemistries and, hence, remarkable extraction capabilities.

Chapter 5 proposes future directions for the study of particle self-assembly at IL-based interfaces. The chapter starts with a discussion on the use of computational fluid dynamics (CFD) to examine the interaction between Pickering emulsions droplets. Such a simulation will be the first of its kind and the CFD simulation regime is particularly suitable since systems of a size relevant to our Pickering emulsions can be studied. Preliminary CFD data on the study of droplet bridging are presented and recommendations on experimental validation are proposed. Another future direction is presented in the second section, which discusses the droplet bridging phenomenon as an unprecedented route to bind liquid droplets together. We recommend exploiting this

behavior using microfluidics to control individual bridge formation and manually generate structures of droplets. Microfluidic device fabrication is discussed and a preliminary device design is proposed. The impact of these studies will not only include insight into the bridging phenomenon (since it can be observed in real time), but also provide a new category of directed assembly and possibly provide an environment for studying chemical kinetics. In the final section, a new method for measuring mixing properties using differential scanning calorimetry (DSC) is proposed. The mixing properties of ILs are quite unexplored and this method provides a straightforward process for calculating these values experimentally. Thermodynamic derivation for this process is provided along with preliminary data.

CHAPTER 2

BACKGROUND

2.1 Particle self-Assembly at Liquid-Liquid Interfaces

Since nature is an inherently multi-phase system, scientists and engineers will always encounter interfaces. Interfaces form upon contact of two immiscible phases. Binary combinations of the three phases of matter give a number of possible interfaces (i.e. solid/gas, liquid/gas, solid/solid), but the liquid-liquid interface is of particular interest for self-assembly. Unlike solid interfaces, the liquid-liquid interface is flexible, deformable, and easily probed. Buoyancy forces are usually negligible because the densities of the liquids are relatively close (in contrast to gas/liquid interfaces). Furthermore, small particles (< 10 microns) readily adsorb to the liquid-liquid interface via capillary attraction [6, 7]. Therefore, the liquid-liquid interface is an ideal template for the self-assembly of small particles. Ramsden [6] and Pickering [7] discovered this phenomenon at the beginning of the 20th century in the form of what are now termed "Pickering emulsions." While not widely recognized until the latter end of the century, the discoveries of Ramsden and Pickering have become a major topic in colloid science today. Stability of these emulsions is maintained because the liquid droplets are "armored" with solid particles that self-assemble at their surfaces. Pickering emulsions are one of the primary applications of particle self-assembly at liquid-liquid interfaces. This section will discuss the fundamental mechanisms governing self-assembly at the liquid-liquid interface and give a summary of the many applications in which this phenomenon is utilized.

Liquid-liquid interfaces can all be characterized by their interfacial tension, γ. Thermodynamically, γ represents the change in free energy of the system, G, upon a differential increase in interfacial area, A, as shown in Equation 2.1.

$$\gamma = \left(\frac{\partial G}{\partial A}\right)_{T,P,n} \tag{2.1}$$

As will be shown later, this property provides the driving force for particle adherence to the interface. In a model system with two immiscible liquids (A and B) and a colloidal particle, three possible interfacial tensions can be measured: $\gamma_{AB}, \gamma_{AP}, \gamma_{BP}$ representing the interfacial tensions of liquid A/liquid B, liquid A/particle surface, and liquid B/particle surface, respectively. Since the energies involved are area-dependent, the equilibration of the particle at the interface occurs at the point where the sum of interfacial energies (Aγ) reaches a minimum. For a spherical particle, this interfacial position is defined by the contact angle, θ, as shown in Figure 2.1.

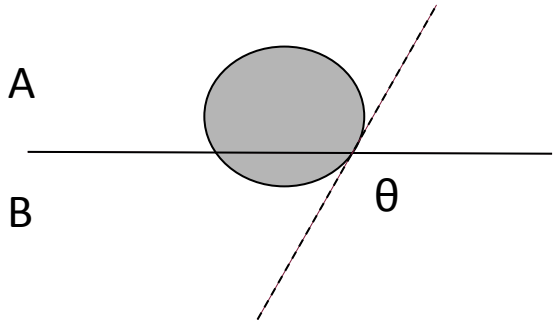

Figure 2.1 Definition of contact angle, theta, to describe the interfacial position of a colloidal particle between fluids A and B.

For a spherical, small colloidal particle, the contact angle can be defined in terms of the interfacial tensions by Young's equation [8].

$$cos\theta = \frac{\gamma_{AP} - \gamma_{BP}}{\gamma_{AB}} \tag{2.2}$$

From the free, suspended state, to the interfacially adsorbed state, the particle experiences a total decrease in free energy, ΔG is given by [9-11]

$$\Delta G = \pi\gamma r^2(1 \pm cos\theta)^2 \tag{2.3}$$

where r is the particle radius. The $\pm$ symbol allows for the change in free energy to be calculated with respect to a particle suspended in either of the two phases ($+$ for fluid A and – for fluid B).

According to Equation 2.3, the desorption energy depends on the square of the particle radius, as plotted in Figure 2.2a, taking $\theta = 90^o$ and $\gamma = 50$ mN/m[12]. For particles with intermediate hydrophobicity ($\theta = 90^o$) and the size ranging from several nanometers to several microns, the desorption energy is many times that of thermal energy, kT, so that particle attachment is essentially irreversible[12]. Only for extremely small particles ($r \leq 1$ nm), does this energy become comparable to the thermal energy and attachment may be reversible. Wettability is another important parameter, as shown in Equation 2.3 (denoted by the contact angle, θ), and has a significant effect on how strongly a particle is held at the interface. At a contact angle of $\theta = 90^o$, the particle is held most strongly since it is equally wetted by both liquids. Adsorption strength drops off quickly on either side of $= 90^o$ [13]. This is illustrated in Figure 2.2, which shows the dependence of the energy required to remove a 10-nm spherical particle from the oil-water interface with an interfacial tension $\gamma = 36$ mN/m on the contact angle [14].

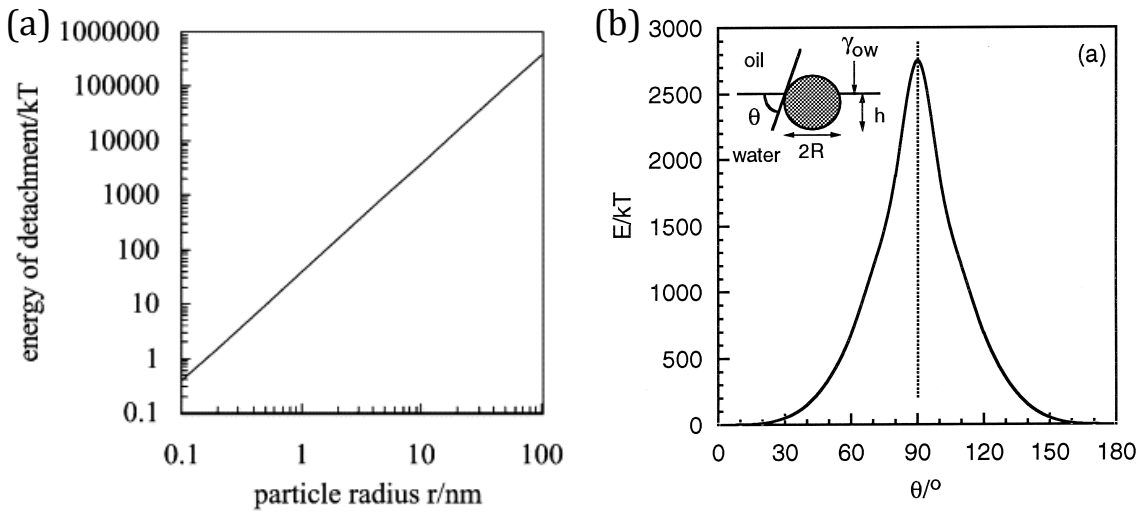

Figure 2.2 Variation of adsorption/desorption energy (E) of a particle at the planar oil/water interface at 298 K with respect to (a) particle radius and (b) contact angle. Adapted from [12] and [14], respectively.

Pieranski [15] proposed an equivalent relationship for particle adsorption:

$$\Delta G = -\gamma_{AB}A_{AB} + \gamma_{AP}A_{AP} + \gamma_{BP}A_{BP} \tag{2.4}$$

$$= \pi\gamma_{AB}{z_c}^2 + 2\pi r^2(\gamma_{AP} - \gamma_{BP})(1 - \frac{z_c}{r})$$

where A represents the area denoted by the subscript, and z_c is the distance between the interface and the center of the particle. Both Equations 2.3 and 2.4 assume flat interfaces, negligible line tension, and spherical smooth particles. Researchers often call this set of assumptions the" Pieranski equation" even though Equation 2.3 is more commonly found in literature. More sophisticated models exist, however, that account for forces not included in the Pieranski equation. Line tension, τ, is effectively the 1-D analogue of interfacial tension, accounting for the change in free energy with respect to the length of the three-phase contact line, ℓ.

$$\tau = \left(\frac{\partial G}{\partial \ell}\right)_{T,P,n,A} \tag{2.5}$$

While this force is usually small and difficult to measure [16], it becomes significant with nano-sized particles. Aveyard and Clint [17] proposed adding an extra term to the Pieranski equation to account for line tension:

$$\Delta G = \pi\gamma_{AB}{z_c}^2 + 2\pi r^2(\gamma_{AP} - \gamma_{BP})\left(1 - \frac{z_c}{r}\right) + 2\pi\tau r\sqrt{1 - ({}^{z_c}/_{r})^2} \tag{2.6}$$

Equation 2.6, however, still assumes a flat interface and was therefore recently further extended by Lehle and Oettel [18] to include the effects of capillary waves:

$$\Delta G = \pi\gamma_{AB}(z_c - z_0)^2 \frac{1 - \frac{\hat{\tau}}{\hat{r}_{0,eq}{}^3}}{1 + ln\hat{\lambda}_c(1 - \frac{\hat{\tau}}{\hat{r}_{0,eq}})} \tag{2.7}$$

$$\hat{\tau} = \frac{\tau}{\gamma_{AB} r} \tag{2.8}$$

$$r_{0,eq} = \sqrt{r^2 - {z_0}^2} \tag{2.9}$$

$$\hat{\lambda}_c \approx \frac{1.12\lambda_c}{r_{0,eq}} \tag{2.10}$$

where z_0 is distance between the flat interface and the center of the particle, and λ_c is the wavelength of the largest capillary wave in the system ($\lambda_c = \sqrt{\frac{\gamma_{AB}}{\Delta\rho g}}$ for systems subject to gravity). The inclusion of these forces somewhat softens the interaction potential, but also extends the range over which the particle and interface interact [18, 19].

Capillary wave and line tension effects become negligible with micron-sized particles. However, deviations from the Pieranski relation may still occur. At curved interfaces (i.e. emulsion droplets), the effect of curvature may be significant. The model

proposed by Komura et al. accounts for the curvature, ε, of the interface in the calculation of particle desorption energy. Curvature is defined as $\varepsilon = r/R_{12}$ according to Figure 2.3 adapted from [20].

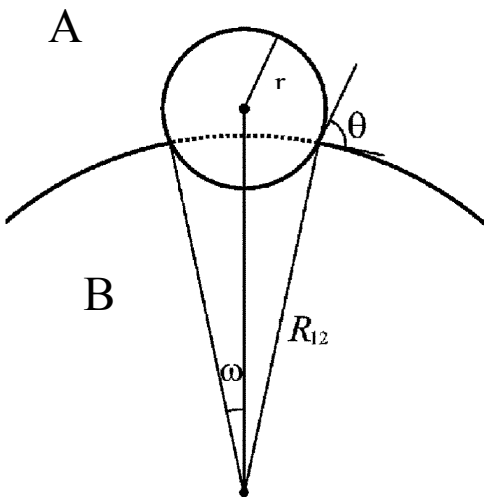

Figure 2.3 Schematic illustration of a spherical particle adsorbed to a spherical interface whose radius of curvature is R_{12}. Adapted from [20].

The relation developed by Komura et al. is shown in Equation 2.11 [20].

$$\Delta G = 2\pi r^2 \gamma_{AB} \left[\frac{\gamma_{AP} - \gamma_{BP}}{\gamma_{AB}} \cos(\theta - \omega) - \frac{1 - cos^3\omega}{3\varepsilon^2} - \frac{\varepsilon}{3}[3\cos(\theta - \omega) - cos^3(\theta - \omega)] \right] \tag{2.11}$$

For a particle at the equilibrium position on the AB interface curved towards liquid B, the volume fraction of the particle located in Liquid B is larger than that in the case of a flat interface since the contact angle is independent of interfacial curvature[20].

Characteristics of the individual particle can also affect its adsorption. Particle roughness increases the total surface of the particle and, as a result, narrows the range of

contact angles over which particle adsorption is stable[21, 22]. Particle shape also plays a major role since it introduces a rotational degree of freedom over which the energy may be minimized. Typically, the most favorable configuration has the longest dimension of the particle oriented parallel to the interface (See Figure 2.4) [23] . Particle surface chemistry plays a major role in defining self-assembled patterns. Some of the surface functionalization schemes include dissociable groups [14, 24-26], Janus particles [27-30], and polymer brushes [31].

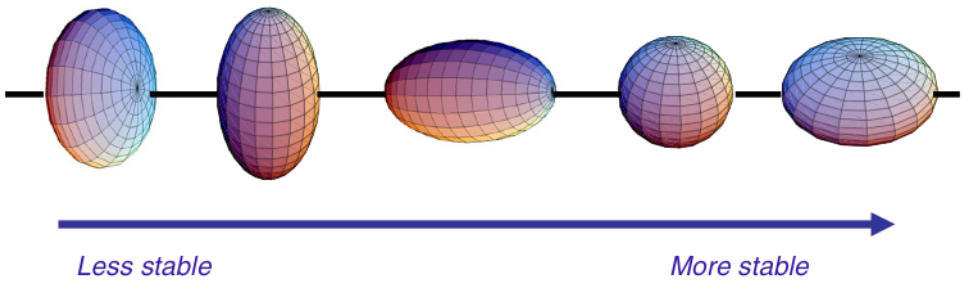

Figure 2.4 Relative stability of non-spherical nanoparticles at the interface with respect to particle shape and orientation. Adapted from [23].

Equations 2.1 – 2.10 govern how particles adhere to the liquid-liquid interface. Using the interface as a 2D scaffold, the particles can then self-assemble into a variety of interesting patterns. Inter-particle forces are the primary driving force behind the formation of these structures. Most significant between micron-sized particles are the electrostatic, Van der Waals, and capillary forces[23]. As will be explained below, the strength and range of these forces depend on the following solvent-tunable parameters: dielectric constants, Hamaker constants, and the interfacial tension, respectively. Although these forces are much weaker than the particle-interface interaction, they warrant some discussion because it is by manipulating these forces that self-assembled

structures are tuned. It should be noted, however, that theory describing inter-particle interactions at the interface is not as well developed as theory describing particle-interface interactions.

Particle charge is usually a result of dissociation of the functional groups on the surface (i.e. R-OH → $R\text{-}O^- + H^+$). In a bulk phase, charged particles would exert repulsive forces uniformly in all directions. At the interface, however, two sides of the same particle exert forces though different media, and the degree of dissociation can differ in each liquid. Therefore, the particle-particle electrostatic interactions are of the dipole-dipole type and are always repulsive[23, 32]. The tunable feature of this interaction is the dielectric constant, ϵ, of either or both of the liquids. Electrostatic interactions depend inversely on ϵ, so a lower ϵ of one liquid will increase the range over which electrostatic repulsions are felt. The resulting self-assembled structures are ordered-lattices of particles [33, 34] as shown in Figure 2.5.

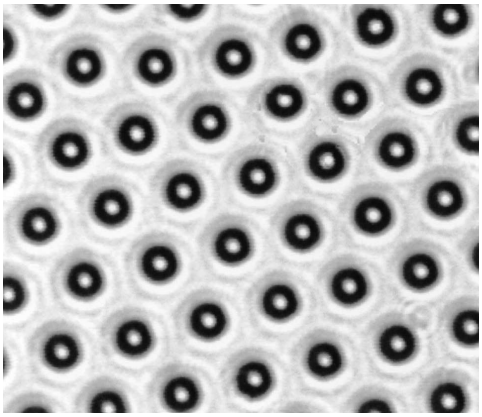

Figure 2.5 Optical micrograph of and ordered lattice of polystyrene particles at the oil/water interface. Particles are 2.7 microns in diameter. Adopted from [33].

Van der Waals are attractive forces that account for dispersion/London forces and depend on the size of the colloidal particle and the Hamaker constant, A_H, which is

solvent dependent[35]. Early studies have shown that these forces are much stronger between particles at the interface than between particles in the bulk[23, 36]. However, Patel and Egorov have shown that the Hamaker constant can be tuned such that these forces are completely screened[37]. These Van der Waals forces have been observed to decay with $1/d^6$ dependence, where d is the distance between the particles, and can thus be accurately described by the well-known Lennard-Jones potential [23].

Capillary forces between particles can be attractive or repulsive and arise due to deformations of the interface, or menisci, around the adsorbed particles. Meniscus-meniscus interactions are attractive if their curvatures are of the same sign (i.e. concave-concave or convex-convex) and repulsive if their curvatures are of the opposite sign (see Figure 2.6a) [38] . Tunability of this force lies in the interfacial tension, to which the magnitude of the interaction is proportional[38]. However in order for menisci to form, some force perpendicular to the interface must be applied. Bowden and coworkers made use of the buoyancy force to create menisci around polymeric plates at the perfluorodecalin/water interface (See Figure 2.6) [39] . By adjusting the hydrophobicity of each side of the hexagon, this group was able to direct self-assembly and influence the final self-assembled structure [39-41].

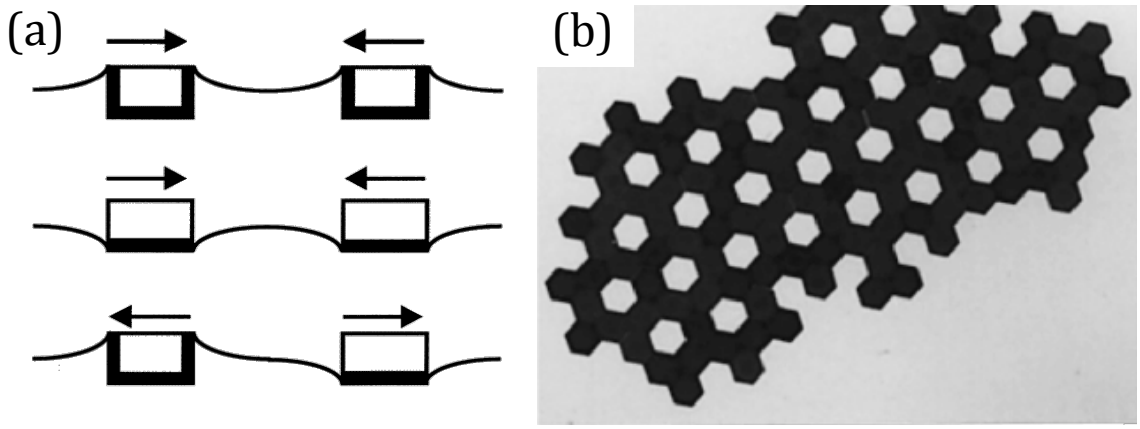

Figure 2.6 (a) Schematic illustration of attractive and repulsive capillary forces. (b) Self-assembled structure of polymeric hexagons at the oil/water interface. Adopted from [40] and [39] respectively.

Particles trapped in the thin film between two droplets can form tightly packed aggregates due to inter-particle capillary forces induced by mechanical forces on the droplets[42-47]. It is evident that the capillary force is easily tunable and significantly affects the self-assembled structure.

Apart from being the least understood, forces in addition to the three mentioned above are generally minor and only apply to nanoparticles. These include solvation forces (i.e. depletion) [23] and attractions due to thermal fluctuations in the interface, like capillary waves[18, 48, 49]. Self-assembly of nanoparticles is not a dormant field, however, and further investigation of these forces may be necessary to successfully control self-assembly at this scale. Table 2.1 provides a summary of all of the inter-particle forces discussed in this section. Manipulating these forces has lead to a wide array of applications, which will be discussed next.

Table 2.1 Characteristics of interaction forces between particles at liquid-liquid interfaces. Adapted from [23].

Interaction	Character	Functionality	Strength (kT)	Particle Size
Capillary	Attractive/Repulsive	ln(R/d)	10 - 10^5	nm - mm
Electrostatic	Repulsive	$(R/d)^3$	10 - 10^5	nm - μm
VdW	Attractive	$(R/d)^6$	0.1 - 1	nm - μm
Fluctuation	Attractive	$(R/d)^8$	1	nm
Solvation	Attractive/Repulsive/ Oscillatory		1	nm

The primary application of particle self-assembly at liquid-liquid interface is Pickering emulsions. As discussed before, the solid particles are adsorbed at the liquid-liquid interface and are expected to form a barrier preventing droplet-droplet coalescence, thereby stabilizing the emulsion. Ramsden [6] and Pickering [7] were the first to observe this type of emulsion in the early 1900's, but their findings did not receive wide attention until nearly a century later. Now Pickering emulsions are often encountered in the recovery, separation and cleaning of crude oil [50, 51], wastewater treatment [52], food industry [53], etc. In the last 20 years, there has been increased interest in Pickering emulsions because the open avenues for potential new applications. For example, emulsions stabilized by metal oxide particles are potentially attractive alternatives for conventional surfactants and may lead to new skincare and sunscreen formulations [54, 55]. Emulsions are widely encountered in food technology and effective emulsification is crucial to the quality, appearance and taste of many food products. Some of the particles that act as emulsifiers in food products are fat crystals and starch granules [56]. Fuller's group employed paramagnetic solid particles to prepare water-decane emulsions whose stability could be tuned and controlled using an external magnetic field [57]. In other

applications, the Pickering emulsion droplets can act as drug delivery vehicles for controlled release of therapeutic substances [58, 59]. Pickering emulsion droplets as template also offer novel synthetic routes for the synthesis of nanocomposites, with a polymeric core and outer shell of solid particles via a surfactant-free emulsion polymerization method [60, 61]. Our group has developed framework to synthesize temperature responsive core-shell nanoparticles for drug delivery [62, 63]. Using Pd, Resasco's group has shown that the stabilizing particles can be used as catalysts for hydrogenation reactions [2, 3]. Such a system significantly simplifies hydrogenation reactions because the products are separated from the reactants within the reactor, eliminating the need for expensive separation equipment [2, 3]. Recently, a new macroscopic structure call a "bijel" has started to draw attention. These are soft materials where both liquid phases are continuous and interpenetrating, separated by a "jammed layer" of solid particles [64]. Because of their unique bicontinuous nature, these materials may application as novel catalysis or mass transfer devices [64].

Self-assembly of microstructures and nanostructures is also of interest since it provides a "bottom-up" approach to synthesis of novel devices as opposed to lithography or microprinting, for example [65]. Self-assembled hollow spheres with a permeable shell of microparticles are known as "colloidosomes." Colloidosomes have potential application in controlled delivery and cosmetics, arising from the controllable permeability of the particle shell [59, 66-72]. Velev et al. first reported a technique for the preparation of hollow spheres by the assembly of micron-sized sulfate latex particles on the surface of octanol droplets in water [58]. Particles are generally cross-linked at the interface, leaving a stable colloidosome of a few nm to microns in diameter [65]. These

structures are generally very sturdy [73] and can be functionalized to be pH-sensitive [74]. Silica, CdSe, CdSe/ZnS, gold, Fe_3O_4 nanoparticles, carbon nanotubes, and nanorods can all self assemble into colloidosomes [65]. Figure 2.7 shows an example of a colloidosome formed from a Pickering emulsion droplet. Raspberry-type formations are solid cores decorated with smaller colloidal particles and can be formed by polymerizing or gelling the Pickering emulsion droplets covered with particles [65]. Other structures formed from Pickering emulsion droplets include rod-shaped liquid cylinders [75] and partially coalesced droplets [76].

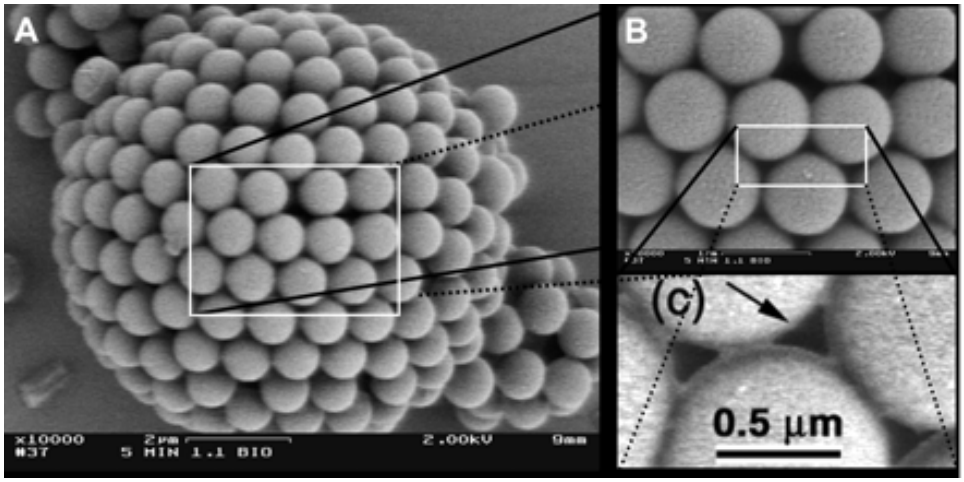

Figure 2.7 SEM images of a colloidosome formed by the self-assembly of polystyrene particles. Adopted from ref [59].

Nanoscale structures can also self-assemble at the liquid-liquid interfacial template. Russell and coworkers observed the size-dependent self-assembly and transport of ligand-stabilized CdSe nanoparticles across toluene-water interfaces [77, 78]. They also demonstrated a technique to crosslink the reactive ligand groups after the nanoparticles formed an interfacial layer, which yielded an ultrathin nanoparticle membrane with significant mechanical strength [79]. Moehwald and coworkers

extensively investigated the self-assembly of gold and silver nanoparticles capped with a variety of ligands with varying chain lengths [80, 81]. They also demonstrated the feasibility of using Fe_3O_4 nanoparticles to prepare novel magnetic colloidosomes with selective permeability to precisely control the transport across the self-assembled shell [82].

Apart from ligand-stabilized nanoparticles, other nanoparticles have also been employed. Simovic and Prestidge investigated the self-assembled structure of hydrophobic and hydrophilic silica nanoparticles at the polydimethylsiloxane (PDMS)-water emulsion interfaces [83-85]. In a unique application, Russell et al. used liquid-liquid interfaces for self-assembling and crosslinking of bionanoparticles [86]. The self-assembly of carbon nanotubes [87, 88] and lipid nanotubes [89] at Pickering emulsion interfaces has also been reported. Other instances of self-assembly of nanoparticles at liquid-liquid interfaces are the composite hollow spheres formed by gold nanoparticles-tetrapyridylporphine [90], formation of "breath figures" – nanoparticle assemblies confined to ordered arrays of spherical cavities [91], and shells of heterodimers of nanoparticles with functionalized surfaces [92].

One of the most interesting applications of this phenomenon is the self-assembly of biomaterials. Significant findings in this area have emerged mainly in the last 5-7 years. Russell and coworkers recently demonstrated that virus particles could self-assemble and crosslink at the oil/water interface to create "virus-based" membranes [86, 93]. Virus particles remained intact and the membrane was stable[86, 93]. Proteins and viruses can also self-assemble at Pickering emulsion droplet interfaces to create bio-"cages" [94]. Similar to the raspberry structures mentioned above, solid cores can be

functionalized with biomaterials after they have self-assembled at the soon-to-be solidified droplet interface [95-97]. Finally, by increasing the viscosity of one of the liquid phases, Kaur et al. induced the self-assembly of and cross-linked turnip yellow mosaic viruses at the oil/water interface[93]. The resulting 2D crystal could be transferred to a solid substrate for further use (See Figure 2.8) [93] . A more complete review of interfacial self-assembly of viruses can be found in ref [94].

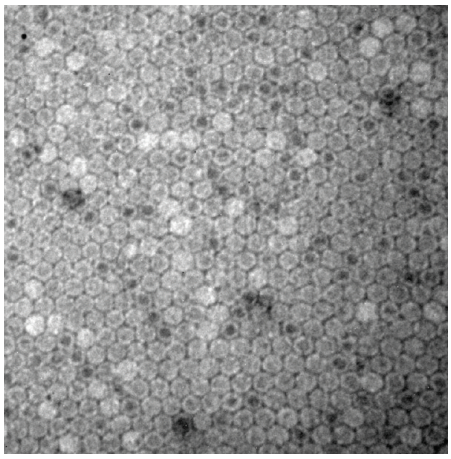

Figure 2.8 TEM image of the self-assembled 2D crystal of turnip yellow mosaic viruses. Adapted from ref [93].

Particle-self assembly at liquid-liquid interfaces has already seen significant application, as demonstrated by the wide array of Pickering emulsions, particle types, and micro/nano structures available in the literature. Tuning of this phenomenon is primarily accomplished by functionalization of the particles themselves. However, tuning by the solvent is certainly viable, as demonstrated by the dependence of the inter-particle forces on solvent properties. Manipulating these properties can be difficult and somewhat prohibitive given the fixed molecular nature of each type of solvent. Ionic liquids, however, may overcome this obstacle, as discussed in the next section.

2.2 Ionic Liquids

Nearly every field of science and engineering deals with liquids to some degree. Consequently, liquids are generally well characterized and their thermophysical properties can be accurately predicted by theoretical and empirical relationships. In fact, so great is our familiarity with liquids that qualitative judgments are easily made upon examination of the molecular structure alone (i.e. large molecules have lower vapor pressures). Ionic liquids (ILs, sometimes referred to as "molten salts at room temperature" [98]) present significantly different behavior and often exhibit exciting capabilities. They are, in fact, a new class of liquids. In contrast to the common liquids consisting of a single molecular component, ILs are binary mixtures of charged species. Effectively, they are molten salts whose melting point is below 100^{o}C[99, 100]. The unusually low melting point is due to steric resistance to packing[101]. Unlike most ionic compounds, the components of ILs are irregularly shaped and do not readily form crystalline lattice structures. Figure 2.9 gives a basic comparison of ILs to crystalline salts and conventional oils.

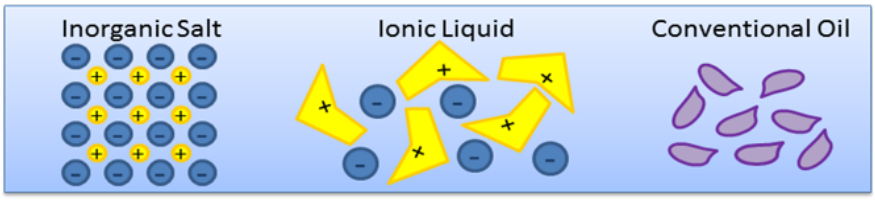

Figure 2.9 General comparison of inorganic salts, ionic liquids, and conventional oils.

The liquid state is very advantageous since most industrial settings have frameworks in place for liquid handling. In fact, one of the hallmark advantages ILs present is negligible volatility, which makes them excellent candidates as "green

solvents" to replace their air-polluting counterparts in existing chemical plants[100]. Even so, little is known about their thermodynamic and transport properties and there are few studies on their interaction with other species. As exemplified by their unusually low melting point, traditional thermodynamic relations do not easily predict the behavior of ILs. Much work remains to be done in order to understand this new class of liquids as well as the old. Despite this relative difference in understanding, applications involving ILs have become prolific in the last 20 years. This section will touch briefly on their history, general properties, and exciting applications.

Paul Walden was the first to report the evidence of an IL, ethylammonium nitrate, in 1914[99]. This IL was formed upon combination of ethylamine and nitric acid and had a melting point of 13-14^{o}C[99]. However, as with Pickering and Ramsden, Walden's discovery received negligible attention for nearly a century. The few publications that surfaced between that time and the early 1990's primarily dealt with non water-stable, and consequently non air-stable, ILs based on the chloroaluminate (III) anion[98, 102, 103]. The inherent water instability of these ILs presented great restriction to their application chemical processes[100]. Hence the sparse work. It was not until 1992 that alternative anions were suggested and water-stable ILs could be formulated[104]. Soon after this groundbreaking publication, researchers realized that it was possible to formulate a large number of ionic liquids simply by generating combinations of different cations and anions. Although there are over 10^6 possible ion combinations that result in an IL [105], Figure 2.10 lists a few of the most commonly used ions [106].

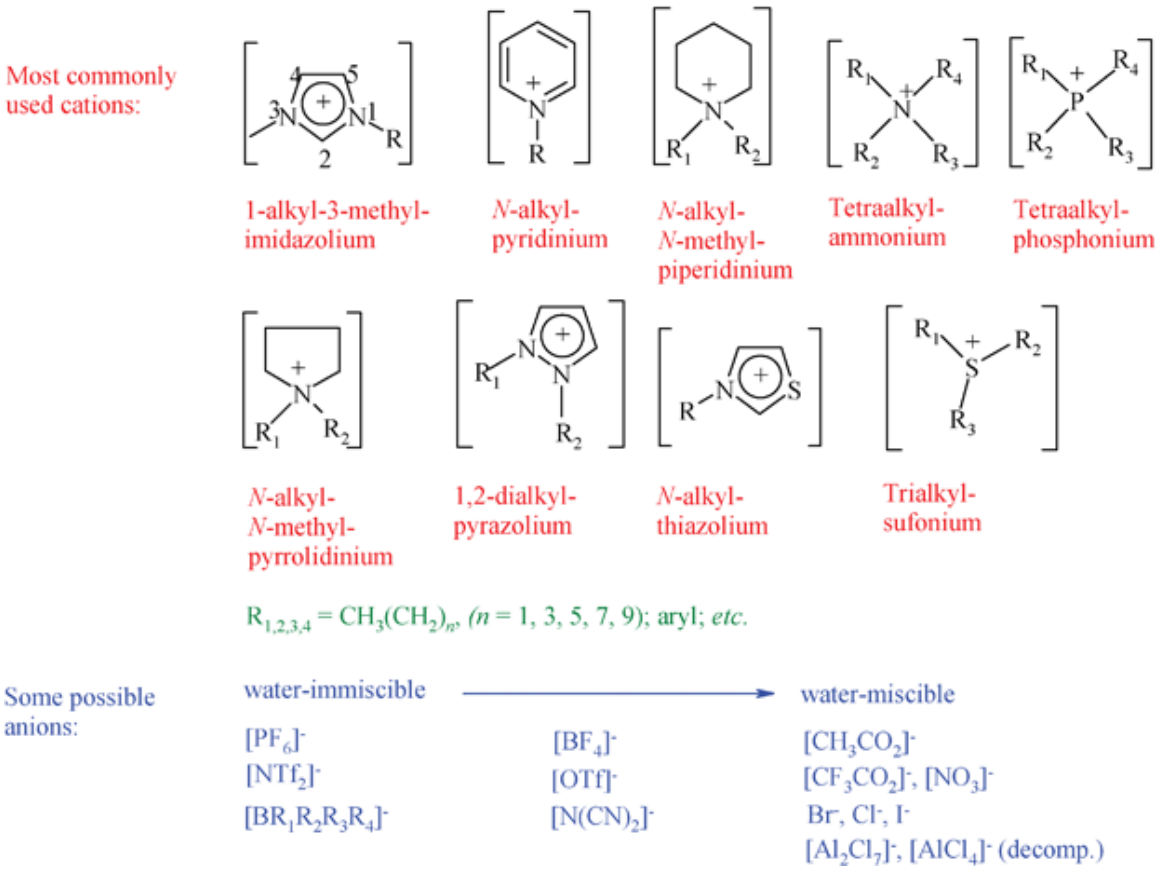

Figure 2.10 Commonly used IL ions. Adopted from [106].

Even within this small group, a large number of ILs are possible. However, only two ILs seem to receive widespread attention across multiple literature sources: 1-butyl-3-methylimidazolium hexafluorophosphate and 1-butyl-3-methylimidazolium tetrafluoroborate [107]. Imidazolium-based ILs are the most widely studied of all, probably due to ease of synthesis [108]. Since the seminal publication of Wilkes and Zaworotko [104], articles and patents with reference to with ILs have proliferated extensively, especially in the last 10 years. Figure 2.11 shows the number of publications including the words "ionic liquid" each year since 1992.

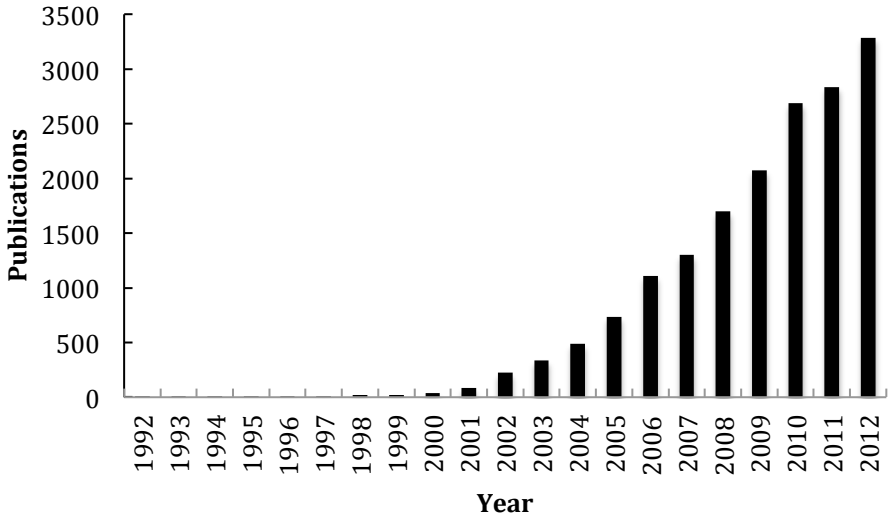

Figure 2.11 Publications per year that include the words "Ionic Liquid." [109]

As of the writing of this document, there have been already over 1000 such publications for 2013 [109]. Some of the leading research groups in this area are those of Edward Maginn and Joan Brennecke at the University of Notre Dame, Kenneth Seddon at Queens University Belfast, Gregory Warr at the University of Sydney, and Jose Nuno A. Canongia Lopes at the Technical University of Lisbon. A more detailed history of IL research can be found in an in-depth review by Plechkova and Seddon [100].

Synthesis of ILs is usually performed near ambient conditions. Reagents are generally commercially available or easily synthesized in the laboratory. The two most common methods of preparation are metathesis and acid-base neutralization [110]. Metathesis reactions occur when two molecules exchange a bond [111] as shown below in Equation 2.12.

$$AB + CD \rightarrow AD + CB \qquad (2.12)$$

Metathesis is how most of the imidazolium and tetraalkylammonium ILs are synthesized [110]. For example, in 1992, Wilkes and Zaworotko synthesized [EMIM][BF_4] by combining [EMIM]I and Ag[BF_4] in methanol[104]. [EMIM][PF_6] was first prepared by mixing [EMIM][Cl] and HPF_6 [112]. The resulting ILs can purified (often by evaporation of the contaminants), but trace halides are sometimes still present[113]. Acid-Base reactions are used to formulate monoalkylammonium ILs. The general scheme is shown below in Equation 2.13.

$$R\text{-}NH_3 + H\text{-}B \rightarrow NH_4^+ + B^- \qquad (2.13)$$

The first IL by Walden [99] as well similar ILs are prepared by combining equimolar amounts of the appropriate amine with nitric or formic acid[114]. Water and other impurities can be removed in vacuum. A more complete summary of IL synthesis can be found in refs [110, 115].

As mentioned before, thermodynamic relations to describe ionic liquids are far from developed. It has been noted that lack of knowledge is one of the major obstacle preventing widespread industrial applications of ILs[107, 108, 116]. A number of general characteristics of ILs are known, however, and it is worthwhile to discuss them here. As fluids, they are generally Newtonian [117], highly viscous, and denser than water. These properties, as well as others such as water miscibility, melting point, decomposition temperature, self-diffusivity, heat capacity, and solvation properties can be tuned to the desired application simply by judicious choice of anion and cation. A list of properties and their general ranges for ILs is shown in Table 2.2. It should be noted that the data for this table was determined by a scan of the literature, not individual experiments.

Table 2.2 General properties of pure ILs with their respective ranges as determined experimentally.

Property	Units	Range	References
Melting Point	^{o}C	-30 - 100	[118, 119]
Specific Gravity	-	0.8 - 3.3	[100]
Viscosity(20oC)	cP	22 - 40,000	[119, 120]
Surface Tension	mN/m	34 - 55	[120]
Heat Capacity (300 K)	J/mol*K	300 - 360	[107]
Liquid Range	^{o}C	Up to 400	[108]
Decomposition T	^{o}C	374 - 500	[108, 118]

Vapor phase data are not included in Table 2.2 because one of the hallmark features of ILs, and the main reason they are termed "green solvents," is their unusually high resistance to evaporation. This does not mean, however, that they cannot exist in the vapor phase. In a publication in *Nature* [121], Earle et al. showed that under low pressures (0.1-5.0 mbar) and high temperatures (300^{o}C), ILs could actually vaporize and mixtures of ILs could be purified via distillation. The vapor "particles" have been determined to be single pairs of ions [122], thus maintaining charge neutrality. Given that measureable quantities of vapor existed only at high temperature vacuum conditions, the vapor pressure of ILs at room temperature can be considered negligible (it usually immeasurable).

Wide tunability of most properties is possible simply by changing the size, shape, or functionality of one of the constituent ions. Since the resistance to crystalline packing maintains the liquid state, one can infer that melting points would be a function of the geometric mismatch of the ions. Holbrey et al. showed that increasing the alkyl chain length on the imidazolium cation resulted in lower melting points[123]. Small anions tend to decrease the melting points as well[100]. Melting points show also a strong

dependence on a subtler characteristic of the IL: cation symmetry. Bonhote et al. and Seddon have shown that cation asymmetry greatly decreases the melting point [119, 124]. Therefore, in order to lower the melting point of an IL, ions with a higher geometric mismatch can be chosen.

On the other end of the liquid range, ILs generally undergo thermal decomposition instead evaporation. The thermal decomposition temperature is most affected by the nature of the anion. Huddleston et al. showed that for imidazolium-based ILs, the decomposition temperature followed the following trend: Tf_2N > BF_4 > PF_6 > halides [125]. Therefore, for high-temperature applications, Tf_2N ILs should be used. It should also be noted that PF_6-based ILs risk hydrolysis of the anion upon contact with small amounts of water, which releases HF [126]. Even so, [BMIM][PF_6] is one of the most widely studied ILs. Therefore, the upper end of the liquid range can be tuned by judicious choice of the anion.

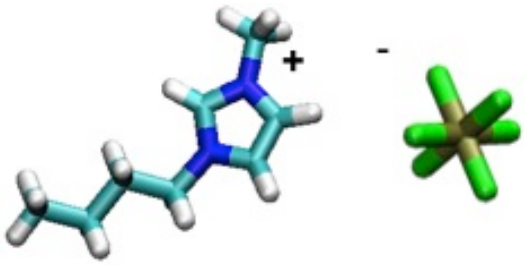

Figure 2.12 1-Butyl-3-Methylimidazolium Hexafluorophosphate ion pair, the most widely studied IL despite its hygroscopic nature and subsequent reaction with water that produces HF. C, N, H, P, and F atoms are represented in cyan, blue, white, gray, and green, respectively.

Of particular interest to this study, ion choice also affects water miscibility. For example, we have observed that [BMIM][BF_4] is miscible with water, while [BMIM][PF_6] is not. Seddon et al. present evidence that in 1-alkyl-3-methylimidazolium

ILs, the anion is the primary factor in determining water miscibility as follows: ILs with $[PF_6]$ and $[(CF_3SO_2)_2N]$ anions are immiscible with water, while those with halide, ethanoate, nitrate, and trifluoroacetate ions are miscible with water [127]. The chain length of the alkyl group can also influence water miscibility, with longer chain lengths resulting in decreased miscibility [127, 128].

Prediction schemes for other properties are not as straightforward. Viscosity is affected by the ion structures in a more subtle way. The research group of Dr. Mark Kobrak has proposed that this property depends on the "charge arm" or distance between the center of mass and the center of charge on each ion[129]. As of yet, this seems to be the most obscure structural characteristic used to predict bulk properties. Structural features, however, currently form the basis of all prediction schemes for ILs. No equations of state are available for predictions of PVT behavior. However, group contribution theory [130, 131] has been used to estimate critical properties and acentric factors of many ILs [132]. Those properties were indirectly validated by calculating densities with correlations that used them and comparing to experimental measurements [132]. Empirical models like this currently constitute the primary method for prediction of thermophysical properties[108]. Along with high cost and viscosity, this problem represents the main obstacle in industrial IL applications.

Despite these complications, applications that include ILs are not few in number. Foremost are applications taking advantage of IL solvent capabilities. Compared to the 600 solvents currently used in industrial processes [100], the number possible pure IL formulations (not to mention binary and ternary mixtures) is nearly infinite. It is therefore believed that ILs could be tailored to fit the needs of any solvent application. For this

reason, they are often called "designer solvents." Seddon even commented, "For the first time, it is possible to design a solvent to optimize a reaction (with control over both yield and selectivity), rather than to let the solvent dictate the course of the reaction[133]." Indeed, there is evidence that reactions can be carried out with higher yield in ILs and sometimes undergo new mechanisms[108, 110, 124, 134-136]. Another advantage of ILs is that they can solubilize both polar and non-polar solvents. [BMIM][PF_6] can dissolve a number compounds from benzene to alcohols[137]. Clearly, ILs have great potential as versatile solvents. While technology is still evolving to live up to that potential, IL researchers in academia have repeatedly predicted widespread industrial application of ILs. Table 2.3 is an adaptation from ref [100] that gives a good comparison of ILs to organic solvents in light of industrial application.

Table 2.3 Comparison of ILs to organic solvents in light of industrial application. Adapted from ref [100].

Property	**Organic Solvents**	**Ionic Liquids**
# of Solvents	>1,000	>1,000,000
Applicability	Single function	Multifunction
Catalytic ability	Rare	Common and tunable
Chirality	Rare	Common and tunable
Vapor Pressure	Obeys the Clausius-Clapeyron Eqn.	Negligible under normal conditions
Flammability	Usually flammable	Usually nonflammable
Solvation	Weakly solvating	Strongly solvating
Tune ability	Limited range of solvents available	Virtually unlimited range
Cost	Normally cheap	2x to 100x the cost of organic solvents
Recyclability	Green imperative	Economic imperative

One of the famous applications of ILs is in CO_2 absorption. Joan Brennecke and Edward Maginn have pioneered this subject with both experimental and theoretical

studies[138-142]. Gurkan and coworkers (Brennecke research group) even showed that for every mole of IL, nearly a mole of CO_2 can be absorbed (See Figure 2.13) [140] . After absorption, the CO_2 can be removed from the IL by applying lowering the pressure and raising the temperature. This application is of particular interest given the recent focus on CO_2 emissions. Fortuitously, the negligible volatility of ILs makes them excellent candidates for supported liquid gas separation membranes, which suffer degradation due to liquid loss [108, 143-145].

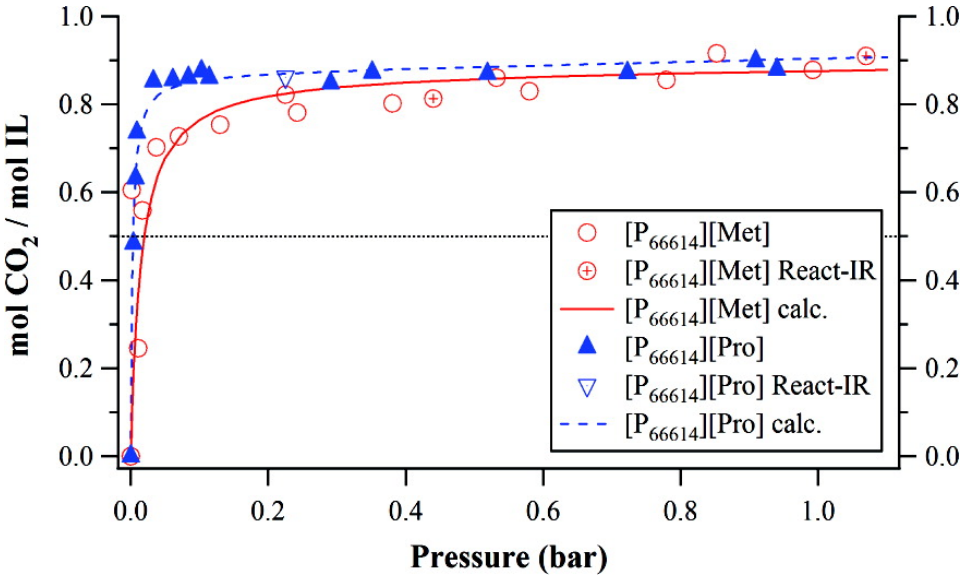

Figure 2.13 CO_2 absorption by ILs $[P_{66614}][Met]$ and $[P_{66614}][Pro]$ at 22°C. Adapted from ref [141].

ILs also readily absorb other gas species. A revolution in gas storage technology is taking place at Air Products. Two patents submitted in 2006 [146, 147] describe a system in which gases can be stored and transported at sub-atmospheric pressures by absorbing them in an IL. Gases can be easily removed at room temperature upon applying a vacuum [148]. The authors tuned the IL by selecting anions that complex with the gas (Lewis acid-base chemistry) to be stored [148]. Air Products' invention is a prime

example of how ILs can be tailored to specific applications and dramatically improve process safety. Plechkova and Seddon call it “a true green chemistry success [100].”

Gas molecules are only the beginning for IL absorption technology. In a recent article in *Science*, Dr. Paul Painter’s group at Penn State showed that ILs successfully separated silica particles from oil/sand mixtures (See Figure 2.14) [149] . Actual sand from the contaminated BP spill site was clean within seconds [149]. AFM measurements suggest that the silica-oil binding energy is reduced in the presence of the IL, which may aid in their separation [150].

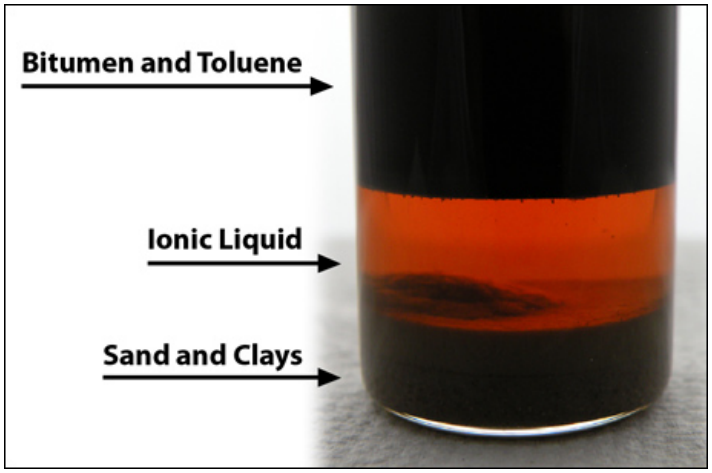

Figure 2.14 An oil/sand mixture separated by an IL. Adopted from ref [149].

Providing a way of efficiently cleaning oil sands would have significant environmental impacts. Industrial implications are also likely since this process would significantly reduce the cost of processing oil tars for gasoline and oil production. Solid particle absorption has also been observed in our lab where sulfate-treated polystyrene particles were absorbed from the water phase into IL emulsion droplets [151]. This unique absorption capability may allow ILs to see applications in water treatment and novel cleaning products.

The applications mentioned thus far represent only the more famous developments to date. ILs have also seen use in extraction [152-154], lubrication [155, 156], batteries [157, 158], surfactants [159, 160], and paint additives [161]. Using the feature of negligible vapor pressure, Linde has developed a gas compressor that uses an IL piston and has only eight moving parts [162-164]. ILs have also been used to break common azeotropes such as water-ethanol and water-tetrahydrofuran [100, 165]. Many large chemical companies such as ExxonMobil, SASOL, BP, Chevron, and PetroChina have started to show interest in developing IL technology[100]. A recent review in *Nature Materials* commented that ILs were "the basis of a quiet revolution in materials science[156]." It can only be expected that more exciting IL innovations are on the horizon.

ILs represent a new class of liquids of great interest to the science and engineering community. New applications are surfacing every year and ILs are expected to replace volatile organic solvents in favor of greener processes. However, fundamental understanding of IL properties and behavior is only in its infancy. Liquid-liquid interfaces are no exception: there is much work to be done. The purpose of this study is to obtain fundamental understanding of the unique properties and phenomena of self-assembly at IL-based liquid-liquid interfaces. Interfacial self-assembly is currently governed by the particle properties, which sometimes requires expensive particle functionalization. Solvent-tuned self-assembly may allow for formation of the same micro- and nano- structures regardless of particle properties. The remarkable tunability of ILs makes them ideal candidates for such a potentially advantageous process. It is hoped

that further study of their interfaces will enhance existing understanding and promote new and exciting applications for a variety of fields.

CHAPTER 3

IONIC LIQUID-BASED INTERFACES AND THEIR INTERACTIONS WITH MICROPARTICLES

3.1 Introduction

Since excitement about ILs is still rather recent, little is known about IL-based interfaces. In general, interfacial tensions are rather low: IL/water and IL/oil interfacial tensions are between 10 and 20 mN/m [166]. We have measured the interfacial tension between two ILs (Ethylammonium nitrate and trihexyltetradecylphosphonium bis(2,4,4-trimethylpentyl)phosphinate) to be 0.952 mN/m. As ILs possess many unique properties and capabilities, so do their interfaces. Section 3.3.1 will discuss some of these properties with special attention to the dynamics of IL-based interfaces. Particularly, section 3.3.1 will address the transitory nature of the interface between mutually miscible ILs. When two mutually miscible liquids come in contact, a sharp concentration gradient is initially formed. Despite the fact that the liquids indeed mix, this concentration gradient represents a difference in chemical potential and can result in a transitory interfacial tension, as shown in Equation 3.1 [167, 168].

$$\gamma \propto \int_{x_1}^{x_2} \left(\frac{dc}{dx}\right) dx \tag{3.1}$$

Here γ represents the interfacial tension, c represents the concentration, and the x direction is perpendicular to the interface. While this interfacial tension is often small and decays quickly (with $t^{-1/2}$) [168, 169] , it can be measured [168, 170-173] and even influence mixing behavior [169, 174-177]. As the two liquids mix, interesting optical and structural phenomena emerge such as graded profiles of refractive index [178], fingering

[179, 180], and fractal structures similar to crystal growth[181, 182]. More importantly, this phenomenon is of great importance to the field of microfluidics. In contrast to macroscopic systems, laminar flow dominates in microfluidic devices and introduces difficulties in mixing, especially at high Peclet numbers[183-186]. Microfluidic technology has begun to revolutionize fields of analysis [187], particle synthesis[188, 189], and reaction engineering[190]. ILs are also gaining ground in these fields [100, 110, 115, 191] and have been seen in recent microfluidics applications [192, 193]. Given this trend, we believe that investigation of non-convective mixing of ILs is imperative.

Why should mixing ILs be different than mixing molecular liquids? The first difference lies in the binary nature of ILs: ions within one IL may diffuse into the other IL at different rates. This feature turns a binary diffusion problem into a quaternary diffusion problem. Secondly, very little is known about the interface between two ILs. These interfacial species experience high coulombic interactions and many orientational degrees of freedom over which to influence interfacial behavior, due the binary nature of ILs (i.e. more interfacial molecular configurations are possible with four species than with just two). It is expected that the effect of coulombic interactions would be especially significant because of the long-range nature of these forces. In this study we primarily explore the mixing of two ILs: 1-butyl-3-methylimidazolium hexafluorophosphate ([BMIM][PF_6]) and ethylammonium nitrate (EAN). Both experimental and computational results are discussed in section 3.3.1.

Section 3.3.2 will introduce particles at IL-based interfaces and observe their interactions. Interactions between particles and liquid-liquid interfaces have received increased attention in recent years, specifically with self-assembly processes [65] and

Pickering emulsion formulation [6, 7]. These applications are driven by strong adhesive forces between the particles and the liquid-liquid interface (on the order of 10^6 kT for microparticles [14]). For example, in Pickering emulsions the strongly adhered particles form an "armor" around each droplet, preventing coalescence during collision [6, 7]. In fact, this adhesive force is so strong that an excess of microparticles can "jam" the interface, causing droplets to deform into a variety of shapes [75, 194]. In light of this strong interaction, one may ask a trivial question: is it possible to transport a microparticle *through* the liquid-liquid interface? Such a phenomenon has relevance to applications such as particle extraction [150, 195-197], nanoparticle synthesis [198-200], and microstructure self-assembly [67]. To pass from one liquid phase to another, a particle must overcome those strong forces that would cause it to adhere to the interface. To our knowledge, *spontaneous* occurrence of this phenomenon has not yet been observed at oil/water interfaces. Only by propelling the particles with shear forces (and sometimes functionalizing them with surfactants) can particles be forced to cross. Section 3.3.2 presents direct observations of a new phenomenon in which microparticles were spontaneously transported through liquid-liquid interfaces with the aid of neither shear forces nor surfactants. These interfaces were based on a class of materials named ionic liquids (IL), some of which can absorb micron-sized particles from water or oil without any external agitation.

Even with the help of shear forces and surfactants, examples of particle transport across the interface are not very numerous. One of these examples is the work of Velev et al. [67] in which surfactant-covered latex beads were transported from the water continuous phase into octanol emulsion droplets. The authors suggested that the

surfactant provided a positive charge to the particles, increasing their attraction to the negatively charged octanol droplets [67]. Recently, Dai and co-workers reported that apart from covering 1-butyl-3-methylimidazolium hexafluorophosphate (an IL) emulsion droplets, some polystyrene microparticles could be completely extracted from the water phase by the IL [151, 201]. Wei et al. showed that upon agitation, gold nanoparticles could also be extracted from water into an IL phase [202]. Painter et al. have shown that sand particles can be removed from oil/sand mixtures within seconds by mixing with an IL [150, 195-197]. This separation technique has potential in oil sand processing as well as oil spill beach cleanup since the separated sand is "so clean you could toss it back on the beach [149]." In the field of nanoparticle synthesis, phase transfer is necessary where the synthesis phase differs from the application environment [198-200]. For example, metal nanoparticles can be synthesized with high precision and unique functionality in organic phases, but must be (and are) transferred to an aqueous phase to realize any biological application [198, 199].

Again, in all of these examples, mixing (and sometimes surfactant) was used to help particles overcome the adhesive effect of the oil/water interface. To accomplish this task without these aids requires a new interfacial phenomenon in which the adhesive forces can be bypassed. Our report demonstrates that some IL-based systems possess this unique capability and can actually transport microparticles across the interface spontaneously. This phenomenon was recorded microscopically in real time.

Having discussed the fundamentals of particle interactions with IL-based interfaces, section 3.3.3 will explore applications of these interactions in the context of Pickering emulsions. As mentioned in Chapter 2, the standard morphology in Pickering

emulsions consists of single droplets armored with a monolayer of solid particles. One important aspect of Pickering emulsions is that depending on the nature of the solid particles as well as the properties of the liquid phases, the self-assembled particles at the liquid-liquid interface may exhibit a variety of patterns. For example, the self-assembly of polystyrene microparticles at oil-water emulsion droplet interfaces has been well studied and the structure ranges from aggregated domains to ordered lattices [24, 203-205]. The morphology of these structures depends strongly on the surface chemistry of the solid particles and the nature of the interface. Figure 3.1 shows some standard examples of Pickering emulsion droplets covered with particles.

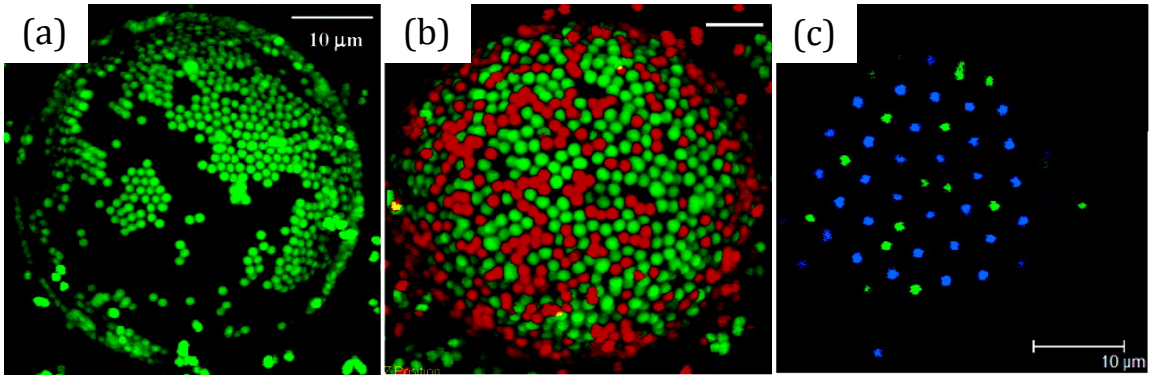

Figure 3.1 Oil droplets in water covered with polystyrene particles (1.0 micron diameter) in various morphologies. Images a and b were adopted from ref [24] and image c was adopted from ref [34].

Particle self-assembly at IL-water interfaces differs significantly in morphology to that at oil-water interfaces. Ma and Dai observed that the microparticles on the [BMIM][PF_6] droplets in water did not form colloidal lattices, but partially to completely covered the droplets in a close-packed configuration (See Figure 3.2) [151] . One hypothesis is that because of the higher ionic strength of the ionic liquid, the repulsive forces between the particles were screened, thus eliminating the lattice structure and

enabling closer packing [151, 206]. Nakashima et al. showed that particle packing at the same IL-water interface could be tuned by adjusting the chemical structure of the IL and the pH of the aqueous phase [207]. These authors suggested that adsorption of negatively-charged nanoparticles was electrostatically driven because the IL interface might carry a net positive charge [207]. Interestingly, in the experiments of Ma and Dai, positively-charged microparticles adhered to the IL-water interfaces just as well as negatively charged microparticles [151]. Clearly more research on particles at interfaces involving ILs is needed due to the complex nature of these systems.

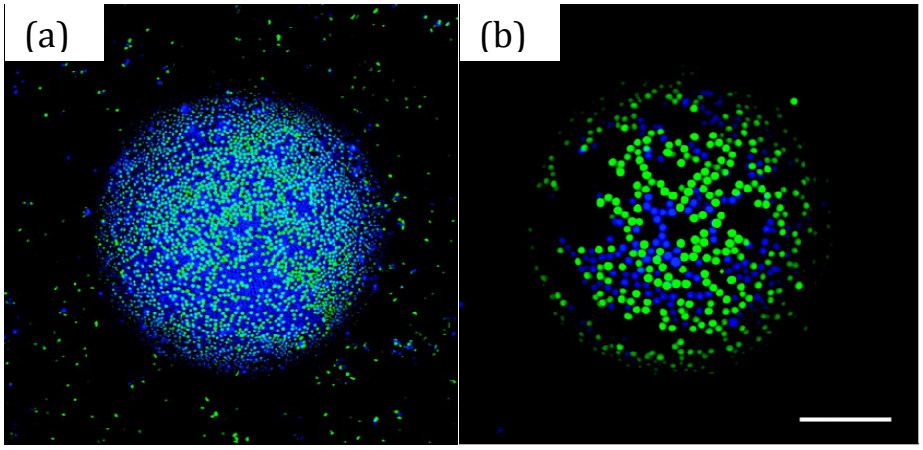

Figure 3.2 IL Pickering emulsion droplets in water covered with polystyrene particles. Adapted from ref [151].

The above morphologies were observed on isolated Pickering emulsion droplets (with the exception of the work of Nakashima et al., which used flat interfaces). As a particle-laden droplet approaches another interface, the solid particles can self-assemble into new structures, coined "bridges" [42-47, 208, 209] that resemble disc and/or ring shapes [43-45, 47]. These bridges can serve as adhesives between liquid interfaces [46, 47]. Fuller and co-workers have conducted extensive and elegant studies of particle self-assembly in an oil layer confined between a droplet and a flat interface of water [44-47].

They showed that the particles formed tightly packed ring and disk shapes in the film [44, 45, 47]. Due to capillary forces, the particles bridged and provided adhesive forces between the droplet and the planar interface [46]. Horozov et al. studied a controlled particle-laden film and found that film stability depended on the hydrophobicity of the particles and corresponded directly to emulsion stability [43].

It is worthwhile to note that bridging plays an important role in emulsion stability. The coalescence process of two emulsion droplets is dependent on the drainage rate of the thin film separating them [210]. Normally, this drainage rate depends primarily on the force bringing the droplets together and the viscosity of the film itself [211, 212]. With the presence of particles in the film, however, elastic inter-particle interactions must be taken into account [213]. By approximating these interactions with a bead-and-spring model, Tambe and Sharma showed that the presence of particles in the inter-droplet film caused the film to behave like a viscoelastic material [213]. Hence, the film drainage rate could be slowed significantly and even halted at sufficiently high particle packing in the bridge [213]. In this manner the solid particles stabilized emulsion droplets against coalescence.

Herein we report a unique and new phenomenon that in oil (polydimethylsiloxane, PDMS)-in-[BMIM][PF_6] Pickering emulsions, solid particles only formed bridges between the oil droplets and avoided in contact with the ionic liquid phase. Thus, this behavior represents a sharp contrast from conventional Pickering emulsions (see Figure 3.1 and Figure 3.2). Although the bridges prevented droplet-droplet coalescence, surprisingly, the presence of solid particles hurt the overall emulsion stability by increasing the rate of flocculation and creaming. In addition, we report on

how the morphology of these bridges and the consequent droplet structures depended on the surface chemistry and composition of the solid particles.

However, to further control these Pickering emulsions, an additional component was needed. By incorporating an organogelator, 12-hydroxystearic acid (12-HSA), we were able to stabilize as well as reveal new applications for IL-based Pickering emulsions. There has been a growing interest in making semi-solid colloidal particles through hot emulsification followed by cooling to room temperature [34,35]. Ma and Dai reported that [BMIM][PF_6] had good extraction ability for certain types of particles in [BMIM][PF_6]-in-water Pickering emulsions [32]. The motivation of this study is to perturb these Pickering emulsions by employing a gelator, 12-Hydroxystearic acid (12-HSA), to solidify ionic liquid droplets containing extracted particles. The gelator 12-HSA, mainly produced from castor oil by hydrogenation of the double bond, has been used as a low molecular mass organogelator (LMOG) [36-39]. LMOG-based gels are prepared by mixing the melted gelator and solution at high temperature and then cooling the solution mixture at gelation point. Most of them are physical gels that are thermally reversible because the fiber structure network that immobilizes the solution is formed by non-covalent interactions [38]. Voss et al. prepared ionic liquid solid membranes for CO_2 separation application by physical gelation of 1-hexyl-3-methylimidazolium bis-(trifluoromethylsulfonyl)imide [C_6mim][Tf_2N] using a small weight percent of 12-HSA [36]. In this report, we will study how 12-HSA affects [BMIM][PF_6]-in-water and PDMS-in-[BMIM][PF_6] Pickering emulsions. The original objectives were to gel IL by 12-HSA to solidify IL droplets with extracted particles in water and to stabilize the oil-in-

IL Pickering emulsion by taking the advantage of the sol-gel transition of 12-HSA. These results are discussed in Section 3.3.4

Finally, we return again to the IL/IL interface in section 3.3.5. To our knowledge, a Pickering emulsion in which both droplet and continuous phases are ILs has not yet been explored. This section discusses our findings on this type of system. Indeed, an IL/IL Pickering emulsion is a novel formulation. However, both phases and particles offering high tunability, the IL/IL Pickering emulsion may be suited for the widest array of applications. Furthermore, since ILs exhibit negligible volatility and high stability, this type of emulsion may be well suited for extreme environments. The first step was to determine pairs of mutually immiscible ILs. In the literature, ILs are often mixed completely for enhanced tunability [214]. However, mutually or partially immiscible ILs have been reported [215-217]. These immiscible pairs are generally between imidazolium- and phosphonium- based ILs. The mechanism behind this immiscibility is that as the smaller imidazolium ions diffuse into the phosphonium IL they form strong hydrogen bonds that increase the degree of order within the phosphonium IL, resulting in a negative entropy of mixing [216]. Both bridging and particle absorption were observed in these emulsions, but the phenomena were mutually exclusive. The appearance of either one depended on droplet phase, continuous phase, and particle surface chemistry.

3.2 Methodology

3.2.1 Materials

Table 3.1 lists the chemicals employed in the studies of this chapter. The particles (FluoSpheres® fluorescent microspheres from Molecular Probes™) were received as a 2% dispersion in distilled water with 2 mM sodium azide. Particles of 0.2, 1.0, and 4.0

μm in diameter were used in this study. 4.0 μm particle dispersions also contained 0.02% Tween 20. Four types of particle surface chemistries were incorporated in these studies; each type had various surface chemistries, fluorescent labels, surface charge densities, as shown in Table 3.2. It is also worthwhile to note that the S-PS and AS-PS particles were both relatively hydrophobic whereas the C-PS and A-PS particles were both relatively hydrophilic.

Table 3.1 Chemicals employed in studies of Chapter 3

Chemical	Supplier	Purity
1-Butyl-3-methylimidazolium Hexafluorophosphate	Aldrich	97%
Choline Bis(trifluoromethylsulfonyl)imide	Iolitech	99%
Ethylammonium Nitrate	Iolitech	97%
1-Methyl-1-propylpyrrolidinium Bis(trifluoromethylsulfonyl)imide	TCI America	NR
1-Butyl-3-methylimidazolium Bis(trifluoromethylsulfonyl)imide	Aldrich	98%
Trihexyltetradecylphosphonium Bis(2,4,4-trimethylpentyl)phosphinate	Aldrich	95%
1-Butyl-3-methylimidazolium Tetrafluoroborate	Aldrich	97%
Nitric Acid	VWR	68-70%
Ethylamine Solution	Aldrich	66-72%
Polydimethylsiloxane (PDMS, Rhodorsil Fluid 47, kinematic viscosity of 20 cSt at 20oC)	Rhodia Silicones	NR
Water	Fisher Scientific/Arcos Organics	HPLC Grade
12-Hydroxystearic Acid	Aldrich	NR
Poly(ethylene glycol) (200 MW)	Sigma-Aldrich	NR
Phosphorus Pentoxide	Sigma-Aldrich	NR

Table 3.2 Characteristics of Polystyrene Particles

Type	Surface Dissociable Group	Diameter (μm)	Surface Charge Density (C/m^2)	Excitation/Emission Wavelengths (nm)
S-PS	Sulfate	1.0 ± 0.031	-0.029	580/605
S-PS	Sulfate	1.0 ± 0.031	-0.288	505/515
S-PS	Sulfate	0.19 ± 0.006	-0.010	505/515
S-PS	Sulfate	4.2 ± 0.21	-0.110	505/515
AS-PS	Aldehyde Sulfate	1.0 ± 0.028	-0.088	505/515
C-PS	Carboxylate	1.1 ± 0.035	-0.325	540/560
C-PS	Carboxylate	0.21 ± 0.01	-1.947	540/560
A-PS	Amine	1.0 ± 0.023	0.152	505/515

3.2.2 Synthesis and Formulation

Synthesis of Ethylammonium Nitrate (EAN)

EAN was synthesized via acid-base neutralization of ethylamine and nitric acid. The reaction scheme is shown below.

$$CH_3CH_2NH_2 + HNO_3 \rightarrow [CH_3CH_2NH_3^+][NO_3^-] \quad (3.2)$$

Ethylamine was received as a solution in water in order to minimize vapor loss. According to the material safety data sheet (MSDS), ethylamine solution is fairly volatile, with a vapor pressure of 1148 mmHg at 50°C. It is also a serious eye, skin, and lung irritant and should thus handled only under the hood with gloves and proper eye protection. This solution is very basic, having a pH greater than 14 at room temperature. Ethylamine solution is also highly flammable (flash point = -17°C) and should be stored at refrigeration temperatures. Nitric acid is also toxic, and should be handled with the same personal protection equipment as with ethylamine. Also, one should keep in mind that this is a concentrated acid with a very low pH.

The reaction shown in Equation 3.2 was be accomplished by combining nitric acid and excess ethylamine solution. The synthesis apparatus can be seen in Figure 3.3. Nitric acid was added drop-wise to the ethylamine solution under constant stirring in an ice bath, as has been done in the literature [114, 218]. This reaction was considerably exothermic, especially in the initial stages when ethylamine concentrations were the highest. After the reaction finished, water impurities were removed in two stages. In the first, the entire reaction mixture was placed in a rotary evaporator and allowed to dry at 80^{o}C for three to five hours. The remaining product was then placed in a vacuum oven with P_2O_5 as a desiccant and allowed to dry at 80^{o}C for two days. It should be noted that the desiccant and reaction product should be placed in separate containers on separate shelves in the vacuum oven (see Figure 3.4) to avoid contamination and dangerous oxidation reactions. This process was repeated two or three times until the water content was sufficiently low.

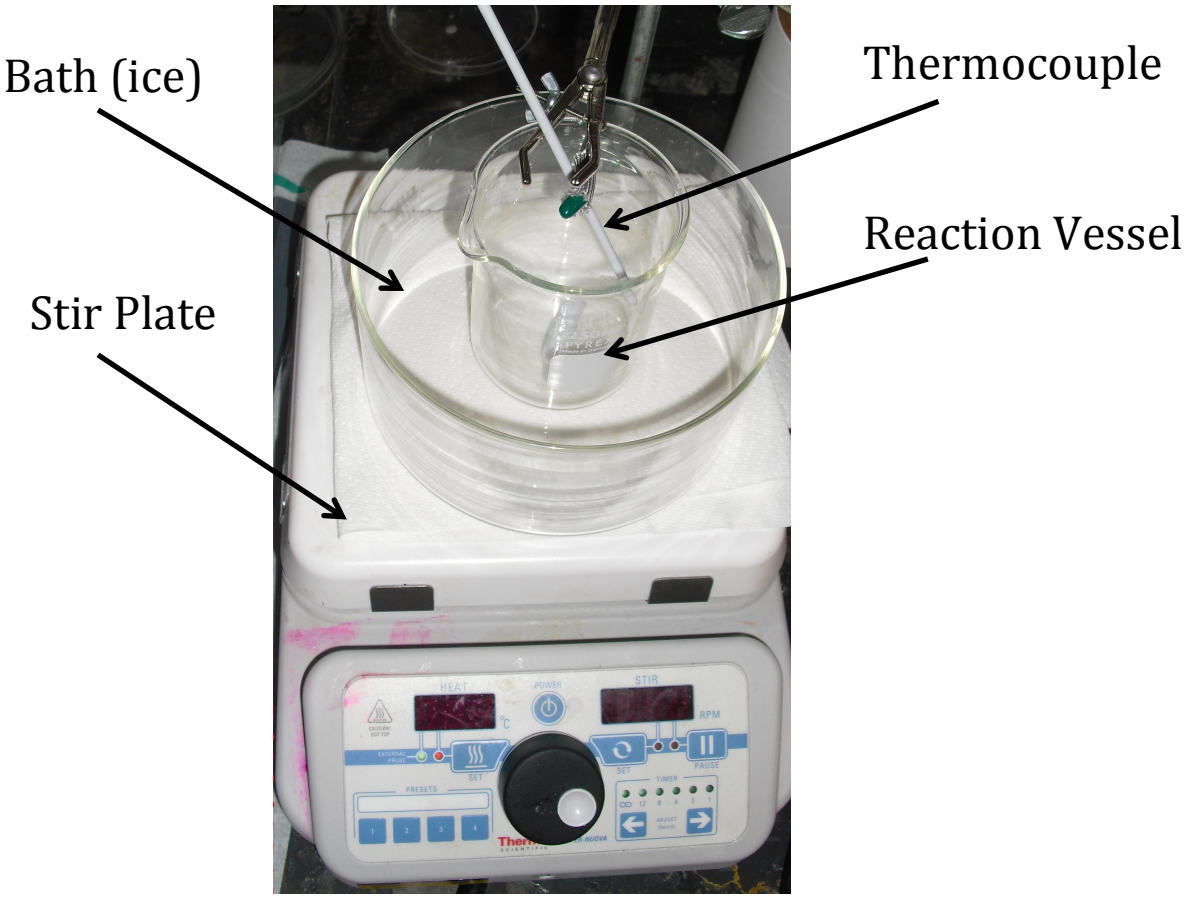

Figure 3.3 Apparatus for the synthesis of EAN. Ice was placed in the bath before synthesis.

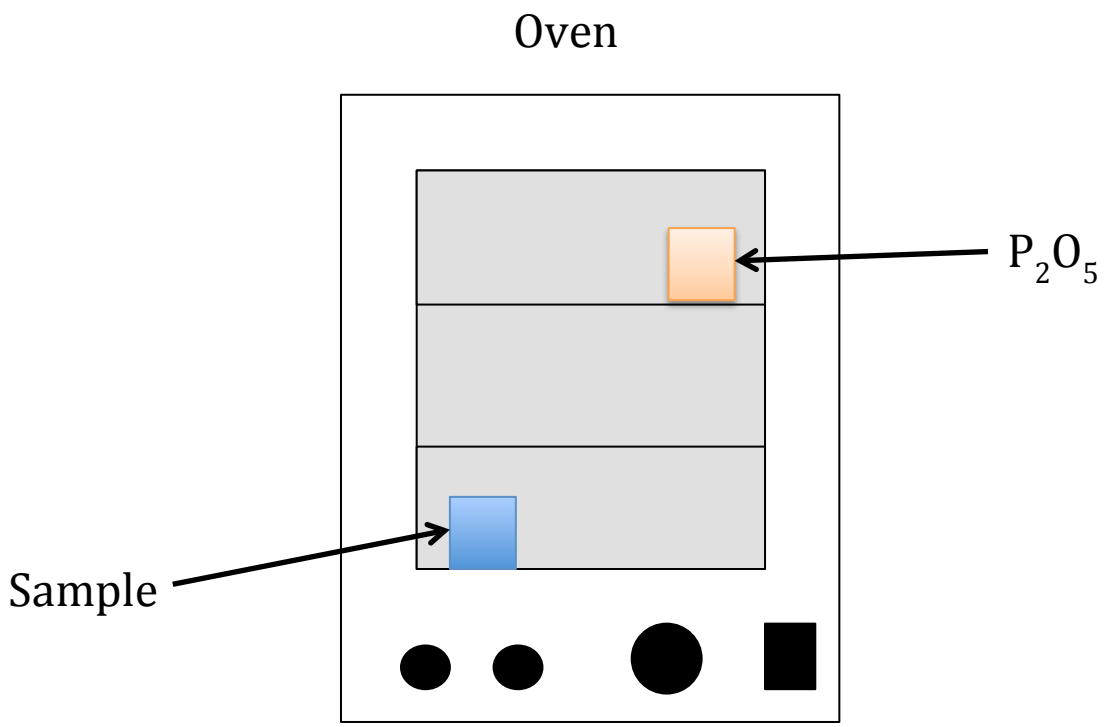

Figure 3.4 Recommended placement of synthesis product and desiccant in vacuum oven.

Emulsion Formulation

The oil-in-IL and water-in-IL emulsions consisted of 0.1 g of PDMS or HPLC Water, 1.1 g of [BMIM][PF_6], and polystyrene particle dispersions in masses ranging from 9.0E-4 g to 1.2 g (binary systems were at a 1:1 split of the two species). For the IL-in-IL systems, we formulated Pickering emulsions from two immiscible pairs: (1) Trihexyltetradecylphosphonium bis-(2,2,4-trimethylphentyl)-phosphinate ([P_{66614}][Phos])/EAN and (2) [P_{66614}][Phos]/[BMIM][PF_6]. The particles were weighted then dried using a vacuum oven. Particles of 0.2, 1.0, and 4.0 micron in diameter were used in this study. The emulsions were prepared using a Sonics VibraCell 500 W ultrasonic processor. Each system was prepared by first adding the ionic liquid to a vial containing the dried particles, then sonicating until the particles were dispersed in the ionic liquid. For binary systems, a sample was made for each particle type, then 0.55 g

from each vial was taken out and placed into a separate vial to create a 1:1 ratio of particles. The sample containing binary heterogeneous particles was then sonicated to create a homogenous binary system. Once the system (single or binary) became homogenous, the droplet phase was added and the sample was sonicated in an ice water bath for 10 seconds at an amplitude of 21%. Other methods of formulation included sonicating the particles in the oil phase first and then adding the ionic liquid. This, and other methods, yielded no change in the final droplet morphology or stability.

Gel System Formulations

Three systems were formulated using the 12-HSA gelator: neat [BMIM][PF_6], a [BMIM][PF_6]-in-water Pickering emulsion, and a PDMS-in-[BMIM][PF_6] Pickering emulsion. The ionic liquid gel with 0.5 wt. % and 1 wt. % 12-HSA was prepared by heating and mixing 0.005 g and 0.01 g 12-HSA with 1 g [BMIM][PF_6] (≥97%, Aldrich), respectively, in a water bath maintained at 80 °C. For a good dispersion of 12-HSA, the mixture was agitated by the ultrasonic processor once 12-HSA was completely melted, and then cooled at room temperature to form an opaque white soft gel. The [BMIM][PF_6]-in-water Pickering emulsions contained 0.1g [BMIM][PF_6], 1.1 g water and 0.1 g particle dispersion. The emulsions were prepared using an ultrasonic processor in an ice bath at 21% amplitude for 10 pulses at duration of 1 second each pulse. For the system with 12-HSA, the mixture contained 0.1 g prepared 1 wt. % ionic liquid gel and 1.1 g water and 0.1 g particles . The emulsions were dispersed by the ultrasonic processor once the gel became transparent in 80 °C water bath and then cooled at room temperature. The PDMS-in-[BMIM][PF_6] Pickering emulsions contained 0.1 g PDMS and 1.1 g [BMIM][PF_6] with 0.002 g dry S-PS particles. The emulsion was prepared

using an ultrasonic processor. For the system with 12-HSA, the mixture consisted of 0.1 g PDMS, 1.1 g prepared 0.5 wt. % and 1 wt. % [BMIM][PF_6] gel and 0.002 g dry S-PS particles. The emulsion was dispersed by the ultrasonic processor in 80 °C water bath and cooled at room temperature, unless stated otherwise.

3.2.3 Characterization

Ethylammonium Nitrate

For the physical properties of EAN, other groups have reported the following values at ambient conditions: density = 1.21 g/cm^3 [114, 218] and surface tension = 47.3 mN/m [219]. Density is a measure of mass per unit volume. Therefore, the most straightforward way to determine density is to measure the mass of a specific volume. Specific gravity bottles are glass containers designed to hold a known volume of liquid (i.e. 2 mL) and have been used to measure the density of ILs [220]. The main advantage of this method is that all measurements can be taken using a standard mass balance. After weighing the empty bottle, we filled the bottle with our product and measured the mass. Subtracting the bottle mass from this gave the mass of the liquid and allowed us to calculate the density with the known bottle volume. Using HPLC water, we found the volume of our bottle to be 1.96857 ± 0.0017 mL. For our sample, we measured a density of 1.2094 g/cm^3, which agrees very well with the literature. The surface tension was measured at 47.95 ± 0.24 mN/m using a Sigma 701 tensiometer; also in good agreement with the literature. Another standard method of characterizing ILs is to determine water content using Karl-Fisher titration. We determined our water content to be on the order of 0.03%, which was an acceptable value [218].

The IL-IL Interface

Molecular structures of the two ILs employed in this study are shown in Figure 3.5. [BMIM][PF_6], EAN, and poly(ethylene glycol) (PEG) were used as received. Liquid-liquid interfaces between these chemicals were observed in two environments: a standard 4 mL glass vial, and a Hele-Shaw type cell. In the first case, approximately 1 g of each liquid was placed in the vial whereupon an interface was formed. The contents were mixed using a Sonics VibraCell 500 W ultrasonic processor, heated, and cooled examine mutual miscibility of the liquids involved.

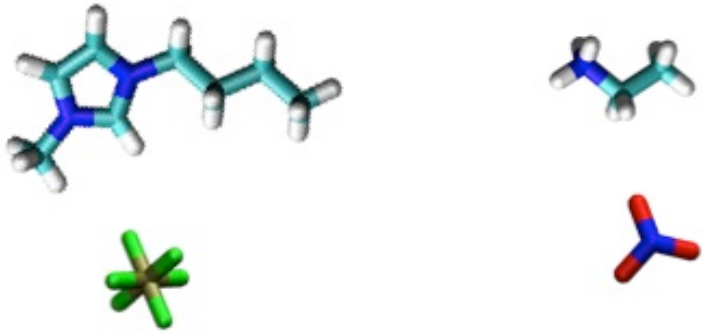

Figure 3.5 Molecular structures of [BMIM][PF_6] (left) and EAN (right) ions. H, C, N, O, P, and F atoms are shown in white, cyan, blue red, gray, and green, respectively.

The Hele-Shaw type cell was constructed to approximate a 2-D view of the liquid-liquid interface. The cell consisted of two 22mm x 40 mm glass coverslips (Fisher) mounted in parallel orientation approximately 1 mm apart using silicone glue. The top side of the cell was left open to the air to allow for easy addition of liquids. To form the interface, the denser of the two liquids in question was added until it filled half of the cell. The less dense liquid was then added until the cell was full. The cell was then placed approximately 20 mm front of an automatic digital camera with a sheet of lined paper approximately 50 mm behind it (See Figure 3.6). The lined paper was oriented diagonally

so as to make clear the location of the interface to the camera - lines were distorted by the interface due to differences in refractive indexes. Images were obtained every hour and analyzed using ImageJ to determine the area occupied by the undistorted lines at each point. As the interface became more diffuse (i.e. the liquids mixed), these distortions became less noticeable until the liquids had completely mixed. The lifetime of each interface was defined as the time required for these line deformations to become negligible. This point was indicatd by an asymptotic maximum in area occupied by the undistorted lines, as measured using ImageJ.

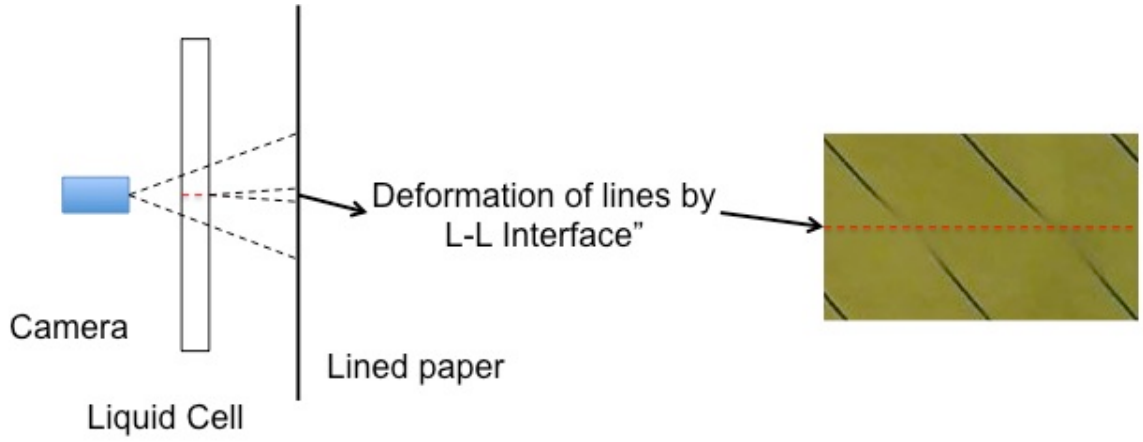

Figure 3.6 Schematic of a Hele-Shaw type cell apparatus for examining the IL-IL interface.

The MD simulations used to study this interface will be explained in more detail in Chapter 4, but some important details for this study follow. MD simulation is a discreet model where the equations of motion are integrated for each atom involved. The force term is determined by the repulsive and attractive forces of a molecule, parameterized as a force field. The force field used for [BMIM][PF_6] was first developed by Lopes, et al. [221, 222] and modified by Bhargava and Balasubramanian [223] to provide more accurate interfacial behavior. It should be noted that the authors of this

force field optimized the atomic charges of these ions to give total charges of ±0.8, which somewhat accounts for charge transfer [224]. For EAN, we employed the force field developed by Song et al. [225] with the exception that atomic charges were scaled down to ±0.87 and bonded parameters for the NO_3 ion were taken from the AMBER database [226, 227] with non-bonded parameters taken from the OPLS database [228]. Simulated densities of pure [BMIM][PF_6], EAN, and the mixture of the two yielded densities within 2.6%, 2.1%, and 0.4% of experimental values, respectively [125, 219]. The simulations were performed under NPT conditions (constant number of molecules, constant pressure, and constant temperature) with P = 1 bar and T = 300K. The pressure was maintained using the Parrinello-Rahman barostat [229, 230] and the temperature was maintained using the Berendsen thermostat [231].

Characterization of Emulsions and Gels

All microscopic images and fluorescence intensity spectra were obtained using a Leica SP5 confocal laser-scanning microscope under ambient conditions. The fluorescence intensity spectra were obtained by using a wavelength scan over the range of 500-599 nm for A-PS particles and AS-PS particles under excitation at 488 nm, over the range of 650-750 nm for S-PS particles under excitation at 633 nm, and over the range of 550-649 nm for C-PS particles under excitation at 543 nm. The spectra for the bulk phases before and after emulsification were collected under the same laser intensity and averaged from three to five runs in various locations in the bulk. Bridged structures were characterized primarily by analyzing the images obtained from the confocal microscope. The number of droplets in each structure was estimated by visual inspection. Image J was used to estimate the cross-sectional area of each droplet present in the

structures. By assuming spherical droplets, the diameter of each droplet was extracted to obtain a droplet size distribution for each system.

Viscosities for the three ILs were measured using a TA Instruments AR-G2 rheometer at 25 °C. They are 82.4 cP, 2.61 cP, and 22.3 cP for $[P_{66614}]$[Phos], EAN, and [BMIM][PF_6], respectively. The strain sweep test in the 12-HSA gelator studies was also performed with this instrument. Strain % ranged from 0.05-200, at a frequency of 1 Hz. There were three types of samples tested: pure [BMIM][PF_6], 0.5 wt. %, and 1 wt. % 12-HSA [BMIM][PF_6] gel. For each type, the final results were calculated by averaging two measurements of fresh samples.

3.3 Results and Discussion

3.3.1 Ordering and Dynamics of Ionic Liquid-Based Interfaces

Cation Ordering at Ionic Liquid Interfaces

One interesting behavior in IL-based interfaces is the ordering of cations at the IL-oil interfaces, both with and without nanoparticles. MD simulations allow for a molecular view of this phenomenon. In these systems, the IL density profile exhibited small peaks at the interfaces, whereas the peaks were absent in the IL/water systems. We hypothesized that the peak was likely due to some ordering of the IL molecules at the interface thus calculated the order parameter S_z defined in Equation 3.3. The value of S_z ranges from -0.5 to 1.0 and corresponds to chain orientation perpendicular and parallel to the z-axis, respectively. If $S_z = 0$, the chains are ordered isotropically.

$$S_z = \frac{3}{2}(cos^2\theta) - \frac{1}{2} \tag{3.3}$$

where θ is defined as the angle between the carbon chain (N-C vector, where N is the nitrogen attached to the butyl chain and C is the terminal carbon of the butyl chain) and the z-axis.

Figure 3.7 compares the ordering of the cations at the IL-water (a, c) and IL-hexane (b, d) interfaces, with and without the presence of the nanoparticles. Other than the ordering parameter, the density of the ionic liquid is included as a reference to illustrate the interface location. These plots represent an average of the last 2 ns of each 4 parallel runs. Figure 3.7a shows that the carbon chains were oriented isotropically throughout the IL/water system. This is in agreement with the work done by Chaumont et al. [128] , who also found that the carbon chains on the [BMIM] cation oriented isotropically throughout the system. In addition, they found that with increased cation chain length, some ordering was observed at the IL/water interfaces [128]. These larger cations preferentially oriented themselves with their long carbon chains pointing away from the water phase and the charged ring pointing toward the water phase [128]. From these results, we can infer that the carbon chain on the [BMIM] cation is the component primarily responsible for the hydrophobic nature of this IL. We report later on that when water was replaced with hexane, these carbon chains showed much higher interactions at the interface. When nanoparticles were added into the IL/water system, there appeared no ordering throughout the system, with the exception of the interfaces, as shown in Figure 3.7c. S_z exhibited small peaks of about -0.05 at the interfaces, indicating that the carbon chains have a slight tendency to orient themselves perpendicular to the z-axis (parallel to the interface). It appears that this was because the carbon chains tended to flatten

themselves across the surfaces of the nanoparticles, which were also hydrophobic (See inset of Figure 3.7c).

In contrast to the IL/water system, the IL/hexane system shows distinct peaks in S_z at the interfaces (See Figure 3.7b,d), supporting the ordering hypothesis. The positive values of S_z, with peak values of approximately 0.20, suggest that the carbon chains tended to orient themselves parallel to the z-axis (perpendicular to the interface). This behavior has been observed with the same IL cation at IL-vacuum interfaces [232, 233]. Lynden-Bell et al. observed that the densities of each consecutive carbon in the butyl chain had maxima "further and further toward the vacuum [232]." They also observed that while the butyl groups do show heightened ordering, they do not completely saturate the interface [232]. Sarangi et al. observed that this ordering decreased with cation symmetry [233].

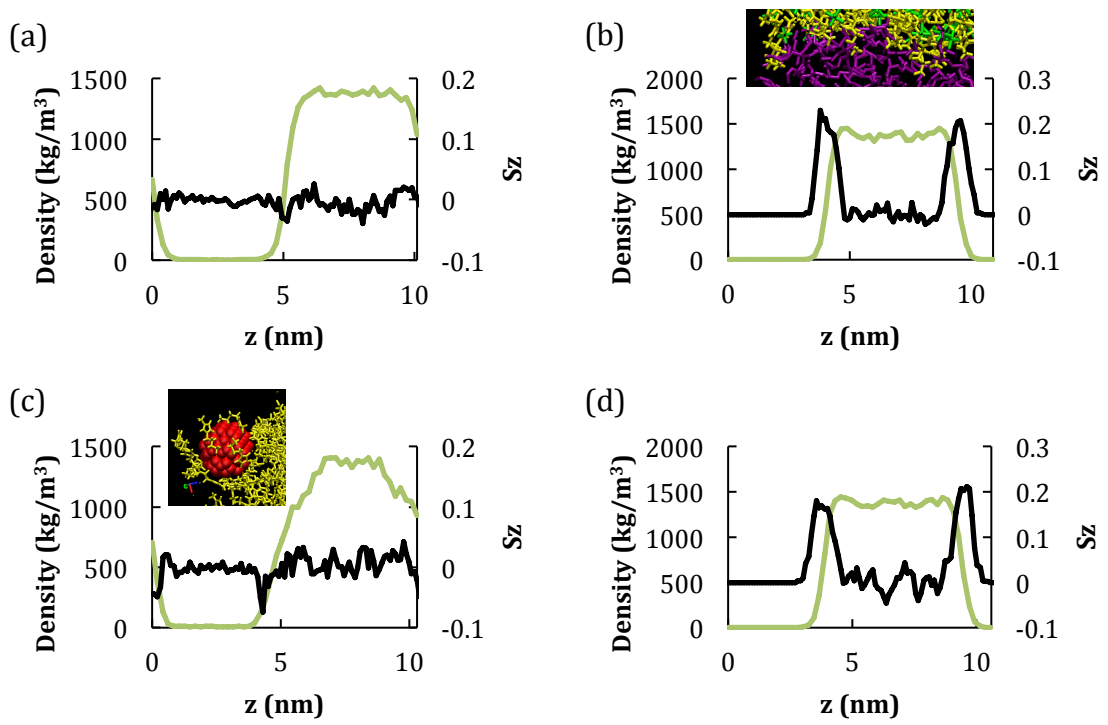

Figure 3.7 Ordering parameter S_z with respect to box length in IL/water systems without (a) and with (c) nanoparticles and IL/hexane systems without (b) and with (d) nanoparticles. The inset in (b) demonstrates the extension of cation carbon chains into the hexane phase. The inset of (c) shows how the carbon chains of the cations lay across the nanoparticle.

In the case of the [BMIM] cations, this orientation was favorable since the charged ring remained in the IL phase, while the carbon chain extended into the hydrophobic hexane phase (See inset of Figure 3.7b). To maintain this orientation, the cations had to transverse the interface. This explains their tendency to order parallel to the z-axis. In contrast to isotropic orientation, the cations with carbon chains parallel to the z-axis would be able to pack more efficiently due to a reduction in steric hindrance [233, 234]. Therefore, this ordering may explain the heightened IL density at the interfaces. This ordering was independent of the presence of nanoparticles since they did not penetrate the IL/hexane interface.

It is interesting to note that the cation ordering at the IL-hexane interface had more implications other than the increased interfacial density. Figure 3.8 shows the charge density distribution throughout the simulation box for the IL/hexane system. It is also an average of the last 2 ns of each 4 parallel runs. Clearly there were large fluctuations in the bulk IL phase because of the ions. At the interface, however, there consistently existed a net positive charge. This was likely a result of the cation ordering explained above. By extending their carbon chains into the hexane phase, the cations occupied the outermost layer of the interface. Their dominance in this region resulted in a net positive charge. Although the charge was small relative to the fluctuations in the IL phase, it was nevertheless consistently present in all parallel runs of this system. Sarangi et al. observed a similar phenomenon with a different IL (still with imidazolium cations, however) at the IL-vacuum interface [233]. They found that this slight positive charge at the outer layer of the IL was only present in ILs with cations of long carbon chains [233]. In relevance to our case, the slightly positive charge density is likely due to the alkyl group extending into the hexane phase. This phenomenon was not observed in the IL/water systems. Despite the peaks in S_z at the interfaces, the polar nature of the water molecules created great charge fluctuations that rendered any residual charge at the interface due to insignificant cation ordering.

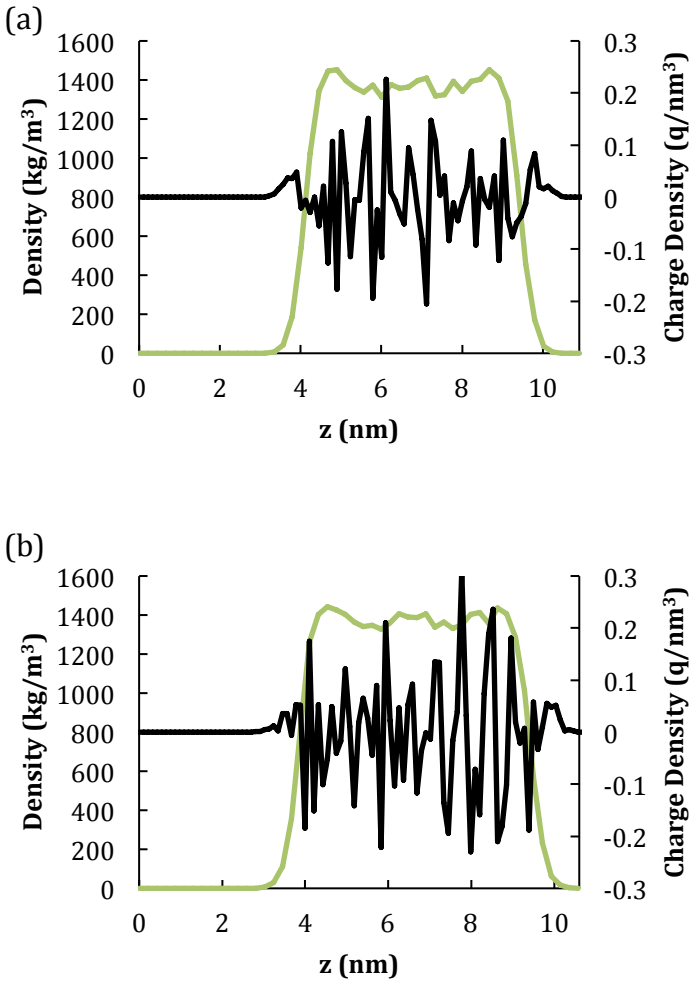

Figure 3.8 Charge density with respect to box length in the IL/hexane simulations without (a) and with (b) nanoparticles. The charge densities are represented in black and are overlaid on the IL density profiles, which are represented in green, to illustrate the location of the interface.

Dynamics of an IL-IL Interface

The focus of this study is the interaction between EAN and [BMIM][PF_6] as they mix. PEG was employed to provide a reference to which we could compare the mixing behavior of the two ILs. We originally hypothesized that high viscosities would yield longer interface lifetimes, so we chose PEG with a viscosity in between those of EAN and [BMIM][PF_6] (See Table 3.3 for a list of pertinent properties). Using the Hele-Shaw-

type apparatus described above, we compared the lifetimes of three interfaces: EAN-PEG, [BMIM][PF_6]-PEG, and EAN-[BMIM][PF_6]. The results are shown in Figure 3.9. The EAN-PEG interface was the shortest lived, with an average lifetime of only 12 hours. Since EAN and PEG were the least viscous of the three species studied here, their relatively quick inter-diffusion was expected. By the same token, when EAN was replaced by the more viscous [BMIM][PF_6], mixing slowed and the average interface lifetime increased to approximately 50 hours. Therefore, judging by viscosities alone, one would expect the lifetime of the interface between EAN and [BMIM][PF_6] to be between 12 and 50 hours. Instead, we consistently measured interface lifetimes above 120 hours, with an average of 141 hours. Such slow interfacial decay suggests that other factors besides viscosity played a significant role during this mixing process.

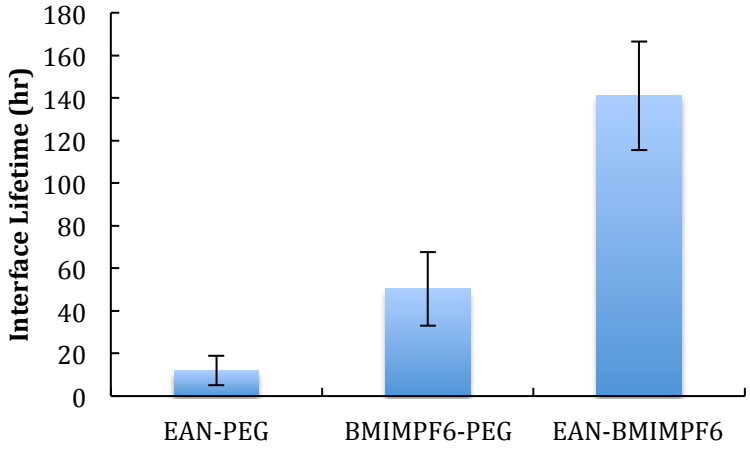

Figure 3.9 Interfacial lifetimes as measured in the Hele-Shaw apparatus.

Table 3.3 Viscosities and refractive indexes (n_D) of [BMIM][PF_6], EAN, and PEG.

Liquid	Viscosity (cP)	n_D
BMIM PF_6	22.30	1.4089
EAN	2.61	1.4524
PEG	4.90	1.4600

Our first inclination was to examine the energetics of the mixing of these species. By energetics, we mean the Gibbs energy of mixing, as described in Equation 3.4.

$$\Delta G = \Delta H - T\Delta S \tag{3.4}$$

Trivedi and Pandey recently reported that [BMIM][PF_6] and PEG exhibit very favorable mixing energetics because "extensive H-bonding between the IL and PEG [235]" as evidenced in FTIR spectra. Similar mixing behavior is likely in the EAN/PEG system. Since widespread attention to ILs has only been recent, data on their thermodynamics mixing properties is sparse. However, the mixing energetics of molten salts have been studied and provide some insight into IL behavior. Kleppa and coworkers experimentally investigated mixtures of alkali halide and alkali nitrate salts and found that coulombic repulsions between like-charged ions play a major role in mixing energetics [236, 237]. They observed that the enthalpy of mixing could be either positive or negative, depending on the relative sizes of the ions. Essentially, when salts of a common ion (cation or anion) were mixed, the sign of the enthalpy of mixing depended on whether the common ion was larger or smaller than the other ions. If it was smaller, then the enthalpy of mixing was positive (presumably because of lattice disruptions caused by the large mismatched ions), and vice versa [236, 237]. In our case, the anions were closest in size and were, on average, smaller than the cations. Granted that this theory is not completely general [236], we could tentatively expect a positive enthalpy of mixing based on the features of our mixture.

In light of the interface lifetime measurements, we first studied the interface between the two ILs in the unmixed system. Figure 3.10 shows snapshots at 5 ns and 40

ns of the [BMIM][PF_6]/EAN system with all ions (a, d), cations only (b, e), and anions only (c, f). At 5 ns, inter-diffusion between the ILs has begun, although at a very slow rate. Figure 3.10b and c show most cations and anions had not yet left their native IL at this point. By 40 ns, the interface had become more diffuse as ions began to penetrate into the opposite IL. Despite their differing sizes, the anion and cation of each IL diffused into the opposite IL at approximately the same rate (i.e. BMIM diffused just as quickly as PF_6). We quantified the effect of this inter-diffusion by calculating the interfacial width with time.

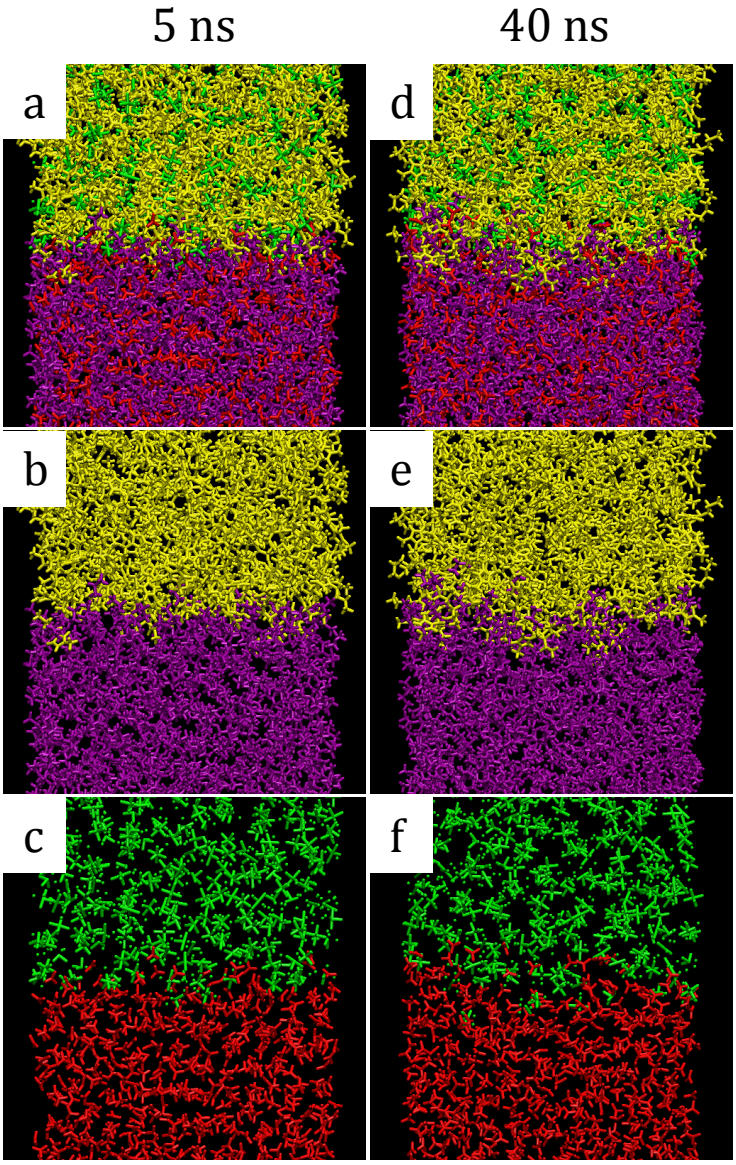

Figure 3.10 Snapshots at 5 ns and 40 ns of the simulated [BMIM][PF_6]/EAN interface with (a, d) all ions, (b, e) cations only, and (c, f) anions only.

The interfacial width was defined in context of the density profile of this interfacial system. A sample density profile is shown in Figure 3.11a (averaged over 1 ns at a simulation time of t = 20 ns). Here dotted lines were added to show the points at which the densities of each IL dropped to 90% of their bulk values. Specifically, the interfacial width was the distance between these two points. As the ILs inter-diffused, we

expected that the interface would widen. The green line Figure 3.11b plots the interfacial width calculated at every ns for the entire 40 ns run. On average, the interface widened at a constant rate, as indicated by the overall linearity of the plot. We, therefore, set out to determine an average diffusion constant for this process. This was done by solving the continuity equation for transient diffusion in one direction shown below, where *c* represents the concentration of each IL.

$$\frac{dc}{dt} = D\frac{d^2c}{dz^2} \tag{3.5}$$

Equation 3.5 was evaluated numerically using a density profile from the simulation at t = 0 as an initial condition, a time step of 1 ns, and z-step of 0.2 nm. The results of this evaluation were compiled into new theoretical density profiles at each ns that could be compared to the density profiles obtained from the simulation. By calculating the interfacial width from these theoretical density profiles, we were able to optimize the diffusion constant, D, to give the same *rate* of interfacial widening as seen in the simulation. The result of this optimization is shown as the black line in Figure 3.11b, which has the same *slope* as the linear regression fit of the simulation data. The optimized value of *D* to give this rate was 2.2 x 10^{-8} cm^2/s and represents an average diffusivity of all the species at the interface. We then set out to determine how this interfacial diffusivity compared to the bulk diffusivities.

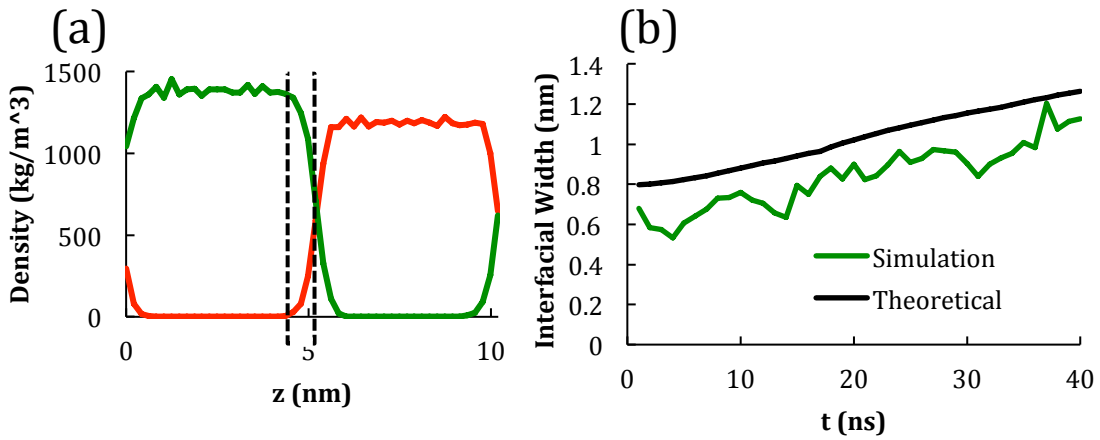

Figure 3.11 (a) Definition of interfacial width with the densities of [BMIM][PF_6] and EAN indicated by the green and red lines, respectively, and the interfacial width denoted by the dotted lines. (b) Recorded interfacial widths throughout the simulation time (green line) with corresponding theoretically calculated widths (black line).

Slower diffusion at the interface would certainly explain the unusually long interface lifetimes observed in the EAN/[BMIM][PF_6]. Here we begin to incorporate data from the simulation of the mixture of EAN and [BMIM][PF_6]. Using the mean-squared displacement method, we calculated the diffusivities of each ion in their native ILs (i.e. ethylammonium in EAN) as well as in the mixed system, with the expectation that the mixed system would approximate the environment at the interface. Figure 3.12 shows the results of these calculations. Three out of the four ions exhibited lower diffusivities in the mixture than in their native ILs. The most drastic decrease was seen in the diffusion of the $[BMIM]^+$ and $[PF_6]^-$ ions. The average of all of the mixture diffusion constants was 1.95×10^{-8} cm^2/s, indicating that the mixture simulation gave a reasonable approximation of the environment at the interface. Overall, these results suggest that lower diffusivities upon mixing may indeed explain the usually slow decay of the EAN/[BMIM][PF_6] interface. The question remains, however, as to why this phenomenon occurs.

Furthermore, even at with this slower diffusion, the rate of interface widening was approximately 12 mm/s, meaning that the two ILs would have mixed within a few minutes. However, our experimental data (See Figure 3.9) showed that this was clearly not the case. Therefore, other factors contributing to the slow interfacial decay were investigated.

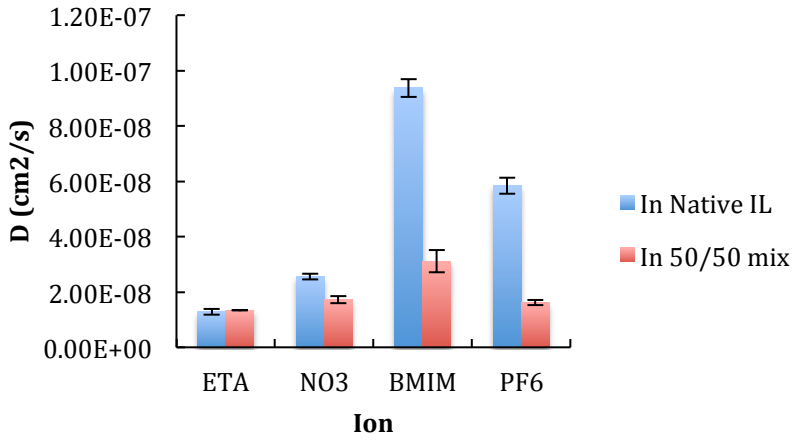

Figure 3.12 Diffusivities of each ion calculated in their native and opposite ILs calculated from mean squared displacement measurements.

One possible explanation for the unusually slow mixing behavior is that the mixing energetics were less favorable than those of ideal mixing (i.e. positive excess enthalpy). This phenomenon upon mixing is a result of the relatively weak attractions between the unlike species [238] and has also been observed in molten salt systems where the ions have similar sizes [236]. We hypothesized that these unfavorabilites may have dampened the driving force behind spontaneous mixing. Using the equilibrium mixed IL simulation (subscript "mix) and the two pure IL simulations (subscripts "1" and "2"), we calculated the thermodynamic mixing properties shown in Table 3.4. Gromacs analysis tools were used to calculate potential energy due to intermolecular interactions

and thus derive internal energy, U, and enthalpy, H, for all three systems. Molar volumes, V, were also obtained using the Gromacs analysis tools. These properties and were employed to compute the remaining mixing properties using the standard thermodynamic relations shown in Equations 3.6-3.10. We observed a positive enthalpy of mixing. Upon dissecting this energy term into electrostatic and van der Waals contributions, we found that the largest contributor to this positive enthalpy of mixing were the short-range Coulombic interactions between the ions. This suggests that the charge-based attractive forces in the mixture were weaker than in the pure ILs. Therefore, due to a weakening of net Coulombic attraction, the enthalpy of mixing for this system was positive, indicating that the mixing process must have been entropy-driven.

Table 3.4 Mixing Properties of [BMIM][PF_6] and EAN.

Mixing Property	**Δ**	**Excess**
U (kJ/mol)	7.73E-01	7.73E-01
H (kJ/mol)	7.76E-01	7.76E-01
V (m^3/mol)	-4.69E-07	-4.69E-07
S (kJ/mol*K)	2.58E-03	-4.96E-02

$$U^E = \Delta U = U_{mix} - x_1 \tag{3.6}$$

$$H^E = \Delta H = H_{mix} - x_1 H_1 - x_2 H_2 \tag{3.7}$$

$$V^E = \Delta V = V_{mix} - x_1 V_1 \tag{3.8}$$

$$S^E = \Delta S + R \sum x_i \ln(x_i) \tag{3.9}$$

$$\Delta S = \frac{\Delta U + P\Delta V}{T} \tag{3.10}$$

However, the entropy of mixing showed negative deviation from ideal solution. Negative excess entropy indicates a degree of structuring in the mixed state, whereas in an ideal solution all species would be perfectly randomly dispersed [238-240]. Furthermore, negative S^E indicates that not all interactions between molecules in the mixture were of equal strength, as would be the case in an ideal mixture [239, 240]. Figure 3.13 shows a snapshot at 20 ns of the mixture. Here distinct regions of EAN (purple) and [BMIM][PF_6] (yellow) were visible, indicating a significant deviation from a random dispersion. This structuring reflects the positive excess entropy reported in Table 3.4. In light of the spontaneous mixing we studied experimentally, the formation of this bicontinuous-like structure offers some insight into the long interfacial lifetime. If such a configuration appeared during inter-diffusion, concentration gradients along the z-axis (normal to interface) would be disrupted significantly, hindering transport in that direction. Hence, while the macroscopic concentration gradient across the interface may have remained constant, ordering on the molecular level created concentration micro-gradients in many directions, which may have decreased the net overall diffusion rate in the direction normal to the interface. In the final stage of this study, we examined the inter-molecular interactions responsible for this ordering.

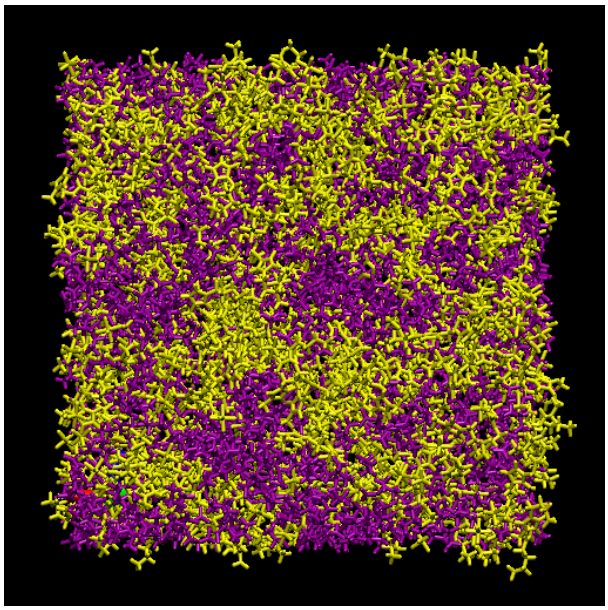

Figure 3.13 Snapshot of the [BMIM][PF_6]/EAN mixture at 20 ns. [BMIM][PF_6] ions are represented in yellow and EAN ions are represented in purple.

Radial distribution functions allow for one to compare specific intermolecular interactions in different systems. Here we compared interactions between IL ions in their respective pure versus mixed states. The interactions we compared were the O-HN interaction between the nitrate and ethylammonium ions, carbon chain-carbon chain interactions between the $[BMIM]^+$ cations, F-CW interactions between the $[BMIM]^+$ and $[PF_6]^-$ anions, and the F-CR interactions between the $[BMIM]^+$ and $[PF_6]^-$ anions. Figure 3.14 shows the radial distribution functions, which were averaged over the last ns of each run. In Figure 3.14a, the height of the O-HN peak increases by 70% from the pure IL state to the mixed state. This indicates that the EAN ions were more strongly associated on average in the mixed state than in the pure IL state. Similarly, the $[BMIM]^+$ carbon chains exhibited a 42% increase in peak height upon mixing, indicating stronger association. The other two interactions yielded nearly identical radial distribution

functions, which is what all interactions should yield in an ideal solution. Therefore, the first two interactions represent an imbalance in intermolecular forces between the species, leading to ordering in the mixed state. Imbalances such as these are often seen in mixtures that include associating fluids [238], like these ILs.

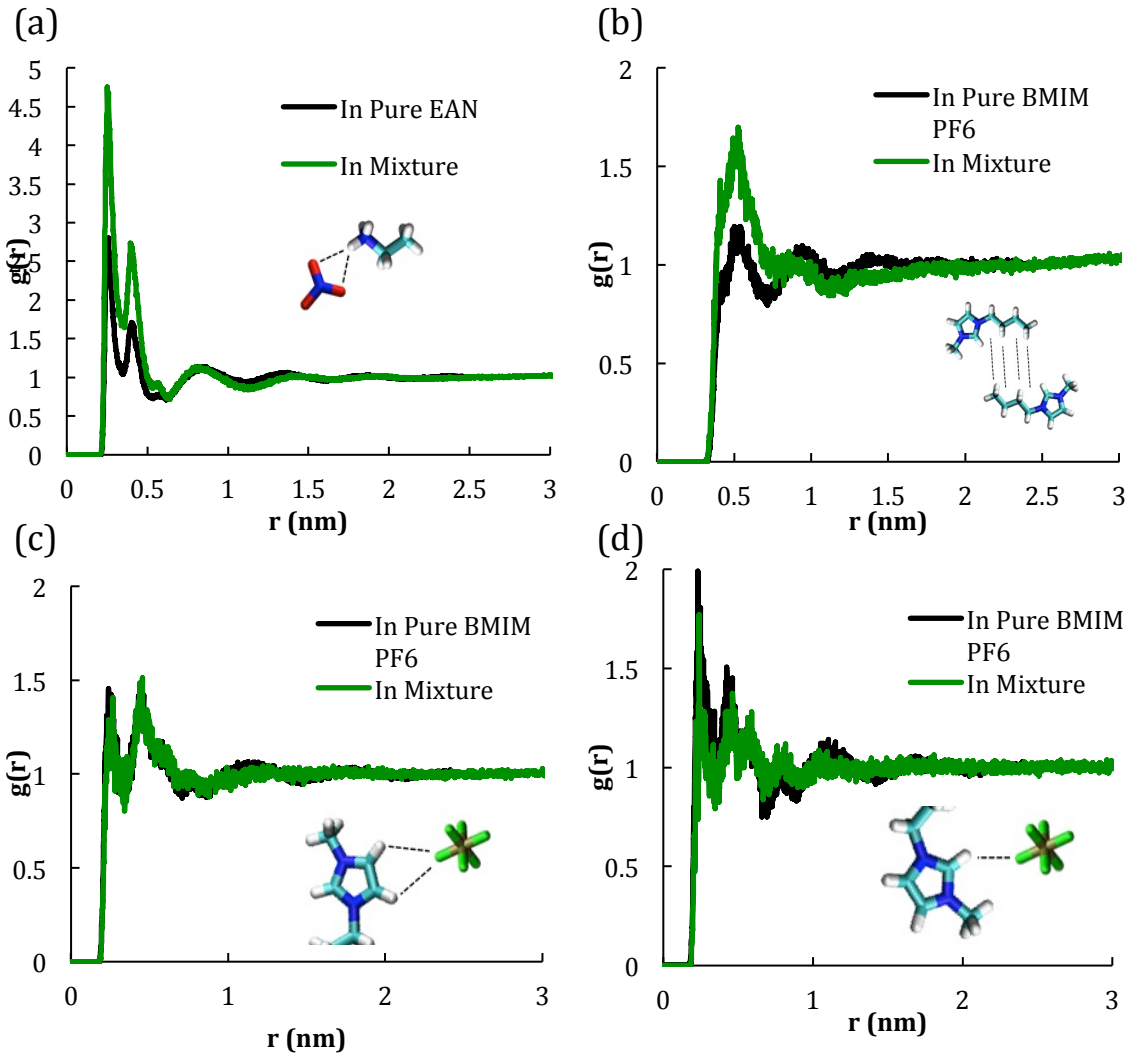

Figure 3.14 Comparison of radial distribution functions of various inter-ionic interactions before (black) and after (green) mixing the two ILs.

3.3.2 Spontaneous Particle Transport Across Ionic Liquid-Based Interfaces

Having discussed some behaviors at the bare interface, we will now investigate the interaction between IL-based interfaces and particles. The first to be discussed is the spontaneous transport of particles through IL-based interfaces. Our first observation of this phenomenon was made by placing a drop of particle dispersion next to a drop of IL on a glass microscope slide. Figure 3.15 shows the transport of fluorescent sulfate-treated polystyrene (SPS) microparticles (1.0 μm in diameter, negatively charged) from the water phase (bottom left) to the IL (trihexyltetradecylphosphonium bis(2,2,4-trimethylpentyl)phosphinate) (P_{66614} Phos, upper right) phase. These images were taken while the droplets were still establishing equilibrium with one another, thus the interface was in motion. As the interface moved, we were able to observe how it interacted with the particles that weakly adhered to glass slide. This configuration was advantageous since it allowed us to watch the particle-interface interaction without adjusting the microscope position. In Figure 3.15a, a single particle "jumped" through the interface onto the IL side at t = 0.8 s. After "jumping" into the IL, the particle remained attached to the IL/water interface for a time before finally detaching.

This "jumping" and detaching was also observed with clusters of particles, as shown in Figure 3.15b, where a cluster of four particles quickly moved through the interface at t = 0.4 s. After 5.4 s, the particles detached from the interface and migrated to the IL phase. Figure 3.15c shows a cluster of particles that was transported through the interface in two parts. At t = 0.4 s, a cluster of four particles "jumped" through the interface, followed by two more particles at t = 4.3 s. The latter event forced the first cluster to detach from the interface on the IL side. As the interface moved downward,

only one particle of the cluster remained attached until complete absorption of the cluster was achieved by t = 15.6 s. Thus, by this "jumping" and detaching mechanism, single particles and particle clusters were transported though the liquid-liquid interface into the IL.

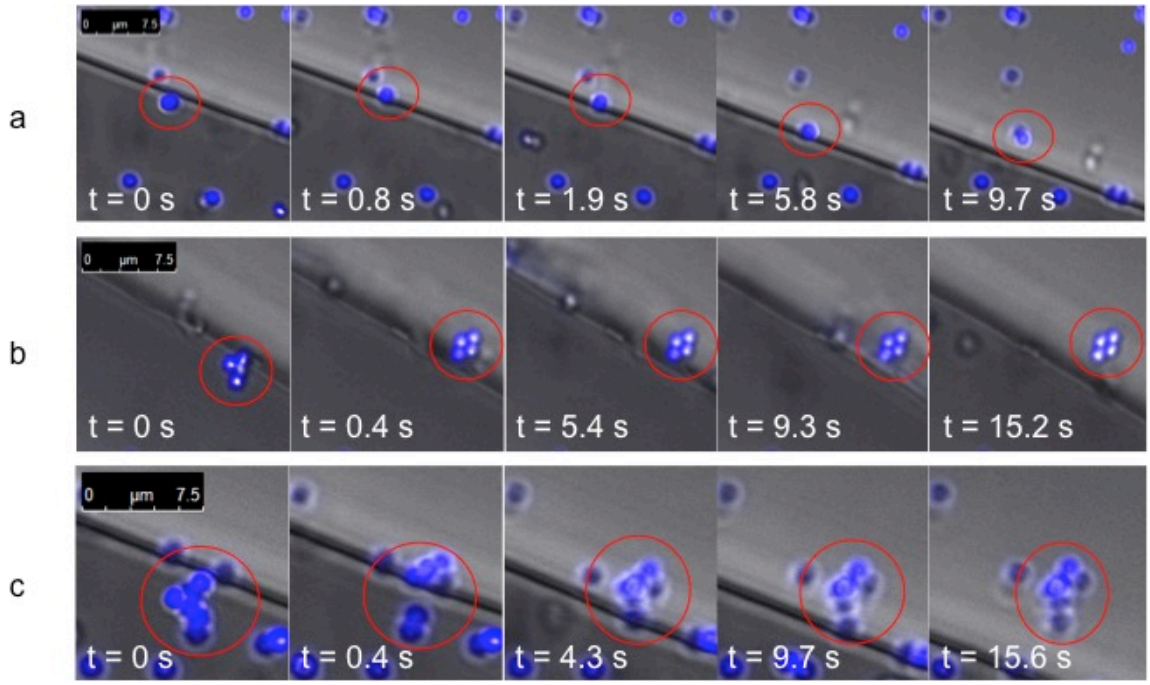

Figure 3.15 Snapshots of the transport of (a) single, as well as (b, c) clusters of 1.0-micron polystyrene particles (blue) across the IL (upper right)/water (bottom left) interface. Scale bars represent 7.5 microns.

While the above configuration was advantageous for directly observing particle transport across the interface, particle transport into dispersed IL droplets would provide a more global view of this process. In the subsequent experiments, 0.1 g of IL was dispersed in 1.0 g of water by sonication after which 0.1 g of SPS particle dispersion (2% particles) was added via pipet. No further mixing was applied, thus ensuring that external shear forces could not aid particle transport into the droplets. Figure 3.16a shows the SPS microparticles absorbed in 1-butyl-3-methylimidazolium hexafluorophosphate (BMIM

PF_6). Besides considerable interfacial coverage, the IL droplet also exhibited a high internal concentration of particles that had crossed the IL/water interface. In contrast, polydimethylsiloxane (PDMS) droplets in water showed negligible particle absorption (Figure 3.16b), as indicated by the lack of particles inside the droplets. This latter behavior was expected due to the high interfacial adsorption energy of the liquid-liquid interface. Only in the IL-based systems did we see a significant number of particles overcome this adsorption energy and enter the droplet. It should also be noted that very few particles had adsorbed to the interface of the PDMS droplets (Figure 3.16b). In a previous study by our group, the particles and PDMS droplets were dispersed by sonication and exhibited high interfacial adsorption [34, 203]. Since the particles were not sonicated in this study, the lack of interfacial adsorption suggests that such agitation was necessary for the particles to come in contact with the droplet surfaces and be adsorbed. The relatively higher interfacial adsorption in the IL droplet (Figure 3.16a) further highlights the capability of the IL to extract particles from the water phase.

Since interfacial adsorption energy increases quadradically with particle radius [14]. Therefore, by using 4.0-micron SPS particles, we increased the interfacial adsorption energy by a factor of 16. Surprisingly, even these particles were readily transported across the interface (See Figure 3.16c). This latter figure emphasizes the strong absorption capability of this IL. It should also be noted that these experiments were performed at room temperature. Similar studies at 80 ^{o}C produced identical results, suggesting that this phenomenon did not exhibit significant temperature dependence. These findings led us to hypothesize that the interaction between the particles and IL must have been unusually strong to overcome the interfacial adhesion energy.

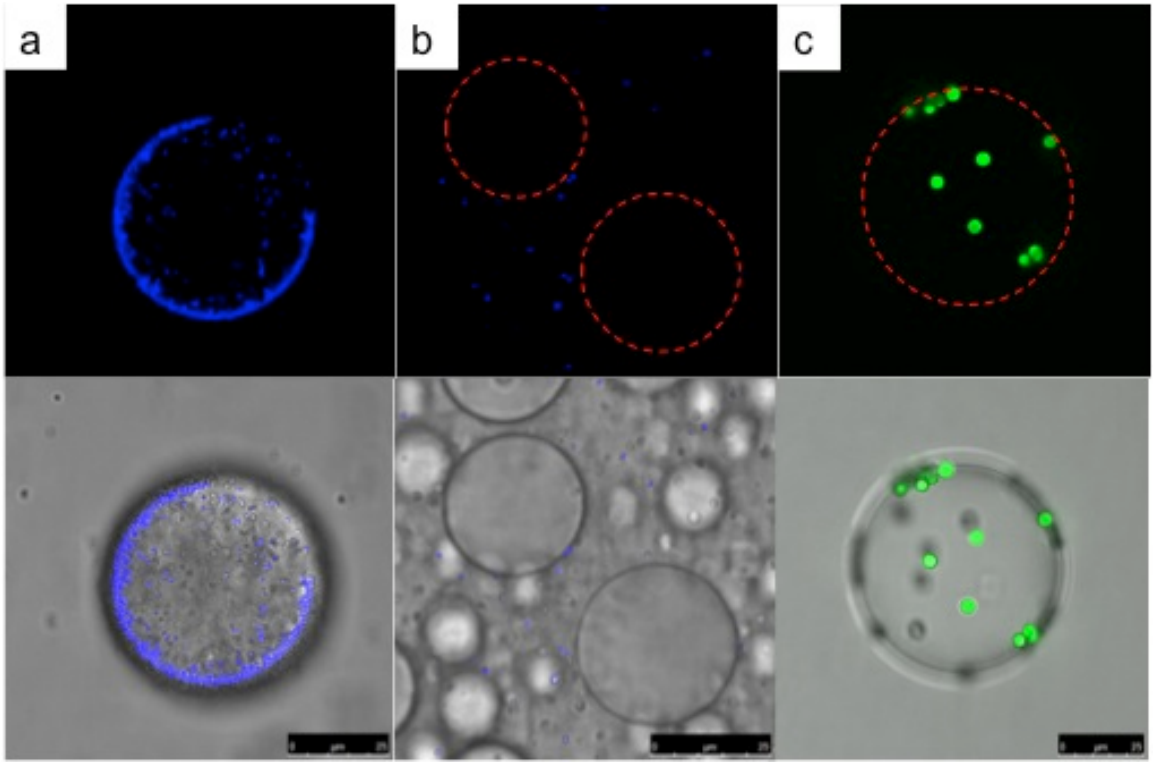

Figure 3.16 Confocal (top) and DIC/confocal overlays (bottom) showing the behavior of 1.0 micron SPS particles with (a) [BMIM][PF_6] droplets and (b) PDMS droplets in water. Droplet surfaces are denoted by the red dotted lines in the confocal images. Fluorescent dyes in the particles produced the different colors seen here. Changing the fluorescent dyes did not affect the results. Image c shows 4.0-micron SPS particles absorbed by [BMIM][PF_6] droplets in water. Scale bars represent 25 microns.

To explore this possibility, we conducted a systematic study of particle absorption as a function of IL and continuous phase. Figure 3.17 shows the confocal/differential interference contrast (DIC) overlays of 5 IL-in-water and 5 IL-in-PDMS systems with 1.0-micron SPS particles. Particle absorption from water was high in systems with BMIM PF_6, choline bis(trifluoromethylsulfonyl)imide (Tf_2N), and P_{66614} Phos, but negligible in systems with BMIM Tf_2N and 1-propyl-1-methylpyrrolidinium Tf_2N (not shown) droplets. It should be noted that in the P_{66614} Phos system, no interfacially absorbed particles were observed; particles were either totally absorbed into the droplets or

dispersed in the bulk phase. When the continuous phase was changed to polydimethylsiloxane (PDMS), all ILs except ethylammonium nitrate (EAN) and choline Tf_2N absorbed some particles. However, the internal particle concentrations were not as high as the water systems. Interestingly, BMIM PF_6 absorbed the particles regardless of the continuous phase. PMP Tf_2N and BMIM Tf_2N only absorbed particles from the oil phase. This stark difference begs the question: what IL properties allowed for particle absorption? The densities, viscosities, melting points, IL/water surface tensions, and ion mass ratios are listed in Table 3.5, but among these properties there was nothing unique about the non-absorbing ILs.

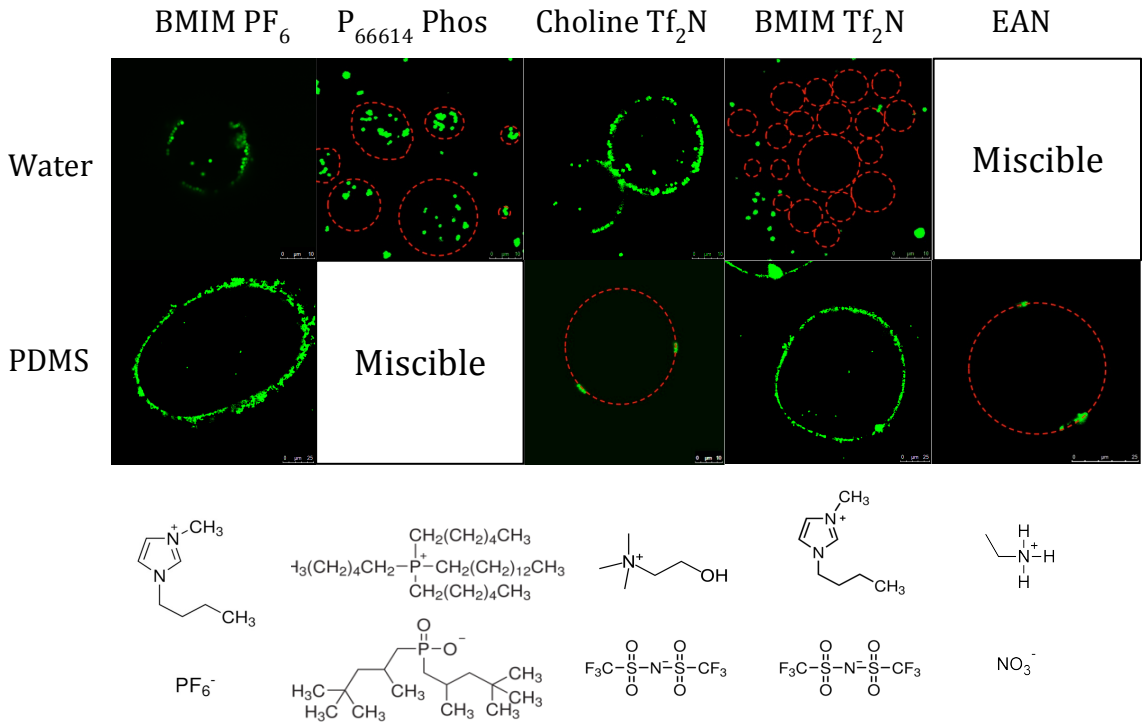

Figure 3.17 1.0-micron SPS particle absorption from water (top row) and PDMS (bottom row) into droplets of various ILs. Chemical formulas for each IL are shown below their respective images.

Table 3.5 Properties of ILs used at 25°C. *Measured at 30°C.

Properties	BMIM PF_6	BMIM Tf2N	PMP Tf2N	P_{66614} Phos	EAN	Choline Tf2N
Density (g/cm^3)	1.36	1.44	1.45	0.895	1.21	>1.0
Viscosity (cP)	22.3	4.66	5.52	82.4	2.61	6.27*
Melting point (°C)	9.95	-88.05	-18	Below 25	12	30
m+/m-	0.96	0.5	0.46	1.67	0.74	0.37
IL/Water γ (mN/m)	9	8.5		3.0	-	
Absorbs SPS From Water	Yes	No	No	Yes	-	Yes
Absorbs SPS from Oil	Yes	Yes	Yes	-	No	

Therefore, we began to explore some other possible mechanisms behind this new phenomenon. First, we focused on determining the time frame in which particle absorption occurred. We noted that no significant absorption occurred during microscopic experiment, suggesting that all absorption had been completed prior to this point. One hypothesis was that high concentration gradients between the pure particle dispersion and the IL droplets provided a needed driving force for particles to cross the interface. Therefore, we minimized this gradient by diluting the particle dispersion in 1 mL of water. However, these experiments yielded identical absorption behavior. The next proposed mechanism was that particles were absorbed during droplet collisions and coalescence, which would provide some local shear forces. Furthermore, the absorbed particles were often observed in larger droplets that were presumably products of coalesced droplets. Given that collisions and coalescence were more frequent immediately after dispersion, we tested this hypothesis by waiting 3 minutes after sonication to add the particle dispersion. Again, the absorption behavior was unchanged from the original experiments, suggesting that some feature of the ILs was responsible.

In search of this feature, we quantified the degree of absorption with respect to each IL. To do this, we measured the peak fluorescence intensity using the confocal

microscope mentioned above. Measurements of bulk phase peak fluorescence intensity were compared to a IL-free system. Consequently, the degree of particle adsorption was indicated by a decrease in peak fluorescent intensity (due to particles being absorbed) relative to that of the droplet-free system. Figure 3.18 shows these measurements of SPS particles in the water phase with respect to each IL. These data correspond well to those of Figure 3.17, and provide more insight into the degree to which each IL absorbed SPS particles. $[P_{66614}]$[Phos] and Choline Tf_2N were the strongest absorbers, indicated by near-zero peak fluorescence intensities. [BMIM]$[Tf_2N]$ and [PMP]$[Tf_2N]$ were the weakest absorbers, showing only a slight drop in fluorescence intensity probably due to some interfacial particle absorption. Most notable, however, was that [BMIM]$[PF_6]$ exhibited intermediate absorption, suggesting that there was a gradient of absorbing power between the ILs, not just binary behavior (total absorption or zero absorption). The question arose as to why [BMIM]$[PF_6]$ absorbed less than some ILs, but more than others.

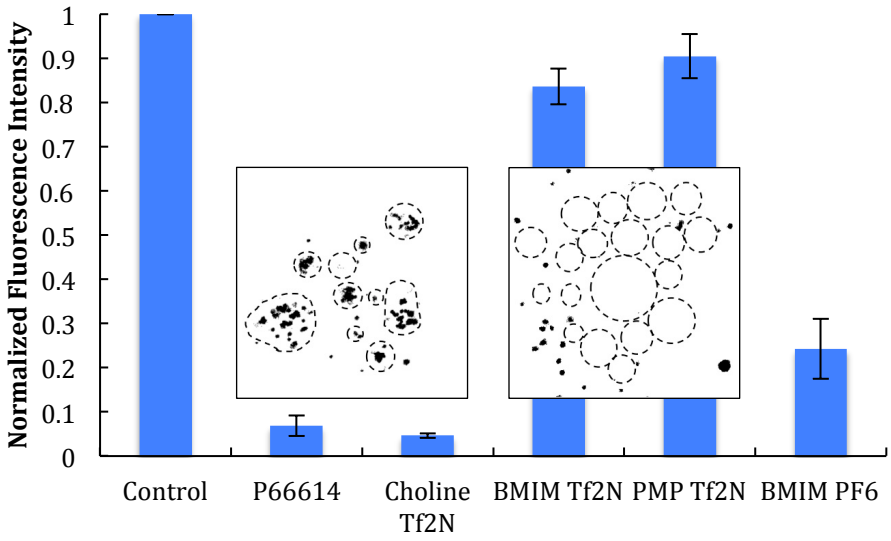

Figure 3.18 Peak fluorescence intensity measurements of SPS particles in the continuous water phase in the presence of various IL droplets. Measurements were normalized against measurements in an IL droplet-free system.

Because the ILs removed particles from the continuous phase, we hypothesized that the dissolved IL ions in this phase played a role in the absorption process. It is known that IL solubility in water depends on both the cation and the anion hydrophobicities [127, 128, 241]. For example, [BMIM][BF_4] is completely soluble in water, while [BMIM][PF_6] forms a two-phase system because PF_6 is a more hydrophobic anion [242]. The ions dissolved in water (from the respective IL) would have experienced electrostatic interactions with the charged particles and possibly affected their surface chemistry through physical absorption. To test this hypothesis, we prepared a system like the ones mentioned above with [BMIM][Tf_2N] as the IL (which did not absorb particles in the previous studies) and added a small amount of [BMIM][BF_4], to increase the concentration of IL ions in the water phase. We expected that these ions would physically adsorb to the charged particles and elucidate their absorption in the [BMIM][Tf_2N]

droplets. Figure 3.19 indicates that higher degrees of particle absorption were observed with increased amounts of [BMIM][BF_4], in support of our hypothesis. Therefore, ions dissolved in the continuous phase played an important role in particle absorption, as schematically shown in Figure 3.20.

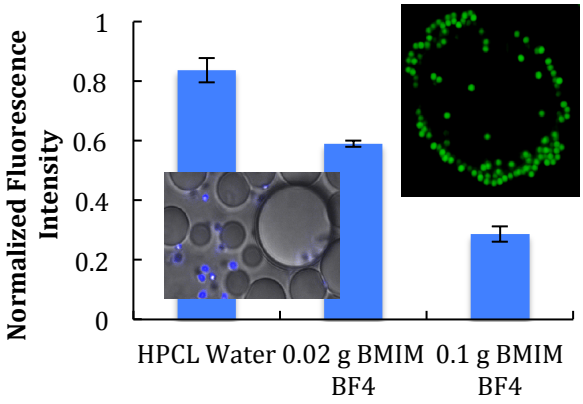

Figure 3.19 Peak fluorescence intensity measurements of SPS particles in the continuous water phase in the presence of [BMIM][Tf_2N] droplets and varying amounts of water-soluble [BMIM][BF_4]. Measurements were normalized against measurements in an IL-free system.

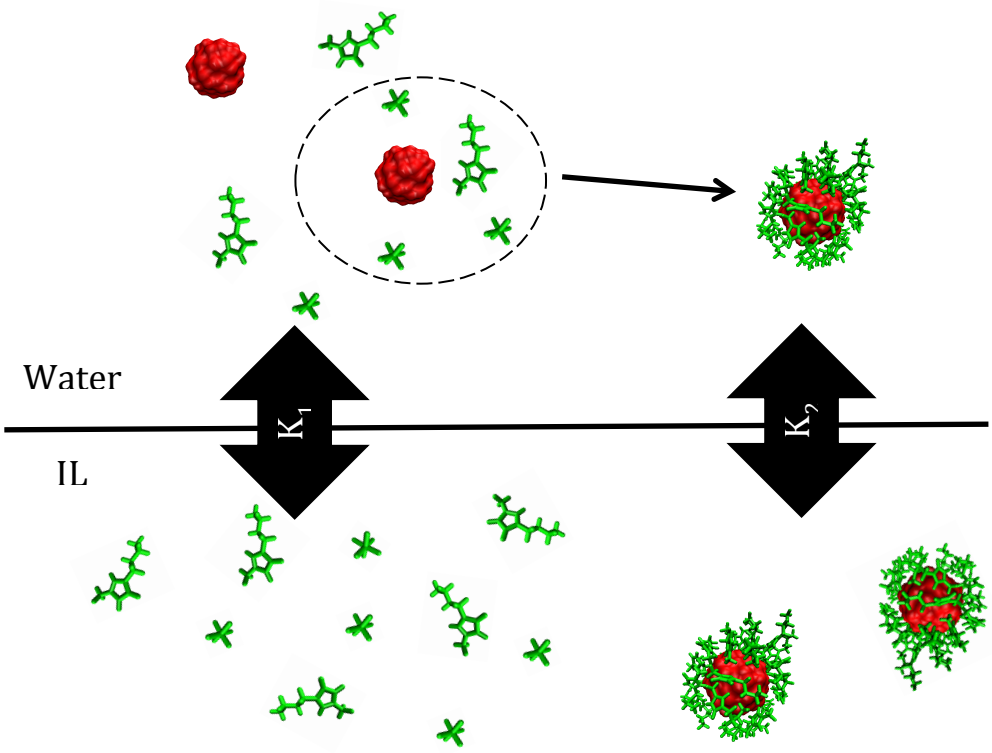

Figure 3.20 Schematic for the proposed mechanism for particle (red) extraction from the water phase to the IL phase.

This mechanism can be summarized via a series of equilibrium relationships, (Equations 3.11-3.13). In these equations, only the cation interaction with the particle is taken into account, where both anion and cation could theoretically play a role by the formation of solvation layers, as has been shown in MD simulations [243].

$$C^+A^-{}_{IL} \leftrightarrow C^+{}_{Solvent} + A^-{}_{Solvent} \qquad K_1 = \frac{[C^+{}_{Solvent}][A^-{}_{Solvent}]}{[C^+A^-{}_{IL}]} \tag{3.11}$$

$$C^+P^-{}_{Solvent} \leftrightarrow C^+P^-{}_{IL} \qquad K_2 = \frac{[C^+P^-{}_{IL}]}{[C^+P^-{}_{Solvent}]} \tag{3.12}$$

$$K = K_1K_2 \tag{3.13}$$

Here C^+, A^- and P^- represent the cation, anion, and particles, respectively and activities are approximated by concentrations. In this scheme, the degree of particle absorption is proportional to the magnitude of equilibrium constant K, and thus dependent on both steps of the mechanism. K_1 represents the equilibrium between IL ions in the original IL phase and those dissolved in the solvent phase. The dissolved ions can then interact with and cover the particles dispersed in the solvent phase. Similarly, K_2 represents the equilibrium between solvophobized particles dispersed in the solvent phase and those extracted into the IL phase. The total equilibrium constant, K, is the product of K_1 and K_2. This organization also allows us to identify ways in which an IL-particle-solvent system may be adequate to experience particle absorption. For example, $[P_{66614}][Phos]$ is minimally soluble in water, thus exhibiting a low K_1, but the constituent ions would exhibit strong binding to- and subsequent hydrophobization of a particle, exhibiting high K_2. We expect that for this reason, $[P_{66614}][Phos]$ was one of the most efficient particle absorbing ILs. In contrast, EAN in PDMS would likely have exhibited high K_2 values, but the small, hydrophilic ions would have been the least soluble in PDMS of all of the ILs, hence a low K_1 (ILs with larger and more branched ions would having a higher K_1 and did exhibit particle absorption. See Figure 3.17). In light of this mechanism, it should be noted that future applications for this process must take into account the finite partitioning of the IL into the opposite phase.

This mechanism is similar in many ways to the one presented by Velev et al. In their mechanism, surfactants were attracted to the particles via electrostatic and hydrophobic interactions [67]. Here, instead of surfactants, IL ions adsorbed (likely

through the same interactions) to the particle surfaces, causing hydrophobization. Thus, both mechanisms required a water-soluble species to change the surface properties of the particles. The mechanisms differ in that with the ILs, the molecules that interact with particle surfaces could come directly from the droplet phase. In this way, ILs could act as the sole extracting agents, eliminating the need for additional surfactants.

Other groups have observed that IL ions in the aqueous phase aided the phase transfer of metal nanoparticles into an organic phase [244-246]. Lee and coworkers proposed that these ions aided phase transfer by making the particle surface more hydrophobic upon contact [244]. Furthermore, it appears that efficiency of phase transfer increases with aqueous ion concentration [244, 246]. Again, we emphasize that these results did not represent *spontaneous* microparticle absorption as they were performed under agitation conditions and with nanoparticles, which experience adhesion forces 10^6 times smaller than those of microparticles. These findings agree with our results: the degree of particle absorption depended on aqueous ion concentrations. [BMIM][Tf_2N] was less soluble in water than [BMIM][PF_6] [241] and therefore unable to provide a sufficient aqueous ion concentration to hydrophobize the particles enough for phase transfer. With the addition of [BMIM][BF_4], the increased ion concentration allowed for the particles to be hydrophobized and extracted into the [BMIM][TF_2N]. Judging by relative IL/continuous phase solubilities, application of this mechanism to the other systems shown in Figure 3.17 appears valid. Choline Tf_2N is very soluble in water (requiring 0.2 g of IL to form droplets) and showed very high particle absorption. Similarly, [PMP][Tf_2N] and [BMIM][Tf_2N] were the more hydrophobic ILs and were thus able to absorb particles from an oil phase. [P_{66614}][Phos], while not very soluble in

water, possessed very large ions, which were likely more effective at hydrophobizing the particle surface upon contact.

Recent molecular dynamics simulations [247] shed more light on the mechanism behind particle transport through the interface. At the simulated [BMIM][PF_6]/water interface, hydrophobic nanoparticles dispersed in the water phase adsorbed to, and equilibrated on, the IL side of the interface. Interestingly, as the nanoparticles approached the interface, ions from the IL diffused though the water to form layers on the surfaces of the nanoparticles. After this layer was formed, the nanoparticle quickly left the water phase to be almost completely absorbed by the IL [247]. This "hydrophobizing" capability of the IL can aid the transport of particles through the liquid-liquid interface. Furthermore, the unusually low interfacial tension of IL-based interfaces (See Table 3.5) not only lowers the adhesion energy [14], but also allows for larger capillary waves, which can aid in particle absorption [248]. In these ways, particle transport through the liquid-liquid interface can be further facilitated by an IL.

3.3.3 Self-Assembly in Oil-in-Ionic Liquid and Water-in-Ionic Liquid Pickering Emulsions

Bridging of Solid Particles at Oil-Oil Interfaces

Expanding beyond the interaction between particles and IL-based interfaces, we investigated the morphologies in IL-based Pickering emulsions, where particle self-assembly played a critical role. A unique, highly visible bridging phenomenon can be seen in Figure 3.21 (a-c) for the S-PS, AS-PS, and C-PS stabilized PDMS-in-[BMIM][PF_6] Pickering emulsions. We observed that the particles mainly resided

between the PDMS oil droplets, creating flocculated droplet structures of varying size and morphology. While there was much variation in droplet size, every oil droplet larger than 3 μm was attached to at least one other droplet. The larger droplets (above about 20 μm) formed chains or large aggregates of droplets, stabilized by many particles. This behavior was in sharp contrast to that of the same solid particles at the IL-in-water emulsion droplet interface. In those systems, the solid particles nearly covered the entire IL droplet [151]. Here the solid particles did not generally equilibrate at the oil-IL interfaces, they instead bridged the oil droplets. Since this was the only structure present in these emulsions, we can infer that that the particles halted droplet coalescence by hindering drainage of the inter-droplet film. Tambe and Sharma explained that this hindrance is due to the inter-particle interactions in the film [213].

These structures were similar to some emulsion systems studied by others [42, 209] in which the bridged droplets formed chains and aggregates. However, most notably, the oil-in-IL systems here differed from other studies in that the oil-IL droplet interfaces were almost completely devoid of particles. Also, droplet deformation at the bridges was much higher in these systems; the bridges occupied more of the droplet surface area. Droplets in other bridging oil-water systems remained mostly spherical with a few particles connecting their interfaces together [42, 209]. Notable also is that despite the low amount of PDMS used relative to the IL, this flocculation was the primary structure present in these systems: no un-bridged droplets of this size were observed except for systems using A-PS particles as a stabilizer.

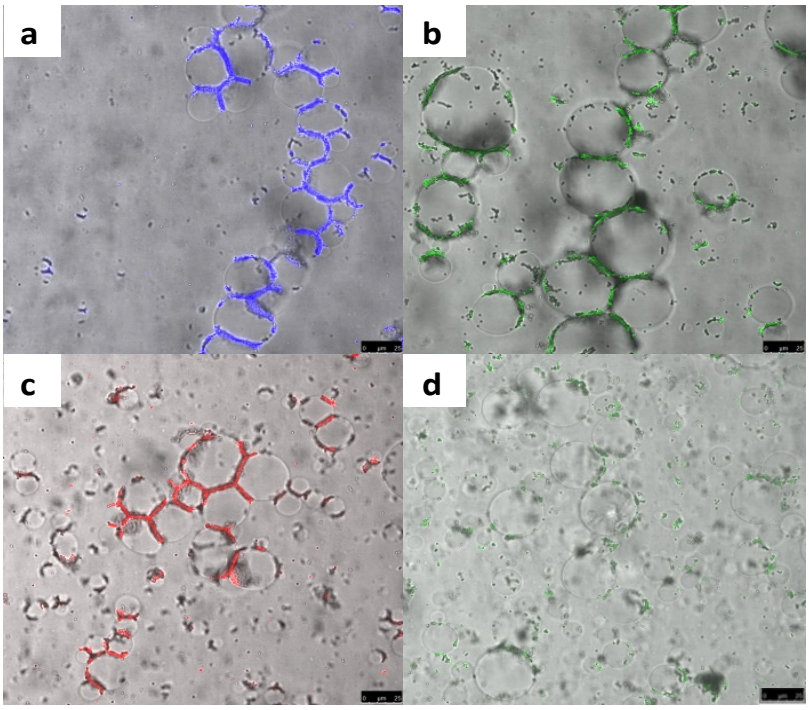

Figure 3.21 Overlays of confocal and differential interference contrast (DIC) images of oil-in-IL Pickering emulsions. Particles of different surface chemistries were employed: (a) S-PS; (b) AS-PS; (c) C-PS; and (d) A-PS. The scale bars represent 25μm.

The A-PS system differed significantly from the previous three systems (see Figure 3.21d). Although some bridging was observed, this was not by any means the dominant structure. Bridged structures that were observed only contained two or three droplets. The majority of the particles remained in the IL bulk phase. Excluding bridges, the A-PS system showed more droplet coverage than the other three. Droplet coalescence processes actually occurred while the A-PS sample was being evaluated under the confocal microscope, which further suggests that particle bridging played an important role in preventing droplet coalescence. The primary feature that distinguished the A-PS particles from the other three was their positive charge in the dissociated state. While the

mechanism for this phenomenon is not fully understood, it appears that the sign of the charge plays a significant role.

Most solid-stabilized emulsions feature individual dispersed droplets covered by solid particles [34, 57, 151, 205, 249]. Why, then, did the S-PS, AS-PS, and C-PS in PDMS-in-IL Pickering emulsions prefer the bridge location over the interface? One possibility is that most of the particles preferred the IL phase (due to the charged surface of the particle) until they were trapped between two droplets as they approached each other, as hypothesized in the work by Elias et al. with immiscible polymers and silica particles [250]. The bridges may then grow in size due to particle-particle attraction. Another possible contributing factor is the charge distribution at the oil-IL interfaces. Our molecular dynamics simulations of hexane-[BMIM][PF_6] interfaces suggested that the carbon chains on the imidazolium cations extended into the oil phase, allowing for high ordering of cations at the interface and a high concentration of anions behind the cations. This high concentration of anions may have created a negatively charged layer and repelled the negatively charged particles to some degree.

It should also be noted that no solid particles were transported into the oil phase in oil-in-IL Pickering emulsions. This observation was also in contrast to the IL-in-water systems reported be Ma and Dai, where other than equilibrating at the IL-water interfaces a fraction of the particles could cross the interfaces and dispersed in the IL phase, although they were initially in the water phase [151].

Figure 3.22 compares the amount of particles in the bulk phase (IL) before and after emulsification for each of the four systems. The reduction of the peak in each graph shows that the particles were taken out of the bulk ionic liquid phase and adsorbed into

either the bridges or the liquid-liquid interfaces. Figure 3.21 and Figure 3.22 both show, however, that a significant amount of particles remained in the IL phase. By counting particles through visual observation of many images, we were able to determine the preferred equilibrium locations (whether it be the bulk, interface, or bridge configuration) for each type of particle. Figure 3.23 shows the results of this study. With the exception of the APS particles, all showed first preference for the bridge configuration, followed by the interface configuration (not bridged, but adsorbed to a droplet surface) and finally bulk phase dispersion. Both the SPS and CPS particles exhibited strong preference for the bridge configuration, while the ASPS particles favored the interface and bridge configurations equally. The APS particles gave highest preference to the interface configuration, followed by the bulk configuration. APS particles in the bridge configuration were rare. Overall, it is evident that most particles had left the bulk phase to interact with a liquid-liquid interface in some way. The choice of interfacial configuration was highly dependent on surface chemistry.

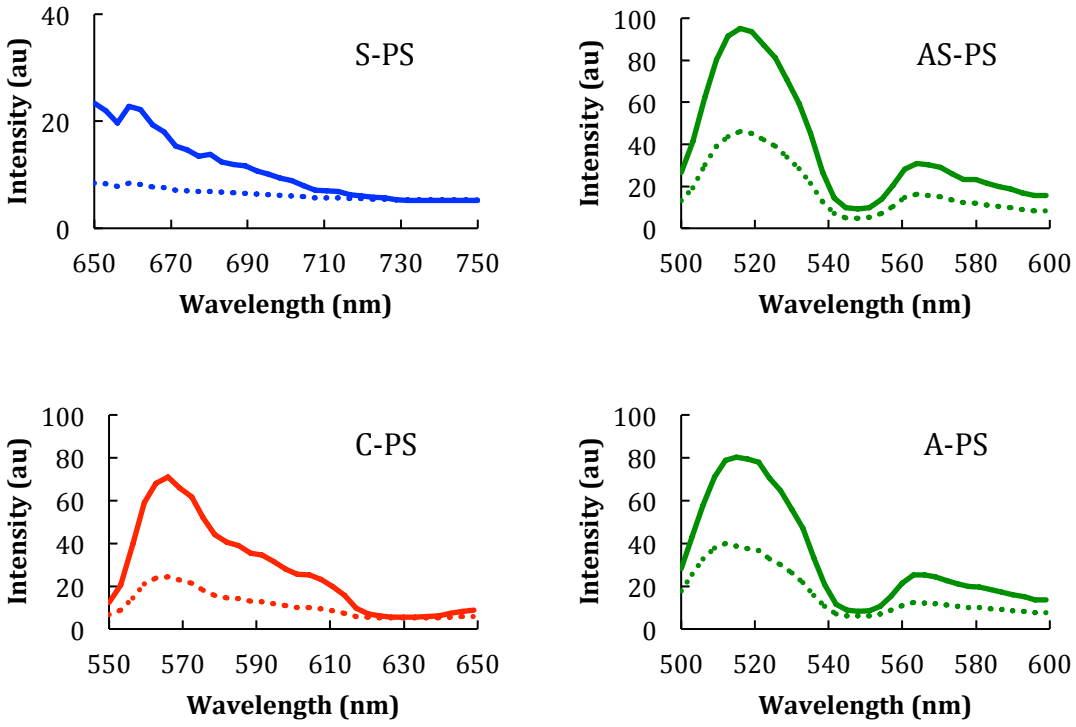

Figure 3.22 Fluorescence intensity measurements of particles dispersed in the IL phase before (solid line) and after emulsification (dashed line).

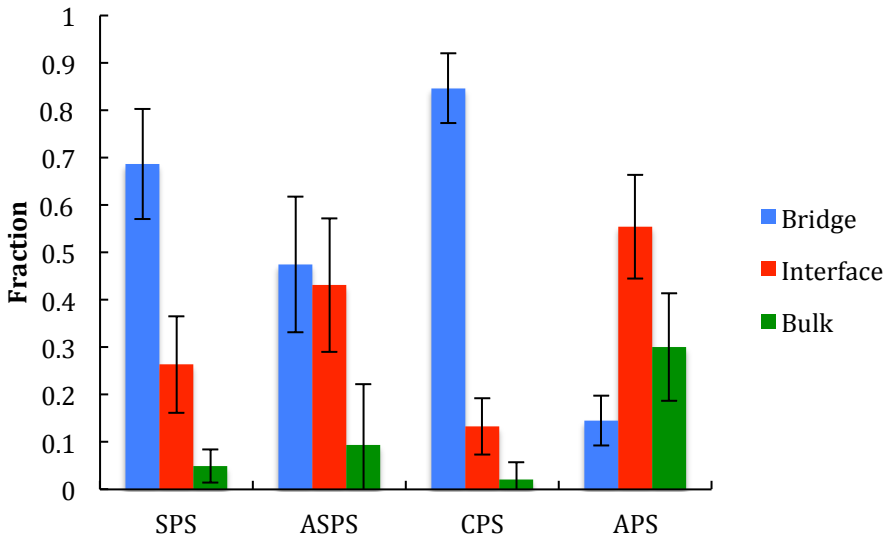

Figure 3.23 Fraction of particles appearing in bridges (blue), at non-bridged interfaces (red), and in the bulk phase (green) with respect to particle surface chemistry.

It is worthwhile to note that the particles within the bridges assembled into a monolayer at the oil-oil interfaces. Some of the bridges in this section might appear wider than 1.1 μm (the largest diameter of the particles), but this is simply an anomaly from the overlay of confocal and differential interface contrast (DIC) images. The confocal images, which represent a very thin view plane, show that these bridges were clearly monolayers of particles (See Figure 3.24).

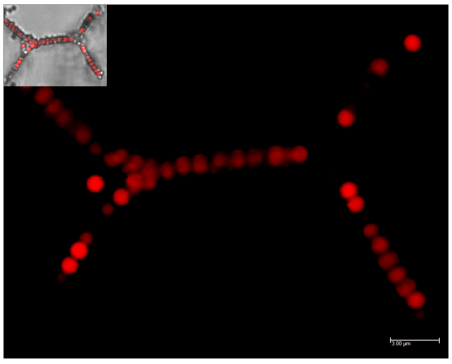

Figure 3.24 A confocal image of a C-PS particle bridge formed between two oil droplets. The inset shows the overlay with the corresponding DIC image. The Scale bar represents 3μm.

Dynamics and Droplet and Emulsion Stability

It is worthwhile to note that in our experiments, most bridges formed during the emulsification process; although we did capture some growth dynamics. Figure 3.25 shows how a particle (circled) at an oil-IL interface approached the already-formed bridge. The particle diffused along the droplet interface by Brownian motion until it was sufficiently close enough to the particles in the bridge and experienced an attraction. Once the collision occurred, the attachment of the free particle to the bridged particles

was irreversible. Although the bridges formed quickly, it appears that they may grow over time by the addition of free solid particles drawn in by inter-particle forces. This is similar to the behavior observed by Xu et al. where the oil bridge between two water phases (a droplet and a flat interface) grew over time as solid particles from the bulk aggregated to the already-bridged particles [45].

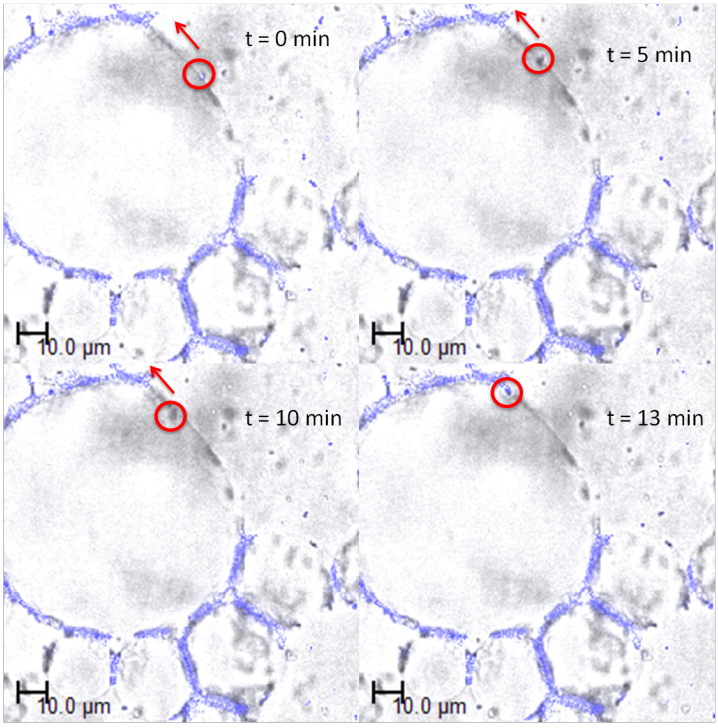

Figure 3.25 Dynamics of an S-PS particle (circled) at the oil-IL interface until it joins the other particles bridge two oil droplets. The scale bars represent 10µm.

As mentioned previously, solid particle bridging plays an important role in the stability of oil-water Pickering emulsions. Surprisingly, although particle bridging inhibited individual droplet-droplet coalescence, it did not promote, but actually distressed, the overall emulsion stability. Figure 3.26 captures the stability of the Pickering emulsions as a function of time; as a control experiment, we prepared PDMS-in-IL emulsions with no particles in the same manner as the particle-stabilized emulsions.

The oil-in-IL Pickering emulsions were homogenous after sonication but only stable for approximately 2.5 hours in those systems using S-PS, AS-PS, and C-PS as stabilizers. At approximately 2.5 hours, a distinct cream oil layer with particles formed at the top of the sample and left a light-colored emulsion underneath. The cream oil layer grew as a function of time. In contrast, the stabilizer-free control became cloudy with the formation of oil droplets but was stable for about 23.5 hours until a layer of PDMS was clearly visible at the top. It appears, therefore, that the S-PS, AS-PS, and C-PS actually promoted the destabilization of the Pickering emulsions. We hypothesize, that this observation is due to particle-induced adhesion between oil droplets. Due to the low density and large volume (thus the buoyant effect), the aggregated oil droplets quickly rose to the top of the samples. These particles, therefore, did not stabilize the emulsions, but acted as flocculating and creaming agents in the presence of vigorous agitation. The A-PS system did not exhibit these characteristics until much later, likely due to a lack of bridging; however, it also worthwhile to note that due to the poor particle coverage at the oil-IL interfaces, the A-PS particles did not provide strong emulsion stabilization.

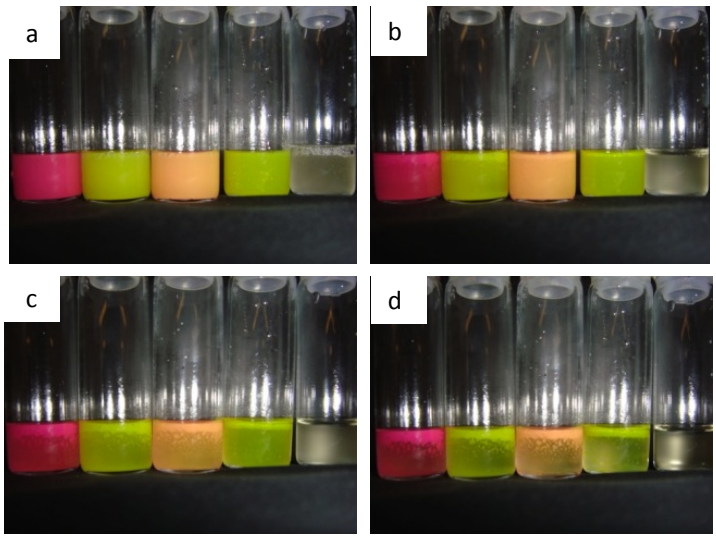

Figure 3.26 Emulsion stability as a function of time. The vials from left to right contain S-PS, AS-PS, C-PS, A-PS, and emulsifier-free, respectively. (a) t = 0 min; (b) t = 2.5 hours; (c) t = 6.5 hours and (d) t = 23.5 hours.

Upon examination of the cream top layer of an emulsion 60 days after sonication we found that the individual droplets had not coalesced, but were still separated by solid particle bridges. Figure 3.27 shows confocal and DIC images of a sample of the cream top layer of an S-PS system. Compared to the structures in Figure 3.21, these aggregates were much more extensive and the droplets exhibited much higher particle coverage. The latter observation was likely due to particle-particle attraction between bridged particles in an analogy to the dynamics shown in Figure 3.25. Because particles in the inter-droplet bridges severely hinder film drainage [213], we expect that these droplets will remain in this state for extended periods of time, possibly months and years.

Some experiments we have performed suggest that the degree of bridging might depend on the frequency of droplet-droplet and droplet-particle collisions. In this scenario, adhesive forces between the bridged droplets would be important. Considering only capillary forces and neglecting curvature effects, the adhesion force between two droplets can be calculated using [46]

$$F = 2\pi^2 \gamma R cos^2\left(\frac{\theta}{2}\right) \tag{3.14}$$

where F is equal to the force required to separate the droplets, γ is the interfacial tension between the oil and IL, R is the radius of bridge and θ is the contact angle of the solid particle. The interfacial tension for this system was 13.5 ± 0.1 mN/m as measured using a Sigma 701 Tensiometer. As an example, we calculated the adhesive force between two

bridged droplets shown in the top right corner of Figure 3.21c. The particles have a diameter of 1.1 μm and the width of the bridge is about 12.9 μm. For these droplets, assuming a contact angle of 100°, the adhesion force was on the order of 7.1E-7 N. Assuming that this adhesive force is overcome when the droplets are separated to the point that particles do not touch any interface, we can integrate this equation to find the energy required to separate bridged droplets. This energy, therefore is represented by

$$E = 2\pi^2 \gamma R \int_{h_0}^{a} cos^2 \left(\frac{\arcsin\left(\frac{h}{a}\right) + \frac{\pi}{2}}{2} \right) dh \tag{3.15}$$

where E is equal to the separation energy, a is the particle radius, h is the distance between the centerline of the particle and the oil/IL interface. Given the parameters above, the energy of separation for these droplets was on the order of 10^7 kT.

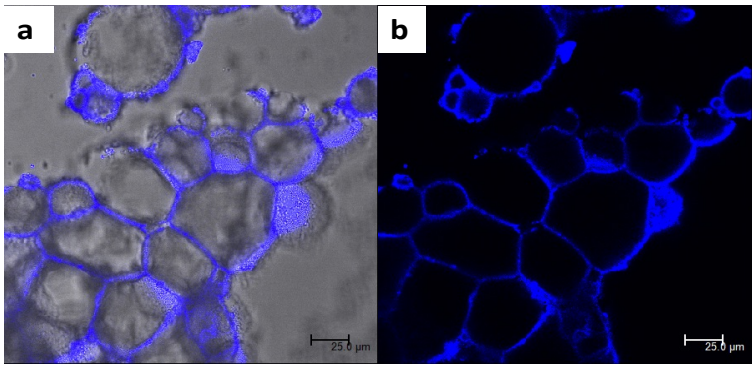

Figure 3.27 Images of the structure for a cream layer collected from a S-PS stabilized emulsion 60 days after initial emulsification. (a) An overlay of the confocal and DIC images; (b) The confocal image. The scale bars represent 25µm.

Effect of Particle Heterogeneity

To further investigate this bridging phenomenon, oil-in-IL Pickering emulsions with binary mixtures of particles were prepared. The binary systems studied were A-

PS/S-PS and C-PS/S-PS. Each emulsion contained 0.001g of each type of particles, making 0.002g of solid particles in total. Figure 3.28 shows representative confocal images of the droplet structures that were formed with heterogeneous particles. The structures seemed to be a hybrid of the structures formed by the respective single-particle systems. Figure 3.28a shows that the A-PS/S-PS system exhibited significant bridging. This is surprising because the A-PS particle did not readily form bridges on their own (See Figure 3.21d), but appeared well incorporated into all bridges with the S-PS particles. The bridges appeared to be monolayers of both A-PS and S-PS particles in nearly equal number. To verify this observation, we analyzed 15 confocal images of such bridges using ImageJ® to determine the fraction occupied by each species. We found that in the A-PS/S-PS system, the fraction of A-PS particles present was 0.44 ± 0.12, indicating that the particles did indeed mix well in the bridges (See inset of Figure 3.28a). Inter-particle interactions between the positively charged A-PS and negatively charged S-PS particles were likely responsible for this mixing since the A-PS particles did not readily form bridges on their own (See Figure 3.21d). Similarly, the bridges in the C-PS/S-PS system also showed good mixing between the particles (Figure 3.28b). Such behavior was expected, since both particles readily formed bridges of this size and packing density in single particle systems. Analysis (of 8 images) showed that the average fraction of the bridge occupied by the C-PS particles was 0.49 ± 0.11, suggesting good mixing (See inset of Figure 3.28b).

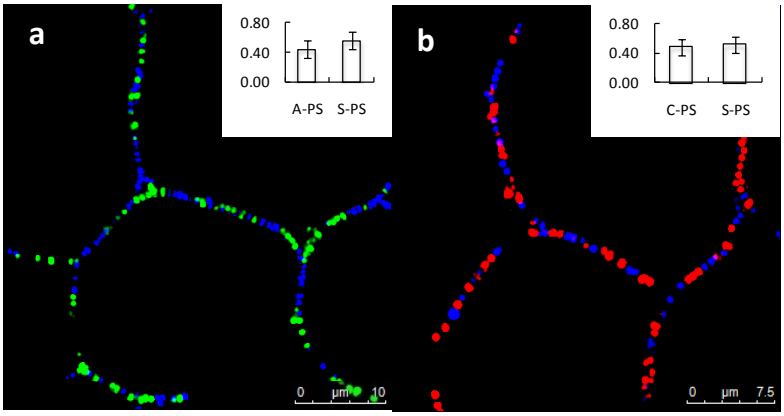

Figure 3.28 Confocal images of inter-droplet bridges in the Pickering emulsions contain (a) A-PS/S-PS; (b) C-PS/S-PS. The A-PS, C-PS and S-PS particles are shown in green, red, and blue respectively. Fractions occupied by each respective particle are shown as insets. Scale bars represent 10μm and 7.5μm for (a) and (b), respectively.

The bridging morphology in oil-in-IL Pickering emulsions is a unique phenomenon that challenges much of the conventional wisdom on Pickering emulsions. Since this behavior destabilizes emulsions (due to buoyancy) we predict that this phenomenon may be used to de-emulsify natural emulsions in place of chemicals [251] that are more difficult to handle. Droplet bridging easily lends itself to the creation of high internal phase emulsions (HIPEs): an emulsion where the droplet phase occupies more than 74% of the total volume [252]. By polymerizing the continuous phase of HIPE, these emulsions may serve as templates [252] for highly porous structures with applications in biological tissue scaffolds [253], sensors [254], and hydrogen storage [255]. Because the bridged droplets already self assemble into structures of high droplet phase volume, this phenomenon may provide a simple route to HIPE formulation.

However, the underlying mechanism for this behavior remains elusive. Therefore, in the second section of this chapter we systematically evaluate the conditions under which bridging may occur and the parameters that affect the extent of bridging. We also

present some possible explanations behind this unique phenomenon. The results suggest that when the IL is the continuous phase of an emulsion, bridging may occur over a wide range of particle sizes and concentrations. The work also suggests that the extent of bridging may be easily tuned by manipulating these parameters. A qualitative phase diagram is proposed to illustrate this concept.

Phase Diagram Generation

Normally, Pickering emulsions are stabilized against coalescence because the droplets are "armored" by a monolayer of solid particles [8, 12, 24, 25, 34, 57, 203, 256]. At low particle concentrations, droplets that may not be completely covered and the particles can form bridges with adjacent droplets, halting their coalescence [42, 44-47, 208, 257]. Therefore, it was expected that increasing particle concentration would result in more fully covered droplets and, consequently, less bridging. Employing the S-PS particles as stabilizers, we studied PDMS-in-IL emulsions at particle number concentrations of 0.4 M, 0.8 M, and 1.6 M, respectively. Figure 3.29 shows the overlays of representative differential interference contrast (DIC) and confocal image of the emulsion droplets. Contrary to expectations, the extent of bridging increased remarkably with concentration. It is interesting to note that the particles did not generally assemble at the droplet surfaces (oil-IL interfaces), even at high concentrations, seemingly avoiding the IL phase.

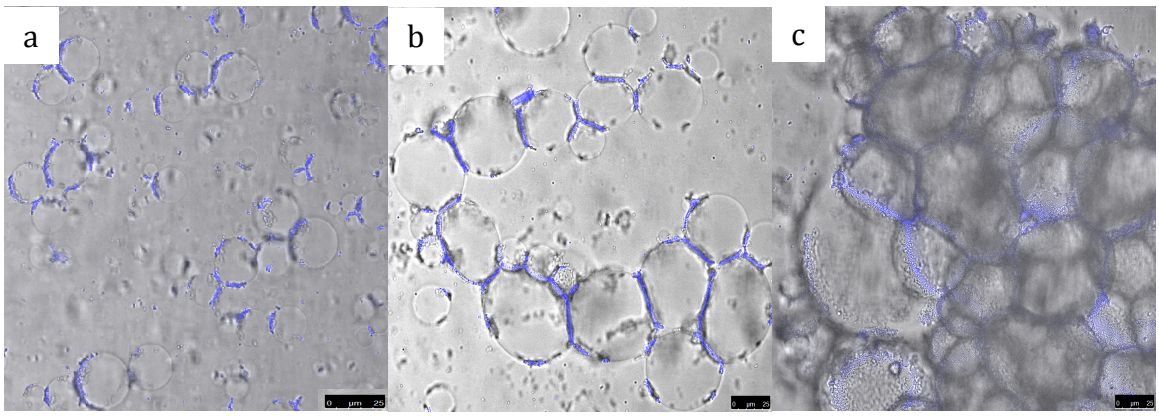

Figure 3.29 PDMS droplets in [BMIM][PF_6] bridged by 1.0-micron S-PS particles at number concentrations of (a) 0.4 M, (b) 0.8 M, and (c) 1.6 M. Scale bars represent 25 microns.

Horozov and Binks suggested that the reason for bridge formation between two approaching droplets laden with charged particles was due to repulsive forces between particles residing on the droplet surface and particles in the inter-droplet film [42]. The repulsive forces would prevent the particles from convectively exiting the inter-droplet film during drainage [42]. The structures in oil-in-IL emulsions, however, must have formed in a different way because no particles existed on the non-bridged droplet interfaces to exert repulsive forces on the bridged particles. Some hypotheses on how these structures formed will be discussed later on.

The degree of bridging in each of these systems was quantified by measuring the two entities: the droplet size distribution and number of droplets per structure. Figure 3.30a shows the droplet size distribution for different particle concentrations. The particles used were 1.0-micron S-PS particles. The 0.4 M emulsion exhibited a reasonably narrow distribution of droplet sizes with a peak between 10-20 microns. Increased concentration allowed for a wider distribution of droplets sizes in bridged structures. Higher concentration also allowed for bridging of larger droplets (>45 microns

in diameter). This was anticipated since with increasing concentration there were enough particles to form increasingly larger bridges between droplets. The median droplet diameters for the 0.4 M, 0.8 M, and 1.6 M emulsions were 16.1 microns, 20.6 microns, and 25.7 microns, respectively. These data indicate a steady shift toward larger droplets with increasing particle concentration.

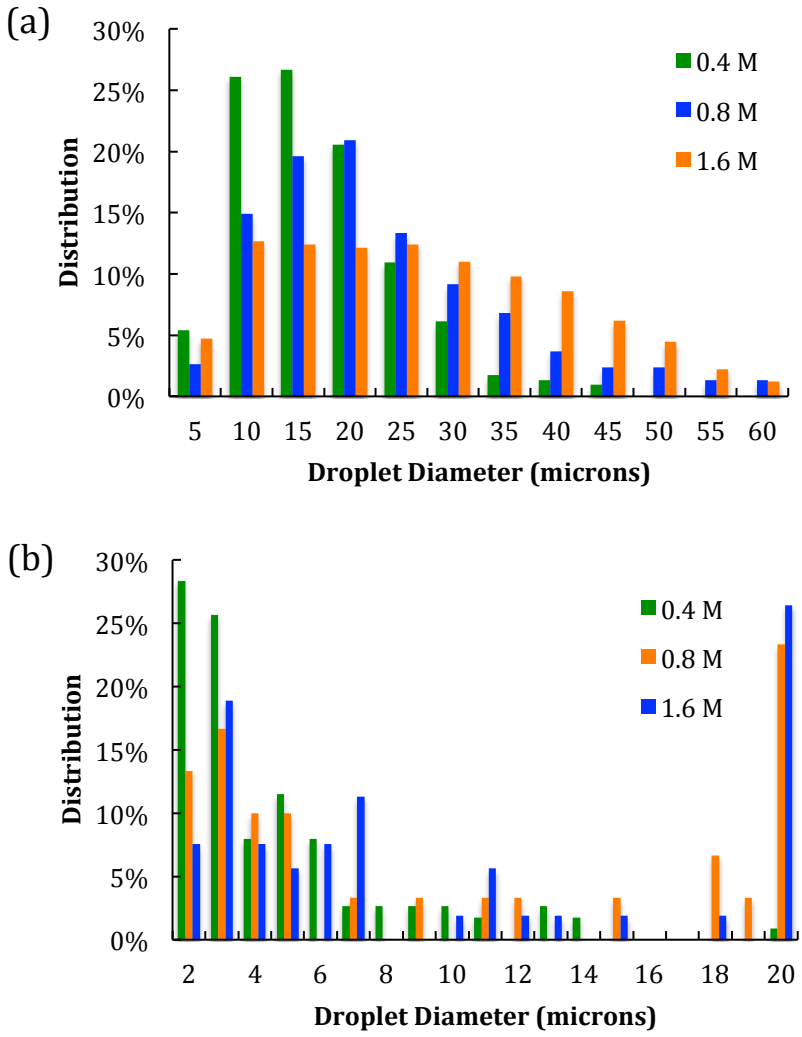

Figure 3.30 (a) Droplets size distributions and (b) structure size distributions for the PDMS-in-IL emulsions stabilized by 1.0-micron S-PS particles at number concentrations of 0.4 M, 0.8 M, and 1.6 M.

Figure 3.30b shows the distribution of droplets per structure for the same systems. In contrast to the droplet size distributions, we observed more pronounced changes in the distribution shape with increased particle concentration. At 0.4 M, the bridged structures mostly consisted of 2-3 droplets. There were still many 2-droplet structures in the 0.8 M emulsion, but a significant number of structures with 20-30 droplets formed as well. As can be seen in Figure 3.30b, the bridged structures in the 1.6 M emulsions contained even more droplets. The last data point for the 1.6 M emulsion in Figure 3.30b represents the fraction of structures with 20 or more droplets. Therefore, 27% of the structures in this emulsion contained more than 20 droplets. Thus, instead of exhibiting increased droplet coverage, this system bridged more droplets with increasing concentration.

Having established that the extent of bridging could be tuned with particle concentration, we wished to explore the limits of bridge formation. At the lower concentration limit, we expected that only single droplets would be seen since there were be two few particles to form bridges. At the upper limit, all droplets would be bridged together, since the extent of bridging seemed to increase with concentration. Using S-PS treated particles of 0.2-□□ diameter, we were able to prepare PDMS-in-IL emulsions of 0.16 M, 4.0 M, and 100 M particle concentrations. The DIC/confocal image overlays of these systems are shown in Figure 3.31. At the very low particle concentration (Figure 3.31a), there is no significant bridging occurred, as expected. However, it is surprising to observe that no monolayer bridging was observed at the highest concentration (Figure 3.31c). Instead, a third morphology was seen in which the droplets were not bridged, but completely covered by the S-PS particles. In fact, coverage was so high that significant droplet deformation was observed due to jamming of the particles at the droplet

interfaces. Although the droplets were in close proximity, their interfaces were not joined because of the high particle coverage (see inset to Figure 3.31c). Thus, there appeared to be three regimes of bridging emulsion morphologies occurring with increasing particle concentration: (I) single, sparingly covered droplets, (II) bridged clusters of droplets, and (III) fully covered droplets. Bridging, therefore, was only one phase in the morphological range of these systems. Regime II is the focus of this paper and will be discussed in the next two sections. Regime III also deserves some discussion and will be touched upon in the last section.

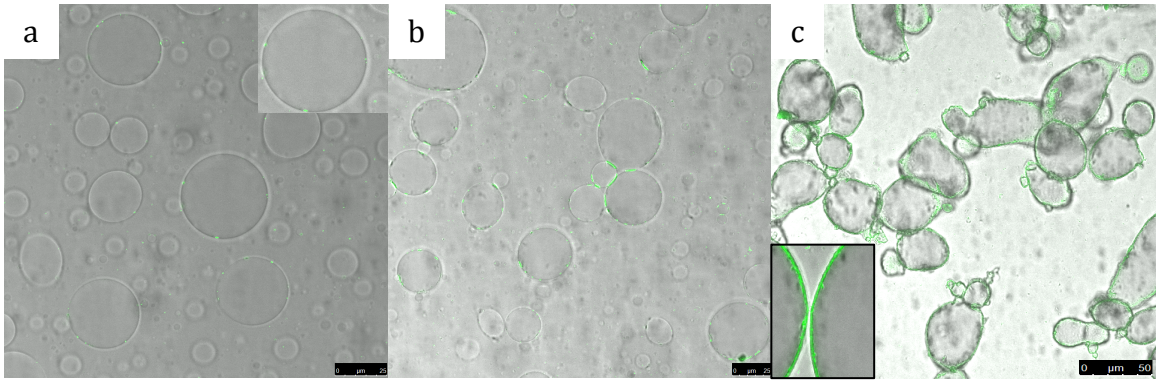

Figure 3.31 DIC/confocal overlays of PDMS droplets in [BMIM][PF_6] bridged by S-PS particles at concentrations of 0.16 M (a), 4.0 M (b), and 100 M (c).

Because particles in these systems tended to bridge rather than cover droplets, flat monolayers were the dominant self-assembled particle structure. Therefore, it was proposed that the area (σ) of a hypothetical monolayer formed by all of the particles in a given system could be a good predictor of the bridging extent. A system with a high σ would exhibit a greater degree of bridging than that of a lower σ. Assuming that all bridges are planar and circular and exhibit tight packing (as has been observed in other particle bridges [43, 44, 47]), the potential bridging area is proportional to the sum of the

cross sectional areas of all particles in the system. Thus, total potential bridging area, σ, is given by

$$\sigma \propto n\pi {r_p}^2 \tag{3.16}$$

where n is the number of particles, and r_p is the individual particle radius. It should be noted that not all particles in a given system self-assembled into bridge structures; many particles remained dispersed in the IL phase. Therefore, σ represents the maximum bridging area attainable by a system. To test this hypothesis, we formulated two emulsions of the same particle concentration (0.016 M), but different particle sizes. According to Equation 3.16, the system with 4.0-micron particles had 16x greater bridging potential than the system with 1.0-micron particles. **Figure 3.32** shows the DIC/confocal overlay images of PDMS droplets in IL stabilized by S-PS stabilized particles of (4a)1.0 micron and (4b) 4.0 micron, diameters.

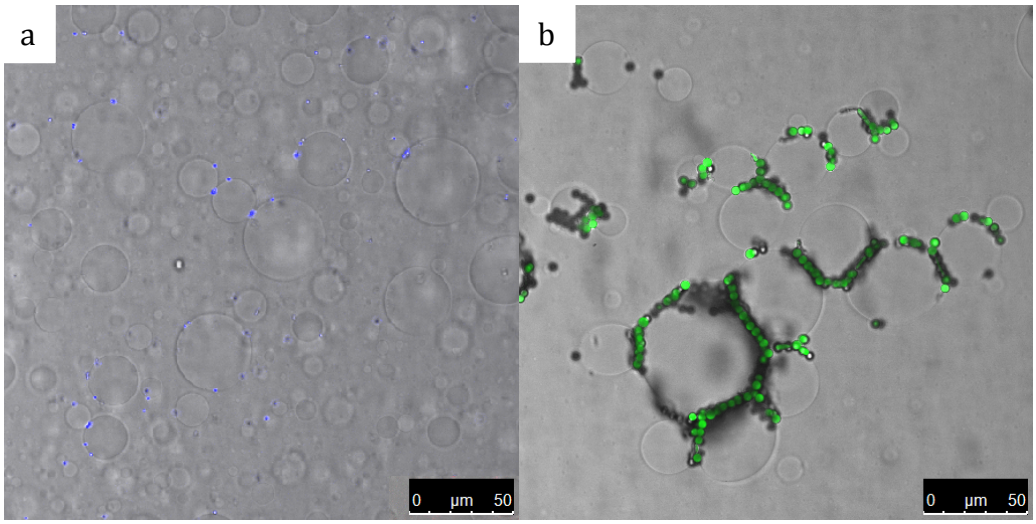

Figure 3.32 DIC/confocal overlays of PDMS droplets in [BMIM][PF_6] bridged by S-PS particles of (a) 1.0 and (b) 4.0 micron diameters. Scale bars represent 50 microns.

Distributions of droplet size and droplets per structure were quantified for these two systems and are shown in Figure 3.33. Figure 3.33a shows that increasing particle size broadened the droplet size distribution. Larger droplets were bridged in systems with larger particles. This was expected, since the larger particles had more potential bridging area (see Equation 3.16). This relationship was also verified by the distributions of droplets per structure (Figure 3.33b). The structures in the system with small particles were confined primarily to 2 or 3 droplets while the larger particles created structures as containing as many as 20 droplets. Even though the most common structures consisted of 2-3 droplets in both systems, increasing the particle size broadened the distributions.

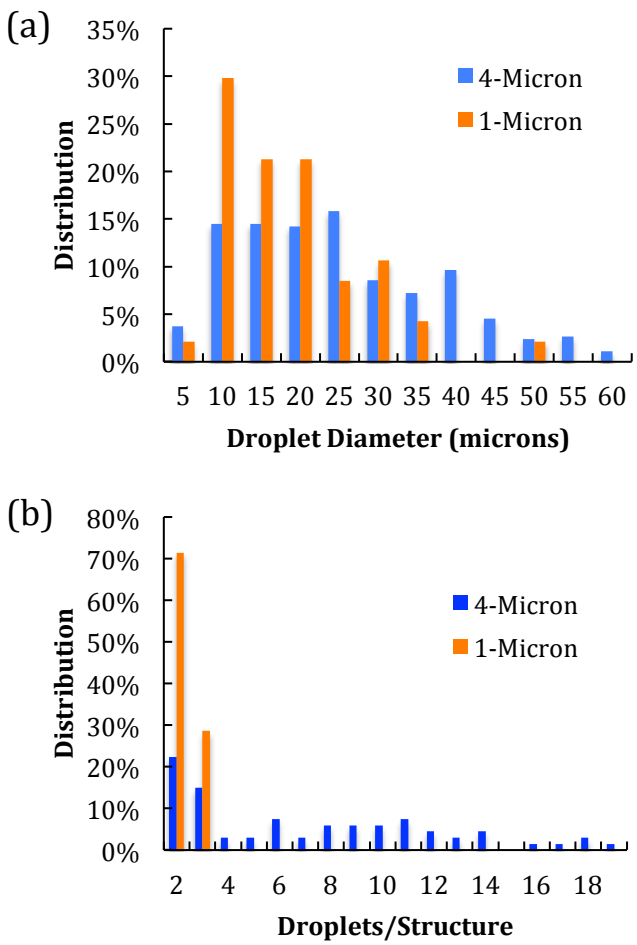

Figure 3.33 Droplet size (a) and bridged structure (b) size distributions for PDMS-in-IL system stabilized by S-PS particles of 4.0- and 1.0-micron diameters.

These results showed that systems of differing σ exhibited correspondingly different extents of bridging. Therefore, a new question arose: how would particle size affect bridging if all of the systems had the same σ? To make this comparison, we prepared emulsions using 0.2-micron, 1.0-micron, and 4.0-micron particles at concentrations of 3.98 M, 0.16 M, and 0.01 M, respectively. Figure 3.34 shows droplet and structure size distributions for these three systems. The droplet size and structure size distributions showed a great degree of overlapping, indicating that the extent of bridging was not significantly affected by particle size under these conditions. These findings

indicated that systems of the same potential bridging area showed nearly identical morphologies. Potential bridging area, σ, therefore, could be used as the primary predictor of the degree of bridging in systems of varying particle concentration and size within the ranges studied here.

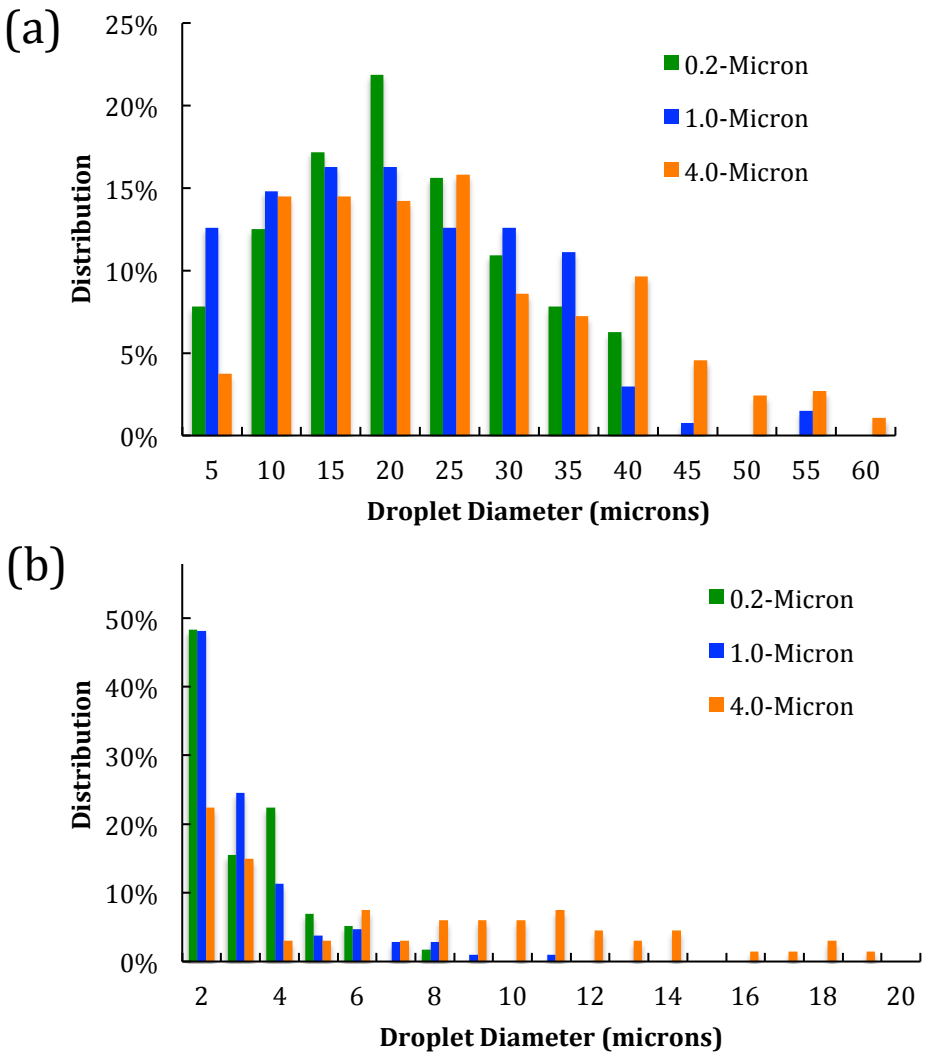

Figure 3.34 (a) Droplet size distributions and (b) droplets/structure distributions for the PDMS-in-IL emulsions stabilized by 0.2, 1.0, and 4.0-micron S-PS particles at number concentrations of 3.98 M, 0.16 M, and 0.1 M, respectively.

We will now briefly discuss some interesting phenomena that occurred in the third regime: single, fully covered droplets. Emulsions of 100 M particle concentration were formulated with 0.2-micron particles. Figure 3.35a shows several emulsion droplets of PDMS-in-IL stabilized by S-PS particles. Normally liquid droplets assume a spherical shape to minimize interfacial area. However, the PDMS droplets in this figure were distinctly non-spherical due to the high particle concentration. This phenomenon has been observed experimentally in both liquid droplets and air bubbles and is due to particle "jamming" at the interface [17, 75, 258, 259]. A number of droplet shapes have been observed including cylinders [75, 258], toroids, and saddles [258]. Bon et al. have suggested that this behavior may be useful for self-healing polymer composite applications [75].

Another interesting phenomenon observed in this region is illustrated in Figure 3.35b, which was an emulsion of water in IL stabilized by 0.2-micron C-PS particles. Once the particle concentration was high enough to prevent any bridging (because the droplets were fully covered), the water droplets began to absorb excess C-PS particles. These particles were relatively hydrophilic, which partially explains why they were absorbed into the water droplet. Ma and Dai also observed particle transport across the IL/water interface, but at much lower particle concentrations and the emulsion droplet interfaces were not fully covered [151]. The energy required for desorption, ΔG, of a spherical particle from a liquid-liquid interface is given by Equation 2.3 Desorption energy for these particles was on the order of 10^5 kT, which was likely overcome under sonication conditions at such high concentration. The uncommonly low interfacial tension of the IL/water system may explain this behavior (and that observed by Ma and

Dai) since desorption energy is directly proportional to γ. Further investigation in this area is underway to obtain a conclusive explanation.

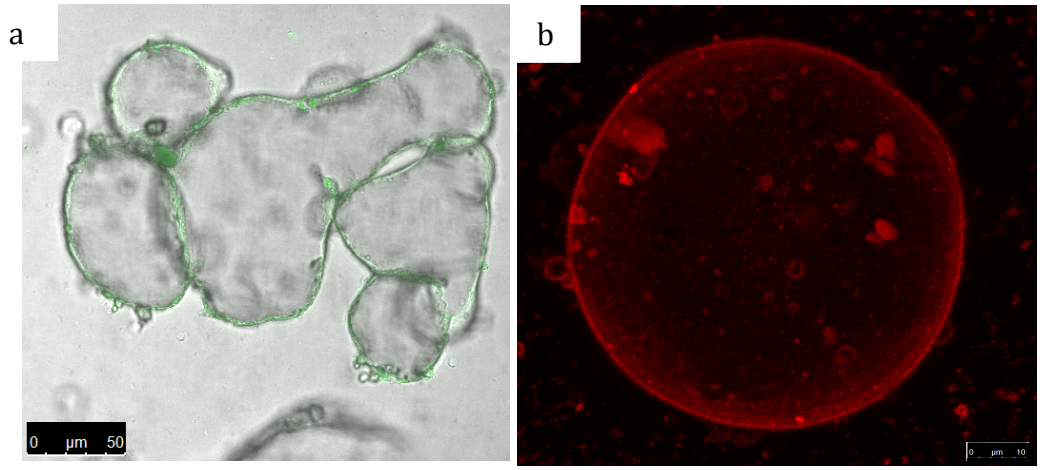

Figure 3.35 Microscope images of droplet behavior of emulsions corresponding to the third regime of **Figure 3.36**. On the left is a confocal/DIC overlay of PDMS/IL emulsion with 0.2-micron S-PS particles at a concentration of 100 M. On the right is a confocal image of a water droplet absorbing (after being covered with) 0.2 micron C-PS particles at a concentration of 100 M. Scale bars represent 50 and 10 microns, respectively.

Having established Equation 3.16 as an effective predictor of bridging extent, we could describe the various morphologies of this emulsion system with respect to a single parameter, σ. A "phase" diagram relating the three morphologies discussed in this paper in terms of the bridge structure size is shown in Figure 3.36.

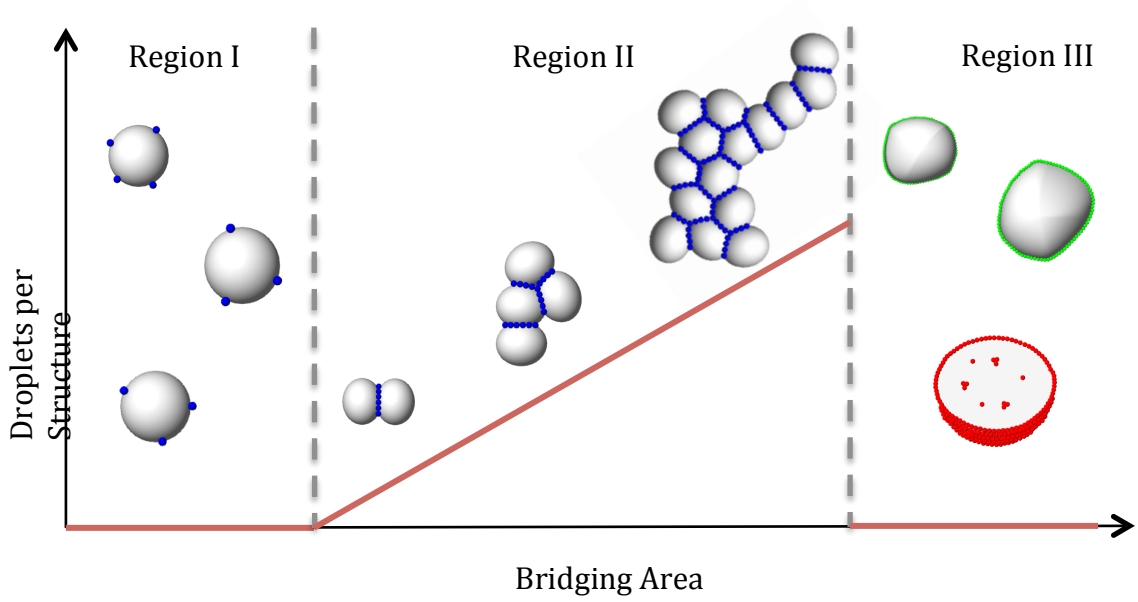

Figure 3.36 "Phase" diagram of the bridging IL emulsions discussed in this paper. The regimes are denoted as: Region I, single sparingly covered droplets; Region II, bridged clusters of droplets; Region III, fully covered droplets. In the third phase, S-PS and C-PS particles are represented in green and red, respectively.

Bridging of Water Droplets

Our previous publication and the work above [257] only dealt with oil-in-IL Pickering emulsions. As a matter of fact, self-assembly at IL-water interface has received greater attention [151, 207, 249]. Naturally the question arose as to whether or not bridging would still occur if the droplet phase was aqueous. Since the particles were known to be stable in water (they were received in dispersion form), it was originally hypothesized that the water droplets would reabsorb the particles, making the bridge formation impossible. Surprisingly, bridging occurred with all particle surface chemistries except for the A-PS particles and there was no particle absorption into the water droplets. The confocal/DIC overlay images are shown in Figure 3.37. In general, these bridged structures were nearly identical to the oil-in-IL structures. Both cases

showed minimal droplet coverage (except for the bridges) and exhibited networks of many droplets. The A-PS particles did not form bridges in either system. The water droplet structures were slightly more compact and the AS-PS particles showed significant water droplet coverage outside of the bridges. These results indicate that bridging in IL-based Pickering emulsions was possible over a wide range of droplet phases: from aqueous to hydrophobic.

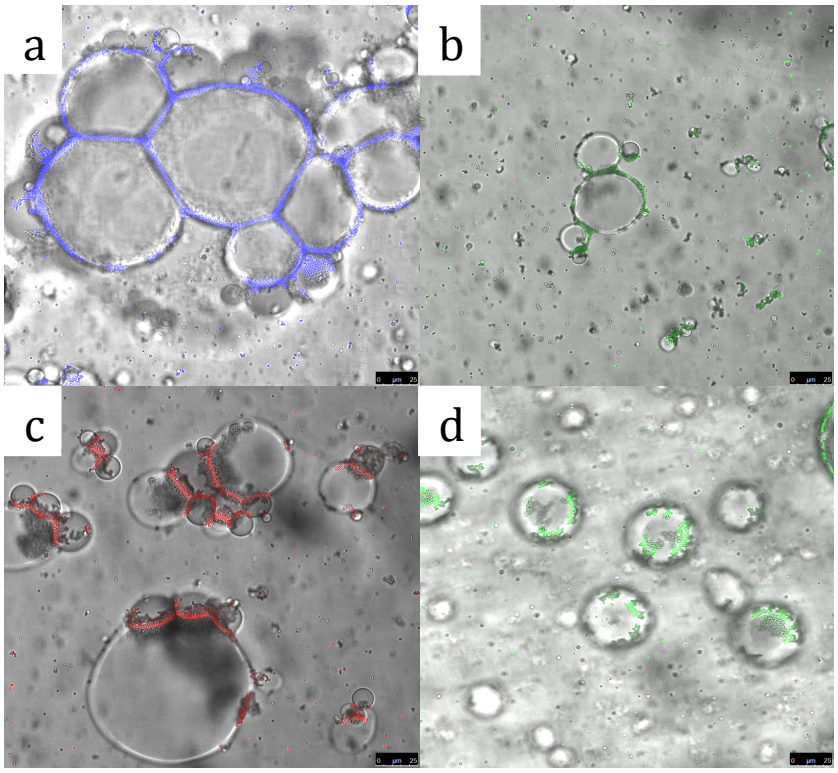

Figure 3.37 DIC/confocal overlays of water droplets in [BMIM][PF_6] stabilized by 1.0-micron (a) S-PS, (b) AS-PS, (c) C-PS, or (d) A-PS particles. Scale bars represent 25 microns.

Bridging in the water-in-IL Pickering emulsions is a surprising observation in light of the role of contact angles. In order to prevent rupture of an oil (or IL) film between to water regions, the particles must have a contact angle greater than 90^o [13, 43, 47]. Observations of the reverse emulsions (the IL-in-water type) [151], however,

suggested that the contact angles of the polystyrene particles were less than 90^o, a condition that is necessary to stabilize droplets in a continuous phase of water [12]. Nevertheless, these particles demonstrated unusual film stabilizing capability and bridged numerous water droplets in IL. Explanation for this behavior requires a greater understanding of the liquid film stabilization mechanism for this self-assembly process.

Possible Mechanisms

Thermodynamically, the change in free energy from single droplets to bridged droplets can be described as a sum of the free energies of the constituent processes. These include particle adsorption to the liquid-liquid interface ($\Delta G_{Capillary}$), increases in droplet surface area due to deformation ($\Delta G_{Deformation}$), van der Waals forces between the droplets (ΔG_{VdW}), electrostatic forces between the droplets ($\Delta G_{Electrostatic}$), and particle-particle interactions ($\Delta G_{Particle-Particle}$) [32]. Equation 3.12 summarizes this relationship. In the case to two droplets, the change in free energy can be calculated by solving Equation 3.12. $\Delta G_{Capillary}$ and $\Delta G_{Deformation}$ are expressed in Equations 3.13 and 3.14, respectively. In these equations, $\Delta G_{Capillary}$ is simply two times (to account for both interfaces) the adhesion energy for all of the particles in the bridge (n_p). In Equation 3.14, A_0 and A_1 are the surface areas of the unbridged and bridged droplet, respectively, r_0 is the radius of the droplet before bridging, r_1 is the radius after bridging ($r_1 > r_0$), and a is the radius of the bridge. While r_0 and a are specified, r_1 must be solved imperatively using the assumption that droplet volume is conserved. Being purely ionic, ILs present an environment of extremely high electrolyte concentration. Therefore, electrostatic forces were not calculated due to the absence of reliable models to account for this feature. However, we can expect that these interactions would have positively contributed the

total bridging energy, since the droplets would have exhibited like charges. Relationships for the other the van der Waals and particle-particle forces [32, 260] were considered, but their contributions to the total free energy were negligible compared to the capillary and deformation contributions.

$$\Delta G_{Bridge} = \Delta G_{Capillary} + \Delta G_{Deformation} + \Delta G_{VdW} + \Delta G_{Electrostatic} + \Delta G_{Particle-Particle} \quad (3.17)$$

$$\Delta G_{Capillary} = -2n_p {r_p}^2 \gamma (1 + cos\theta)^2 \quad (3.18)$$

$$\Delta G_{Deformation} = 2\gamma(A_1 - A_0) = 2\pi\gamma\left[2\left({r_1}^2 + r_1\sqrt{{r_1}^2 - a^2} + a^2 - 4{r_0}^2\right)\right] \quad (3.19)$$

We calculated these forces for the formation of a single bridge between two droplets. Figure 3.38 shows how the capillary, deformation, and total free energy changed with increasing bridge size and at contact angles of 95^o (Figure 3.38a) and 110^o (Figure 3.38b). For the 95^o contact angle calculations, the capillary energy dominated, resulting in a negative free energy for all bridge sizes. With increasing bridge size, the more this term dominated. However, increasing the contact angle caused a decrease in capillary energy contributions, and deformation energy dominated for the 110^o contact angle case. Therefore, it appears that bridging was favorable at 95^o, but unfavorable at a contact angle of 110^o. Figure 3.39 shows how these three energies changed with contact angle and indicates that there was only a very small window in which the total free energy was negative (approximately 95^o-99^o). These results suggest that bridging was not likely a thermodynamically favorable configuration, unless other forces are accounted for.

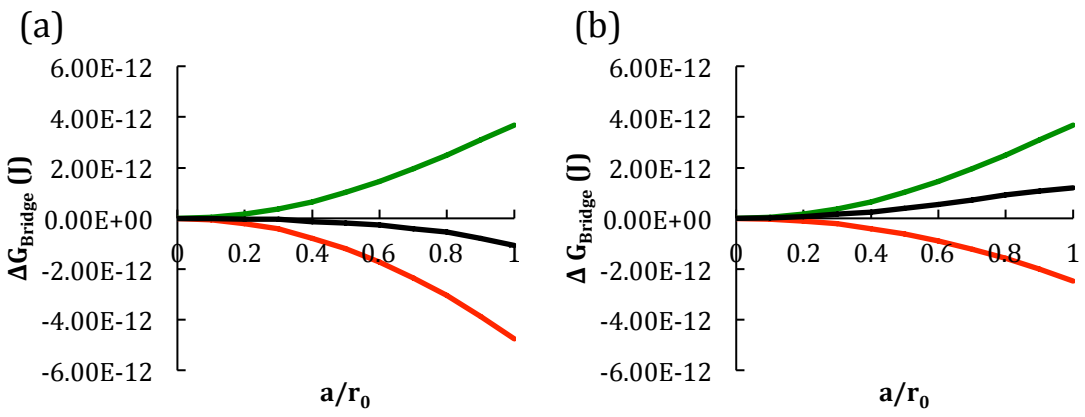

Figure 3.38 Calculation of capillary (red), deformation (green), and total energy (black) of the bridging of two droplets with respect to bridge size at contact angles of (a) 95° and (b) 110°.

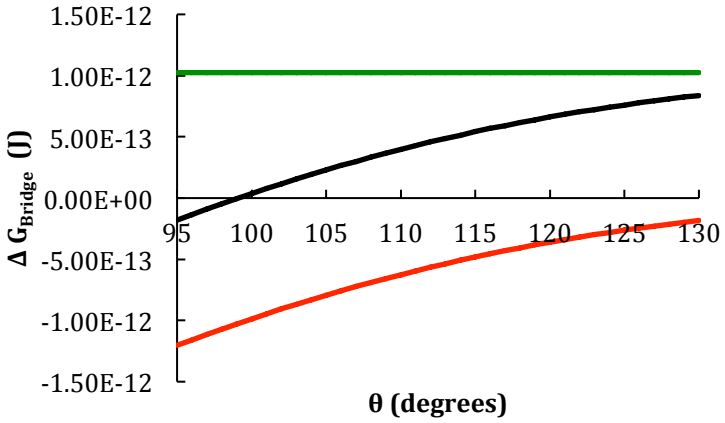

Figure 3.39 Calculation of capillary (red), deformation (green), and total energy (black) of the bridging of two droplets with respect to contact angle.

Lee and coworkers recently reported on a similar bridging morphology in non-IL Pickering emulsions stabilized by hydrophobized silica microspheres [261]. In that study, the authors showed that only particles with a sufficiently large three-phase contact angle could bridge emulsion droplets resulting in extensive percolating structures [261]. Droplets in that system, however, were fully covered whereas the key feature of the IL-

based system was exclusive bridging in the absence of droplet coverage. Also, since bridging occurred in both oil/IL and water/IL with a variety of particle surface chemistries, it is unlikely that contact angles played a major role. This is also evident from the theoretical results presented in Figure 3.38 and Figure 3.39, indicating a very small window of contact angles that produced favorable free energies. Therefore, we looked for other forces that may have played a role in bridge formation.

The distinctive feature of these systems was that they favored droplet bridging over droplet coverage. It should be noted, however, that significant agitation was necessary to form bridged structures; emulsions under mild agitation (for example, shaking by hand) exhibited only single, sparsely covered droplets. Therefore, bridges likely formed during mixing as particles were trapped between colliding droplets, as hypothesized in Figure 3.40. One unique property of these systems is the high viscosity of the bulk phase. [BMIM][PF_6], like most ILs, has a relatively high viscosity, 217.9 cP, at room temperature [166]. Since high viscosity is known to slow the inter-droplet film drainage rate [213] it was suggested that the particles may not have been able to exit the film before the droplets collided. However, in testing this theory we observed that water droplets in an oil phase of similar viscosity were not bridged by polystyrene particles. Another unique feature of these systems was the unusually low interfacial tension. Using a Sigma 701 Tensiometer, we measured the interfacial tensions of the water/IL and PDMS/IL interfaces to be 9.9 $\pm$ 0.1 mN/m and 13.5 ± 0.1 mN/m, respectively. The lower interfacial tension may have allowed for the menisci around the particles to extend further away in the radial direction, allowing for longer-range inter-particle attraction.

Sonication of a system of similar interfacial tension (water/1-decanol) [262] yielded no bridged structures.

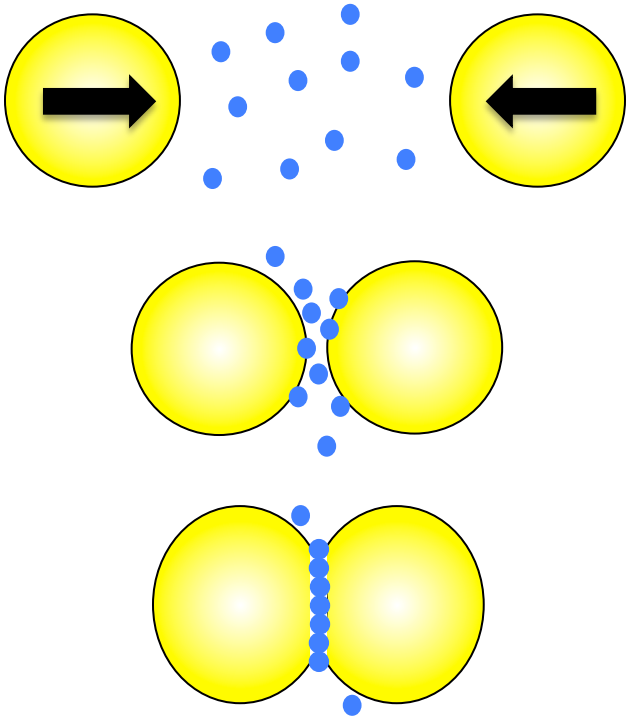

Figure 3.40 Schematic depiction of a possible mechanism for bridge formation: Particles (blue) are trapped between colliding droplets (yellow).

We hypothesized that this bridging phenomenon formed due to the unique ionic nature of the IL. To test this hypothesis, we formulated two oil-in-IL emulsions with 1.0-micron S-PS particles and replaced [BMIM][PF_6] with 1-butyl-3-methylimidazolium tetrafluoroborate ([BMIM][BF_4]) in the first emulsion and 1-methyl-1-propylpyrrolidinium bis(trifluoromethylsulfonyl)imide ([PMP][Tf_2N]) in the second emulsions. While [BMIM][BF_4] is quite similar to [BMIM][PF_6] with the exception of the anion, [PMP][Tf_2N] has a much lower viscosity (71 cP) and slightly higher density (~1.44 g/cm^3) than [BMIM][PF_6]. In support of our hypothesis, these emulsion formed bridged structures identical to the ones observed with [BMIM][PF_6] (see Figure 3.41). It

is worthwhile, therefore, to discuss what IL properties may be responsible for this phenomenon.

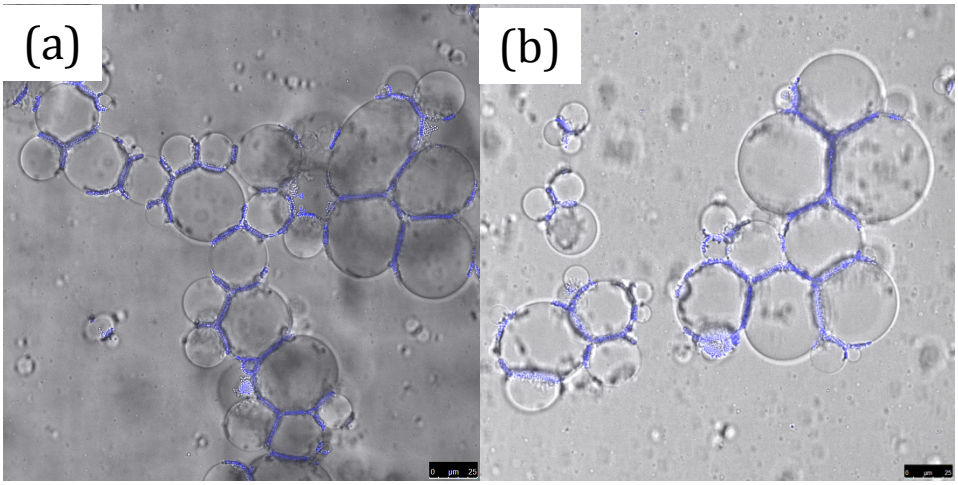

Figure 3.41 Bridging of PDMS oil droplets by 1.0-micron S-PS particles in (a) 1-butyl-3-methylimidazolium tetrafluoroborate and (b) 1-methyl-1-propylpyrrolidinium bis(trifluoromethylsulfonyl)imide. Scale bars represent 25 microns.

The formation of bridges may have been due to some unique interactions between the particles and the IL. Clearly, for the assembly scheme in Figure 3.40 to occur, some driving force must have existed to keep the particles trapped between droplets. Curiously, only the particles with acidic dissociable groups formed bridges. It is possible that strong hydrogen bonding between the surface groups and the fluorine groups of the anions enhanced the stability of the particle-laden IL film. Furthermore, ionic liquids are known to exhibit a degree of ordering (i.e. layering) upon contact with solid surfaces [263, 264]. Confined between tightly packed particles (in bridges), the IL would have interacted with many surfaces may have assumed an ordered structure. Recent AFM studies have indicated that this layering phenomenon is important in IL-particle interactions [150]. The existence of such a structure would also enhance the stability of the inter-droplet bridges. Molecular dynamics (MD) simulations of nanoparticles at the oil/IL interface

have indicated that particle aggregation may be enhanced by the presence of counterions [248]. While the scales are much different, this phenomenon may have provided some driving force for the aggregation of these microparticles at the bridges. Undissociated surface groups may have also provided some dipole-dipole interactions between particles at the interface, which can be significant [23, 32, 33]. Finally, particle surface chemistry may have affected contact angle hysteresis, which can enhance film stability [13].

3.3.4 Controlling Stability and Transport with an Organogelator

Ionic Liquid Gels

Given the unique phenomena observed in the last sections, we set out to determine if these behaviors could be controlled via rheological modification. This was accomplished by adding a gelator, 12-HSA. We first investigated the effect of 12-HSA on pure [BMIM][PF_6]. Experimental evidence indicates that 12-HSA effectively gels a number of oils including Canola oil [265, 266], methyl oleate [267], glycerol [267], methanol [268], toluene [268], mineral oil [267, 269], and an IL, [C_6MIM][Tf_2N] [270]. In order for effective gelation to occur, the 12-HSA molecules must immobilize the solvent by self-assembling into 3D networks of thin, entangled fibers [271, 272]. Zhu and Dordick showed that this process only occurs when the interactions between the gelator molecules and the solvent are minimized [273]. Otherwise, large structures form and macroscopic phase separation occurs [272]. Therefore, only if the IL-gelator interactions were small could 12-HSA successfully gel [BMIM][PF_6].

A super-saturated solution of 1.0 wt. % 12-HSA in [BMIM][PF_6] was mixed at 80^{o}C and allowed to cool. No macroscopic phase separation was observed and the 12-

HSA effectively gelled the IL. The top right image of Figure 3.42 shows that the resulting gel was opaque and did not flow under gravity (vial is upside down). In contrast, we found that at 0.5 wt. % 12-HSA was unable to gel the IL. Due to an insufficient amount of 12-HSA molecules to form a completely gelled network, the mixture was translucent (see the middle image of Figure 3.42) and flowed under gravity. Clearly, a rheological transition took place between these two concentrations.

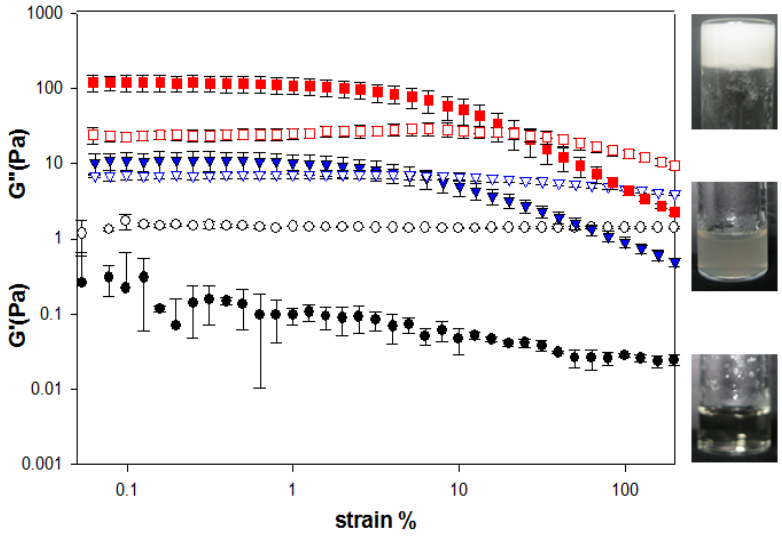

Figure 3.42 Variation of rheological properties as a function of strain %. The solid symbol is storage modulus G' and the open symbol is loss modulus G". ● pure IL; ▼ 0.5 wt.% gel; ■ 1 wt.% gel. The frequency is 1 Hz.

Therefore, we compared the rheological properties of these two mixtures with the pure IL. Specifically, we measured the storage modulus (G', elastic component) and the loss modulus (G", viscous component) for each sample as a function of strain percentage (a strain-sweep test). Figure 3.42 shows that the elastic component, G', of the 1.0 wt% mixture was dominant in gel state at low strain %. With increasing strain rate, however, the gel structure was overcome to exhibit more liquid-like behavior (shear-thinning), evidenced by the dominant viscous component. Increased 12-HSA concentration also

resulted in higher G' and G". These results confirmed the visual observations that a rheological transition (liquid to gel) indeed took place upon addition of 12-HSA and that complete gelation of [BMIM][PF_6] by 12-HSA only occurred above 0.5 wt%.

Since the Pickering emulsions studied herein included water and PDMS, we briefly investigated how 12-HSA behaved in these two solvents. It was found that 12-HSA effectively gelled the PDMS at 1 wt%. In water, 12-HSA did not gel the solvent, but aggregated, causing a macroscopic phase separation. The structure difference under the microscopy was also apparent. Microscopic images of 12-HSA in the IL, PDMS, and water are displayed in Figure 3.43, respectively. For reference, the original 12-HSA powder is shown as an inset of Figure 3.43a. Long and highly entangled fibers were observed in gels formed in both IL and PDMS. The presence of these macroscopic fibers accounted for the cloudy white, non-transparent appearance of the gels. In water, 12-HSA molecules self-assembled into branched structures centered on nuclei, resulting in large clusters. This morphology is a result of isotropic self-assembly and is characteristic of weak or non-existent gelation [273]. As mentioned before, good gelation (formation of fibrous networks) is disrupted by high gelator-solvent interactions. High solvent-gelator interactions (or higher solubility) allow the gelator molecules to move more freely and thus aggregate isotropically rather than form thin fibers [273]. We can conclude, therefore, that PDMS and [BMIM][PF_6] maintained minimal interactions with 12-HSA, whereas water interacted more favorably. H-bonding between water and 12-HSA was likely the main factor behind aggregation, leading to macroscopic phase separation rather than microscopic phase separation [265, 273]. However, the fact that the fibers were thicker in IL than in PDMS is evidence that the former interacted more with 12-HSA. It

should be noted that even though the fibers were thicker, 1-dimension growth was still dominant, which is the defining feature of gelled structures [273]. Strong interaction between the charged species of the IL and the hydroxyl groups of the 12-HSA can only be expected, but it was not strong enough to induce significant branching in the fibrous structures.

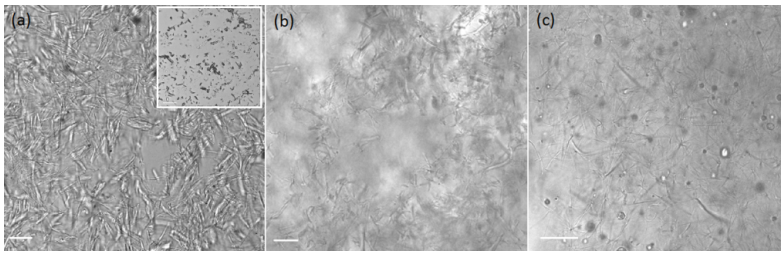

Figure 3.43 Microscope images of 12-HSA fiber structure in (a) IL, the inset is original morphology the 12-HSA powder, (b) PDMS, and (c) water. The scale bars represent 20 μm.

Fiber growth is also affected by the rate of cooling [274]. Typically, slower cooling rates allow for longer fibers [274]. We prepared IL gels at three different cooling rates and measured the fiber lengths using ImageJ ®. Figure 3.44 shows representative images of these three gels with their respective fiber lengths. At cooling rates of 0.1°C/s, fibers of ~50 microns (with large standard deviation) in length were formed. These fibers were significantly shortened and branched at faster cooling rates. Such behavior follows what is called the nucleation-growth-crystallographic mismatch branching (CMB) mechanism [275]. CMB suggests that one-dimensional growth is favored at low cooling rates due to the relatively high energy required to form branches [275]. Gelation of [BMIM][PF_6], therefore, appears to have followed conventional mechanisms.

Gelation of ILs has received increasing interest in the wake of the proliferation of IL-based applications. Many applications require properties unique to ILs, but are unable

to support a liquid phase. For example, ILs offer excellent gas separation qualities and tunability, but are not easily employed in membranes because they can be displaced by the pressure difference. Voss et al. showed how gelation overcomes this obstacle without inhibiting the advantageous properties of the IL. Gelled ionic liquids, or ionogels, have numerous other applications. Dye-sensitized solar cells based on ionogels have shown high efficiency and temperature durability [276, 277]. Ionogels have also been used to create controlled-release drug devices, where the IL itself has antibacterial qualities [278]. Other applications include catalytic membranes, lithium-ion batteries, fuel cells, sensors, and actuators [279]. Having established that 12-HSA gels the pure IL, we will now investigate how this gelator behaves in the heterogeneous systems: IL-based Pickering emulsions.

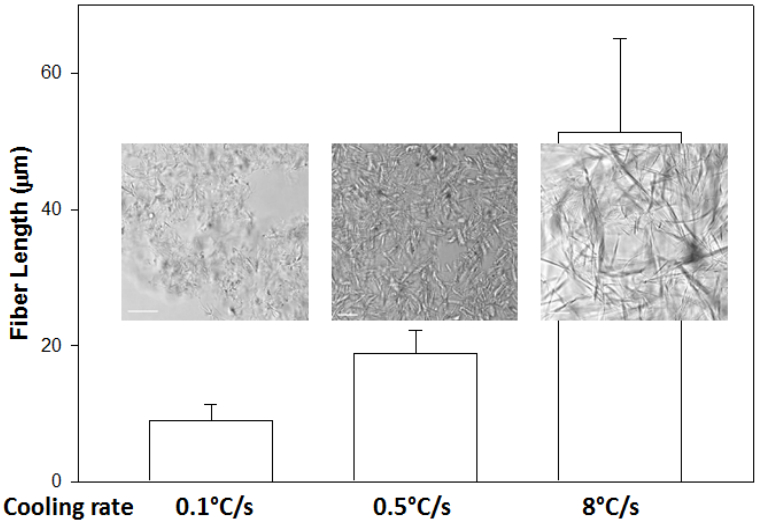

Figure 3.44 The effect of cooling rate on the self-assembled 12-HSA fiber lengths with representative images. The scale bars represent 20 um.

Effect of 12-HSA on [BMIM][PF_6]-in-Water Pickering Emulsions

For reference, we formulated three gelator-free IL-in-water Pickering emulsions. The representative confocal images in Figure 3.45(a-c) show that the particles generally

self-assembled at the interfaces of the IL droplets. This is in agreement with general consensus of Pickering emulsion morphology [24, 203]. In the S-PS and C-PS systems, droplets were generally only partially covered. For the A-PS system, both fully- and partially-covered droplets were observed. Cross-sectional images of the Pickering emulsion droplets are included in Figure 3.45(d-f). Interestingly, many S-PS and C-PS particles were observed in IL phase, which indicates that they must have been transported across the IL/water interface since the particles were originally dispersed in water phase. No A-PS particles were transported to IL phase. This phenomenon is unusual because the energy required for a particle to desorb from the interface is on the order of 1000-10^6 kT due to capillary effects [14]. Particle transport across the liquid-liquid interface appears to be unique to IL systems and has been discussed in recent literature and section 3.3.2, usually with emphasis on extraction applications [32,54-58] [150, 151, 195-197, 202] . The observation that only particles with acidic functional groups were extracted into the IL phase suggests that proton exchange between the surface groups and the [PF_6] may have lead to more favorable particle-IL interactions. Layering of IL ions at the particle surface may also play a role in this phenomenon [150]. Admittedly, the mechanism behind this extraction is not yet fully understood. However, it promises useful applications in oil sand/tar processing and oil spill beach cleanup: recent work has shown that imidazolium ILs can efficiently extract sand particles from oil at ambient conditions [150, 195-197].

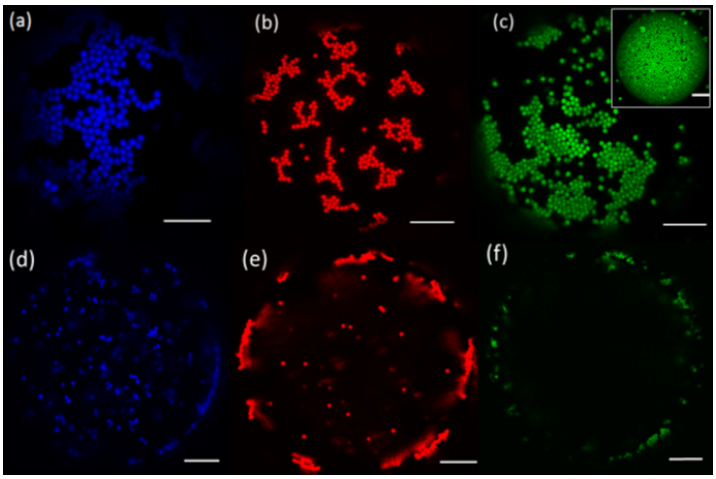

Figure 3.45 (a-c) Overlays of depth-series confocal microscope images of IL droplets in water in the presence of particles; (d-f) Confocal microscope images of IL droplet cross-sections in the presence of particles. (a, d) S-PS particles, (b, e) C-PS particles, (c, f) A-PS particles. The scale bars represent 10 μm.

Based on the results of the previous experiments, we expected that 12-HSA would exclusively gel the IL droplets, immobilizing the S-PS and C-PS particles inside. Melted IL-gelator mixture was dispersed in water in the presence of particles via sonication at 80^{o}C. An emulsion resulted and was allowed to cool at room temperature. Interestingly, it was observed that the 12-HSA did not gel the IL droplets as a whole, but the fibers aggregated exclusively at the droplet interfaces (see Figure 3.46a-c). Also, the number particles (S-PS and C-PS) in the individual droplets was significantly less than in these systems. An explanation on how the addition 12-HSA facilitated these effects is due.

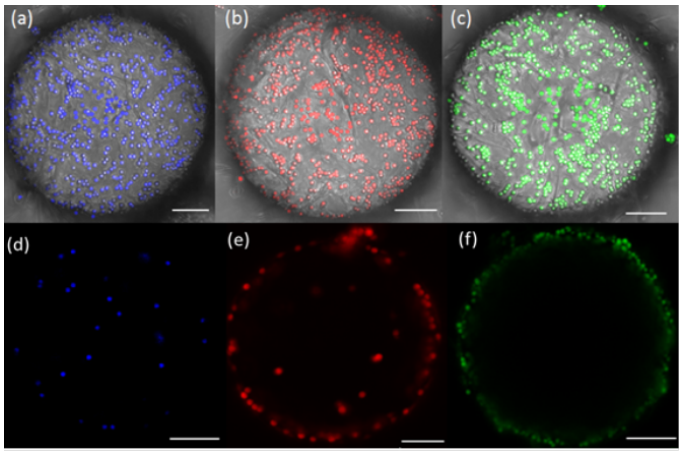

Figure 3.46 (a-c) Overlays of depth-series confocal and differential interference contrast (DIC) images of IL droplets in water in the presence of particles w/12-HSA; (d-f) Confocal microscope images of IL droplet cross sections in the presence of particles. (a, d) S-PS particles, (b, e) C-PS particles, (c, f) A-PS particles. The scale bars represent 10 μm.

A separate experiment was performed to study the behavior of 12-HSA at the IL/water interface. One sample containing equal amounts of water and prepared 1 wt. % 12-HSA IL gel was kept at 80°C in hot water bath for five minutes and then cooled to room temperature. During heating, some liquid 12-HSA was noticeably transported out of the IL phase and into the bulk water phase (partially favoring the top of the water phase because of buoyancy). After cooling, white solids were observed at the water/IL interface and partially in the bulk water phase. The IL phase was no longer a gel. This phase partitioning was expected since we had already observed that 12-HSA was more "soluble" in (or has higher interactions with) water than in the IL. This relatively higher "solubility", however, prevented the 12-HSA from forming any gel in the bulk water phase, as was discussed in the previous section. Consequently, the 12-HSA could only form gel fibers in close contact with the IL: at the interface. Capillary forces likely aided their adhesion to the IL/water interface. In this way the 12-HSA exclusively gelled

IL/water interfaces, rather than either of the liquid phases. Thus, the results from this experiment explain why fibers were only seen at droplet surfaces as in Figure 3.46a-c.

It is likely that this phenomenon was related to the observed decreased number of particles in the IL droplets. We quantified particle absorption by measuring the particle occupancy for the S-PS particles (μm^2) in individual droplets of systems without 12-HSA and with 12-HSA as a function of cooling rate. Figure 3.47 suggests that these measurements verified the microscopic observations. It was observed that at slower cooling rates, the fibers grew longer at the droplet interfaces; correspondingly, the fibers were significantly shortened at fast cooling rates. However, compared to the fiber length in bulk IL, these fibers were relatively small, only reaching approximately 20 microns in length at a cooling rate of 0.1 °C/s. We hypothesized that was due to the restrictive geometric nature of the droplet template. Particle transport was affected by the fiber length: longer fibers trapped more particles on interfaces, possibly because of the interpenetration and entanglement of long fibers which made the gel shell thicker at the interface, hindering the particle motion into the droplets. Oppositely, the shorter fiber matrix did not hinder particle transport across the interface. Therefore, quite a few particles were observed inside of the droplets. In this way, 12-HSA perturbed the original Pickering emulsion morphology and the particle transport process could be controlled by manipulating the degree of interfacial gelation via cooling rate.

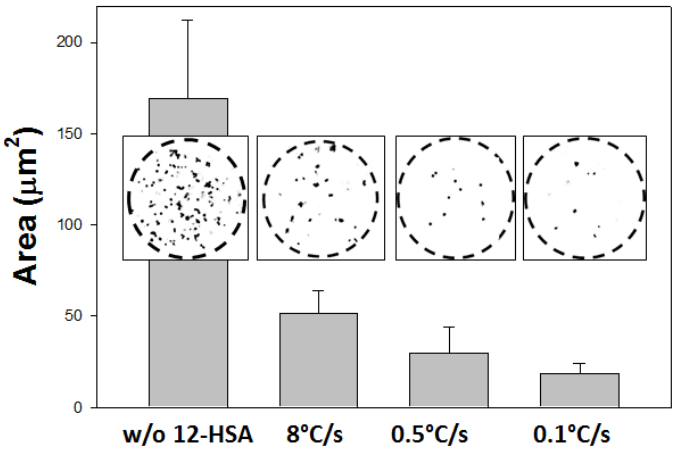

Figure 3.47 Occupancy of particles in the individual emulsion droplets without 12-HSA as well as with 12-HSA at varying cooling rates. The insets are sample images from ImageJ analyses and the particles are approximately 1 micron in diameter.

Also of interest is the number of particles absorbed from the water phase. To better compare the number of particles in the bulk phase before and after emulsification for each system, the concentration of particles in water phase was characterized by quantifying the fluorescence intensity over the emission wavelength range of the corresponding fluorescent particles in the bulk. The top panels in Figure 3.48 show the fluorescence intensity spectra of the water phase before and after emulsification without 12-HSA. For S-PS and C-PS systems, the fluorescence intensity after emulsification fell nearly to zero level, suggesting that almost all the particles were transferred out of the water phase either to the droplets or to the interfaces. For the A-PS system, the fluorescence intensity dropped only slightly, indicating that many particles remained in water phase after emulsification. Intensity measurements of the systems with 12-HSA are shown in the bottom panel of Figure 3.48. While the S-PS and C-PS systems showed negligible change upon addition of 12-HSA, the A-PS system showed a significant decrease in bulk particle concentration. Since IL-absorbed A-PS particles were not

observed in the confocal images, we can assume that these particles were adsorbed at the droplet interfaces. The presence of fibers at the droplet interfaces provided more surface area with which the particles could interact and this may have lead to higher interfacial adsorption. Furthermore, the S-PS and C-PS fluorescence intensities exhibited little change, indicating that the previously absorbed particles migrated to only to the interface, rather than to the bulk. Therefore, greater degrees of interfacial particle adsorption were observed in the presence of 12-HSA.

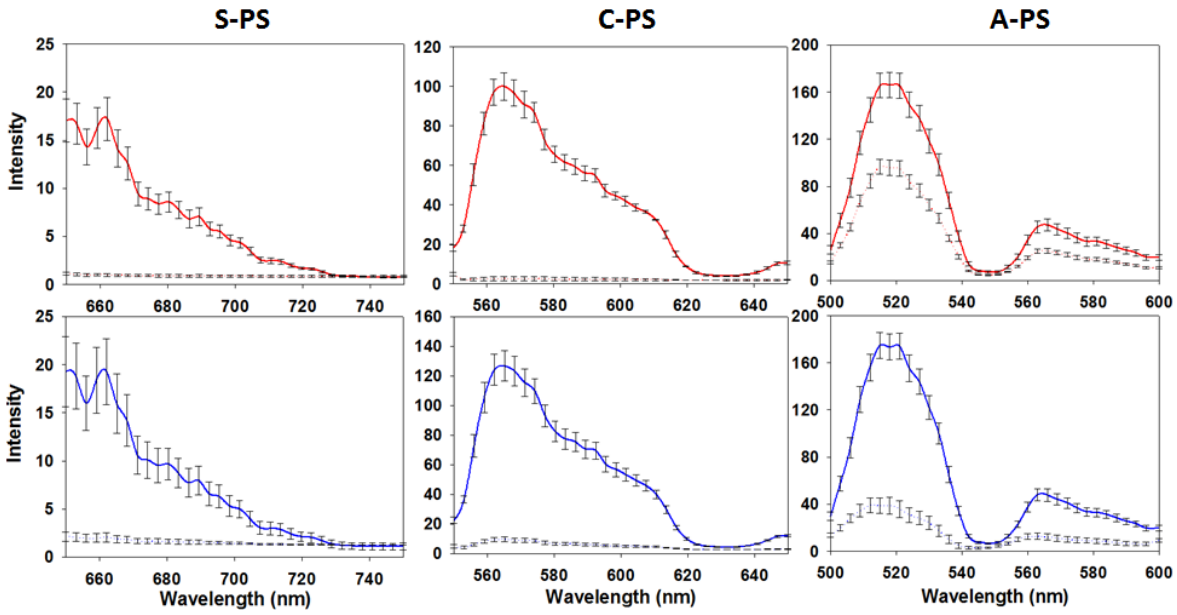

Figure 3.48 Fluorescence intensity spectra of the emulsions (top: no 12-HSA; bottom: with 12-HSA) before (solid line) aqueous phase and after (dashed line) emulsification.

Some brief discussion of the effect of particle surface chemistry on their behavior in these systems is warranted. As discussed in section 3.2.1, particles in these experiments had various surface dissociable groups, so the phase preference was likely a function of particle properties including hydrophobicity, sign and density of surface charge, and specific surface chemistry. First, hydrophobicity was considered, but since

both hydrophobic (S-PS) and hydrophilic (C-PS) particles were absorbed by the IL, it was ruled out as a dominant factor. The fact that both of these particles were absorbed also rules out the possibility that charge density played a major role. These results support the conclusions made in ref [151]. Next, the sign of surface charge may have affected partition preference. Positive charge (in the dissociated state) is one feature unique to the A-PS particles, which were not absorbed. There is some experimental evidence indicating that the large cations can inhibit the solvation of positively charged species [280-282]. Another feature unique to the A-PS particles was the fact that it had basic surface functionality, while the S-PS and C-PS particles had acidic groups. The latter two particles could undergo dissociation in either the water or IL phase since the PF_6 anion could accept acidic protons. On the other hand, A-PS particles could undergo dissociation only in the water phase since the IL, being aprotic, had no free protons. Therefore, while we can rule out surface charge density and hydrophobicity as important factors in this process, surface chemistry and charge sign likely played a defining role.

Effect of 12-HSA on PDMS-in-[BMIM][PF_6] Pickering Emulsions

In contrast to the IL-in-water emulsion, oil-in-IL Pickering emulsions exhibit a completely different morphology. It was observed in the previous section that in PDMS-in-[BMIM][PF_6] Pickering emulsions, the particles exclusively bridged the oil droplets, creating flocculated droplet structures of varying size and morphology [194, 257]. A representative microscopy image of a Pickering emulsion of oil-in-IL in the presence of S-PS particles is shown in Figure 3.49(a). The possible explanation of bridge formation is that the particles, which were dispersed in IL phase, were trapped between oil droplets as they approached each other during mixing. This bridge formation inhibited droplet-

droplet coalescence, but these aggregated droplets distressed the overall emulsion stability by promoting creaming due to buoyancy [257].

Emulsion stability is usually a desirable quality, so we hypothesized that gelling the IL to immobilize oil droplets would stabilize these emulsions. As demonstrated in the previous experiments, 12-HSA was able to gel both the IL and PDMS phases. A measured amount of 12-HSA was added to see how it would affect the emulsions. At low (0.5 wt. %) 12-HSA concentration, bridged droplets were not observed, suggesting that the bridging effect was limited in the presence of a gelator. This may have been due to partial gelation of the IL, which would greatly slow the motion of droplets during mixing, decreasing the chance that the droplets collided with each other. Very few particles were attached to the droplet interfaces. Even without bridging, droplets were still aggregated together to form clusters of varying sizes. The corresponding image is displayed in Figure 3.49(b). At high (1 wt. %) 12-HSA concentration, droplet clusters were larger and packed more tightly. Particles were observed to be trapped at the droplet interfaces. Representative images are included in Figure 3.49(c). Additionally, it should be noted that droplets with and without fibers on interface were both observed under microscopy.

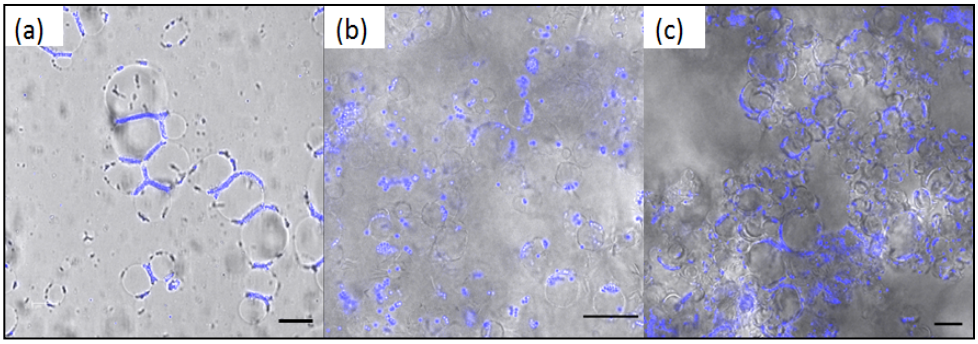

Figure 3.49 Overlays of confocal and differential interference contrast (DIC) images of oil-in-IL Pickering emulsions in the presence of S-PS particles.(a)w/o 12-HSA; (b) 0.5 wt.% 12-HSA; (c) 1 wt.% 12-HSA. The scale bars represent 20 μm.

Droplet cluster formation may be explained by two mechanisms. One is that bridged flocculation occurred as 12-HSA fibers were bound directly to multiple droplet interfaces. 12-HSA on the interfaces or around the droplets would form fibrils to interconnect the droplets acting as a bridge. A similar behavior has been observed with long proteins that may bridge droplets in gelled food emulsions [283, 284]. In these studies, evidence of this bridging mechanism lies in the fact that, droplet flocculation increased with protein concentration [284]. Such behavior appears analogous to the dependence of flocculation on 12-HSA concentration in the present study (see Figure 3.49). Another important cluster-forming mechanism is depletion flocculation. Effectively, this means that before complete gelation, the shell immediately surrounding the droplets was free of 12-HSA, creating a concentration gradient. The osmotic pressure difference because of concentration gradient would then induce an attractive force between the droplets. Flocculated droplet would be subsequently gelled upon cooling. Recent theoretical and experimental work has shown that droplet packing is dependent on both attractive and repulsive forces included in the depletion mechanism [285-287]. This

packing, and not the forces themselves, determines the rheology of depletion-induced emulsion gels [285]. The depletion force depends on a concentration gradient, which gives rise to effective osmotic pressure to push the droplets together. This may explain why droplet clusters were more tightly packed in the emulsion at 1 wt.% 12-HSA.

Despite cluster formation, we found that higher concentrations of 12-HSA increased the stability of the bridging emulsions significantly. Figure 3.50 compares the stability of oil-in-IL Pickering emulsion with and without 12-HSA. Due to the low density and large volume, the bridged oil droplets in the system without 12-HSA quickly rose to the top and finally separated from IL phase to form a cream layer. At high 12-HSA concentration, oil droplets were immobilized in IL gel matrix, therefore, no separation occurred. Low 12-HSA concentration could not immobilize oil droplets completely because the storage modulus was not big enough to withstand the buoyant force. These observations confirmed our hypothesis that gelation would stabilize these unique emulsions.

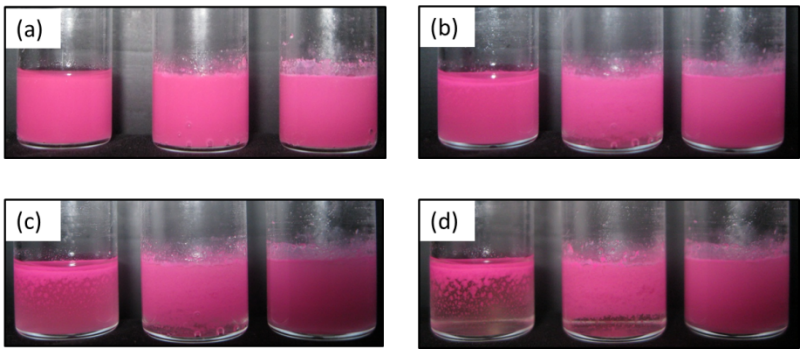

Figure 3.50 Emulsion stability as a function of time. The vials from left to right contain no 12-HSA, 0.5 wt. % 12-HSA, 1 wt. % 12-HSA. They all have the same amount of S-PS particles. (a) t = 0; (b) t = 0.5 h; (c) t=6 h; (d) t= 24 h.

The characteristics of bridged droplets and droplet clusters can produce a number of benefits in high internal phase emulsions (HIPEs) manufacturing for which their internal phase has a high volume fraction (up to 74% by volume or above) [252]. HIPEs have many potential applications in different fields, such as encapsulation [288] and synthesis of porous materials [252, 289] for tissue scaffolds [253], sensors [254], and hydrogen storage [255]. The thermoreversible gelation opens new possibilities for the control of emulsion properties and performance in the preparation of advanced materials with respect to the improvement of chemical release, manipulation of emulsion rheology, and stability by temperature control.

3.3.5 Self-Assembly in Ionic Liquid-in-Ionic Liquid Pickering Emulsions

In this final section, we return to the IL-IL interface to investigate self-assembly for the first time in IL-in-IL Pickering emulsions. The first system, $[P_{66614}][Phos]$ + EAN, was quite stable against mixing as long as EAN was the continuous phase of the emulsion. Arce et al. report that smaller ILs are much more soluble in phosphonium ILs than vice versa[216]. The second IL-IL system we emulsified was $[P_{66614}][Phos]$ in $[BMIM][PF_6]$. We observed that $[BMIM][PF_6]$ slowly gelled $[P_{66614}][Phos]$ over time (See Appendix I), but interdiffusion between the two ILs was slow enough to allow for droplets to remain for hours. We observed the self-assembled morphologies in these systems using confocal laser-scanning microscopy.

Figure 3.51 shows representative confocal/differential interface contrast overlays of this emulsion with three different particles. Both SPS (a) and CPS (b) systems exhibited morphologies comparable to conventional Pickering emulsion behavior, with the exception that a large number of particles were absorbed into the $[P_{66614}][Phos]$. APS

particles were not absorbed. In a notable similarity, Ma and Dai reported that another IL ([BMIM][PF_6]) also absorbed SPS and CPS particles, but not APS particles, from water [151]. This phenomenon is unusual because micron-sized particles are usually strongly bound to the liquid-liquid interface (~10^6 kT desorption energy) [14] . The authors suggested that the sign and density of the particle surface charge played a primary role in this phenomenon, though the underlying mechanism is still unclear[151]. This similarity in particle "selectivity" in the present system and the IL/water system suggests that particle absorption occurred under the same mechanism for both systems.

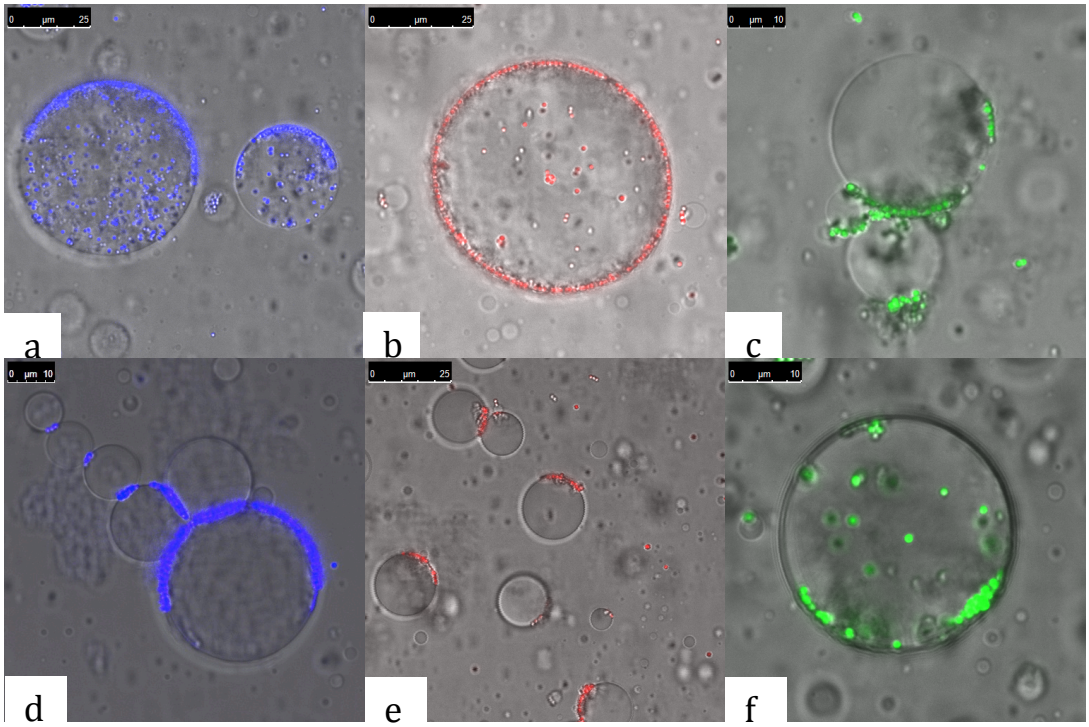

Figure 3.51 DIC/confocal overlays of [P_{66614}][Phos] droplets in EAN with (a) SPS, (b) CPS, and (c) APS microparticles and [P_{66614}][Phos] droplets in [BMIM][PF_6] with (d) SPS, (e) CPS, and (f) APS microparticles.

While the morphologies of the SPS and CPS systems readily compare to that the IL/water Pickering emulsions, the APS system does not. Figure 3.51c shows that APS

particles exhibit some of the bridging behavior reported by us previously[194, 257]. Interestingly, APS particles were the only particles that did *not* form bridges in either water/IL or oil/IL systems[257]. Thus, we were surprised to see bridging with this particle type. One major difference between this system and the bridging systems reported previously was that the continuous phase here was protic. This is significant because in order for the APS particles to assume a surface charge, the amine groups needed to accept a proton (becoming ammonium ions). Consequently, these results support the hypothesis that an active surface chemistry was necessary in order for particles to exclusively form bridges in IL-based Pickering emulsions [194].

Having discussed the first system, we will now move on to the second: $[P_{66614}][Phos]$ in $[BMIM][PF_6]$. Most obvious is that the particle self-assembly phenomena was a strong function of the continuous phase. In contrast to Figure 3.51a, Figure 3.51d shows that SPS particles in this system were not absorbed, but exclusively formed bridges between the droplets. Likewise with the CPS particles (Figure 3.51e), though bridging was only an anomaly rather than the dominant morphology. As if to complete reversal of morphologies, APS particles did not form bridges (Figure 3.51f), but were readily absorbed into the $[P_{66614}][Phos]$ droplets. Comparative analysis of these two systems yields important conclusions.

First, it is clear that phenomena generally unique to IL-based Pickering emulsions, exclusive bridging and particle absorption, may also occur when both phases are ILs. Secondly, these results show that these morphologies can be tuned by the constituent ILs, not just the particles. These phenomena have important implications for IL-based applications. In particle synthesis, phase transfer is often necessary either to

place the particles in their working environment or apply additional functionalization[198-200, 200, 202]. These processes usually require additional surface modification of the particles, but our results indicate that such measures may not be necessary in an IL environment. Also, since bridging can be tuned by the continuous phase, this morphology may be used more readily in self-assembly and high internal phase emulsion (HIPE) applications [252-255].

3.4 Conclusions

We have investigated ordering and dynamics of IL-based interfaces as well as particle-interface interactions in the context of Pickering emulsions. Interesting ordering and charge distributions were observed at the IL-liquid interfaces. At the IL-hexane interface, the [BMIM] cations preferentially oriented themselves so that they immersed more into the hexane phase and packed efficiently to reduce steric hindrance. The ordering likely contributes to a heightened IL density and slightly positive charge at the IL-hexane interface. In contrast, the cations at the IL-water interface were oriented isotropically unless in the presence of nanoparticles, where the cations aligned across the nanoparticle surfaces. Experimental studies showed that the interface between EAN and [BMIM][PF_6] was unusually long-lived, despite the ILs being miscible with one another, and that their mixing was endothermic. MD simulations supported these findings and provided insight into the micro-mixing behavior of the ILs. We found that not only did the ions experience diffusion as they mix, but also exhibited significant ordering into distinct regions. We suspect that this ordering disrupted concentration gradients in the direction normal to the interface, thus hindering diffusion in this direction and allowing

the macroscopic interface to remain for long periods of time. Intermolecular interactions responsible for this behavior included the O-NH interaction between the EAN ions and the carbon chain-carbon chain interactions between the $[BMIM]^+$ cations, which associated more strongly in the mixed state than in the pure IL state.

The interactions between particles and IL-based interfaces presented interesting findings. We have presented direct observation a new phenomenon in which microparticles were successfully transported through liquid liquid-interfaces without the aid of shear forces. Both single particles and clusters of particles were observed to adsorb to, then "jump" across the interface and finally detach. In the absence of external mixing, particles as large as 4 microns (in diameter) could completely penetrate the IL/water interface, despite the significant adhesive forces. We have presented evidence that these forces were overcome by ions dissolved in the bulk phase, which helped by covering the particle surfaces, allowing for more favorable interactions with the IL. This particle extraction mechanism is similar to those proposed by previous work in which IL ions can attach to particle surfaces, making them less soluble in their original solvents and forcing them to migrate into the IL phase. ILs, therefore, possess powerful and tunable extraction properties for solid particles of many sizes. In this way, ILs have extended separation phenomena beyond molecular species to include micron-sized solids.

PDMS-in-[BMIM][PF_6] Pickering emulsions stabilized by PS microparticles with different surface chemistry were also studied. Surprisingly, in contrast to the consensus originating from oil/water Pickering emulsions in which the solid particles equilibrate at the oil-water droplet interfaces and provide effective stabilization, here the S-PS, AS-PS, and C-PS particles mostly formed monolayer bridges among the oil droplets rather than

residing at the oil-ionic liquid interfaces. The bridge formation inhibited individual droplet-droplet coalescence; however, due to the low density and large volume (thus the buoyant effect), the aggregated oil droplets actually promoted oil/ionic liquid phase separation and distressed emulsion stability. Systems with binary heterogeneous polystyrene microparticles exhibited similar, even enhanced (in terms of surface chemistry dependence), bridging phenomenon in the PDMS-in-[BMIM][PF_6] Pickering emulsions. Water droplets also exhibit bridging behavior in the IL.

Subsequently, we characterized the bridging behavior of oil-in-IL emulsions with respect to particle concentration, particle size, and droplet phase. The emulsions exhibit three morphology regimes: (1) single, sparingly covered droplets, (2) bridged clusters of droplets, and (3) fully covered droplets. The degree of bridging was directly proportional to the total potential bridging area, which can be determined from particle size and concentration. This type of emulsion diverges from much of the conventional wisdom of Pickering emulsions including the liquid film stability and particle self-assembly on droplet interfaces. Some possible explanations include hydrogen bonding between the PF_6 anion and the particle surface groups, as well as IL ordering within the confined spaces of the of the bridge structure. We also reported some interesting phenomena observed in the fully covered droplet regime; these included non-spherical oil droplets and absorption of particles by water droplets. The work identified new self-assembled particle structure and morphology in solid-stabilized emulsions that contributed to the fundamental understanding of these unique systems.

In an effort to control these unique phenomena due to IL interface-particle interactions, we modified the rheology of system. In this work, we have examined the

perturbation effects of HSA on IL-based Pickering emulsions. The 12-HSA gelled pure [BMIM][PF_6] and PDMS effectively by the formation of entangled networks of thin fibers but not the water phase since proper gelation can only occur in the presence of a less polar solvent. In IL-in-water Pickering emulsions, the 12-HSA gelled the IL-water interfaces rather than the entire IL droplets since they partitioned into the water phase. In addition, we found that the morphology of interfacial gelation could be engineered by manipulating cooling rate and consequently provided a new way of controlling the solid particle transport into the dispersed phase. The 12-HSA effectively stabilized oil-in-IL Pickering emulsions by increasing the elastic modulus of the bulk phase and consequently overcoming the buoyancy force of the bridged droplets. These results indicate that phenomena unique to IL based Pickering emulsions can be tuned by the addition of an organogelator.

Finally, we explored self-assembly phenomena at the IL-IL interface. IL-in-IL Pickering emulsions exhibited an array of self-assembled morphologies including the previously observed particle absorption and bridging phenomena. The appearance of these morphologies depended on the particle surface chemistry as well as the ILs used. Therefore, these unique behaviors so prevalent in IL-based Pickering emulsions can be controlled using these parameters. We expect that these findings will increase in importance as ILs see more use in self-assembly applications.

CHAPTER 4

MOLECULAR DYNAMICS SIMULATIONS OF PARTICLE SELF-ASSEMBLY AT IONIC LIQUID-BASED INTERFACES

4.1 Introduction

Self-assembly of nano-sized objects at liquid-liquid interfaces is important in natural and industrial applications. However, the fundamentals of the self-assembly of nanoparticles at liquid-liquid interfaces are not fully explored. One of the remaining challenges is to understand multiphase interactions, self-assembly processes, and self-assembled structures of nanoparticles, especially when the size of the nanoparticles is comparable with the molecular dimension of the surrounding liquids. Among various techniques, molecular dynamics (MD) simulation is a powerful tool for obtaining molecularly detailed information and the underlying physics of various systems, including liquid-liquid interfaces [290, 291] and liquid-liquid interfaces containing surfactant molecules[292-296]. Recently, our group simulated the self-assembly and diffusion of nanoparticles at water-trichloroethylene (TCE) [292, 297] and water-polydimethylsiloxane (PDMS) [298] interfaces. Hydrocarbon nanoparticles with diameter of 1.2 nm equilibrated at water-TCE and water-PDMS interfaces and the surface charge of the nanoparticles played an important role in the self-assembled structure and location of nanoparticles [292, 297, 298]. In this report, we discuss the nanoparticle self-assembly at ionic liquid (IL)-water and IL-oil (hexane) interfaces using MD simulations.

MD simulation is a discreet model that aims to capture intra- and intermolecular behavior with respect to time. This method differs from ab initio calculations in that it does not calculate the full wave functions, but replaces them with parameterized potential

functions. Consequently, MD simulations can be performed on systems of much larger size and time scales than is currently possible with ab initio calculations. MD potential functions capture a variety of forces including electrostatic and Van der Waals intermolecular interactions as well as bond and angle stretching and torsions. All of these forces are parameterized in separate functions that are used at each time step of the MD simulation to calculate the total energy, U. The function we used is called the optimized potential for liquid systems (OPLS) [228] and is shown in Equation 4.1 where r represents interatomic distance, θ represents and angle between three atoms, φ represents a dihedral angle between 4 atoms, ϵ_0 is the vacuum permittivity, and q represents atomic partial charge. Energies are summed over all bonds (b), angles (a), dihedrals (d), and between all atoms (i and j). All other variables are parameters fitted to duplicate the experimental behavior of a specific species. This collection of parameters determines the calculation of all molecular forces for the species and is consequently named a force field.

$$U = \sum_b \frac{k_{r,b}}{2}(r_b - r_{0,b})^2 + \sum_a \frac{k_{\theta,a}}{2}(\theta_a - \theta_{0,a})^2 + \sum_d \sum_{m=1}^{3} \frac{V_{m,d}}{2}[1 + (-1)^{m+1}\cos(m\varphi_d)] + \sum_i \sum_j \left\{ 4\epsilon_{ij}\left[\left(\frac{\sigma_{ij}}{r_{ij}}\right)^{12} - \left(\frac{\sigma_{ij}}{r_{ij}}\right)^{6}\right] + \frac{1}{4\pi\epsilon_0}\frac{q_i q_j}{r_{ij}} \right\} \quad (4.1)$$

With the development of accurate force fields for imidazolium ionic liquids, [222, 299-306] multiple MD simulations have been performed and provided insights into the transport and interfacial behavior of ionic liquids [128, 232, 307-313]. However, there

has been sparse work on their interfacial behavior involving other liquids. Chaumont et al. have used MD simulations to study the behavior of the IL-water interface and the transport of large solvent molecules across the interface [128, 307-309]. To our best knowledge, there are no MD simulations performed to examine the IL-oil interface and there is still much to explore when the systems involve self-assembly of nanoparticles at IL-water and IL-oil interfaces.

Section 4.3.1 will discuss the self-assembly of neutral particles at the IL-water and IL-hexane interfaces. In Section 4.3.2, we will extend this study to explore the effect of charge on the nanoparticle self-assembly at the interface. The necessity of such a study is inherent since most experimental research on particle self-assembly at ionic liquid interfaces has been performed with charged particles [151, 207, 257]. Particle charge is especially important at interfaces involving ILs because the constituent ions respond with varying repulsive and attractive behaviors. Song et al. observed via MD simulations that at the water-polydimethylsiloxane interface, uncharged nanoparticles equilibrated in the oil phase but charged nanoparticles adhered to the interface and showed increased preference for the water phase with charge [298]. We expected that charge would also affect the nanoparticle placement at IL/water and IL/oil interfaces and corresponding self-assembly phenomena.

Section 4.3.3 addresses the importance of particle surface chemistry in interfacial self-assembly as well as the unique particle extraction phenomena observed in Chapter 3. In addition to partition preference, the extraction of solid particles from one liquid to another also requires consideration of interfacial effects. As mentioned previously, the energy required for a microparticle to cross an oil-water interface can be on the order of

10^6 kT [14]. ILs, however, seem to overcome this barrier and non-destructively absorb both nanoscopic and macroscopic particles from other liquids. Gold nanoparticles [202] and CdTe quantum dots [314] have been extracted by ILs from aqueous solutions. Other groups have demonstrated that ILs can quickly extract sand and clay particles from oil or tar sands [150, 195-197]. This remarkable behavior lends itself to oil recovery, oil spill beach cleanup [149], and water treatment applications. With the help of surfactants, particle transport across the oil/water interface has been observed [67], but to our knowledge, unaided particle transport across the liquid-liquid interface has only been observed with ILs. Therefore, some explanation is needed on how the unique nature of ILs plays a role in particle extraction.

Experimental and computational studies have indicated that ILs exhibit ordered morphologies in the presence of solid surfaces. Atkin and Warr performed atomic force microscopy (AFM) measurements on various ILs in contact with mica, silica, and graphite surfaces [315]. In their studies it was found that when in contact with hydrophilic surfaces, some ILs could form as many as nine solvation layers [315]. Imidazolium-based ILs exhibited more layering in contact with graphite than with silica or mica possibly due to favorable interactions between the carbon chain of the cation and the surface [315]. Molecular dynamics simulations have shown that within the layers, the ions of the ILs can exhibit enhanced packing leading to higher densities at the surface [316, 317]. Recent experiments by Nordström et al. on silica colloids in ILs have suggested that stable solvation layers are important features in solid particle-IL interactions [318] and Hogshead et al. observed similar layering in the oil tar-IL system mentioned before [150]. In addition to effective solvation layer formation, ILs posses

other qualities that may enhance their capability to absorb solid particles. Being a binary mixture of oppositely charged species, ILs posses increased orientational degrees of freedom with which to interact with surfaces. Furthermore, functionalities of the individual ions can influence the favorability of IL interaction with other species (i.e. facilitating Lewis acid-base interactions and complexation). The purpose of this study is to observe how these characteristics play a role in the absorption of particles by ILs.

In last section, we used MD simulations to observe how a model IL (1-butyl-3-methylimidazolium hexafluorophosphate or [BMIM][PF_6]) responded to nanoparticles of differing surface chemistries at the liquid-liquid interface and in the bulk. In particular, we wished to compare the IL response to hydrophobic vs. hydrophilic nanoparticles. The nanoparticles we studied were silica- and hydrocarbon-based (hydrophobic and hydrophilic, respectively) and the interfaces were IL/water and IL/hexane. Results from this study provide insight into how the interface and the IL itself respond to nanoparticles of differing surface chemistries. In this way, we hope to uncover some of the underlying mechanisms behind the experimentally observed particle absorption by ILs.

4.2 Methodology

Two types of simulations were performed: interfacial and non-interfacial. All MD simulations were performed using GROMACS 4.5 package [319-321]. The initial simulation box for interfacial systems system was approximately 5.5 x 5.0 x 11.0 nm^3 while the simulation box for the non-interfacial system was cubic with a side length of 5 nm. After the initial configurations were obtained, 1,000 energy minimization steps were performed using the steepest descent method. The leap-frog algorithm was used for

integrating Newton's equation of motion with a time step of 0.002 ps. All simulations were carried out under the NPT (constant number of molecules, constant pressure, and constant temperature) ensemble using the Berendsen-thermostat [231] to a temperature and pressure bath at 300 K and 1 bar respectively. Periodic boundary conditions (PBC) were applied to all three directions of the simulated boxes. The initial atomic velocities were generated with a Maxwellian distribution at the given absolute temperature. The Particle-Mesh Ewald (PME) method was used for the long-range electrostatic interactions. The cut-off distance for Lennard-Jones forces was set as r = 1.2 nm, as was done by the developers of the force field [222]. After the simulation, the physical properties were characterized using the GROMACS analysis tools, and the structures were visualized by Visual Molecular Dynamics (VMD) [322].

Water was described by the extended simple point charge model (SPC/E) model [323], which has been demonstrated to perform well in the IL/water system [309]. Hexane was described by the OPLS united atom model as developed by Jorgensen et al. [228].The geometry of the spherical modified hydrocarbon nanoparticle (HCP, mean diameter of 1.2 nm) was truncated from a diamond-like lattice made of carbon atoms bonded in nonplanar hexagonal structure and saturated with united CH, CH_2 and CH_3 atoms [297, 324]. The force field for this particle consisted of non-bonded parameters from the OPLS united atom model [228] and bonded parameters from the work of Mazyar and Hase [324] to simulate a rigid hydrophobic nanoparticle. This structure has been used in other simulations focused on interfacial self-assembly [292, 297, 298]. The surface charge of the HCP was modified by adding to or removing protons from these

groups. Because all charge was located at these two sites, the consequent charge distribution was asymmetrical.

The force field for the IL, 1-butyl-3-methylimidazolium hexafluorophosphate ([BMIM][PF_6]), was carefully chosen because many ionic liquid force fields do not model interfacial behavior well although they give reasonable values for density. [223]For example, Wipff and co-workers found that [BMIM][PF_6] force fields with ionic charges of ±1.0 exhibited exaggerated mixing with water [128]. We also confirmed such observations in our preliminary MD simulations. We evaluated an all-atom model for the [BMIM] cation developed by Lopes et al. [222] based on the OPLS force field [228, 325]. We also examined the force field for the [PF_6] anion developed by the same group [221]. This force field gave reasonable values for density, but not for surface tension or self-diffusion coefficients [223]. We therefore considered a force field with the capability to model the surface behavior of this ionic liquid accurately. Bhargava and Balasubramanian [223] optimized the atomic charges in Lopes' model as well as some of the Lennard-Jones parameters to match essential pair correlations obtained from Car-Parrinello MD calculations [326] resulting in individual ion charges of ±0.8. The optimized force field yields accurate values for surface tensions and diffusion coefficients [223, 310]. Here we employed this optimized force field to simulate self-assembly of nanoparticles at the ionic liquid-water and ionic liquid-oil interfaces.

The liquid-liquid interfaces were simulated by placing a cubic box of water or hexane adjacent to a cubic box of IL. Prior to this step, the hexane and IL boxes were equilibrated under NPT conditions (constant number of molecules, pressure, and temperature) to ensure that they exhibited the correct density at 300 K and 1 bar. The

hexane box gave an equilibrium density of 0.638 g/cm^3, which is within 3% of the experimental value [327]. The IL box gave an equilibrium density of 1.385 g/cm^3, which is within approximately 2% of the experimental value of 1.360 g/cm^3 [125, 328, 329]. We calculated the surface tensions of pure hexane and the IL by doubling the z-vector of the equilibrated boxes (to allow liquid/gas surfaces to form) and continued the MD simulations for 20 ns. The surface tension measured from the IL box was 41.8 mN/m, which deviates approximately 1% from the experimental value of 42.3 mN/m [330, 331]. The surface tension measured from the hexane box was 17.3 mN/m, which is within 4% of the experimental value [327]. The MD simulation package contains a near-equilibrium coordinate file for SPC/E water, therefore it was not necessary to equilibrate the water simulation box. After validating the densities and surface tensions of the hexane and IL force fields, the IL-water and IL-hexane interfaces were constructed as described above. Parallel runs were then performed with and without nanoparticles in the water or hexane phase. A summary of the system configurations is detailed in Table 4.1.

Table 4.1 Detailed Composition of Simulation Systems.

Run	# of HCPs	HCP Charge	[BMIM]	[PF_6]	2nd Phase
Water/IL Interface					
W	0	-	400	400	4483
W_{+6}	8	+6	400	400	4165
W_{+4}	8	+4	400	400	4181
W_{+2}	8	+2	400	400	4197
W_0	8	0	400	400	4213
W_{-2}	8	-2	400	400	4197
W_{-4}	8	-4	400	400	4181
W_{-6}	8	-6	400	400	4165
Hexane/IL Interface					
H	0	-	400	400	652
H_{+6}	8	+6	400	400	457
H_{+4}	8	+4	400	400	473
H_{+2}	8	+2	400	400	489
H_0	8	0	400	400	505
H_{-2}	8	-2	400	400	489
H_{-4}	8	-4	400	400	473
H_{-6}	8	-6	400	400	457

To provide contrast to the hydrocarbon-based surface of the nanoparticle mentioned above, we also generated a silica-based nanoparticle. A unit cell of α-quartz [332] was generated and multiplied in space using VESTA [333]. This structure was truncated to a sphere of 1.1 nm diameter and saturated with silanol groups using WebLab Viewer Pro [334]. To account for the electrostatic and van der Waals forces of the silanol groups, we used the force field proposed by Wensink et al. [335] . Figure 4.1 shows the resulting structures for (a) the hydrocarbon nanoparticle (1.2 nm in diameter) and (b) the silica nanoparticle. Equilibrium simulations of nanoparticle self-assembly were performed with eight silica nanoparticles at the IL/water (24,836 atoms) and IL/hexane (15,866 atoms) interfaces with equilibration for 20 ns. Nanoparticles were initially

dispersed in the non-IL phase. Simulations of single nanoparticles in pure IL were also equilibrated for 20 ns.

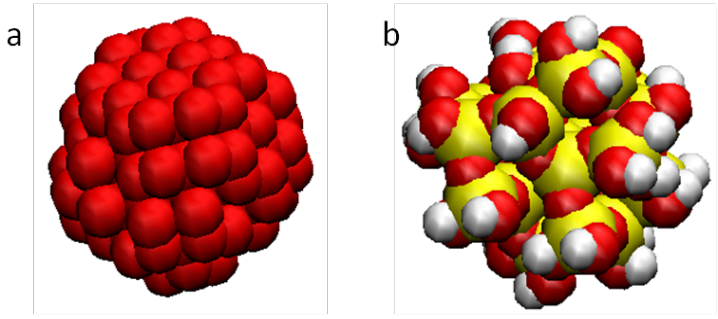

Figure 4.1 Geometric structures of the nanoparticles employed in this study. The hydrocarbon nanoparticle (a) consisted of only carbon atoms. In the silica nanoparticle (b) H, O, and Si atoms are represented in white, red, and yellow, respectively.

In addition to these simulations, we also performed potential of mean force (PMF) calculations on single nanoparticles of 0, -4, and +4 charge moving through the IL/water and IL/hexane interfaces. As the nanoparticle was pulled through the interface, snapshots were saved every 0.016 nm for a total of 4 nm of pulling. Each snapshot was then equilibrated for 5-20 ns and the weighted histogram analysis method (WHAM) [336, 337] was used to determine the PMF with respect to the z position of the nanoparticle. Error analysis of these PMF studies was performed by averaging two parallel runs for each system.

Cell Size Independence

Each simulation in this study was evaluated at approximately 3.5-4.5 ns/day due to the small step size of 0.002ps. Since there were four simulations of 20ns, each consisting of four parallel runs, this simulation cell size was not by any means conservative for our purposes. We did, however, create a large simulation of the IL/water system with a box size of 8.9x8.9x18.2 nm^3. Due to the high computational cost of this system, we

concluded the run at 5ns. Table 4.2 below shows a comparison of this run to the results from run A described in the results section. These values represent averages over the last ns of run time (4-5ns). The values from the large run are very close to those calculated from run A at 5ns. Discrepancies in these calculated values may in part be due to non-equilibrium conditions at this run time. We therefore conclude that the results obtained from our simulations in this study were reasonably independent of the cell size used.

Table 4.2 Comparison of calculated values from a large IL/water simulation and run A.

	Values	
Data	**Large Run**	**Run W**
Density of Water Phase (kg/m^3)	993	990 ± 1
Density of IL Phase (kg/m^3)	1389	1392 ± 2
Interfacial Width Defined by IL (nm)	0.95	0.89 ± 0.09
Interfacial Width Defined by Water (nm)	0.98	0.85 ± 0.06
Mole fraction of IL in interface defined by IL	0.06	0.08 ± 0.01
Mole fraction of Water in interface defined by IL	0.94	0.92 ± 0.01
Mole fraction of IL in interface defined by Water	0.06	0.07 ± 0.00
Mole fraction of Water in interface defined by Water	0.94	0.93 ± 0.00

4.3 Results and Discussion

4.3.1 Interfacial Self Assembly of Neutral Particles

Figure 4.2a shows the in-situ nanoparticle self-assembly at the [BMIM][PF_6]-water interfaces. At t = 0 ns, the nanoparticles were dispersed in the water phase. As time progressed, the nanoparticles rapidly migrated toward the ionic liquid phase and reached the interface within 5 ns. This was also the period in which aggregates of 2-3 particles formed. At 20 ns, the nanoparticles finally equilibrated more on the IL side of the interface as shown in Figure 4.2a and Figure 4.4a-c. The nanoparticles interacted more

readily with the hydrophobic IL than the water phase. As a result, the IL almost completely immersed the nanoparticles (see Figure 4.4a).

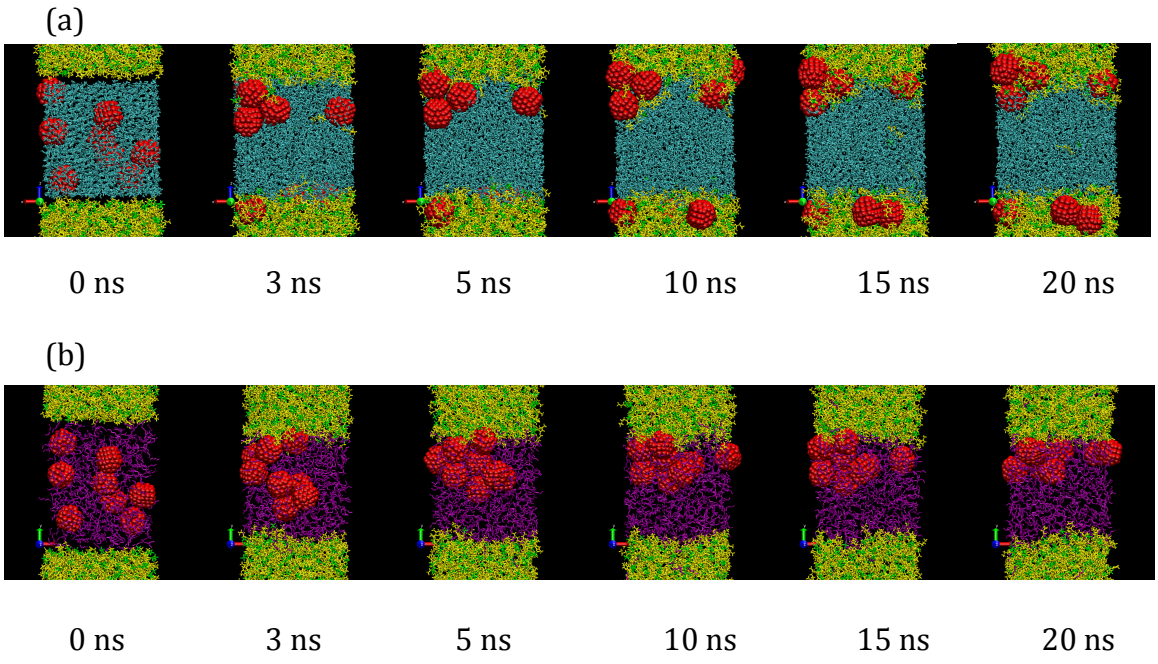

Figure 4.2 Sample snapshots of (a) the IL/water/HCP and (b) IL/hexane/HCP systems at various time intervals. The water is represented in blue, [PF_6] in green, [BMIM] in yellow, hexane in purple, and HCP in red, respectively. Snapshots of all parallel runs are shown in Supporting Information.

It should be noted that the particles were dispersed in the water and hexane phases because they had significantly lower viscosities than the IL. Theoretically, the particles would equilibrate at the same interfacial location regardless of their original location (as will be seen in the PMF studies), but the dynamics of these processes differed significantly. Figure 4.3 shows snapshots at 40 ns and 20 ns of the IL/hexane and IL/water systems, respectively, where the particles were initially dispersed in the IL phase. In consequence of the high viscosity of the IL phase, the particles did not exhibit significant translational motion during reasonable simulation times and remained in the

IL phase. Therefore, in terms of computational resources, simulation of the self-assembly process from this approach was cost-prohibitive and was not pursued further.

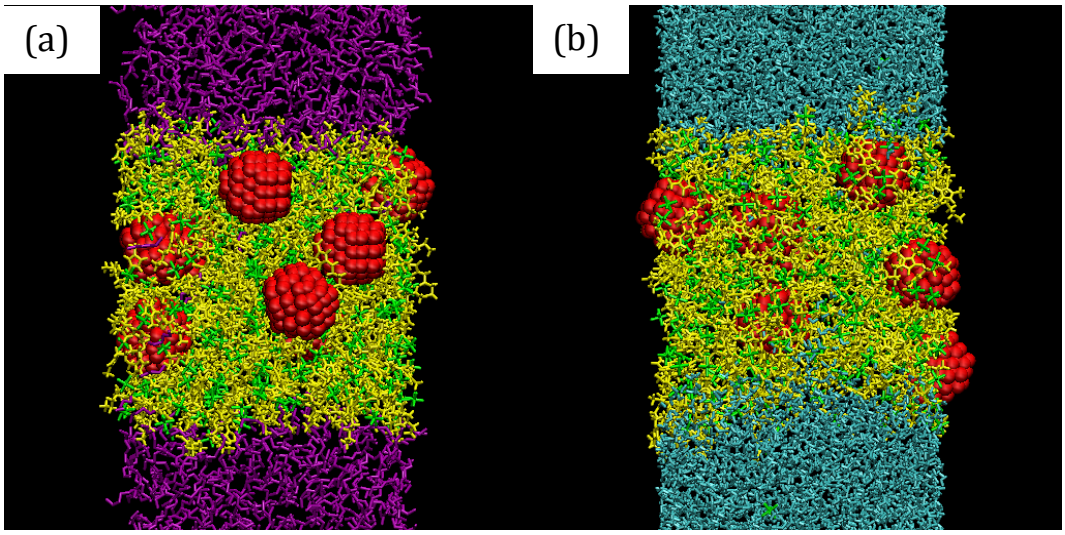

Figure 4.3 Snapshots of (a) the IL/hexane interface at 40 ns and (b) the IL/water interface at 20 ns with particles having been initially dispersed in the IL phase.

Interestingly, the IL ions diffused around the nanoparticles at the interface and formed a thin layer at 10 ns in this run. It is worthwhile to note that although the cations contained hydrophobic carbon chains, they diffused quite far into the water phase as they formed the thin layer. A closer inspection shows that the carbon chains of the cations generally laid flat across the surface of the nanoparticles (see Figure 4.4a and inset of Figure 3.7c). The nanoparticles were mostly immersed in the water phase at this point in the self-assembly process. Therefore, this attraction between the ions and the nanoparticles resulted in an increased concentration of IL in the water phase.

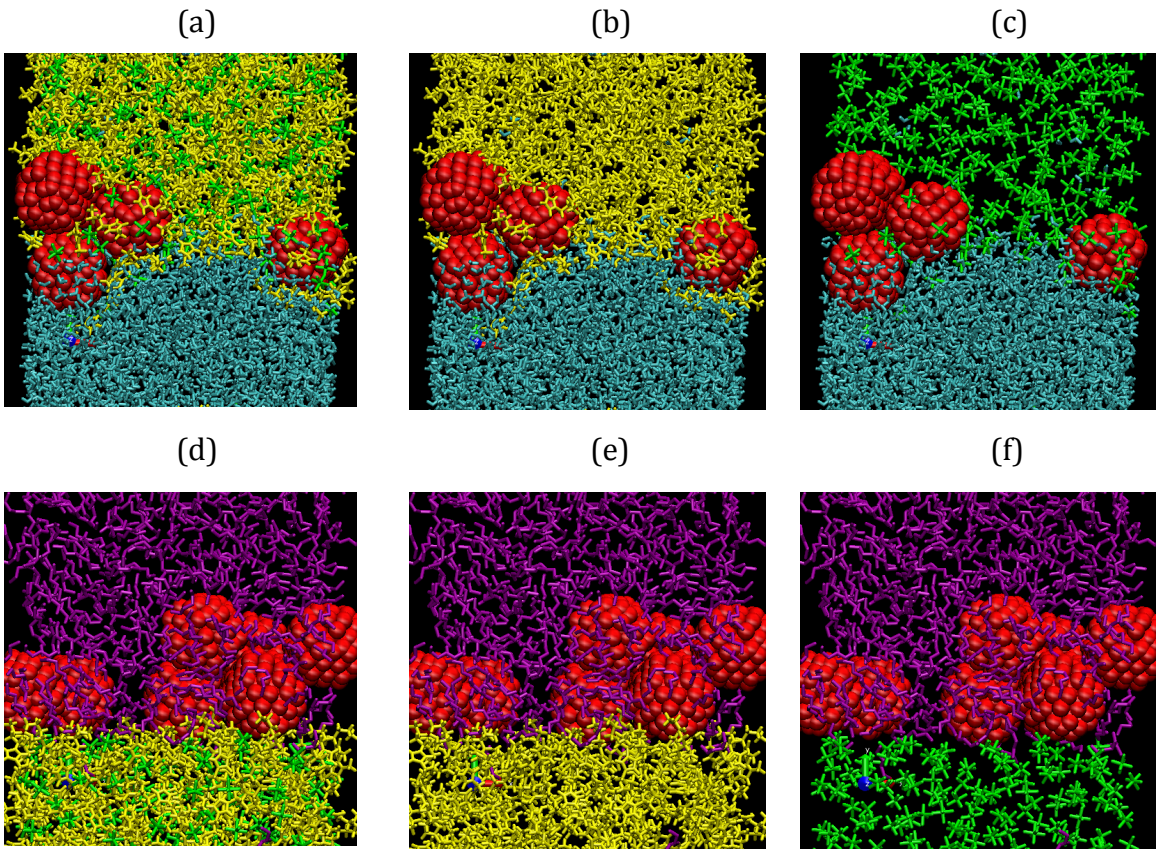

Figure 4.4 Closer snapshots at 20 ns of the nanoparticles in the IL/water (a-c) and IL/hexane (d-f) systems with respect to all ions (a and d), cations only (b and e), and anions only (c and f).

A radial distribution function from this run of the ions around the nanoparticles (based on centers of mass) from the time period of 8-10 ns in the simulation is shown in Figure 4.5. Peaks at about 0.9nm were indications of the IL layer forming around the nanoparticles. The figure suggests that the BMIM cations were generally slightly closer to the nanoparticles than the anions in terms of center of mass (peaks at r = 0.916nm and r = 0.998nm, respectively). The elongated geometry of the BMIM cation allowed its center of mass to lie closer to the surface of the nanoparticle than that of the spherical anion. The PF_6 anion was about 0.31nm in diameter and the BMIM cation was about

0.15nm wide when lying flat. Therefore, this difference in peak locations was not large enough to indicate any layering of the ions around the particle.

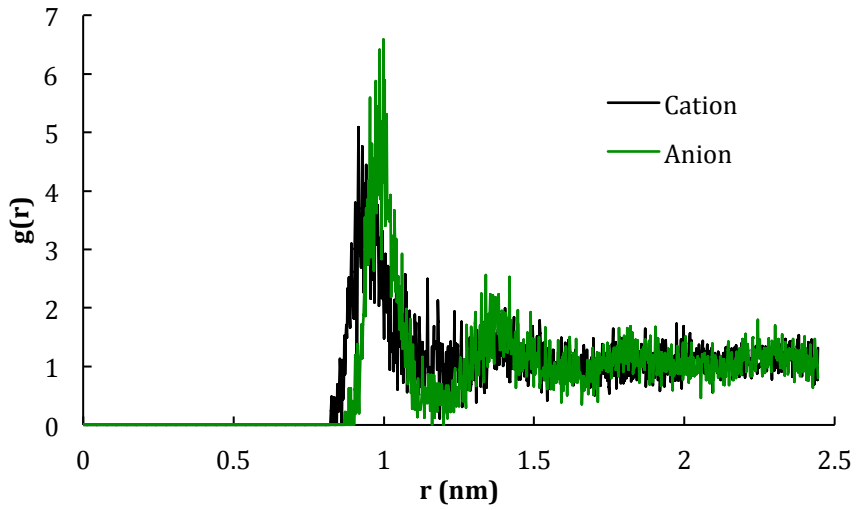

Figure 4.5 Radial distribution function of BMIM and PF_6 anions around the HCP nanoparticle.

Similarly for the IL/oil system (Figure 4.2b), we first dispersed the nanoparticles in the hexane phase (t = 0 ns). Interestingly, the nanoparticles quickly aggregated and equilibrated in the hexane phase, as shown in Figure 4.2b and Figure 4.4d-f. This aggregation was also observed by Luo and Dai [292] in their water-trichloroethylene simulations that employed the same nanoparticle model. The [BMIM] cations, despite the hydrophobic nature of their carbon chains, did not penetrate the oil phase and surround the nanoparticles as those in the IL/water system. Figure 4.4(d-f) shows that the nanoparticles immersed mostly in the hexane phases and were completely surrounded by the hexane molecules. This phenomenon may be explained by the competition between hexane and the [BMIM] cations for the surface of the nanoparticle. The nanoparticle was hydrophobic, electronically neutral, and made only of hydrocarbons. By these criteria, the

hexane molecules were equally hydrophobic, whereas the BMIM cations were slightly less because of their ionic imidazolium ring. Therefore, the hexane molecules had a dominating presence on the surfaces of the nanoparticles.

The corresponding density profiles are shown in Figure 4.6. These were obtained by averaging the last ns of 4 parallel runs of each system. The simulation box was divided into 100 slabs (a slab thickness of 0.01 Å) parallel to the xy plane. The density profiles support the visual inspection about the equilibrium positions of the nanoparticles. The interfacial width was defined as the length over which the density of one phase dropped from 90% to 10% of its bulk value [292]. The analyzed widths are shown in Table 4.3. The interfacial thickness of the water-trichloroethylene interface simulated by Luo and Dai was 0.5 nm [292]. By comparison, the interfacial thicknesses for the IL/water and IL/hexane systems were slightly higher. This may be due to more complex interactions with the ionic liquid. In contrast to the oil/water system, the oil here may interact more readily with the IL because of the organic cation. Also, the polar water molecules would have higher Coulombic interactions with the IL (which consists of charged species) than with an oil phase. Table 4.3 also includes the mole fraction of IL (X_{IL}) in the interfacial region for Systems A and C. The interface region is non-IL rich, with X_{IL} approximated as 0.12-0.13, with the exception of System C, where is more mixing towards the IL side of the interface.

Figure 4.6 and Table 4.3 both show that the IL-water interface was somewhat disrupted by the presence of the nanoparticles. Instead of a sharp decrease at the interface, the IL density gradually decreased over the region where the nanoparticles equilibrated. In this region, the IL molecules formed a thin layer around the

nanoparticles, as shown in Figure 4.4a. Because the nanoparticle aggregates did not completely enter the IL phase, this layer extended a significant distance from the bulk, resulting in a gradual decrease in IL density in the nanoparticle-occupied region. With the disruption of the nanoparticles, the IL-water interfacial width was higher compared to that of the system with no nanoparticles although the average values largely depended on density over which the interface was defined.

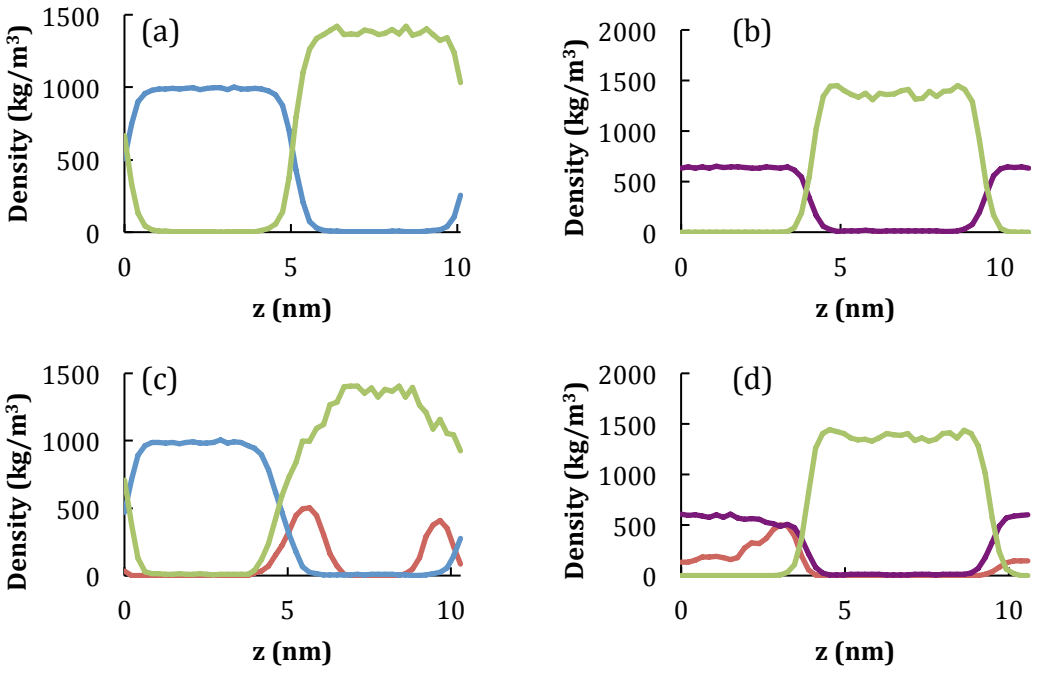

Figure 4.6 Density profiles of IL/Water systems without (a) and with (c) nanoparticles and IL/Hexane systems without (b) and with (d) nanoparticles. The IL, water, hexane, and nanoparticles are represented in green, blue, purple, and red, respectively.

Table 4.3 Equilibrium interfacial widths of Systems A-D.

Run	**Interfacial Width (nm)** (calculated from the IL density)	**Interfacial Width (nm)** (calculated from the solvent density)
W	0.83 ± 0.09 (X_{IL}≈0.13)	0.71 ± 0.15 (X_{IL}≈0.12)
W_0	1.95 ± 0.23	0.91 ± 0.36
H	0.70 ± 0.12 (X_{IL}≈0.22)	0.78 ± 0.13 (X_{IL}≈0.12)
H_0	0.67 ± 0.11	1.28 ± 0.72

Taking into account the standard deviation, the interfacial thickness in the IL/hexane system was comparable to the IL/water system where there is no presence of nanoparticles. Since the nanoparticles equilibrated in the hexane phase, the interface thickness of System H_0 remained unchanged if calculating from the IL density. Defining the interface in terms of hexane density gave a significantly different value in System H_0. The average interfacial thickness was 1.28 nm, but varied by ± 0.72 nm. This unusually high variance is due to the location of nanoparticles. In some of the parallel runs, the aggregated nanoparticles equilibrated close to the interface whereas in other parallel runs, the aggregated nanoparticles equilibrated in the bulk hexane phase. The interfacial thickness was only increased when the nanoparticles equilibrate near the interface, so a high variance in interfacial thickness was observed between the four parallel runs.

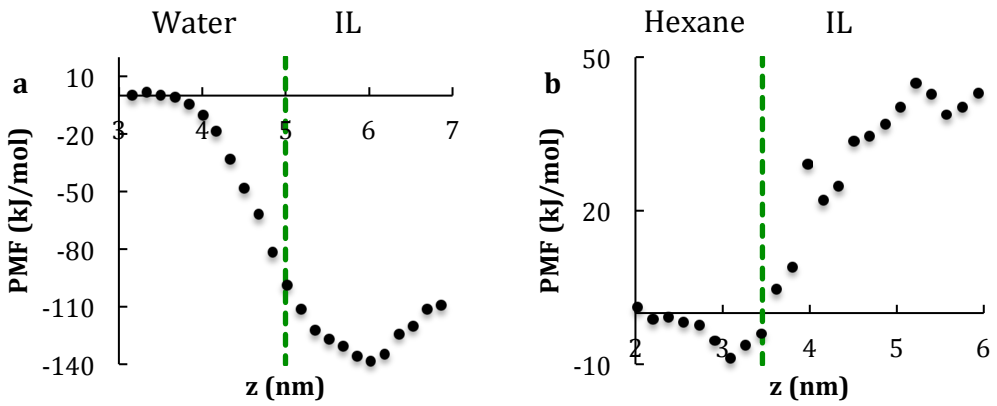

Figure 4.7 Potential of mean force (PMF) calculations of the IL/water system (a) and the IL/hexane system (b). The green dotted line represents the approximate location of the interface. Phases are labeled on either side of the interface line.

Figure 4.7 shows the results from the PMF calculations on a single particle moving through the IL/water system (**Figure 4.7**a) and the IL/hexane system (**Figure 4.7**b). In both figures, the dotted green line represents approximately the point at which the density profiles cross, thus providing the location of the interface along the z axis. As **Figure 4.7**a shows, the PMF profile decreased dramatically as the particle approached and crossed the interface. This profile reached a minimum approximately 1 nm past the interface in the IL, which corresponded well to the observed location of the equilibrated particles in the IL/water system (See Figure 4.2a). The maximum free energy was exhibited while the particle was in the water phase. The PMF profile of the IL/hexane system was notably different. **Figure 4.7**b shows that the minimum free energy was manifested while the particle was still in the hexane phase, close to the interface. As the particle crossed the interface, the free energy gradually increased until it reached a maximum in the hexane phase. This profile also agreed well with the equilibrium positions of the particles in Figure 4.2b. The particles did not cross the interface because

of the consequential increase in free energy. Instead, the particles remained where the free energy was the lowest: in the hexane phase, but still rather close to the interface.

4.3.2 Interfacial Self Assembly of Charged Particles

In the previous section, we reported that the uncharged nanoparticles in the IL/water system showed high interactions with the IL and equilibrated on the IL side of the interface [247]. In contrast, the uncharged nanoparticles in the IL/hexane system did not readily interact with the IL, but aggregated and equilibrated in the hexane phase, though in somewhat close proximity to the interface [247]. Snapshots of these systems are included for reference in Figure 4.8 and we will draw comparisons with them to emphasize the effect of charge on nanoparticle self assembly.

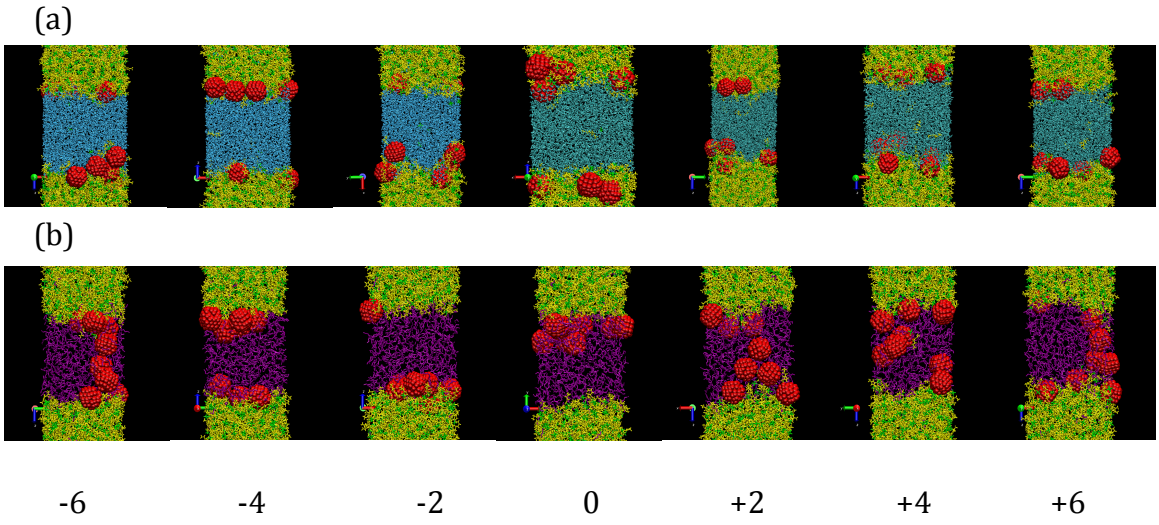

Figure 4.8 Snapshots of (a) the IL/water and (b) IL/hexane systems at 20 ns. Nanoparticle charges are shown underneath the snapshots.

Figure 4.8a illustrates the snapshots of the IL/water systems at 20 ns. Though we hypothesized higher interactions between the nanoparticles and the IL with enhanced charges, the nanoparticles equilibrated at nearly the interfacial position regardless of the

charge sign or magnitude. Compared to the IL/hexane system, these nanoparticles were embedded much deeper into the IL, with the uncharged one immersed the deepest. We attributed this behavior to the hydrophobic nature of the nanoparticles.

Charged nanoparticles exhibited notably different behavior in the IL/hexane system. Figure 4.8b includes snapshots of the IL/hexane systems of different nanoparticle charges at 20 ns. In contrast to the neutral nanoparticles, the charged nanoparticles showed enhanced interactions with the IL phase and equilibrated at the interface (with the exception of the aggregated nanoparticles). The degree of this interaction appears to be independent of charge magnitude and sign. Despite having like charges, the nanoparticles showed a high degree of aggregation. This was due to the fact that the counterions were unable to dissociate from the charged sites into the non-polar hexane phase. Figure 4.9 shows the energetic contributions of various interactions of these systems with respect to particle charge. Both dispersion (LJ) and electrostatic (Coul) were accounted for. It can be seen that despite the repulsive forces felt between the particles, the ion-particle interactions dominated and became more so with increased particle charge. Since the counterions equilibrated at the interstices of the aggregates, the counterion-particle interactions (attractive) occurred over a shorter distance than the particle-particle interaction (repulsive) and were consequently stronger. Figure 4.9 shows that they were significantly stronger and provided the primary contribution to the total energy of each system. Were it not for these counterions, the particles would resist aggregation due to strong repulsions. Therefore, ionic attraction between the nanoparticles dominated due to the high concentration of charged sites and counterions in nanoparticle aggregates.

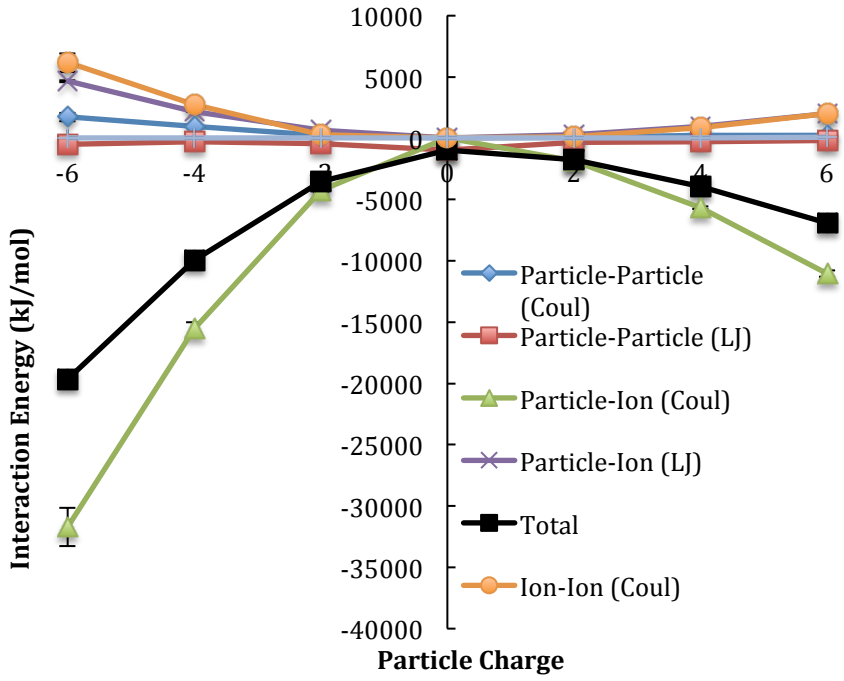

Figure 4.9 Energy contributions of various interactions in the charged particle systems.

Close-up snapshots of the IL/Water (a) and IL/Hexane (b) systems at 20 ns are shown in Figure 4.10. Most notable was that the counterions (dark blue) in the IL/water system remained in the water phase, leaving the nanoparticles free to interact with the IL. The counterions in the IL/hexane system remained tightly bound to the charged sites of the nanoparticles while in the hexane phase, as discussed in the previous paragraph. Some of the Cl^- counterions, however, dissociated into the IL phase, likely due to favorable interactions with the [BMIM] cation. The presence of nanoparticles disturbed the interface significantly, as we will also see upon examination of the density profiles. The IL interacted with the nanoparticles by forming thin layers around them, thus deviating significantly from a flat interface state. This was true of all systems in question except for the IL/hexane system with uncharged nanoparticles, which was the only system in which the nanoparticles did not interact with the IL at the interface. We can

therefore conclude that the presence of charge was necessary for self-assembly of hydrophobic nanoparticles at the IL/hexane interface.

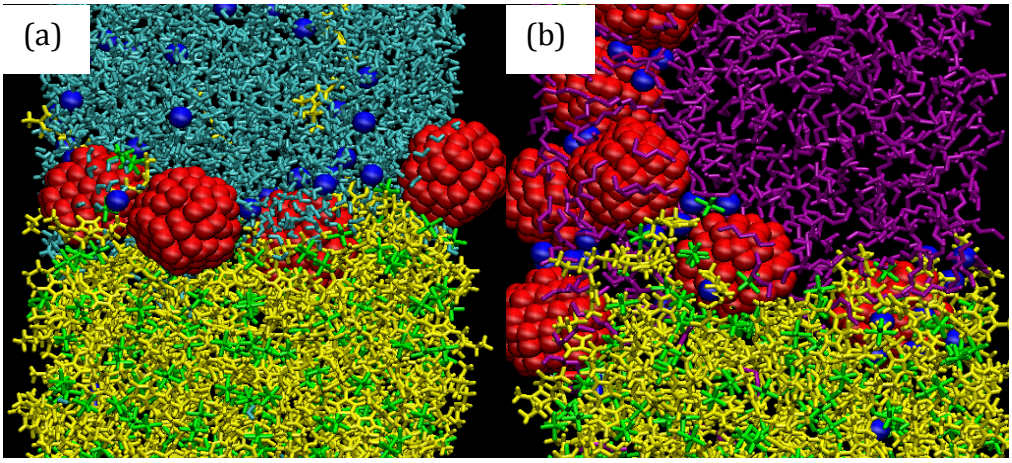

Figure 4.10 Close-up snapshots of (a) IL/water and (b) IL/hexane systems at 20ns. The nanoparticles (in red) have +6 charge and the Cl^- ions are shown as dark blue spheres.

Figure 4.11 shows the density profiles of the systems in question by nanoparticle charge. These were obtained by averaging the last nanosecond of 4 parallel runs of each system. The simulation box was divided into 100 slabs (a slab thickness of 0.01 Å) parallel to the xy plane. The density profiles support the visual inspection in general. The nanoparticles were generally absent from the water phase and the neutral nanoparticles were the furthest embedded into the IL phase in the IL/water systems. The charged nanoparticles in the IL/hexane systems showed higher interactions with the IL than the neutral nanoparticles, but still maintained a significant presence in the hexane phase due to aggregation. It is worthwhile to note that because the density profiles were averaged from all nanoparticles (including the aggregates in the hexane phase), they may not precisely reflect the position of the nanoparticles that equilibrated at the interfaces. In all systems, the presence of nanoparticles caused a disturbance in the density profile

of the species with which they interacted the most. For example, the uncharged nanoparticles of the IL/water system interacted heavily with the IL, which caused a more gradual decrease in IL density at the interface. In contrast, the IL density profile of IL/hexane system with neutral nanoparticles exhibited a sharp decrease at the interface due to a lack of interaction between the nanoparticles and the IL. We quantified this disturbance by measuring the interfacial widths of these systems and hence evaluated the degree of interaction between the nanoparticles and the respective solvents.

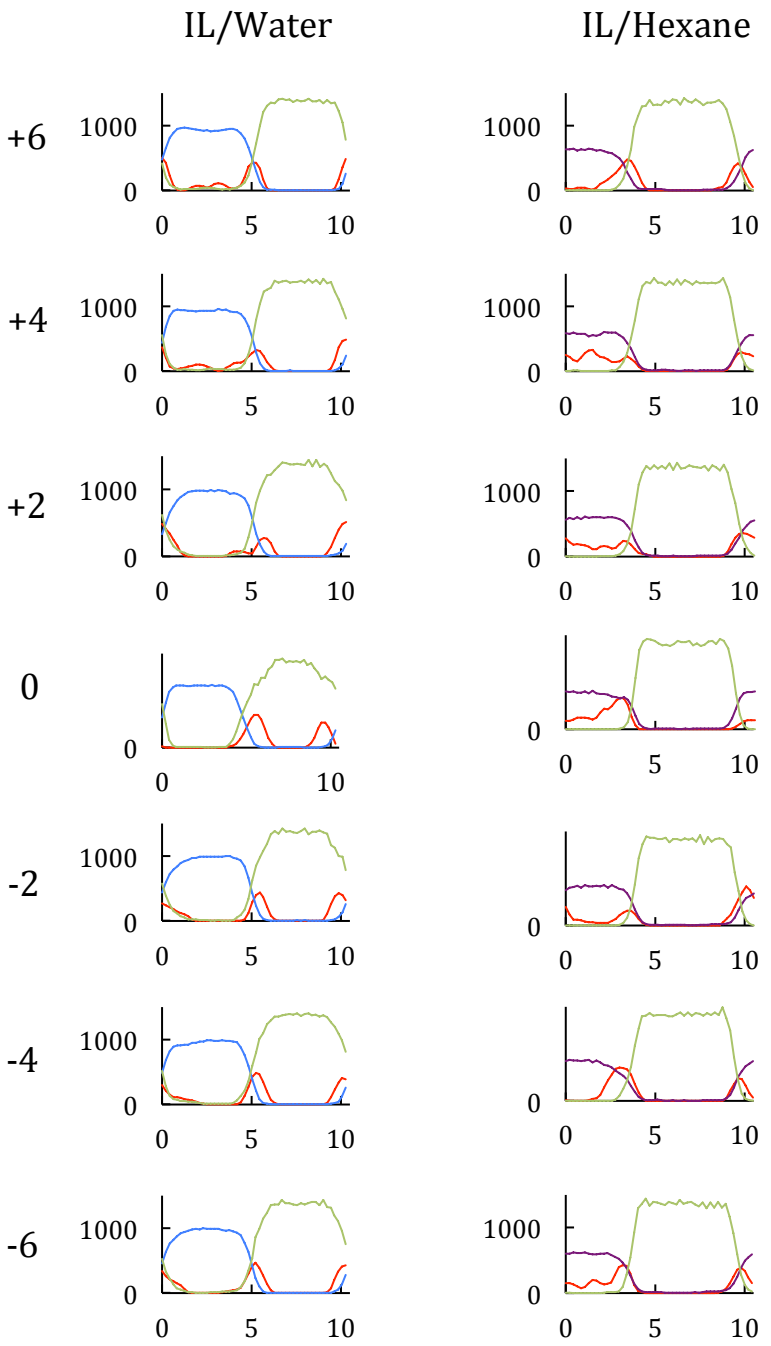

Figure 4.11 Density profiles averaged from last 1 ns of 4 parallel runs for each system. Y-axes represent density (kg/m^3) and x axes represent z position (nm) in the simulation boxes. The green, blue, purple, and red lines represent the IL, water, hexane and HCPs, respectively. Nanoparticle charges are shown in the left column.

The interfacial width was defined as the length over which the density of one phase dropped from 90% to 10% of its bulk value [292]. Since there were two bulk phases present in each simulation, we calculated the interfacial width with respect to each phase. The interfacial widths for all runs are shown in Figure 4.12. Figure 4.10a shows that the interfacial width as defined by the ionic liquid varied somewhat with respect to nanoparticle charge. In the IL/water system, the interfacial width decreased to some extent in the systems with the charged nanoparticles (regardless of charge sign). These data indicate that the IL interacted more with uncharged nanoparticles than with charged ones, i.e. the nanoparticles' preference for the IL phase decreased by adding charge. We did not anticipate this observation since the ions of the IL should have interacted well with the charged sites. However, recent studies have shown that the polarity of water is generally higher than that of ionic liquids [338, 339]. Therefore, increasing the surface charge enhanced the nanoparticle-water interaction rather than the nanoparticle-IL interaction. This behavior coincided well with the hydrophobic character of the nanoparticles (which should become less hydrophobic with charge). Also, this decrease was more pronounced in the systems with positively charged nanoparticles, indicating that the large cations may have exerted repulsive forces on the nanoparticles due to like charges.

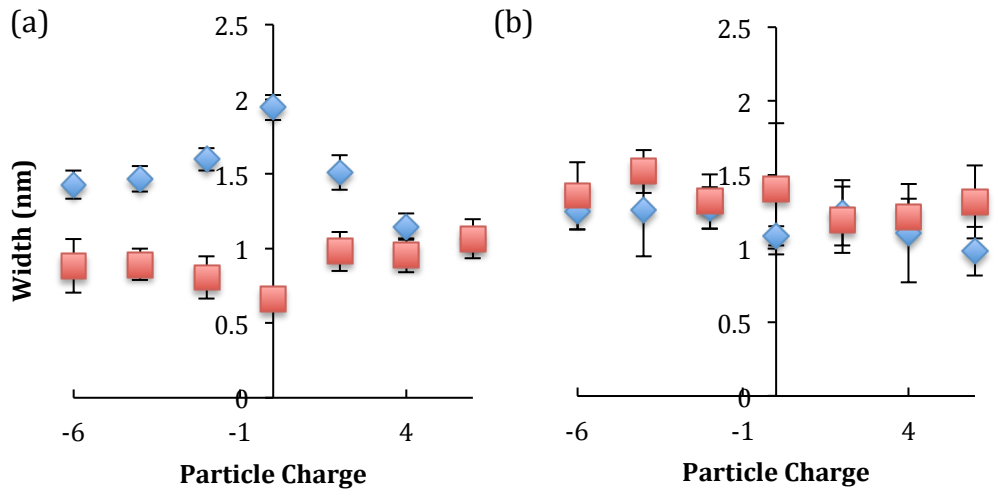

Figure 4.12 Interfacial widths defined by the (a) IL and (b) non-IL solvents with respect to nanoparticle charge. Squares represent IL/Hexane widths and diamonds represent IL/Water widths.

In contrast, the IL/hexane systems showed increased interfacial widths (defined by the IL) due to interaction with charged nanoparticles (see Figure 4.12a). Such behavior was expected, considering the lack of nanoparticles at the interface in the neutral nanoparticle system and significant embedment of nanoparticles into the IL in the charged nanoparticle systems (see Figure 4.8b). Such behavior also coincided with the hydrophobic nature of the nanoparticles: with no charge, the nanoparticles avoided the polar solvent (IL), but with increased charge, the nanoparticles interacted more readily with the polar solvent.

Figure 4.12b shows how the solvent-defined interfacial widths changed with nanoparticle charge. There were no significant changes in interfacial width with respect to charge in either of the systems. Therefore, the nanoparticle charge did not have a substantial effect on the nanoparticle-solvent interactions. In the case of the IL/water system, any changes in the nanoparticle location were not great enough to disturb the

water phase. Comparably, the charged nanoparticles in the IL/hexane system were not displaced from the hexane phase enough to significantly reduce the disturbance of the hexane density at the interface.

These equilibrium studies gave us an approximate view of how deeply particles penetrated the interface. We expected that the PMF calculations would give more exact conclusions as to the equilibrium locations of the particles with respect to the interface. Theoretically, PMF calculations should exhibit minima at the particles' respective equilibrium z locations. Figure 4.13 shows the results from the PMF calculations for the (a) IL/Water and (b) IL/Hexane systems with 0 charge (black), +4 charge (blue) and -4 charge (red) nanoparticles. The y-axis in both graphs represents the approximate location of the interface and is also the point at which the density profiles of the IL and solvent cross. As expected, all particles in the IL/water system exhibited minima in free energy on the IL side of the interface, denoting their equilibrium positions. The minima of the +4 and -4 charged particles were nearly identical, while the minima of the neutral particle occurred approximately 0.5 nm further past the interface, indicating deeper embedment into the IL.

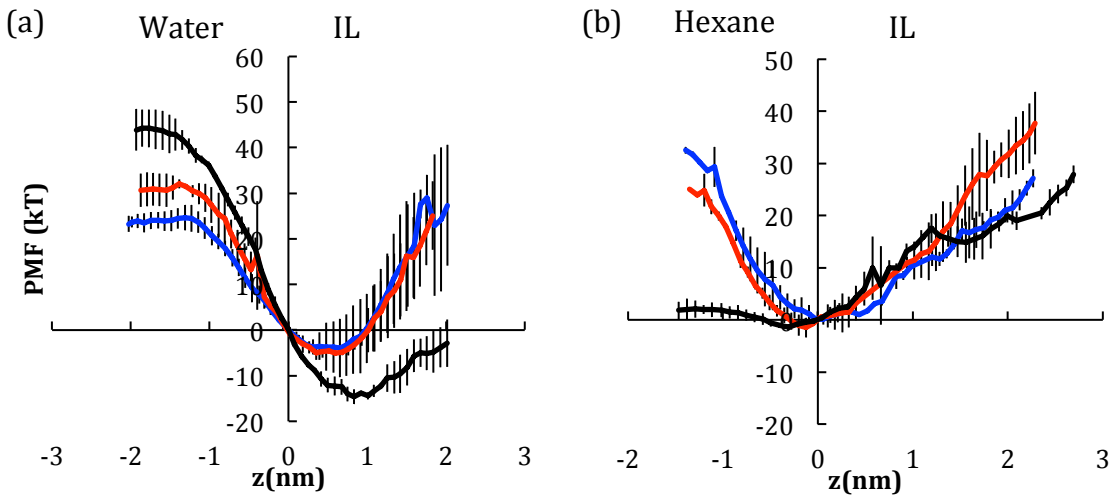

Figure 4.13 PMF calculation results upon pulling single nanoparticles through the (a) IL/water and (b) IL/hexane interfaces (z = 0). Results from neutral nanoparticles, +4 charged nanoparticles, and -4 charged nanoparticles are shown in black, blue, and red, respectively.

Figure 4.13b shows the PMF profile of single nanoparticles as they moved through the IL/hexane interface. Clearly, both charged particles experienced free energy minima at z = 0 with energy increasing rapidly in either direction. Charged particles, therefore, should have been fairly stable straddling the interface, as was seen with many particles in the equilibrium simulations. The free energy of the neutral particle, however, had a very shallow minimum about 0.4 nm on the hexane side of the interface. The uncharged nanoparticles did indeed equilibrate in this region.

Experiments on ionic liquid solvation of charged species have shown that the imidazolium cation plays an important role [280-282]. More specifically, the size of the cation greatly affects the electrostatic interactions between the IL and the solute species. For example, Nusai, et al. recently showed that increasing the imidazolium alkyl chain length decreased the solubility of positively charged ions in the IL [280]. Figure 4.13 shows that, there were no significant differences in the PMFs of the negatively and

positively charged particles in the IL phase. Perhaps in a future study we would begin to see differences with larger cations (i.e. replacing butyl with octyl chains).

Although the primary purpose of the PMF calculations was to determine the equilibrium positions of the particles with respect to the interface, the behaviors beyond the minima are worth noting. We compared these data to the well-known macroscopic calculation for desorption of a spherical nanoparticle from a liquid-liquid interface (Equation 2.3, shown again here for convenience) [9-11].

$$\Delta G=\pi r^2\gamma(1\pm\cos\theta)^2 \tag{2.3}$$

where ΔG is the change in free energy upon desorption of the nanoparticle from the interface to either of the bulk phases, r is the nanoparticle radius, γ is the interfacial tension between the two liquids, and θ is the three-phase contact angle measured through the solvent (non-IL) phase. The positive sign is used for desorption into the IL phase and the negative sign is used for desorption into the solvent phase.

Equation 2.3 indicates that particle-interface interactions exist only when the two are in contact. Thus, ΔG should not change beyond certain distance, in our case, r (0.6 nm). It is clear from Figure 4.13, however, that significant changes in ΔG were felt beyond this distance. The PMF of all particles continued to steadily increase 1.5 nm beyond the IL/hexane interface on both the IL and the hexane side. The same is true of the particles on the IL side of the IL/water interface. Even though the PMFs flattened out on the water side, this saturation point was not reached until the particles were at least 1.2 nm from the interface. At first, we questioned whether the long range interaction was an artifact of an insufficient box length, L_z, for the two liquids. However, simulations with doubled box lengths (~11 nm on each liquid side) and extended runs times produced

similar results (See Figure 4.14). Recent studies by Cheung have shown that Equation 2.3 greatly underestimates the particle-interface interaction range because it does not account for capillary waves, which widen the interface [19, 27]. This is especially true of systems with low interfacial tensions, since the amplitude of the capillary waves varies with $1/\gamma$ [27, 340]. Both the IL/water and IL/hexane systems here exhibited low interfacial tensions of approximately 10-13 mN/m. Therefore, the low interfacial tension allowed the interface to interact with the particle over a wider range than the prediction by macroscopic theory. Figure 4.15 shows that in some cases, the interface deformed enough and formed bridges with particles 1.2 nm from the interface. This phenomenon is unique and important in describing nanoparticle self-assembly at IL-based interfaces because the oil/water systems generally have much higher interfacial tensions.

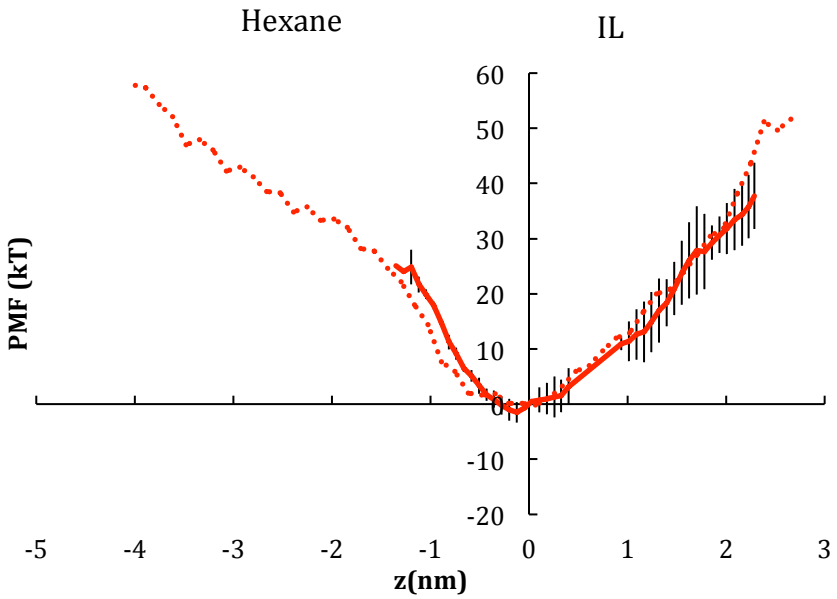

Figure 4.14 PMF of a negatively charged particle at the IL/Hexane interface (z = 0). The solid line and dotted line represent PMF calculations performed in boxes with Lz = 11 nm and 22 nm, respectively.

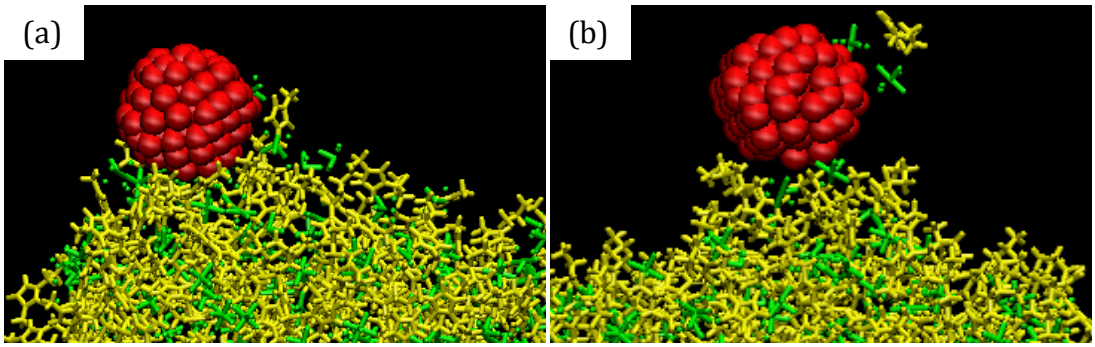

Figure 4.15 Interfacial deformations in the (a) IL/water and (b) IL/hexane systems with +4 charged particles. Solvent molecules were removed so as to create a clear view of the particles and the deforming interface.

Based on the interfacial tensions and particle size of our systems, Equation 2.3 predicts a total desorption energy of 1-10 kT, depending on the three-phase contact angles. Although most of the PMF profiles did not saturate, it is apparent that the desorption energies of these systems were much higher. This discrepancy again brought into question of the lateral box size, since it is well-known that interfacial tensions show

some dependence on the size of the interface at the nanoscopic scale. Ionic liquids are known to show a "non-monotonic variation" in surface tension with respect to L_x [341]. Gonzales-Melchor et al. showed that the surface tension of an IL oscillates with L_x/d, where d is the diameter of the largest ion in the IL. The average diameter of the BMIM cation was about 0.6, which gave a value of $L_x/d = 8.1$ in our systems. At this value, the surface tension of the IL should only vary a few percent from the macroscopic value [341]. Furthermore, we have performed simulations with doubled box lengths (~11 nm on each liquid side) and extended runs times to rule out the possibility of box size effect. Instead, low interfacial tensions, thus high capillary waves, of these systems likely account for this discrepancy. This work supports the comment that the desorption energy predicted by Equation 2.3 for nano-sized systems under-predicts the desorption energy with decreasing interfacial tension [19]. Lehle and Oettel recently showed that capillary waves have a broadening and softening effect on the potential well described by the PMF [18]. This effect is logarithmically dependent on λ_c, the largest capillary wave in the system. The length of the largest capillary wave in our simulation is the lateral box length, L_x (5.5 nm or 11 nm). Based on Lehle and Oettel's model, we expect that the PMF well would become more shallow and broad with increasing L_x but the effect is not obvious (See Figure 4.14) thus further suggest that our simulation boxes are sufficiently large.

It is interesting to note that the interfacial width data and the PMF calculations show evident agreement on the nanoparticle-IL interaction with respect to charge. In the IL/water system, the uncharged nanoparticle showed the greatest decrease in free energy upon contact with the IL compared to the negatively and positively charged

nanoparticles. Correspondingly, the interfacial width data of this system showed that the uncharged nanoparticles caused the greatest disturbance at the interface among all particles. The same comparison can be made with the interfacial width and PMF data of the IL/hexane system (vice versa in terms of particle charge). The decrease in energy represents the relative favorability of the IL-particle interaction over the solvent-particle interaction. With higher particle-IL interaction, the IL surrounded more of the particle surface than the solvent, causing greater interfacial deformation. Because the equilibrium systems contained eight particles each, this effect was likely amplified. This is significant in light of the differing MD techniques (equilibrium MD and PMF) lead to similar results.

4.3.3 Effect of Particle Surface Chemistry on Interfacial Self-Assembly and Particle Extraction

We will first discuss the interfacial equilibrium simulations. Figure 4.16 shows snapshots at 20 ns of each system with an accompanying density profile, which was averaged over four parallel runs. The interfaces simulated were IL/water (Figure 4.16a and Figure 4.16b) and IL/Hexane (Figure 4.16c and Figure 4.16d) and both were simulated with the two nanoparticle types. Figure 4.16a and Figure 4.16c focused on the hydrocarbon nanoparticle and were taken from our previous work on the self-assembly of the hydrocarbon-based nanoparticles at the IL/hexane and IL/water interfaces [247, 248]. In these studies, the nanoparticles equilibrated on the hexane or water side of the interface (see Figure 4.16a and Figure 4.16c) [247, 248]. A brief comparison of this behavior with the silica nanoparticles follows. As expected, the silica nanoparticles exhibited more hydrophilic behavior. Figure 4.16b shows that while some silica

nanoparticles adsorbed to the IL/water interface, most of them remained in the water phase. In contrast, all of the nanoparticles in the IL/hexane system adsorbed to the interface and interacted heavily with the IL (Figure 4.16d). These observations were confirmed by the corresponding density profiles, which are provided to present an average of all 4 parallel runs. Thus, in comparison to the hydrocarbon nanoparticle, the phase preferences of the silica nanoparticles at the IL interfaces were qualitatively opposite. Therefore, we can expect the IL to respond to these two surface chemistries in different ways.

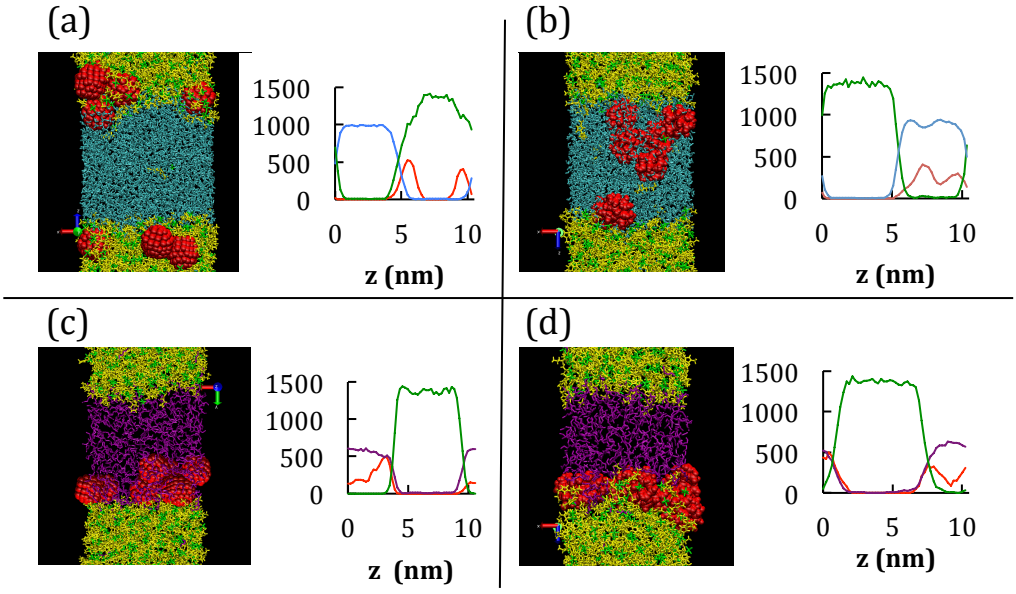

Figure 4.16 Equilibrium snapshots at 20 ns and corresponding density profiles for four systems: (a) hydrocarbon nanoparticles at the IL/water interface, (b) silica nanoparticles at the IL/water interface, (c) hydrocarbon nanoparticles at the IL/hexane interface, and (d) silica nanoparticles at the IL/hexane interface. Densities are in kg/m^3.

Particle extraction inherently requires transport across the liquid-liquid interface and this process was examined via PMF calculations. Figure 4.17 shows the calculations for a single hydrocarbon nanoparticle and silica nanoparticle, respectively, pulled through

the IL/water and IL/hexane interfaces. Relative to the interface, the minima in the PMF profiles corresponded well to the equilibrium nanoparticle locations shown in Figure 4.16. Once again, the phase preference of the hydrocarbon nanoparticle was qualitatively opposite to that of the silica nanoparticle, as exhibited by the location of the respective minima. As the hydrocarbon nanoparticle crossed the IL/water and IL/hexane interfaces, it experienced free energy changes of -58 kT and +25 kT, respectively [247, 248]. As the silica nanoparticle moved from the water to the IL phase, free energy increased by approximately 25 kT. In contrast, free energy decreased by approximately 35 kT as the silica nanoparticle moved out of the hexane to the IL phase. These results suggest that extraction of silica nanoparticles from the water phase is unlikely, but extraction from an oil phase is more viable since the IL can provide better solvation (and vice versa for the hydrocarbon nanoparticle). Indeed, extraction of silica nanoparticles from bitumen oil phase has been reported [150, 195-197].

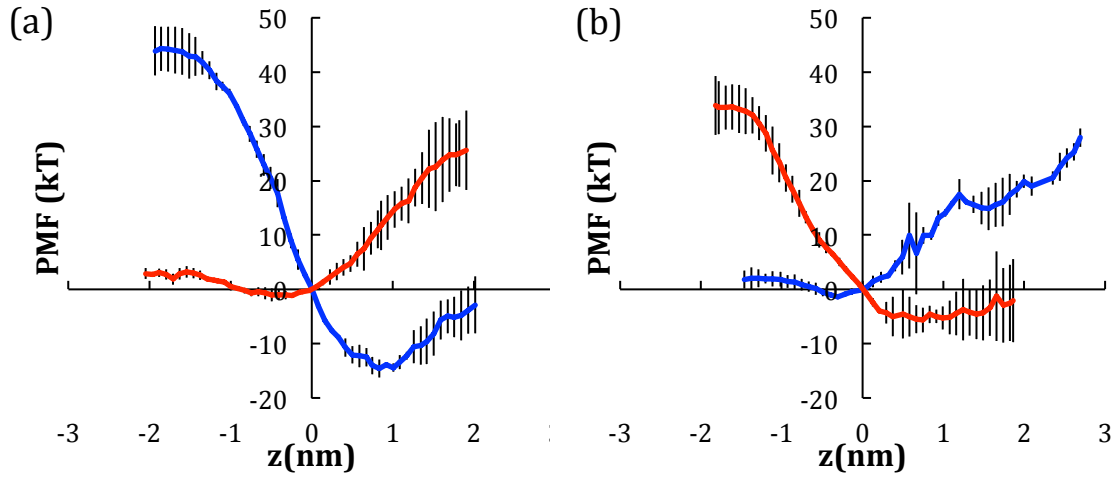

Figure 4.17 Potential of mean force (PMF) results of hydrocarbon (blue lines) and silica (red lines) pulled through the IL/water interface (a) and the IL/hexane interface (b).

Extraction of particles differs from extraction of molecular species in one key aspect: particles must overcome the capillary energy barrier of the liquid-liquid interface since their surfaces can be wetted by both solvents [6, 7]. Particle adherence to the liquid-liquid interface provides the kinetic stability in Pickering emulsions [6, 7, 14]. The energy required to detach a particle from these interfaces can be extracted from the PMF calculations. This can be done by subtracting the energy of the nanoparticle at the interface from the energy of the nanoparticle immersed in the IL. Adhesion energy was determined by assuming that at the interface, half of the particle surface was still "bound" to the non-IL phase. For both nanoparticles, the energy required to detach them from their respective favorable phases (hydrocarbon from hexane and silica from water) was on the order of 25 kT (22.9mJ/m^2). In contrast, nanoparticle adhesion energies to their respective unfavorable phases were 0, within error. These low adhesion energies likely promote particle extraction into the IL. In a similar oil/IL system, Hogshead et al. reported the adhesion energy of a silica particle to the oil (unfavorable) phase to be 0.5 mJ/m^2 [150]. This energy corresponds to a PMF change of 0.55 kT, which is within error of our calculations (see Figure 4.17b)

Once extracted into the IL, the most important interactions arise between the particle surface and the first layer of ions, or the solvation shell. Shells around water-solvated species (hydration shells) have been studied both theoretically and experimentally [342] with particular focus on solvated proteins [343, 344]. A few studies have focused on solvation shells around colloidal particles in both water [345] and oil [346] and indicate that the shells originate from weak interactions between the particle surface and the solvent molecules. Due to the binary nature of the IL, more degrees of

freedom were available over which it could form layers around these nanoparticles. By simulating single nanoparticles in pure IL, we explored these layers as a function of nanoparticle surface chemistry.

Figure 4.18 shows the solvation shells around the hydrocarbon nanoparticle (a) and the silica nanoparticle (b) at 20 ns. It should be noted that like the nanoparticles, the individual ions had differing hydrophobicities. Previous simulations have indicated that BMIM is generally more hydrophobic than PF_6 due to the presence of carbon chains [128]. For this reason, we expected to see strong associations between ions and nanoparticles of similar hydrophobic natures indicated by differences in solvation shell compositions. However, the distribution of cations and anions was nearly the same in each solvation shell (shown below each image of Figure 4.18, respectively). This observation suggests that despite the different hydrophobicities of the nanoparticles and ions, all ions play a role in the solvation shell. Close association of the ions is to be expected due to Coulombic attraction. However, BMIM cations were generally more abundant in the solvation shell.

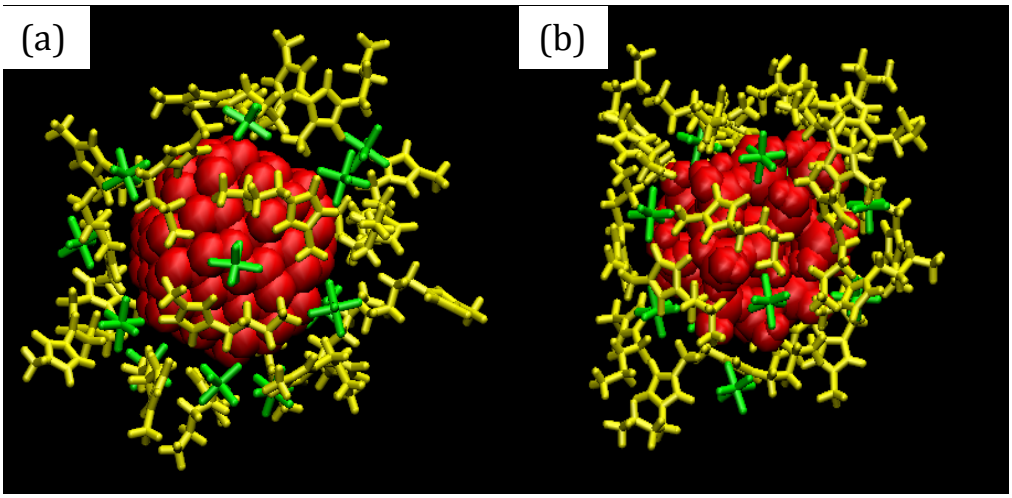

Figure 4.18 IL solvation shells around the hydrocarbon (a) and silica nanoparticle (b). BMIM, PF_6, and nanoparticles are represented in yellow, green, and red, respectively in each image. The number of ions present in each solvation shell (averaged over four parallel runs) is shown below each respective image.

Apart from differing surface chemistries, the nanoparticles also possessed slightly different surface geometries due to their inherent crystal structure. The hydrocarbon nanoparticle, having been generated from a diamond lattice, presented a smoother surface to the IL than the silica nanoparticle (average distances between adjacent surface atoms are 0.156 nm and 0.276 nm for the hydrocarbon and silica nanoparticles, respectively). Consequently, we observed some segregation of ions at the silica nanoparticle surface. The anions, being smaller, often equilibrated in the spaces between silanol groups allowing for closer association with the nanoparticle surface. Ions in the solvation shell of the hydrocarbon nanoparticle were evenly distributed across the surface. Therefore, the binary nature of the IL allowed for some adaptability to the two surfaces in that the anions and cations could interact with the nanoparticles in different ways. However, this

segregation at the silica nanoparticle surface was due not only to differences in size, but also surface chemistry as will be seen later.

Interaction energy between the nanoparticles and the IL differed between the two surface chemistries. Table 4.4 summarizes the Lennard-Jones (LJ) and Coulombic interaction energies for these two nanoparticles, averaged over the last 5 ns of simulation. LJ interaction energies were nearly the same for the PF_6 anion, but the hydrocarbon nanoparticle interacted more favorably with the BMIM cation than the silica nanoparticle did. As a result, the total LJ interaction energy of the IL with the hydrocarbon nanoparticle was approximately 17% greater (in magnitude) than with the silica nanoparticle. These results suggest that the BMIM cation can play a major role in the extraction of hydrophobic nanoparticles. In particular, the high LJ energies are evidence that the IL exhibited significant extraction qualities apart from their Coulombic nature. This feature may explain why both hydrophobic polystyrene [151] and hydrophilic silica [150, 195-197] have been absorbed by ILs.

Table 4.4 Interaction energies between nanoparticles and the IL.

Interacting Species	Silica (kJ/mol)	Hydrocarbon (kJ/mol)
BMIM: Coulomb	-374 +/- 26	0
BMIM: LJ	-361 +/- 11	-484 +/- 8
PF_6: Coulomb	-324 +/- 17	0
PF_6: LJ	-211 +/- 14	-192 +/ 11
Total Coulomb	-698 +/- 37	0
Total LJ	-572 +/- 5	-676 +/- 6
Total	-1270 +/- 35	-676 +/- 6

Of course, Coulombic forces were not insignificant. In fact, these forces (only present with the silica nanoparticle) were of the same magnitude as the LJ forces of the hydrocarbon nanoparticle and dominated the interaction energy of the silica nanoparticle.

Consequently, the silica nanoparticle had nearly twice the total interaction energy as the hydrocarbon nanoparticle. Also, despite there being half as many PF_6 anions in the solvation shell as cations (on average) the Coulombic contributions of each of the ions were nearly equal. This suggests that the PF_6 anions were more closely associated with the silica nanoparticle than the cations, since Coulombic interactions decay with distance. Radial distribution function discussed in the next paragraph show that this was indeed the case. Thus, the IL exhibited not only significant Coulombic extraction features, but also configurational adaptability of the solvation shell to the nanoparticle surfaces. While there are certainly solvents capable of higher Coulombic interactions via polarity [338], the fact that opposite charges are placed on two separate species in ILs may allow them more freedom to interact with a variety of charged surfaces.

Figure 4.19 shows the radial distribution (RDF) functions of each ion with respect to the centers of mass of the nanoparticles (average of the four parallel runs). Most notable are the differences in overlap behavior of the RDFs with respect to each nanoparticle. High overlap of the oscillatory RDFs around the hydrocarbon nanoparticle indicated that both ions exhibited similar layering behavior. Furthermore, the overlap suggests that charge neutrality was generally maintained beyond the first solvation shell. In contrast, the oscillations around the silica nanoparticle were highly mismatched with peaks of one ion RDF corresponding with valleys of the other. This behavior suggests that solvation layers consisted of alternating ions. Furthermore, the width of the layers was also affected by surface chemistry, as indicated by the differences in RDF peak separations. For the hydrocarbon nanoparticle, the RDF peak separations were an average of 4.6Å and 4.5Å for the BMIM and PF_6 ions, respectively. Around the silica

nanoparticle, the peak separations were 7.1Å and 6.3Å, respectively: increases on the order of 50%. It should also be noted that the RDF oscillations decayed at a slower rate around the silica nanoparticle, indicating more well-defined layers. All of these observations point to the importance Coulombic interactions between the nanoparticle and the IL. To illustrate this point, simulations were performed with all of the atomic charges of the silica nanoparticle set to zero. The resulting RDF (shown in Figure 4.20) was nearly identical to the hydrocarbon nanoparticle RDFs (see Figure 4.18). ILs are known to exhibit double-layer behavior at charged surfaces [156, 347, 348]. Recent simulation studies in conjunction with AFM studies have shown that ILs exhibit charge ordering at flat silica surfaces [264, 349-351]. While qualitatively similar, our results differ from these studies in that the separation of ion peaks persisted for over larger distances. This may have been due to our using ions that were more size-mismatched, which aided segregation in this solvation structure.

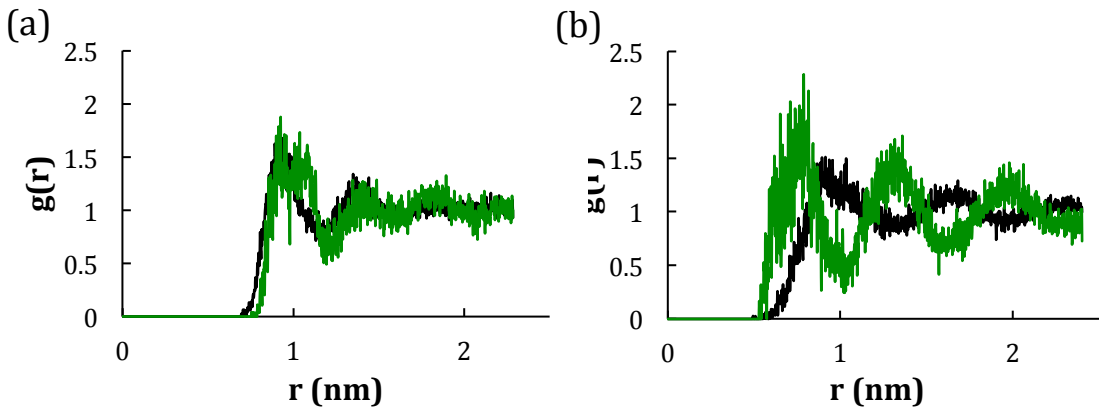

Figure 4.19 Radial distribution functions (RDF) of each ion around the center of the hydrocarbon nanoparticle (a) and the silica nanoparticle (b). RDFs for the BMIM cation and PF_6 anion are shown in black and green, respectively.

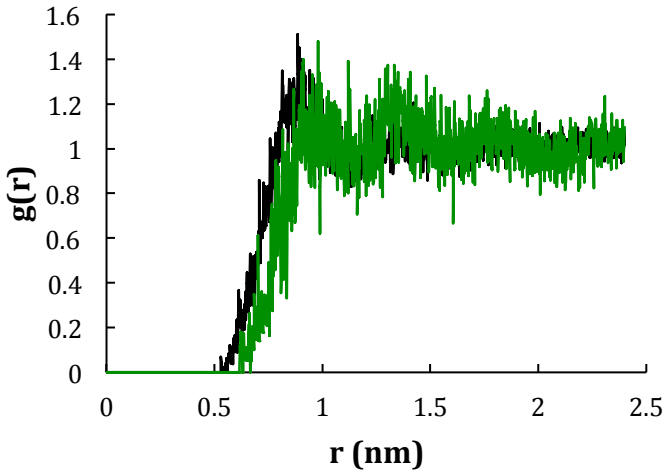

Figure 4.20 RDF of the two ions around a silica nanoparticle with the silanol group charges set to 0. RDFs for the BMIM cation and PF_6 anion are shown in black and green, respectively.

Another feature to note in Figure 4.19 is the relative proximity of the ions to their respective nanoparticles. The BMIM cations exhibited slightly closer association with the hydrocarbon nanoparticle, but the PF_6 anions exhibited a clear dominance in association with the silica nanoparticle until about 8Å from the nanoparticle center. The latter results suggest some favorable surface chemistry and we hypothesized that hydrogen bonding

between the silanol group and the PF_6 anions had occurred. Figure 4.21 shows RDFs of the ions around silanol H's. Here we see that the anions indeed exhibited strong association with the silanol groups. Furthermore, the small size of the anion allowed it fit between multiple silanol groups, maximizing the interaction (see inset of Figure 4.21). It should be noted that this behavior disappears when the atomic charges of the silica nanoparticle are set to zero (see Figure 4.20 and Figure 4.22). Once again, the amphiphilicity of the IL is highlighted here in that the anions segregate from the IL when necessary and provide strong hydrogen bonding with an appropriate surface chemistry.

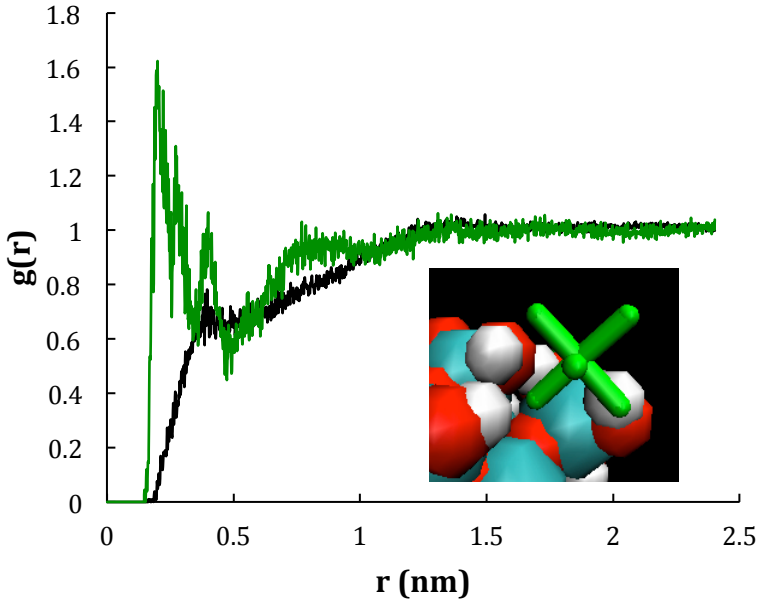

Figure 4.21 RDF of each ion with respect to the hydrogen atoms of the silanol groups of the silica nanoparticle. RDFs for the BMIM cation and PF_6 anion are shown in black and green, respectively.

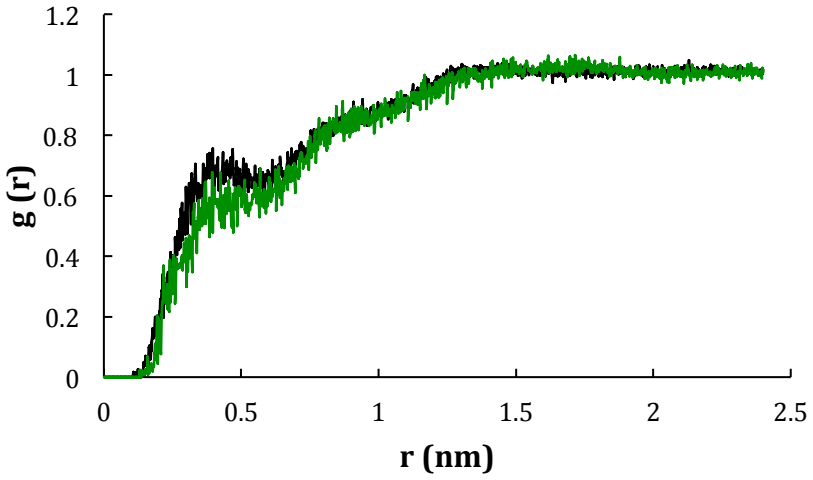

Figure 4.22 RDF of the two ions around the H's of the silanol groups of the silica nanoparticle with the silanol group charges set to 0. RDFs for the BMIM cation and the PF_6 anion are shown in black and green, respectively.

Particle-IL interactions significantly affected the dynamics of the ions in the solvation shell. To quantify this behavior, we measured the root mean squared deviation (RMSD) of interatomic distances between the ions of the solvation shells (see Figure 4.18) and compared them to that of ions in a nanoparticle-free IL system. RMSD is defined in equation 4.2:

$$RMSD(t) = \left[\frac{1}{N^2}\sum_{i=1}^{N}\sum_{j=1}^{N}\left\|\boldsymbol{r}_{ij}(t) - \boldsymbol{r}_{ij}(0)\right\|^2\right]^{\frac{1}{2}} \tag{4.2}$$

where N and r represent the total number of atoms and interatomic distance vectors, respectively. In MD simulations, RMSD is primarily used evaluate differences in structure between protein conformations [352-354]. Instead of a protein, we focused on the solvation shell around each nanoparticle as a separate "structure." Deviations in inter-atomic distances were calculated with respect to the conformation of the solvation shell at t = 0. Since each time step represented a new conformation, this quantity could be used to infer dynamics of the solvation shell and the approach is similar to the mean squared displacement measurement used to calculate diffusivities [355]. The difference lies in the distance measured: in our case it was the distance between two atoms, rather than between one atom and a fixed point. In this way we captured the dynamics of the nanoparticle-solvation shell complex while simultaneously accounting for nanoparticle motion through the bulk. Conclusions about the dynamic behavior of the solvation shell can be extracted in a similar way: fast changes in RMSD with respect to time indicate liquid-like behavior and slow changes indicate more solid-like behavior.

Figure 4.23 shows representative RMSDs for both ions in solvation shells around the hydrocarbon nanoparticle and the silica nanoparticle for the entire 20 ns equilibration.

Bovio and coworkers recently simulated a different IL at a flat silica surface and observed a decrease in dynamics at the solvation shell [350]. Generally, the behavior was similar in this case. Figure 4.23a shows that the BMIM cations in the pure IL had the fastest dynamics (indicated by the steeper slope of the RMSD), but solvation shell cations exhibited less diffusive behavior. Between the two solvation shells, the ions around the silica nanoparticle exhibited the slowest dynamics after reaching equilibrium, likely due to the addition of Coulombic interactions. Similarly for the PF_6 ion, solvation shell anions exhibited less diffusive behavior. However, dynamics were drastically decreased for the PF_6 anions in contact with the silica nanoparticle. The RMSD profile is nearly flat, suggesting significantly more solid-like dynamics. This result highlights, once again, the importance of Coulombic interactions and hydrogen bonding between PF_6 anions and the silanol groups on the nanoparticle surface. Such strong adsorption presents an additional IL-particle interaction that would aid in extraction.

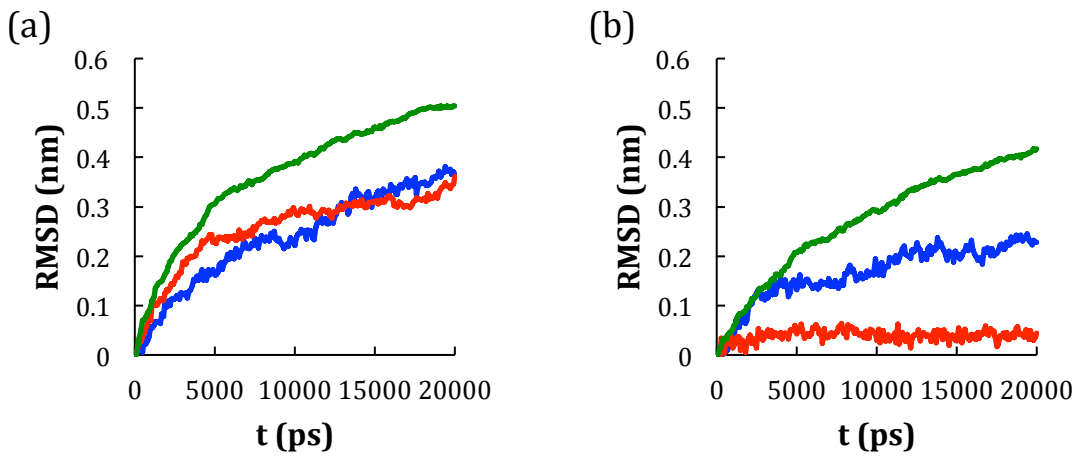

Figure 4.23 Root mean squared deviation (RMSD) of interatomic distances between BMIM cations (a) and PF_6 anions (b). RMSDs for the pure IL are shown in green while RMSDs for the solvation shell around the hydrocarbon nanoparticle and the silica nanoparticle are shown in blue and red, respectively.

Slopes of the RMSDs give an idea of the "diffusivity" of the ions in the solvation shells. The slope of each RMSD was taken by fitting a linear regression to the data from the time steady state was reached (~5 ns) to the end of the simulation. These slopes are summarized in Table 4.5 as well as the fraction of the pure IL slopes they represent. It should be noted that these slopes do not correlate to those of mean square displacement measurements used to calculate diffusivity. Nevertheless, they do provide insight into the rate of movement within the solvation shell and hence the deviation from liquid behavior. Between the two ions, the "diffusivity" of the BMIM cations was generally less affected by the nanoparticle surface. This is somewhat surprising since the cations maintained a slightly closer association with the hydrocarbon nanoparticle (See Figure 4.19a). However, the cation also possessed more orientational degrees of freedom than the anion, which may have allowed for a wider range of favorable configurations within the solvation shell. Silica nanoparticles caused the greatest decrease in dynamics, once again

highlighting the role of coulombic interactions. Particularly, we see that the slope of the PF_6 RMSD decreased by nearly an order of magnitude, which suggests a phase transition. Thus, the PF_6 anions exhibited a significant departure from liquid dynamics upon contact with the silica nanoparticle. While experimental means to measure this phenomenon may not yet be developed [350], the behavior is certainly intriguing. This response in dynamics is significant and compliments the response in structure of the IL upon extraction of nanoparticles.

Table 4.5 Comparison of RMSD slopes with respect to each ion.

System	BMIM Slope (cm/s)	% of Pure IL	PF_6 Slope (cm/s)	% of Pure IL
Silica nanoparticle Solvation Shell	0.63	42%	0.22	14%
Hydrocarbon nanoparticle Solvation Shell	1.12	75%	0.68	44%
Pure IL	1.49	100%	1.53	100%

4.4 Conclusions

We have studied the self-assembly of hydrophobic and hydrophilic nanoparticles at ionic liquid (IL)-water and IL-oil (hexane) interfaces using molecular dynamics (MD) simulations. For the [BMIM][PF_6]/water system, the hydrophobic nanoparticles rapidly approached the IL-water interface and equilibrated more into the IL phase although they were initially in the water phase. In contrast, when the nanoparticles were dispersed in the hexane phase, they slowly approached the IL-hexane interface and remained primarily in the hexane phase. Consequently, the IL-hexane interface was rather undisturbed by the nanoparticles whereas the IL-water interface changed significantly in width and morphology to accommodate the presence of the nanoparticles. Potential of mean force (PMF) calculations supported the equilibrium positions of the nanoparticles.

The effect of particle charge on self-assembly was also investigated. In the IL/water system, nanoparticles equilibrated at the interface, somewhat favoring the IL, but this preference for the IL diminished with increased nanoparticle charge. In the IL/hexane system, all charged nanoparticles interacted with the IL to some degree, whereas the uncharged nanoparticles remained primarily in the hexane phase. PMF calculations provided insight into the particle-interface interaction. In particular, these calculations may suggest that macroscopic theories underestimated the range and magnitude of the particle-interface interaction due to low interfacial tension, thus large capillary waves, of the ionic liquid based interfaces.

We also provided a computational investigation of the effect of surface chemistry in interfacial self assembly and extraction. In addition to the hydrophobic hydrocarbon-based nanoparticle studied in the first two sections, we introduced a hydrophilic silica-based nanoparticle. These nanoparticles were allowed to equilibrate at the IL/water and IL/hexane interfaces to observe how they self-assembled at the interface. At the IL/water interface, hydrocarbon-based nanoparticles were nearly completely absorbed by the IL, while the silica nanoparticles maintained equal volume in both phases. At the IL/ hexane interface, the hydrocarbon nanoparticles maintained minimal interactions with the IL whereas the silica nanoparticles were nearly completely absorbed by it. Studies of these two nanoparticles completely immersed in the IL indicate that the surface chemistry had a great affecting on the corresponding IL liquid structure. These effects include layering of the ions, hydrogen bonding, and irreversible absorption of some ions to the silica nanoparticle surface. We quantify these effects with respect to each nanoparticle. The

results suggest that ILs exhibit nanoparticle absorption capability likely because they can form solvation layers with reduced dynamics around the nanoparticles.

CHAPTER 5

FUTURE WORK

Computational Fluid Dynamics Studies of Pickering Emulsion Droplet Interactions

The MD simulations employed in this study were effective in extracting molecular phenomena that were important in particle self-assembly at IL-based interfaces. They provided a view of our systems on the smallest scale within reasonable computational resources. Furthermore, these simulations provided insight into the energetics and dynamics of particle-interface interactions that would not be attainable otherwise. This is a unique advantage of computational work. However, due to limited computational resources, only nano-scale systems could be examined. For future work, it is proposed that simulations be employed to directly study the emulsion phenomena discussed in this work at the micron scale. Since MD simulations would be too computationally expensive at this scale, a new method would need to be used. Computational fluid dynamics (CFD) is an ideal candidate since it can simulate flow phenomena at larger length scaales and exhibits flexibility in resolution. This latter characteristic allows for computational costs to be managed. Here, we specifically propose to use transient CFD simulations to analyze the bridging phenomenon reported in Chapter 3.

CFD is a method of solving the equations of continuity and motion throughout a flow field. Typically, the user draws a geometry through which fluid can flow (i.e. a cylindrical pipe) and CFD is used to determine the nature of this flow by solving these fundamental equations. These relations are commonly combined in what is called the Navier-Stokes equation (Equation 5.1 [356]), a momentum balance over a unit volume.

$$\rho\left(\frac{\partial \boldsymbol{v}}{\partial t} + \boldsymbol{v} * \nabla \boldsymbol{v}\right) = \boldsymbol{F} - \nabla p + \mu \nabla^2 \boldsymbol{v} \tag{5.1}$$

Here, ρ is the density of the fluid, t is time, **v** is the velocity vector, **F** is a body force acting on the unit volume, p is the pressure, μ is the viscosity of the fluid. While this equation has its limitations [357], it is generally suitable for our application, in which only slow-moving, incompressible fluids are studied. Equation 5.1 is a complex partial differential equation that lacks an analytical solution for most practical applications [357]. Therefore, numerical methods are used to solve this equation (hence the "computational" part of CFD) in conjunction with specified boundary conditions. In order to model flow in complex geometries, it is usually necessary to break down the geometry into smaller volumes (also called elements or cells) in which flow equations can be solved. Furthermore, using methods not described here, Equation 5.1 can be broken down into a set of ordinary differential equations for each element, resulting in a global set of equations to be solved simultaneously [358]. This is called the finite element method. It is this scheme that we propose for this future work.

While CFD is most famous for macro-scale applications, it has also seen extensive use in smaller-scale applications like the one proposed here. CFD analyses have been performed on slug flow through capillary tubes [359], droplet formation from capillary tubes [360, 361], capillary condensation [362], and bubble formation in capillary tubes [363]. Recently, simulations of the formation of emulsion droplets [364] and the dynamics nanodroplet impact [365] have been performed. To our knowledge, no computational study on the interaction between Pickering emulsion droplets has been performed. The key components necessary for this study are the capability to model

multiple phases and account for interfacial tension effects. In preliminary studies, we have employed the volume of fluid (VOF) method in commercially-obtained StarCCM+ CFD package to account for these aspects of our simulation.

The VOF method conserves the mass of all fluids in a simulation by assigning a volume fraction of each fluid to each cell [366]. The geometry cells typically have volume fractions of 1 or 0 for all fluids, except at interfaces, where intermediate values of the volume fraction can be seen. By monitoring these cells with intermediate volume fractions, the VOF model can effectively track the interfaces between immiscible fluids [366]. Interfacial tension forces are then taken into account using the continuum surface force model (CSF) [367]. In the preliminary work discussed below, only the VOF model in conjunction with the CSF model were used. While this model provides reasonable representation of the capillary forces important to our system, additional models may be necessary to capture additional interactions (i.e. particle-particle interactions).

The purpose of these preliminary studies was to evaluate how well the VOF CFD modeled the collision of two micron-sized droplets in the presence of solid particles. To do this, we prepared a flow region in the shape of a cylinder with h = 200 μm and R = 50 μm. All boundaries were specified as walls (no flow in or out). Water was used as the continuous phase with hexane as the droplet phase. The particles were assigned properties of density = 1.105 g/cm^3 and dynamic viscosity = 100 Pa*s (to approximate a solid phase thus allowing for use as particles). Due to the high curvature of the droplets at this scale, interfacial tension forces significantly influenced the stability of the simulations and time steps $\leq$ 1 μs were necessary to avoid destabilization from these forces. A few of our preliminary results are shown below.

In order to test the VOF model on simulating droplet coalescence, we placed two polystyrene droplets on opposite sides of the cylinder (using field functions to delegate the regions of each liquid) and assigned them on a collision course with velocities of 1000 μm/s. Polystyrene was chosen because surface tension effects were very small because of its high viscosity. Polystyrene is referred to as the droplet phase here only because this experiment was designed to make it coalesce. Polystyrene is referred to as the particle phase in subsequent experiments, where the intent was to have the polystyrene entities absorb to liquid-liquid interfaces. Figure 5.1 shows a time progression of this simulation as illustrated by density contours. As the droplets approached each other, the inter-droplet film of water drained out from in between them. At collision (Figure 5.1c), the interfaces of the two droplets began to unite, but it appears that some residual water was still trapped in the film, indicated by the lower density (yellow) of this region. As the droplets completed the coalescence process, this inter-droplet film condensed into a smaller droplet of water inside the polystyrene (yellow in Figure 5.1e). Therefore, we have shown that the VOF model can indeed model the coalescence of droplets. The next step was to determine if this model could account for surface tension affects that allow for particles to adhere to the liquid-liquid interface.

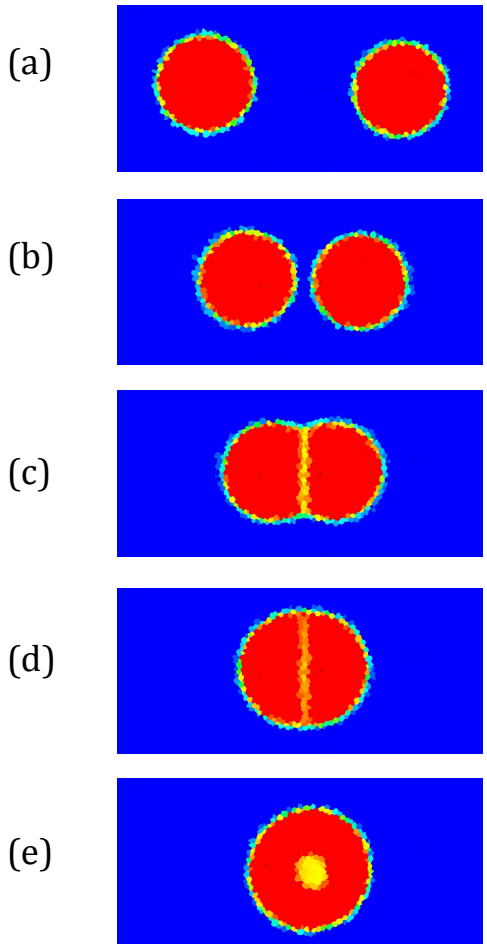

Figure 5.1 Density contours of polystyrene droplets (red) in water (blue). Time steps at (a) t = 0 μs, (b) t = 400 μs, (c) t = 700 μs, (d) t = 1800 μs, and (e) t = 8600 μs are shown.

Figure 5.2 shows the configuration formed upon allowing a polystyrene particle (R = 5 μm) to collide with a hexane droplet (R = 25 μm) in water with all interfacial tensions equal ($\gamma_{pw}=\gamma_{po}=\gamma_{ow}$, i.e. a 90^{o} contact angle for the particle). After coming in contact with the droplet surface, the particle ceased motion relative to the droplet and did not either enter the droplet or return to the water phase. These results suggested that the CSF model sufficiently captured the interfacial tension forces to reflect particle adsorption to the liquid-liquid interface. It should be noted, however, that after remaining stationary for some time, the droplet began to assume an unexpected trajectory until the

simulation was terminated. This sudden increase in droplet velocity remains unexplained, but we hypothesize that it may be due to residual errors in the calculation surface tension forces at the droplet surface, which would be magnified by the small curvature of the droplet-particle contact area. We suggest that further investigation of this issue be conducted.

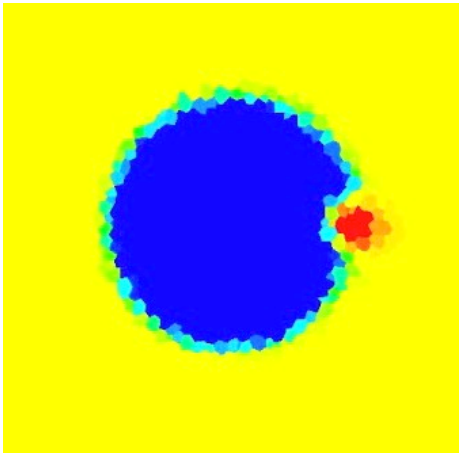

Figure 5.2 Density contour of a polystyrene particle (red) adsorbed to the surface of a hexane (blue) droplet in water (yellow).

The next step in this preliminary study was to combine these two phenomena to observe how colliding droplets interacted in the presence of particles. This was done by placing two droplets of hexane on a collision course with a velocity magnitude of 1000 μm/s. A nine-particle grid was placed between these colliding droplets. Figure 5.3 shows that this particle array effectively arrested droplet coalescence for a time by forming a bridge between them. However, since the contact angle was set to 90^{o} (all interfacial tensions were equal), the droplets eventually came into contact and coalesced. However, none of the particles were absorbed into the hexane droplet during this process, but all remained bound to the interface.

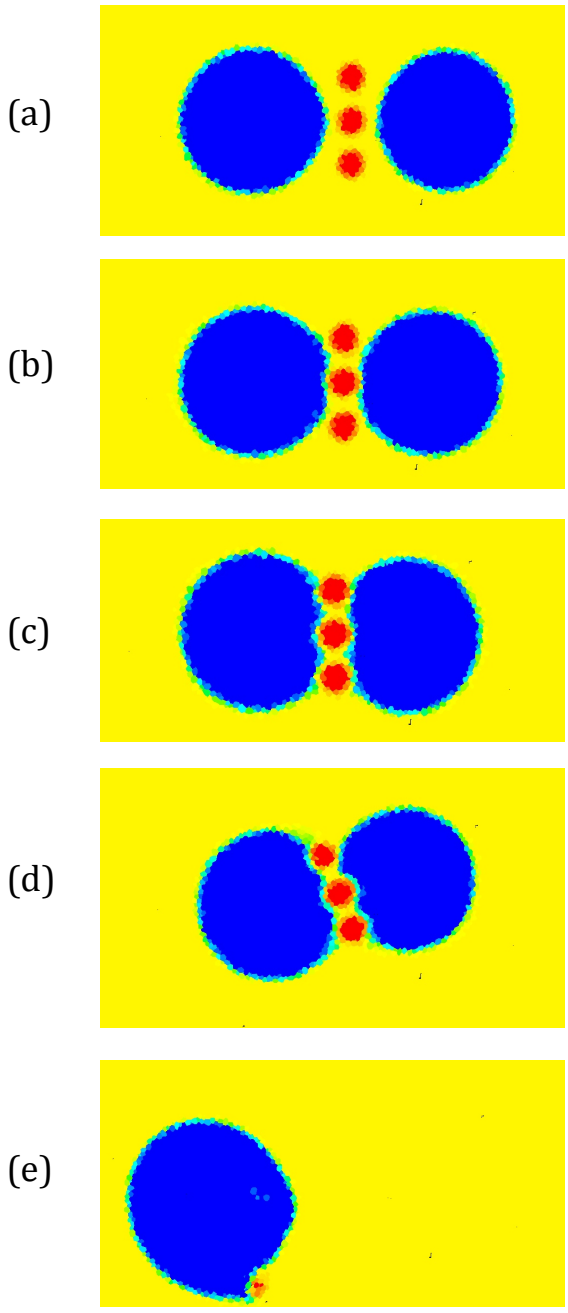

Figure 5.3 Density contours of colliding hexane (blue) droplets in water (yellow) with a grid of nine polystyrene (red) particles in between. Time steps of (a) t = 100 μs, (b) t = 700 μs, (c) t = 1400 μs, (d) t = 3400 μs, and (e) t = 8300 μs are shown.

Given this framework, we suggest that a systematic study of this phenomenon be carried out. Parameters to be studied may include particle size, droplet size, contact

angle, bulk phase viscosity, etc. It is also suggested that some inter-particle interaction term be incorporated (i.e. electrostatic or van der Waals forces), since this type of interaction played an important phenomena discussed in Chapter 3. The main goal should be to determine which conditions facilitate droplet bridging and which facilitate droplet coalescence. Since this is the first CFD simulation of Pickering emulsion droplets, the results of this study will have relevance to both conventional and non-conventional (i.e. bridging) Pickering emulsion behavior. As for external validation, it is recommended that the energy of the particle-interface interaction be calculated and compared to theoretical predictions such as Equations 2.3 and 2.4. Furthermore, inter-droplet interactions at the interface can be compared to experimental results and theoretical predictions [34]. It is hoped that this fundamental study will greatly contribute to the understanding of how Pickering emulsion droplets interact.

Droplet Bridging as a Route to the Assembly of Droplet Structures using Microfluidics

In the bridging systems discussed in Chapter 3, the fundamental novelty was that the particles consistently connected droplets together, rather that just adsorbing to their surfaces. The particles effectively behaved like strong 'droplet adhesive,' an unparalleled phenomenon in colloidal systems studied to date. In this section of future work, we suggest exploiting this unique phenomenon to assemble ordered structures of droplets. Since this is inherently difficult in free-flowing environments like those studied in Chapter 3, we suggest employing microfluidic devices to control this process at the droplet level.

Microfluidic devices consist of arrays of micron-sized fluid channels and are often associated with lab-on-a-chip applications [368]. The idea is that at small scales,

fluid flow can be manipulated with extremely high precision. This is especially true with droplet-based microfluidics, where droplet size, splitting, sorting, and coalescence can be controlled in continuous flow [368-371]. Such control provides means to produce emulsions of uniform droplet size [372], manage droplets as micro-reactors [190, 369], and even manipulate cell life functions[369]. Microfluidic devices have also been designed to control Pickering emulsion droplet coverage with high precision [373]. In this proposed work, we plan to design and implement a device to manipulate the bridging emulsions discussed in Chapter 3.

"Soft lithography," or the fabrication technique used for microfluidic devices is summarized in Figure 5.4a [371]. Effectively, the microflow channels are etched into a PDMS slab, which is then sealed to a flat substrate. An important feature of the flow channels will be some flow pattern in which droplets can be created. One popular way of accomplishing this is by creating a T-junction, at which one phase is pushed perpendicularly into a second, continuously-flowing phase [371]. A schematic of this type of flow pattern is shown in Figure 5.4b [371]. The purpose of the microfluidic device proposed here is to manually control the bridging of individual droplets to assemble droplet structures. As a preliminary design, we propose using the device schematically described in Figure 5.5 to accomplish this. In this design, PDMS (or water) droplets are created upon injection into the IL/particle dispersion phase. As droplets pass the second vertical channel, horizontal flow will be halted while the inter-droplet film is drained through this vertical channel. It is expected that as the droplets draw close to one-another in this process, they will be bridged by the dispersed particles. In this way, individual bridges may be formed manually.

(a)

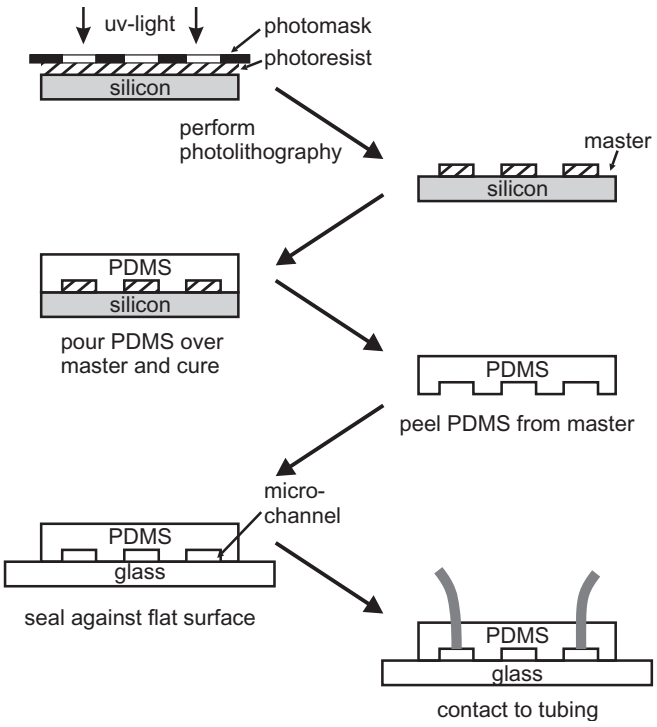

(b)

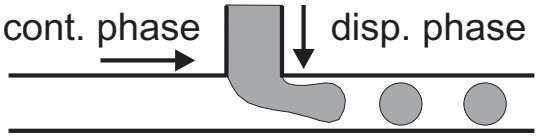

Figure 5.4 (a) Schematic of microfluidic device fabrication and (b) illustration of T-junction droplet formation in microflow. Both images were obtained from ref [371].

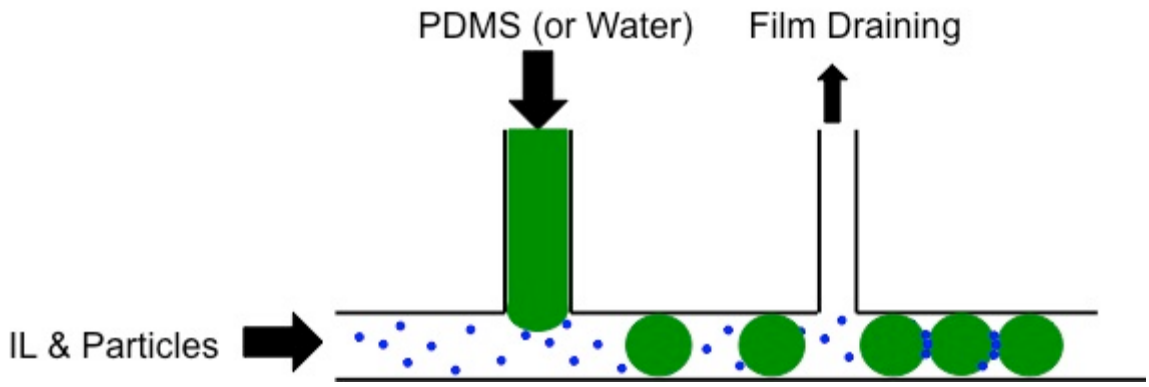

Figure 5.5 Proposed microfluidic design for the manual control of bridge formation.

Long chains of bridged droplets will likely be the first structure formed using this scheme. Future microfluidic designs may allow for the creation of rings, polyhedra, sheets, and hollow capsules (where the droplet would act as a "cell wall"). The profit of this study will be two-fold. Firstly, this scheme will allow us to examine the formation of individual bridges in real time at the microscopic level. Systematic studies using this framework will allow us to more fully extract the mechanism behind this unique phenomenon and determine what role the IL-particle interaction plays. Particularly, we will have the capability of viewing the trajectory of the particles as the droplets to be bridged approach one another. Secondly, colloidal particle interactions are emerging as excellent prototypes for studying chemical kinetics [374]. Dr. Granick's group has shown that colloidal particles can be functionalized to interact much as molecular species do, with the advantage that their interactions can be observed in real time microscopy [374]. In this sense, droplet bridging is analogous to the formation of a chemical bond, where the droplets represent individual atoms. We anticipate that the effect of parameters such as particle concentration and flow rate on the kinetics of bridging could be easily

visualized in a well-controlled microfluidic device. This framework may be particularly well-suited for approximating polymerization kinetics, where the occurrence of branching and crosslinking could be simulated. Clearly, these studies will require more advanced devices than the one proposed in Figure 5.5, but the results and accompanying visualizations are anticipated to provide unprecedented and exciting insight these colloidal (and, by extension, molecular) processes.

Characterization of IL Mixing Properties using Differential Scanning Calorimetry

As a consequence of studying IL-based interfaces, the subject of IL-IL mixing has surfaced occasionally in conjunction with new phenomena. In section 3.3.1 we observed how EAN and [BMIM][PF_6] maintained an interface for long periods of time despite being mutually miscible. MD simulations suggested that this was a result of positive excess entropy. In Appendix B, mixtures of [BMIM][PF_6] and [P_{66614}][Phos] spontaneously and reversible formed a viscoelastic gel in the presence of small amounts of water. We predict that thermodynamic understanding of these mixtures would provide significant insight into their unique behaviors. Currently, the study of mixing properties of ILs is just beginning to emerge. Arce et al. studied mixtures of [P_{66614}][Cl] and 1-alkyl-3-methylimidazoium chloride ILs using H NMR spectroscopy and found that a highly negative entropy of mixing caused them to be "mutually immiscible[215, 216]." Navia et al. investigated the excess enthalpy of mixing imidazolium ILs with a common cation [375] and Annat et al. recently investigated various mixtures of five of ILs in terms of molar conductivity, viscosity, and excess molar volume [376]. Most of these studies focus on small sets of ILs and fewer analyze the thermodynamic properties that determine miscibility, enthalpy and entropy of mixing. For this reason, we propose to

experimentally measure thermodynamic properties of mixing using the large array of ILs (See Table 3.1) discussed in this dissertation.

We propose a new technique for extracting the excess enthalpy of mixing. Differential scanning calorimetry measures the heat flow into a sample subject to manipulation in temperature. By measuring the heat flow during a ramp in temperature, the heat capacity of a sample can be determined via Equation 5.2

$$C_P = \frac{Q}{\beta} \tag{5.2}$$

where C_P is the heat capacity, Q is the heat flow, and β is the temperature ramp rate. By measuring the heat capacity of two ILs as well as their mixture, the excess enthalpy of mixing can be determined in the following manner. Given that H is the enthalpy of the mixture and H_1 and H_2 are the respective enthalpies of the IL components, the enthalpy of mixing can be written as

$$H = H_1 + H_2 + H^E \tag{5.3}$$

where H^E is the excess enthalpy of mixing. If the mixing were ideal, this quantity would be equal to zero. Taking the temperature (T) derivative of Equation 5.3 gives Equations 5.4 and 5.5.

$$\frac{dH}{dT} = \frac{dH_1}{dT} + \frac{dH_2}{dT} + \frac{dH^E}{dT} \tag{5.4}$$

$$C_p = C_{p,1} + C_{p,2} + {C_p}^E \tag{5.5}$$

Using DSC, the C_P, C_{P1}, and C_{P2} can be experimentally measured over a range of temperatures. Rearranging Equation 5.5 gives an explicit expression for ${C_P}^E$ (Equation 5.6), which can be integrated over an arbitrary temperature range to give an expression for H^E (Equation 5.7).

$$C_p{}^E = C_p - C_{p,1} - C_{p,2} \tag{5.6}$$

$$H^E = \int_{T1}^{T2} (C_p - C_{p,1} - C_{p,2}) dT \tag{5.7}$$

Therefore, using the heat capacity data and Equation 5.7, the excess enthalpy for a mixture of ILs may be calculated. This method is proposed as an alternative to another published method [377] with requires mixing to be performed in the DSC, which is inherently problematic.

It is suggested that a systematic study of the excess enthalpy of mixing be conducted for the ILs shown in Table 3.1. Efforts should be made to correlate these findings with molecular structure and behavior. Ideally, MD simulations would supplement these experimental measurements, but force field generation for all of the ILs in question may require large computational and time resources. In addition to the valuable data, this methodology represents a new technique for measuring thermodynamic mixing properties in general. We suggest a thorough investigation of the accuracy of this method as well as theoretical study as to how entropies of mixing may be also calculated from the data.

REFERENCES

[1] Simovic, S.; Ghouchi-Eskandar, N.; Prestidge, C., Pickering Emulsions for Dermal Delivery. *J Drug Delivery Sci Technol.* 21 (2011) 123-133.

[2] Faria, J.; Ruiz, M. P.; Resasco, D. E., Phase-Selective Catalysis in Emulsions Stabilized by Janus Silica Nanoparticles. *Adv Synth Catal.* 352 (2010) 2359-2364.

[3] Crossley, S.; Faria, J.; Shen, M.; Resasco, D. E., Solid Nanoparticles that Catalyze Biofuel Upgrade Reactions at the Water/Oil Interface. *Science.* 327 (2010) 68-72.

[4] Dickinson, E., Use of Nanoparticles and Microparticles in the Formation and Stabilization of Food Emulsions. *Trends Food Sci Technol.* 24 (2012) 4-12.

[5] Dickinson, E., Food Emulsions and Foams: Stabilization by Particles. *Curr Opin Colloid Interface Sci.* 15 (2010) 40-49.

[6] Ramsden, W., Separation of Solids in the Surface-Layers of Solutions and 'Suspensions'. *Proc R Soc London.* 72 (1903) 156-164.

[7] Pickering, S. U., Emulsions. *J Chem Soc Trans.* 91 (1907) 2001.

[8] Binks, B. P., Horozov, T. S., Colloidal Particles at Liquid Interfaces, Cambridge University Press, Cambridge; New York, 2006.

[9] Koretsky, A. F.; Kruglyakov, P. M., *Izv Sib Otd Akad Nauk USSR.* 2 (1971) 139.

[10] Tadros, T. F., Vincent, B., Emulsion Stability in The Encyclopedia of Emulsion Technology: Basic Theory P. Becher (Ed.), Marcel Dekker, New York, 1983, p. 129.

[11] Levine, S.; Bowen, B. D.; Partridge, S. J., Stabilization of Emulsions by Fine Particles I. Partitioning of Particles between Continuous Phase and Oil/Water Interface. *Colloids Surf.* 38 (1989) 325-343.

[12] Binks, B. P., Particles as Surfactants--Similarities and Differences. *Curr Opin Colloid Interface Sci.* 7 (2002) 21-41.

[13] Denkov, N. D.; Ivanov, I. B.; Kralchevsky, P. A.; Wasan, D. T., A Possible Mechanism of Stabilization of Emulsions by Solid Particles. *J Colloid Interface Sci.* 150 (1992) 589-593.

[14] Binks, B. P.; Lumsdon, S. O., Influence of Particle Wettability on the Type and Stability of Surfactant-Free Emulsions. *Langmuir.* 16 (2000) 8622-8631.

[15] Pieranski, P., Two-Dimensional Interfacial Colloidal Crystals. *Phys Rev Lett.* 45 (1980) 569-572.

[16] Amirfazli, A.; Neumann, A. W., Status of the Three-Phase Line Tension: A Review. *Adv Colloid Interface Sci.* 110 (2004) 121-141.

[17] Aveyard, R.; Clint, J. H.; Horozov, T. S., Aspects of the Stabilisation of Emulsions by Solid Particles: Effects of Line Tension and Monolayer Curvature Energy. *Phys Chem Chem Phys.* 5 (2003) 2398-2409.

[18] Lehle, H.; Oettel, M., Stability and Interactions of Nanocolloids at Fluid Interfaces: Effects of Capillary Waves and Line Tensions. *J Phys Condens Matter.* 20 (2008) 404224.

[19] Cheung, D., Molecular Dynamics Study of Nanoparticle Stability at Liquid Interfaces: Effect of Nanoparticle-Solvent Interaction and Capillary Waves. *J Chem Phys.* 135 (2011) 054704.

[20] S. Komura; Y. Hirose; Y. Nonomura, Adsorption of Colloidal Particles to Curved Interfaces. *J Chem Phys.* 124 (2006) 241104.

[21] Nonomura, Y.; Komura, S.; Tsujii, K., Surface-Active Particles with Microstructured Surfaces. *Langmuir.* 21 (2005) 9409-9411.

[22] Nonomura, Y.; Komura, S.; Tsujii, K., Adsorption of Microstructured Particles at Liquid-Liquid Interfaces. *J Phys Chem B.* 110 (2006) 13124-13129.

[23] Bresme, F.; Oettel, M., Nanoparticles at Fluid Interfaces. *J Phys Condens Matter.* 19 (2007) 413101.

[24] Tarimala, S.; Dai, L. L., Structure of Microparticles in Solid-Stabilized Emulsions. *Langmuir.* 20 (2004) 3492-3494.

[25] Dai, L. L.; Sharma, R.; Wu, C., Self-Assembled Structure of Nanoparticles at a Liquid-Liquid Interface. *Langmuir.* 21 (2005) 2641-2643.

[26] Binks, B. P.; Dyab, A. K. F.; Fletcher, P. D. I., Contact Angles in Relation to Emulsions Stabilised Solely by Silica Nanoparticles Including Systems Containing Room Temperature Ionic Liquids. *Phys Chem Chem Phys.* 9 (2007) 6391-6397.

[27] Cheung, D. L.; Bon, S. A. F., Interaction of Nanoparticles with Ideal Liquid-Liquid Interfaces. *Phys Rev Lett.* 102 (2009) 066103.

[28] Glaser, N.; Adams, D. J.; Böker, A.; Krausch, G., Janus Particles at Liquid-Liquid Interfaces. *Langmuir.* 22 (2006) 5227-5229.

[29] Walther, A.; Muller, A., Janus Particles. *Soft Matter.* 4 (2008) 663-668.

[30] Y. Hirose; S. Komura; Y. Nonomura, Adsorption of Janus Particles to Curved Interfaces. *J Chem Phys.* 127 (2007) 054707.

[31] Saigal, T.; Dong, H.; Matyjaszewski, K.; Tilton, R. D., Pickering Emulsions Stabilized by Nanoparticles with Thermally Responsive Grafted Polymer Brushes. *Langmuir.* 26 (2010) 15200-15209.

[32] Fredandez-Toledano, J. C., Moncho-Jorda, A., Martinez-Lopez, F., Hidalgo-Alvarez, R., Theory for Interactions between Particles in Monolayers in Colloidal Particles at Liquid Interfaces B.P. Binks (Ed.), Cambridge University Press, United Kingdom, 2006, p. 108.

[33] Aveyard, R.; Binks, B. P.; Clint, J. H.; Fletcher, P. D. I.; Horozov, T. S.; Neumann, B.; Paunov, V. N.; Annesley, J.; Botchway, S. W.; Nees, D.; Parker, A. W.; Ward, A. D.; Burgess, A. N., Measurement of Long-Range Repulsive Forces between Charged Particles at an Oil-Water Interface. *Phys Rev Lett.* 88 (2002) 246102.

[34] Ma, H.; Dai, L. L., Structure of Multi-Component Colloidal Lattices at Oil-Water Interfaces. *Langmuir.* 25 (2009) 11210-11215.

[35] Hamaker, H. C., The London—van Der Waals Attraction between Spherical Particles. *Physica.* 4 (1937) 1058-1072.

[36] Williams, D. F.; Berg, J. C., The Aggregation of Colloidal Particles at the Air—water Interface. *J Colloid Interface Sci.* 152 (1992) 218-229.

[37] N. Patel; S. A. Egorov, Interactions between Sterically Stabilized Nanoparticles in Supercritical Fluids: A Simulation Study. *J Chem Phys.* 126 (2007) 054706.

[38] Kralchevsky, P. A.; Nagayama, K., Capillary Interactions between Particles Bound to Interfaces, Liquid Films and Biomembranes. *Adv Colloid Interface Sci.* 85 (2000) 145-192.

[39] Bowden, N.; Choi, I. S.; Grzybowski, B. A.; Whitesides, G. M., Mesoscale Self-Assembly of Hexagonal Plates using Lateral Capillary Forces: Synthesis using the Capillary Bond. *J Am Chem Soc.* 121 (1999) 5373-5391.

[40] Bowden, N.; Arias, F.; Deng, T.; Whitesides, G. M., Self-Assembly of Microscale Objects at a Liquid/Liquid Interface through Lateral Capillary Forces. *Langmuir.* 17 (2001) 1757-1765.

[41] Bowden, N.; Oliver, S. R. J.; Whitesides, G. M., Mesoscale Self-Assembly: Capillary Bonds and Negative Menisci. *J Phys Chem B.* 104 (2000) 2714-2724.

[42] Horozov, T. S.; Binks, B. P., Particle-Stabilized Emulsions: A Bilayer Or a Bridging Monolayer? *Angew Chem Int Ed.* 45 (2006) 773-776.

[43] Horozov, T. S.; Aveyard, R.; Clint, J. H.; Neumann, B., Particle Zips: Vertical Emulsion Films with Particle Monolayers at their Surfaces. *Langmuir.* 21 (2005) 2330-2341.

[44] Xu, H.; Kirkwood, J.; Lask, M.; Fuller, G., Charge Interaction between Particle-Laden Fluid Interfaces. *Langmuir.* 26 (2010) 3160-3164.

[45] Xu, H.; Lask, M.; Kirkwood, J.; Fuller, G., Particle Bridging between Oil and Water Interfaces. *Langmuir.* 23 (2007) 4837-4841.

[46] Stancik, E. J.; Fuller, G. G., Connect the Drops: Using Solids as Adhesives for Liquids. *Langmuir.* 20 (2004) 4805-4808.

[47] Stancik, E. J.; Kouhkan, M.; Fuller, G. G., Coalescence of Particle-Laden Fluid Interfaces. *Langmuir.* 20 (2004) 90-94.

[48] Lehle, H.; Oettel, M., Importance of Boundary Conditions for Fluctuation-Induced Forces between Colloids at Interfaces. *Phys Rev E.* 75 (2007) 011602.

[49] Lehle, H.; Oettel, M.; Dietrich, S., Effective Forces between Colloids at Interfaces Induced by Capillary Wavelike Fluctuations. *Europhys Lett.* 75 (2006) 174-180.

[50] Betancourt, O. J.; McLean, A. Y., Changes in Chemical Composition and Physical Properties of a Heavy Residual Oil Weathering Under Natural Conditions. *J Inst Pet.* 59 (1973) 223-230.

[51] Mackay, G. D. M.; McLean, A. Y.; Betancourt, O. J.; Johnson, B. D., Formation of Water-in-Oil Emulsions Subsequent to an Oil Spill. *J Inst Pet.* 59 (1973) 164-172.

[52] Chieu, J. N.; Gloyna, E. F.; Schechter, R. S., Coalescence of Emulsified Oily Wastewater by Fibrous Beds. *Proc Indus Waste Conf.* 30 (1977) 611-620.

[53] Van Boekel, M. A. J. S.; Walstra, P., Stability of Oil-in-Water Emulsions with Crystals in the Disperse Phase. *Colloids Surf.* 3 (1981) 109-118.

[54] Corcorran, S.; Lochhead, R. Y.; McKay, T., Particle-Stabilized Emulsions: A Brief Overview. *Cosmetics and Toiletries.* 119 (2004) 47-50.

[55] Stiller, S.; Gers-Barlag, H.; Lergenmueller, M.; Pflücker, F.; Schulz, J.; Wittern, K. P.; Daniels, R., Investigation of the Stability in Emulsions Stabilized with Different Surface Modified Titanium Dioxides. *Colloids Surf A.* 232 (2004) 261-267.

[56] Jaynes, E. N., Applications in Food Industry II in Encyclopedia of Emulsion Technology P. Becher (Ed.), Marcel Dekker, New York, 1983, p. 367.

[57] Melle, S.; Lask, M.; Fuller, G. G., Pickering Emulsions with Controllable Stability. *Langmuir.* 21 (2005) 2158-2162.

[58] Velev, O.; Furusawa, K.; Nagayama, K., Assembly of Latex Particles by using Emulsion Droplets as Templates .1. Microstructured Hollow Spheres. *Langmuir.* 12 (1996) 2374-2384.

[59] Dinsmore, A. D.; Hsu, M. F.; Nikolaides, M. G.; Marquez, M.; Bausch, A. R.; Weitz, D. A., Colloidosomes: Selectively Permeable Capsules Composed of Colloidal Particles. *Science.* 298 (2002) pp. 1006-1009.

[60] Voorn, D.; Ming, W.; van Herk, A., Polymer-Clay Nanocomposite Latex Particles by Inverse Pickering Emulsion Polymerization Stabilized with Hydrophobic Montmorillonite Platelets. *Macromolecules.* 39 (2006) 2137-2143.

[61] He, Y., Preparation of Polyaniline/Nano-ZnO Composites Via a Novel Pickering Emulsion Route. *Powder Technol.* 147 (2004) 59-63.

[62] Sanyal, S.; Huang, H.; Rege, K.; Dai, L. L., Thermo-Responsive Core-Shell Composite Nanoparticles Synthesized Via One-Step Pickering Emulsion Polymerization for Controlled Drug Delivery. *J Nanomedic Nanotechnol.* 2 (2011) 126.

[63] Ma, H.; Luo, M.; Sanyal, S.; Rege, K.; Dai, L., The One-Step Pickering Emulsion Polymerization Route for Synthesizing Organic-Inorganic Nanocomposite Particles. *Materials.* 3 (2010) 1186-1202.

[64] Cates, M. E.; Clegg, P. S., Bijels: A New Class of Soft Materials. *Soft Matter.* 4 (2008) 2132-2138.

[65] Niu, Z.; He, J.; Russell, T. P.; Wang, Q., Synthesis of Nano/Microstructures at Fluid Interfaces. *Angew Chem Int Ed.* 49 (2010) 10052-10066.

[66] Binks, B. P., Applications of Emulsions in Modern Aspects of Emulsion Science B.P. Binks (Ed.), Royal Chemistry Society, Cambridge, 1998, p. 395.

[67] Velev, O.; Furusawa, K.; Nagayama, K., Assembly of Latex Particles by using Emulsion Droplets as Templates .2. Ball-Like and Composite Aggregates. *Langmuir.* 12 (1996) 2385-2391.

[68] Velev, O. D.; Nagayama, K., Assembly of Latex Particles by using Emulsion Droplets. 3. Reverse (Water in Oil) System. *Langmuir.* 13 (1997) 1856-1859.

[69] Hsu, M. F.; Nikolaides, M. G.; Dinsmore, A. D.; Bausch, A. R.; Gordon, V. D.; Chen, X.; Hutchinson, J. W.; Weitz, D. A.; Marquez, M., Self-Assembled Shells Composed of Colloidal Particles: Fabrication and Characterization. *Langmuir.* 21 (2005) 2963-2970.

[70] Cayre, O.; Noble, P.; Paunov, V., Fabrication of Novel Colloidosome Microcapsules with Gelled Aqueous Cores. *J Mater Chem.* 14 (2004) 3351-3355.

[71] Noble, P. F.; Cayre, O. J.; Alargova, R. G.; Velev, O. D.; Paunov, V. N., Fabrication of "Hairy" Colloidosomes with Shells of Polymeric Microrods. *J Am Chem Soc.* 126 (2004) 8092-8093.

[72] Subramaniam, A. B.; Abkarian, M.; Stone, H. A., Controlled Assembly of Jammed Colloidal Shells on Fluid Droplets. *Nat Mater.* 4 (2005) 553-556.

[73] Gordon, V. D.; Chen, X.; Hutchinson, J. W.; Bausch, A. R.; Marquez, M.; Weitz, D. A., Self-Assembled Polymer Membrane Capsules Inflated by Osmotic Pressure. *J Am Chem Soc.* 126 (2004) 14117-14122.

[74] He, X. D.; Ge, X. W.; Liu, H. R.; Deng, M. G.; Zhang, Z. C., Self-Assembly of pH-Responsive Acrylate Latex Particles at Emulsion Droplets Interface. *J Appl Polym Sci.* 105 (2007) 1018-1024.

[75] Bon, S. A. F.; Mookhoek, S. D.; Colver, P. J.; Fischer, H. R.; van der Zwaag, S., Route to Stable Non-Spherical Emulsion Droplets. *Eur Poly.* 43 (2007) 4839-4842.

[76] Pawar, A. B.; Caggioni, M.; Ergun, R.; Hartel, R. W.; Spicer, P. T., Arrested Coalescence in Pickering Emulsions. *Soft Matter.* 7 (2011) 7710-7716.

[77] Lin, Y.; Skaff, H.; Emrick, T.; Dinsmore, A. D.; Russell, T. P., Nanoparticle Assembly and Transport at Liquid-Liquid Interfaces. *Science.* 299 (2003) pp. 226-229.

[78] Lin, Y.; Böker, A.; Skaff, H.; Cookson, D.; Dinsmore, A. D.; Emrick, T.; Russell, T. P., Nanoparticle Assembly at Fluid Interfaces: Structure and Dynamics. *Langmuir.* 21 (2005) 191-194.

[79] Lin, Y.; Skaff, H.; BÃ¶ker, A.; Dinsmore, A. D.; Emrick, T.; Russell, T. P., Ultrathin Cross-Linked Nanoparticle Membranes. *J Am Chem Soc.* 125 (2003) 12690-12691.

[80] Duan, H.; Wang, D.; Kurth, D. G.; Möhwald, H., Directing Self-Assembly of Nanoparticles at Water/Oil Interfaces. *Angew Chem Int Ed.* 43 (2004) 5639-5642.

[81] Wang, D.; Duan, H.; Mohwald, H., The Water/Oil Interface: The Emerging Horizon for Self-Assembly of Nanoparticles. *Soft Matter.* 1 (2005) 412-416.

[82] Duan, H.; Wang, D.; Sobal, N. S.; Giersig, M.; Kurth, D. G.; Möhwald, H., Magnetic Colloidosomes Derived from Nanoparticle Interfacial Self-Assembly. *Nano letters.* 5 (2005) 949-952.

[83] Simovic, S.; Prestidge, C., Adsorption of Hydrophobic Silica Nanoparticles at the PDMS Droplet-Water Interface. *Langmuir.* 19 (2003) 8364-8370.

[84] Simovic, S.; Prestidge, C., Hydrophilic Silica Nanoparticles at the PDMS Droplet-Water Interface. *Langmuir.* 19 (2003) 3785-3792.

[85] Simovic, S.; Prestidge, C. A., Nanoparticles of Varying Hydrophobicity at the Emulsion Droplet-Water Interface: Adsorption and Coalescence Stability. *Langmuir.* 20 (2004) 8357-8365.

[86] Russell, J. T.; Lin, Y.; Böker, A.; Su, L.; Carl, P.; Zettl, H.; He, J.; Sill, K.; Tangirala, R.; Emrick, T.; Littrell, K.; Thiyagarajan, P.; Cookson, D.; Fery, A.; Wang, Q.; Russell, T. P., Self-Assembly and Cross-Linking of Bionanoparticles at Liquid-Liquid Interfaces. *Angew Chem Int Ed.* 44 (2005) 2420-2426.

[87] Wang, H.; Hobbie, E., Amphiphobic Carbon Nanotubes as Macroemulsion Surfactants. *Langmuir.* 19 (2003) 3091-3093.

[88] Lee, K. Y.; Kim, M.; Hahn, J.; Suh, J. S.; Lee, I.; Kim, K.; Han, S. W., Assembly of Metal Nanoparticle-Carbon Nanotube Composite Materials at the Liquid/Liquid Interface. *Langmuir.* 22 (2006) 1817-1821.

[89] Yui, H.; Sawada, D.; Kamiya, S.; Sawada, T.; Shimizu, T., Self-Assembly and Subsequent Accumulation of Lipid Nanotubes at Oil/Water Interfaces. *Anal Sci.* 20 (2004) 1549-1552.

[90] Shi, N.; Yin, G.; Han, M.; Xu, Z.; Fan, X.; Li, H.; Hong, J., Coordination Driving Self-Assembly of Gold Nanoparticles and Tetrapyridylporphine into Hollow Spheres. *Chem Lett.* 34 (2005) 1468-1469.

[91] Böker, A.; Lin, Y.; Chiapperini, K.; Horowitz, R.; Thompson, M.; Carreon, V.; Xu, T.; Abetz, C.; Skaff, H., Hierarchical Nanoparticle Assemblies Formed by Decorating Breath Figures. *Nat Mater.* 3 (2004) 302-306.

[92] Gu, H.; Yang, Z.; Gao, J.; Chang, C. K.; Xu, B., Heterodimers of Nanoparticles: Formation at a Liquid-Liquid Interface and Particle-Specific Surface Modification by Functional Molecules. *J Am Chem Soc.* 127 (2005) 34-35.

[93] Kaur, G.; He, J.; Xu, J.; Pingali, S.; Jutz, G.; BoÌˆker, A.; Niu, Z.; Li, T.; Rawlinson, D.; Emrick, T.; Lee, B.; Thiyagarajan, P.; Russell, T. P.; Wang, Q., Interfacial Assembly of Turnip Yellow Mosaic Virus Nanoparticles. *Langmuir.* 25 (2009) 5168-5176.

[94] Rong, J.; Niu, Z.; Lee, L.; Wang, Q., Self-Assembly of Viral Particles. *Curr Opin Colloid Interface Sci.* 16 (2011) 441-450.

[95] Li, T.; Niu, Z.; Emrick, T.; Russell, T. P.; Wang, Q., Core/Shell Biocomposites from the Hierarchical Assembly of Bionanoparticles and Polymer. *Small.* 4 (2008) 1624-1629.

[96] Li, T.; Ye, B.; Niu, Z.; Thompson, P.; Seifert, S.; Lee, B.; Wang, Q., Closed-Packed Colloidal Assemblies from Icosahedral Plant Virus and Polymer. *Chem Mater.* 21 (2009) 1046-1050.

[97] Li, T.; Wu, L.; Suthiwangcharoen, N.; Bruckman, M.; Cash, D.; Hudson, J.; Ghoshroy, S.; Wang, Q., Controlled Assembly of Rodlike Viruses with Polymers. *Chem Commun.* (2009) 2869-2871.

[98] Chum, H. L.; Koch, V. R.; Miller, L. L.; Osteryoung, R. A., Electrochemical Scrutiny of Organometallic Iron Complexes and Hexamethylbenzene in a Room Temperature Molten Salt. *J Am Chem Soc.* 97 (1975) 3264-3265.

[99] Walden, P., Molecular Weights and Electrical Conductivity of several Fused Salts. *Bull Acad Imper Sci.* 8 (1914) 405-422.

[100] Plechkova, N. V.; Seddon, K. R., Applications of Ionic Liquids in the Chemical Industry. *Chem Soc Rev.* 37 (2008) 123-150.

[101] Hayes, R.; Warr, G. G.; Atkin, R., At the Interface: Solvation and Designing Ionic Liquids. *Phys Chem Chem Phys.* 12 (2010) 1709-1723.

[102] Hurley, F. H.; Wier, T. P., Electrodeposition of Metals from Fused Quaternary Ammonium Salts. *J Electrochem Soc.* 98 (1951) 203-206.

[103] Gale, R. J.; Gilbert, B.; Osteryoung, R. A., Raman Spectra of Molten Aluminum Chloride: 1-Butylpyridinium Chloride Systems at Ambient Temperatures. *Inorg Chem.* 17 (1978) 2728-2729.

[104] Wilkes, J. S.; Zaworotko, M. J., Air and Water Stable 1-Ethyl-3-Methylimidazolium Based Ionic Liquids. *J Chem Soc , Chem Commun.* (1992) 965-967.

[105] Seddon, K. R., Ionic Liquids: Designer Solvents?in Proceedings of the International George Papatheodorou Symposium S. Boghosian, V. Dracopoulos, C.G. Kontoyannis, G.A. Voyiatzis (Eds.), Institute of Chemical Engineering and High Temperature Processes, Patras, 1999, p. 131.

[106] Stark, A., Seddon, K. R., Ionic Liquids in Kirk-Othmer Encyclopedia of Chemical Technology, 5th Edition A. Seidel (Ed.), John Wiley & Sons, Inc., Hoboken, New Jersey, 2007, p. 836.

[107] Aparicio, S.; Atilhan, M.; Karadas, F., Thermophysical Properties of Pure Ionic Liquids: Review of Present Situation. *Ind Eng Chem Res.* 49 (2010) 9580-9595.

[108] Brennecke, J. F.; Maginn, E. J., Ionic Liquids: Innovative Fluids for Chemical Processing. *AIChE J.* 47 (2001) 2384-2389.

[109] The American Chemical Society, Obtained using Scifinder, Chemical Abstracts Service. .

[110] Welton, T., Room-Temperature Ionic Liquids. Solvents for Synthesis and Catalysis. *Chem Rev.* 99 (1999) 2071-2084.

[111] McNaught, A. D., Wilkinson, A., IUPAC. Compendium of Chemical Terminology, 2nd Ed. (the "Gold Book"), Blackwell Scientific Publications, Oxford, 1997.

[112] Fuller, J.; Carlin, R. T.; De Long, H. C.; Haworth, D., Structure of 1-Ethyl-3-Methylimidazolium Hexafluorophosphate: Model for Room Temperature Molten Salts. *J Chem Soc , Chem Commun.* (1994) 299-300.

[113] Chauvin, Y.; Mussmann, L.; Olivier, H., A Novel Class of Versatile Solvents for Two-Phase Catalysis: Hydrogenation, Isomerization, and Hydroformylation of Alkenes Catalyzed by Rhodium Complexes in Liquid 1,3-Dialkylimidazolium Salts. *Angew Chem Int Ed.* 34 (1996) 2698-2700.

[114] Wakeham, D.; Hayes, R.; Warr, G. G.; Atkin, R., Influence of Temperature and Molecular Structure on Ionic Liquid Solvation Layers. *J Phys Chem B.* 113 (2009) 5961-5966.

[115] Hallett, J. P.; Welton, T., Room-Temperature Ionic Liquids: Solvents for Synthesis and Catalysis. 2. *Chem Rev.* 111 (2011) 3508-3576.

[116] Joglekar, H. G.; Rahman, I.; Kulkarni, B. D., The Path Ahead for Ionic Liquids. *Chem Eng Technol.* 30 (2007) 819-828.

[117] Brennecke, J. F., Blanchard, L. A., Anthony, J. L., Zhiyong, G., Isidro, Z., Leighton, D. T., Separation of Species from Ionic Liquids in Clean Solvents M.A. Abraham, L. Moens (Eds.), American Chemical Society, United States of America, 2002, p. 82.

[118] National Institute of Standards and Technology. Ionic Liquids Database- (IL Thermo) NIST Standard Reference Database #147. Updated: 2010, Accessed: 04/01/2012. URL: http://ilthermo.boulder.nist.gov/ILThermo/mainmenu.uix.

[119] Bonhote, P.; Dias, A.; Papageorgiou, N.; Kalyanasundaram, K.; Gratzel, M., Hydrophobic, Highly Conductive Ambient-Temperature Molten Salts. *Inorg Chem.* 35 (1996) 1168-1178.

[120] Marsh, K. N.; Boxall, J. A.; Lichtenthaler, R., Room Temperature Ionic Liquids and their Mixtures—a Review. *Fluid Phase Equilib.* 219 (2004) 93-98.

[121] Earle, M. J.; Esperanca, J. M. S. S.; Gilea, M. A.; Lopes, J. N. C.; Rebelo, L. P. N.; Magee, J. W.; Seddon, K. R.; Widegren, J. A., The Distillation and Volatility of Ionic Liquids. *Nature.* 439 (2006) 831-834.

[122] Leal, J. P.; Esperanca, Jose M. S. S.; Minas, d. P.; Canongia Lopes, J. N.; Rebelo, L. P. N.; Seddon, K. R., The Nature of Ionic Liquids in the Gas Phase. *J Phys Chem A.* 111 (2007) 6176-6182.

[123] Holbrey, J. D.; Seddon, K. R., The Phase Behaviour of 1-Alkyl-3-Methylimidazolium Tetrafluoroborate; Ionic Liquids and Ionic Crystals. *J Chem Soc , Dalton trans.* (1999) 2133.

[124] Seddon, K. R., Room-Temperature Ionic Liquids: Neoteric Solvents for Clean Catalysis. *Kinet Catal.* 37 (1996) 693-697.

[125] Huddleston, J. G.; Visser, A. E.; Reichert, W. M.; Willauer, H. D.; Broker, G. A.; Rogers, R. D., Characterization and Comparison of Hydrophilic and Hydrophobic Room Temperature Ionic Liquids Incorporating the Imidazolium Cation. *Green Chem.* 3 (2001) 156-164.

[126] Swatloski, R. P.; Holbrey, J. D.; Rogers, R. D., Ionic Liquids are Not always Green: Hydrolysis of 1-Butyl-3-Methylimidazolium Hexafluorophosphate. *Green Chem.* 5 (2003) 361-363.

[127] Seddon, K. R.; Stark, A.; Torres, M. J., Influence of Chloride, Water, and Organic Solvents on the Physical Properties of Ionic Liquids. *Pure Appl Chem.* 72 (2000) 2275-2287.

[128] Chaumont, A.; Schurhammer, R.; Wipff, G., Aqueous Interfaces with Hydrophobic Room-Temperature Ionic Liquids: A Molecular Dynamics Study. *J Phys Chem B.* 109 (2005) 18964-18973.

[129] Li, H.; Ibrahim, M.; Agberemi, I.; Kobrak, M. N., The Relationship between Ionic Structure and Viscosity in Room-Temperature Ionic Liquids. *J Chem Phys.* 129 (2008) 124507.

[130] Klincewicz, K. M.; Reid, R. C., Estimation of Critical Properties with Group Contribution Methods. *AIChE J.* 30 (1984) 137-142.

[131] Joback, K. K.; Reid, R., Estimation of Pure Component Properties from Group Contribution. *Chem Eng Comm.* 57 (1987) 233-247.

[132] Valderrama, J. O.; Robles, P. A., Critical Properties, Normal Boiling Temperatures, and Acentric Factors of Fifty Ionic Liquids. *Ind Eng Chem Res.* 46 (2007) 1338-1344.

[133] Seddon, K. R., Ionic Liquids for Clean Technology. *J Chem Technol Biotechnol.* 68 (1997) 351-356.

[134] Freemantle, M., Designer Solvents. *Chem Eng News Archive.* 76 (1998) 32-37.

[135] Deng, Y.; Zhang, Q.; Zhang, S., Recent Advances in Ionic Liquid Catalysis. *Green Chem.* 13 (2011) 2619-2637.

[136] Hubbard, C. D.; Illner, P.; van Eldik, R., Understanding Chemical Reaction Mechanisms in Ionic Liquids: Successes and Challenges. *Chem Soc Rev.* 40 (2011) 272-290.

[137] Blanchard, L. A.; Brennecke, J. F., Recovery of Organic Products from Ionic Liquids using Supercritical Carbon Dioxide. *Ind Eng Chem Res.* 40 (2001) 287-292.

[138] Goodrich, B. F.; de la Fuente, Juan C.; Gurkan, B. E.; Lopez, Z. K.; Price, E. A.; Huang, Y.; Brennecke, J. F., Effect of Water and Temperature on Absorption of CO2 by Amine-Functionalized Anion-Tethered Ionic Liquids. *J Phys Chem B.* 115 (2011) 9140-9150.

[139] Schneider, W. F.; Brennecke, J. F.; Maginn, E. J.; Mindrup, E.; Gurkan, B.; Price, E.; Goodrich, B., Ionic Liquids Comprising Heteroaromatic Anions for Removing CO2 from Flue Gas. (2011) 48.

[140] Gurkan, B. E.; de la Fuente, Juan C.; Mindrup, E. M.; Ficke, L. E.; Goodrich, B. F.; Price, E. A.; Schneider, W. F.; Brennecke, J. F., Equimolar CO2 Absorption by Anion-Functionalized Ionic Liquids. *J Am Chem Soc.* 132 (2010) 2116-2117.

[141] Gurkan, B. E.; de la Fuente, Juan C.; Mindrup, E. M.; Ficke, L. E.; Goodrich, B. F.; Price, E. A.; Schneider, W. F.; Maginn, E.; Brennecke, J. F., Chemically Complexing Ionic Liquids for Post-Combustion CO2 Capture. *Int Tech Conf Clean Coal Fuel Syst.* 35 (2010) 931-937.

[142] Cadena, C.; Anthony, J. L.; Shah, J. K.; Morrow, T. I.; Brennecke, J. F.; Maginn, E. J., Why is CO2 so Soluble in Imidazolium-Based Ionic Liquids? *J Am Chem Soc.* 126 (2004) 5300-5308.

[143] Gupta, K. M.; Chen, Y.; Hu, Z.; Jiang, J., Metal-Organic Framework Supported Ionic Liquid Membranes for CO2 Capture: Anion Effects. *Phys Chem Chem Phys.* 14 (2012) 5785-5794.

[144] Joskowska, M.; Kopczynska, I.; Debski, B.; Holownia-Kedzia, D.; Aranowski, R.; Hupka, J., Wetting of Supports by Ionic Liquids used in Gas Separation Processes. *Physicochem Probl Miner Process.* 48 (2012) 129-140.

[145] D. Luebke, H. Nulwala, S. Wickramanayake, D. Hopkinson, C. Myers, Supported ionic liquid membranes for CO2 capture. Abstracts of Papers, 243rd ACS National Meeting & Exposition, San Diego, CA, United States, March 25-March 29, 2012. (2012) PHYS.

[146] Tempel, D. J.; Henderson, P. B.; Brzozowski, J. R., Ionic Liquid Based Mixtures for Gas Storage and Delivery. 2006060817 (2006) .

[147] Tempel, D. J.; Henderson, P. H.; Brzozowski, J. R.; Pearlstein, R. M.; Garg, D., Ionic Liquid Based Mixtures for Gas Storage and Delivery. (2006) .

[148] Tempel, D. J.; Henderson, P. B.; Brzozowski, J. R.; Pearlstein, R. M.; Cheng, H., High Gas Storage Capacities for Ionic Liquids through Chemical Complexation. *J Am Chem Soc.* 130 (2008) 400-401.

[149] Penn State Materials Research Institute, New Process Cleanly Extracts Oil from Tar Sands and Fouled Beaches. *Science Daily.* March 18.

[150] Hogshead, C. G.; Manias, E.; Williams, P.; Lupinsky, A.; Painter, P., Studies of Bitumen-Silica and Oil-Silica Interactions in Ionic Liquids. *Energy Fuels.* 25 (2011) 293-299.

[151] Ma, H.; Dai, L. L., Particle Self-Assembly in Ionic Liquid-in-Water Pickering Emulsions. *Langmuir.* 27 (2011) 508-512.

[152] Poole, C. F.; Poole, S. K., Extraction of Organic Compounds with Room Temperature Ionic Liquids. *J Chromatogr A.* 1217 (2010) 2268-2286.

[153] Visser, A. E.; Swatloski, R. P.; Reichert, W. M.; Mayton, R.; Sheff, S.; Wierzbicki, A.; Davis, J. H.; Rogers, R. D., Task-Specific Ionic Liquids for the Extraction of Metal Ions from Aqueous Solutions. *Chem Commun.* (2001) 135-136.

[154] Huddleston, J. G.; Willauer, H. D.; Swatloski, R. P.; Visser, A. E.; Rogers, R. D., Room Temperature Ionic Liquids as Novel Media for 'clean' Liquid–liquid Extraction. *Chem Commun.* (1998) 1765-1766.

[155] Burmudez, M.; Jimenez, A.; Sanes, J.; Carrion, F., Ionic Liquids as Advanced Lubricant Fluids. *Molecules.* 14 (2009) 2888-2908.

[156] Armand, M.; Endres, F.; MacFarlane, D. R.; Ohno, H.; Scrosati, B., Ionic-Liquid Materials for the Electrochemical Challenges of the Future. *Nat Mater.* 8 (2009) 621-629.

[157] Holbrey, J.; Plechkova, N.; Seddon, K., Recalling COIL. *Green Chem.* 8 (2006) 411-414.

[158] Holzapfel, M.; Jost, C.; Prodi-Schwab, A.; Krumeich, F.; Würsig, A.; Buqa, H.; Novák, P., Stabilisation of Lithiated Graphite in an Electrolyte Based on Ionic Liquids: An Electrochemical and Scanning Electron Microscopy Study. *Carbon.* 43 (2005) 1488-1498.

[159] Mehta, S. K.; Kushwinder, K., Ionic Liquid Microemulsions and their Technological Applications. *J Ind Chem.* 49A (2010) 662-684.

[160] Qiu, Z.; Texter, J., Ionic Liquids in Microemulsions. *Curr Opin Colloid Interface Sci.* 13 (2008) 252.

[161] Weyershausen, B.; Lehmann, K., Industrial Application of Ionic Liquids as Performance Additives. *Green Chem.* 7 (2005) 15-19.

[162] Adler, R., The Demand is Astounding. *Linde Technology.* 6 (2006) 27-29.

[163] Kompf, M., Mobility Under High Pressure. *Linde Technology.* (2006) 24-26.

[164] Adler, R.; Mayer, H., Procedure for Lubricating and/Or Cooling a Compressor by using Ionic Liquids. (2006) .

[165] Beste, Y.; Eggersmann, M.; Schoenmakers, H., Extraktivdestillation Mit Ionischen Flüssigkeiten. *Chemie Ingenieur Technik.* 77 (2005) 1800-1808.

[166] Jiqin, Z.; Jian, C.; Chengyue, L.; Weiyang, F., Viscosities and Interfacial Properties of 1-Methyl-3-Butylimidazolium Hexafluorophosphate and 1-Isobutenyl-3-Methylimidazolium Tetrafluoroborate Ionic Liquids. *J Chem Eng Data.* 52 (2007) 812-816.

[167] Cahn, J. W.; Hilliard, J. E., Free Energy of a Nonuniform System. I. Interfacial Free Energy. *J Chem Phys.* 28 (1958) 258.

[168] Smith, P. G.; van de Ven, T. G. M.; Mason, S. G., The Transient Interfacial Tension between Two Miscible Fluids. *J Colloid Interface Sci.* 80 (1981) 302-303.

[169] Masami Kojima; E. J. Hinch; Andreas Acrivos, The Formation and Expansion of a Toroidal Drop Moving in a Viscous Fluid. *Phys Fluids.* 27 (1984) 19.

[170] Cicuta, P.; Vailati, A.; Giglio, M., Capillary-to-Bulk Crossover of Nonequilibrium Fluctuations in the Free Diffusion of a Near-Critical Binary Liquid Mixture. *Appl Opt.* 40 (2001) 4140-4145.

[171] May, S. E.; Maher, J. V., Capillary-Wave Relaxation for a Meniscus between Miscible Liquids. *Phys Rev Lett.* 67 (1991) 2013-2016.

[172] Lacaze, L.; Guenoun, P.; Beysens, D.; Delsanti, M.; Petitjeans, P.; Kurowski, P., Transient Surface Tension in Miscible Liquids. *Phys Rev E.* 82 (2010) 041606.

[173] Vlad, D. H.; Maher, J. V., Dissolving Interfaces in the Presence of Gravity. *Phys Rev E.* 59 (1999) 476-478.

[174] Mungall, J. E., Interfacial Tension in Miscible Two-Fluid Systems with Linear Viscoelastic Rheology. *Phys Rev Lett.* 73 (1994) 288-291.

[175] Riegler, H.; Lazar, P., Delayed Coalescence Behavior of Droplets with Completely Miscible Liquids. *Langmuir.* 24 (2008) 6395-6398.

[176] Karpitschka, S.; Riegler, H., Quantitative Experimental Study on the Transition between Fast and Delayed Coalescence of Sessile Droplets with Different but Completely Miscible Liquids. *Langmuir.* 26 (2010) 11823-11829.

[177] Karpitschka, S.; Riegler, H., Noncoalescence of Sessile Drops from Different but Miscible Liquids: Hydrodynamic Analysis of the Twin Drop Contour as a Self-Stabilizing Traveling Wave. *Phys Rev Lett.* 109 (2012) 066103.

[178] Tang, S. K. Y., Whitesides, G. M., Optical Components Based on Dynamic Liquid-Liquid Interfaces in Optofluidics: Fundamentals, Devices, and Applications Y. Fainman, L. Lee, D. Psaltis, C. Yang (Eds.), McGraw-Hill, New York, 2010, p. 41.

[179] Pringle, S. E.; Glass, R. J.; Cooper, C. A., Double-Diffusive Finger Convection in a Hele-Shaw Cell an Experimental Exploring the Evolution of Concentration Fields, Length Scales, and Mass Transfer. *Transp Porous Media.* 47 (2002) 195-214.

[180] Wooding, R. A., Growth of Fingers at an Unstable Diffusing Interface in a Porous Medium Or Hele-Shaw Cell. *J Fluid Mech.* 39 (1969) 477-495.

[181] Nittmann, J.; Stanley, H. E., Tip Splitting without Interfacial Tension and Dendritic Growth Patterns Arising from Molecular Anisotropy. *Nature.* 321 (1986) 663-668.

[182] Nittmann, J.; Daccord, G.; Stanley, H. E., Fractal Growth Viscous Fingers: Quantitative Characterization of a Fluid Instability Phenomenon. *Nature.* 314 (1985) 141-144.

[183] Che, Z.; Nguyen, N.; Wong, T. N., Analysis of Chaotic Mixing in Plugs Moving in Meandering Microchannels. *Phys Rev E.* 84 (2011) 066309.

[184] Gunther, A.; Jhunjhunwala, M.; Thalmann, M.; Schmidt, M. A.; Jensen, K. F., Micromixing of Miscible Liquids in Segmented Gas-Liquid Flow. *Langmuir.* 21 (2005) 1547-1555.

[185] Nagy, K.; Shen, B.; Jamison, T.; Jensen, K., Mixing and Dispersion in Small-Scale Flow Systems. *Org Process Res Dev.* 16 (2012) 976-981.

[186] Günther, A.; Jensen, K. F., Multiphase Microfluidics: From Flow Characteristics to Chemical and Materials Synthesis. *Lab Chip.* 6 (2006) 1487-1503.

[187] Whitesides, G. M., The Origins and the Future of Microfluidics. *Nature.* 442 (2006) 368-373.

[188] Cabeza, V. S.; Kuhn, S.; Kulkarni, A. A.; Jensen, K. F., Size-Controlled Flow Synthesis of Gold Nanoparticles using a Segmented Flow Microfluidic Platform. *Langmuir.* 28 (2012) 7007-7013.

[189] Song, Y.; Hormes, J.; Kumar, C. S. S. R., Microfluidic Synthesis of Nanomaterials. *Small.* 4 (2008) 698-711.

[190] deMello, A. J., Control and Detection of Chemical Reactions in Microfluidic Systems. *Nature.* 442 (2006) 394-402.

[191] Mudring, A., Alammar, T., Backer, T., Richter, K., Nanoparticle Synthesis in Ionic Liquids in Ionic Liquids: From Knowledge to Application N.V. Plechkova, R.D. Rogers, K.R. Seddon (Eds.), American Chemical Society, 2009, p. 177.

[192] Wan, J.; Liang, C.; Yan, F.; Gu, K.; Zhang, S.; Xie, Z.; Lin, M., Electromagnetic Drive of Room-Temperature Ionic Liquids and Application. *Applied Mechanics and Materials.* 189 (2012) 374-378.

[193] Lazarus, L. L.; Riche, C. T.; Marin, B. C.; Gupta, M.; Malmstadt, N.; Brutchey, R. L., Two-Phase Microfluidic Droplet Flows of Ionic Liquids for the Synthesis of Gold and Silver Nanoparticles. *ACS Appl Mater Interfaces.* 4 (2012) 3077-3083.

[194] Frost, D. S.; Shoepf, J. J.; Nofen, E. M.; Dai, L. L., Understanding Droplet Bridging in Ionic Liquid-Based Pickering Emulsions. *J Colloid Interface Sci.* 383 (2012) 103-109.

[195] Painter, P.; Williams, P.; Lupinsky, A., Recovery of Bitumen from Utah Tar Sands using Ionic Liquids. *Energy Fuels.* 24 (2010) 5081-5088.

[196] Painter, P.; Williams, P.; Mannebach, E., Recovery of Bitumen from Oil Or Tar Sands using Ionic Liquids. *Energy Fuels.* 24 (2010) 1094-1098.

[197] Williams, P.; Lupinsky, A.; Painter, P., Recovery of Bitumen from Low-Grade Oil Sands using Ionic Liquids. *Energy Fuels.* 24 (2010) 2172-2173.

[198] Gittins, D. I.; Caruso, F., Spontaneous Phase Transfer of Nanoparticulate Metals from Organic to Aqueous Media. *Angew Chem Int Ed.* 40 (2001) 3001-3004.

[199] Wang, Y.; Wong, J. F.; Teng, X.; Lin, X. Z.; Yang, H., "Pulling"⊙ Nanoparticles into Water: Phase Transfer of Oleic Acid Stabilized Monodisperse Nanoparticles into Aqueous Solutions of Alpha-Cyclodextrin. *Nano Lett.* 3 (2003) 1555-1559.

[200] Liu, J.; Alvarez, J.; Ong, W.; Roman, E.; Kaifer, A. E., Phase Transfer of Hydrophilic, Cyclodextrin-Modified Gold Nanoparticles to Chloroform Solutions. *J Am Chem Soc.* 123 (2001) 11148-11154.

[201] Zou, J.; Frost, D. S.; Dai, L. L., Effects of Gelator 12-Hydroxystearic Acid (12-HSA) on Ionic Liquid Based Pickering Emulsions. *Colloids Surf A.* 414 (2012) 477-485.

[202] Wei, G.; Yang, Z.; Lee, C.; Yang, H.; Wang, C. R. C., Aqueous-Organic Phase Transfer of Gold Nanoparticles and Gold Nanorods using an Ionic Liquid. *J Am Chem Soc.* 126 (2004) 5036-5037.

[203] Dai, L. L.; Tarimala, S.; Wu, C.; Guttula, S.; Wu, J., The Structure and Dynamics of Microparticles at Pickering Emulsion Interfaces. *Scanning.* 30 (2008) 87-95.

[204] Tarimala, S.; Wu, C.; Dai, L. L., Dynamics and Collapse of Two-Dimensional Colloidal Lattices. *Langmuir.* 22 (2006) 7458-7461.

[205] Binks, B. P.; Rodrigues, J. A., Inversion of Emulsions Stabilized Solely by Ionizable Nanoparticles. *Angew Chem , Int Ed.* 44 (2005) 441-444.

[206] Min, Y.; Akbulut, M.; Sangoro, J. R.; Kremer, F.; Prud'homme, R. K.; Israelachvili, J., Measurement of Forces Across Room Temperature Ionic Liquids between Mica Surfaces. *J Phys Chem C.* 113 (2009) 16445-16449.

[207] Nakashima, T.; Kimizuka, N., Water/Ionic Liquid Interfaces as Fluid Scaffolds for the Two-Dimensional Self-Assembly of Charged Nanospheres. *Langmuir.* 27 (2011) 1281-1285.

[208] Vignati, E.; Piazza, R.; Lockhart, T. P., Pickering Emulsions: Interfacial Tension, Colloidal Layer Morphology, and Trapped-Particle Motion. *Langmuir.* 19 (2003) 6650-6656.

[209] Thareja, P. P. r., Particle-Induced Bridging in Immiscible Polymer Blends. *Rheol Acta.* 46 (2006) 405-412.

[210] Ivanov, I. B., Effect of Surface Mobility on the Dynamic Behavior of Thin Liquid Films. *Pure & Appl Chem.* 52 (1980) 1241-1262.

[211] Reynolds, O., *Trans R Soc London A.* 177 (1886) 157.

[212] Malhotra, A. K.; Wasan, D. T., Effects of Surfactant Adsorption-Desorption Kinetics and Interfacial Rheological Properties on the Rate of Drainage of Foam and Emulsion Films. *Chem Eng Comm.* 55 (1987) 95-128.

[213] Tambe, D. E.; Sharma, M. M., The Effect of Colloidal Particles on Fluid-Fluid Interfacial Properties and Emulsion Stability. *Adv Colloid Interface Sci.* 52 (1994) 1.

[214] Niedermeyer, H.; Hallett, J. P.; Villar-Garcia, I.; Hunt, P. A.; Welton, T., Mixtures of Ionic Liquids. *Chem Soc Rev.* 41 (2012) 7780-7802.

[215] Arce, A.; Earle, M. J.; Katdare, S. P.; Rodriguez, H.; Seddon, K. R., Application of Mutually Immiscible Ionic Liquids to the Separation of Aromatic and Aliphatic Hydrocarbons by Liquid Extraction: A Preliminary Approach. *Phys Chem Chem Phys.* 10 (2008) 2538-2542.

[216] Arce, A.; Earle, M. J.; Katdare, S. P.; Rodriguez, H.; Seddon, K. R., Mutually Immiscible Ionic Liquids. *Chem Commun.* (2006) 2548-2550.

[217] Cheng, S.; Zhang, J.; Zhang, Z.; Han, B., Novel Microemulsions: Ionic Liquid-in-Ionic Liquid. *Chem Commun.* (2007) 2497-2499.

[218] Belieres, J.; Angell, C. A., Protic Ionic Liquids: Preparation, Characterization, and Proton Free Energy Level Representation. *J Phys Chem B.* 111 (2007) 4926-4937.

[219] Greaves, T. L.; Weerawardena, A.; Fong, C.; Krodkiewska, I.; Drummond, C. J., Protic Ionic Liquids: Solvents with Tunable Phase Behavior and Physicochemical Properties. *J Phys Chem B.* 110 (2006) 22479-22487.

[220] Kilaru, P.; Baker, G. A.; Scovazzo, P., Density and Surface Tension Measurements of Imidazolium-, Quaternary Phosphonium-, and Ammonium-Based Room-Temperature Ionic Liquids:Â€‰ Data and Correlations. *J Chem Eng Data.* 52 (2007) 2306-2314.

[221] Lopes, J. N. C.; Padua, A. A. H., Molecular Force Field for Ionic Liquids Composed of Triflate Or Bistriflylimide Anions. *J Phys Chem B.* 108 (2004) 16893.

[222] Lopes, J. N. C.; Deschamps, J.; Padua, A. A. H., Modeling Ionic Liquids using a Systematic all-Atom Force Field. *J Phys Chem B.* 108 (2004) 2038-2047.

[223] Bhargava, B. L.; Balasubramanian, S., Refined Potential Model for Atomistic Simulations of Ionic Liquid [BMIM][PF6]. *J Chem Phys.* 127 (2007) 114510.

[224] Schroder, C., Comparing Reduced Partial Charge Models with Polarizable Simulations of Ionic Liquids. *Phys Chem Chem Phys.* 14 (2012) 3089-3102.

[225] Song, X.; Hamano, H.; Minofar, B.; Kanzaki, R.; Fujii, K.; Kameda, Y.; Kohara, S.; Watanabe, M.; Ishiguro, S.; Umebayashi, Y., Structural Heterogeneity and Unique Distorted Hydrogen Bonding in Primary Ammonium Nitrate Ionic Liquids Studied by High-Energy X-Ray Diffraction Experiments and MD Simulations. *J Phys Chem B.* 116 (2012) 2801-2813.

[226] Cornell, W. D.; Cieplak, P.; Bayly, C. I.; Gould, I. R.; Merz, K. M.; Ferguson, D. M.; Spellmeyer, D. C.; Fox, T.; Caldwell, J. W.; Kollman, P. A., A Second Generation Force Field for the Simulation of Proteins, Nucleic Acids, and Organic Molecules. *J Am Chem Soc.* 117 (1995) 5179-5197.

[227] Baaden, M.; Burgard, M.; Wipff, G., TBP at the Water - Oil Interface: The Effect of TBP Concentration and Water Acidity Investigated by Molecular Dynamics Simulations. *J Phys Chem B.* 105 (2001) 11131-11141.

[228] Jorgensen, W. L.; Madura, J. D.; Swenson, C. J., Optimized Intermolecular Potential Functions for Liquid Hydrocarbons. *J Am Chem Soc.* 106 (1984) 6638-6646.

[229] Parrinello, M.; Rahman, A., Polymorphic Transitions in Single Crystals: A New Molecular Dynamics Method. *J Appl Phys.* 52 (1981) 7182-7190.

[230] Nosé, S.; Klein, M. L., Constant Pressure Molecular Dynamics for Molecular Systems. *Mol Phys.* 50 (1983) 1055-1076.

[231] Berendsen, H. J. C., Molecular Dynamics with Coupling to an External Bath. *J Chem Phys.* 81 (1984) 3684.

[232] Lynden-Bell, R. M.; Del Popolo, M. G.; Youngs, T. G. A.; Kohanoff, J.; Hanke, C. G.; Harper, J. B.; Pinilla, C. C., Simulations of Ionic Liquids, Solutions, and Surfaces. *Acc Chem Res.* 40 (2007) 1138-1145.

[233] Sarangi, S. S.; Raju, S. G.; Balasubramanian, S., Molecular Dynamics Simulations of Ionic Liquid–vapour Interfaces: Effect of Cation Symmetry on Structure at the Interface. *Phys Chem Chem Phys.* 13 (2011) 2714-2722.

[234] Lynden-Bell, R. M., Gas—liquid Interfaces of Room Temperature Ionic Liquids. *Mol Phys.* 101 (2003) 2625-2633.

[235] Trivedi, S.; Pandey, S., Interactions within a Ionic Liquid + Poly(Ethylene Glycol)] Mixture Revealed by Temperature-Dependent Synergistic Dynamic Viscosity and Probe-Reported Microviscosity. *J Phys Chem B.* 115 (2011) 7405-7416.

[236] Kleppa, O. J.; Meschel, S. V., Thermochemistry of Anion Mixture in Simple Fused Salt Systems. I. Solutions of Monovalent Chlorides and Bromides in the Corresponsing Nitrates. *J Phys Chem.* 67 (1963) 668-671.

[237] Kleppa, O. J.; Hersh, L. S., Heats of Mixing in Liquid Alkali Nitrate Systems. *J Chem Phys.* 34 (1961) 351.

[238] Smith, J. M., Van Ness, H. C., Abbott, M. M., Introduction to Chemical Engineering Thermodynamics, McGraw-Hill, Boston, 2005.

[239] Atkins, P., De Paula, J., Physical Chemistry, Oxford University Press, Great Britain, 2006.

[240] Denbigh, K. G., The Principles of Chemical Equilibrium, Cambridge University Press, Cambridge Eng.; New York, 1981.

[241] Ranke, J.; Othman, A.; Fan, P.; Müller, A., Explaining Ionic Liquid Water Solubility in Terms of Cation and Anion Hydrophobicity. *Int J Mol Sci.* 10 (2009) 1271-1289.

[242] Zhou, T.; Chen, L.; Ye, Y.; Chen, L.; Qi, Z.; Freund, H.; Sundmacher, K., An Overview of Mutual Solubility of Ionic Liquids and Water Predicted by COSMO-RS. *Ind Eng Chem Res.* 51 (2012) 6256-6264.

[243] Frost, D. S.; Machas, M.; Dai, L. L., Molecular Dynamics Studies on the Adaptability of an Ionic Liquid in the Extraction of Solid Nanoparticles. *Langmuir.* 28 (2012) 13924-13932.

[244] Lee, C.; Huang, C.; Wei, G., Behaviors of Ionic Liquids in the Phase Transfer of Aqueous Metal Nanoparticles. *Colloids Surf A.* 367 (2010) 24-30.

[245] Zhao, D.; Fei, Z.; Ang, W. H.; Dyson, P. J., A Strategy for the Synthesis of Transition-Metal Nanoparticles and their Transfer between Liquid Phases. *Small.* 2 (2006) 879-883.

[246] López-Lorente, A. I.; Simonet, B. M.; Valcárcel, M., Rapid Analysis of Gold Nanoparticles in Liver and River Water Samples. *Analyst.* 137 (2012) 3528-3534.

[247] Frost, D. S.; Dai, L. L., Molecular Dynamics Simulations of Nanoparticle Self-Assembly at Ionic Liquid-Water and Ionic Liquid-Oil Interfaces. *Langmuir.* 27 (2011) 11339-11346.

[248] Frost, D. S.; Dai, L. L., Molecular Dynamics Simulations of Charged Nanoparticle Self-Assembly at Ionic Liquid-Water and Ionic Liquid-Oil Interfaces. *J Chem Phys.* 136 (2012) 084706.

[249] Binks, B. P.; Fletcher, P. D. I.; Dyab, A. K. F., Novel Emulsions of Ionic Liquids Stabilised Solely by Silica Nanoparticles. *Chem Commun.* (2003) 2540-2541.

[250] Elias, L.; Fenouillot, F.; Majesté, J. C.; Martin, G.; Cassagnau, P., Migration of Nanosilica Particles in Polymer Blends. *J Polym Sci , Part B: Polym Phys.* 46 (2008) 1976-1983.

[251] Grace, R., Commercial Emulsion Breaking in Emulsions L.L. Schramm (Ed.), AMER CHEMICAL SOC, WASHINGTON, 1992, p. 313.

[252] Cameron, N. R., High Internal Phase Emulsion Templating as a Route to Well-Defined Porous Polymers. *Polymer.* 46 (2005) 1439-1449.

[253] Bokhari, M.; Carnachan, R.; Przyborski, S.; Cameron, N., Emulsion-Templated Porous Polymers as Scaffolds for Three Dimensional Cell Culture: Effect of Synthesis Parameters on Scaffold Formation and Homogeneity. *J Mater Chem.* 17 (2007) 4088-4094.

[254] Zhao, C.; Danish, E.; Cameron, N.; Kataky, R., Emulsion-Templated Porous Materials (PolyHIPEs) for Selective Ion and Molecular Recognition and Transport: Applications in Electrochemical Sensing. *J Mater Chem.* 17 (2007) 2446-2453.

[255] Su, F.; Bray, C. L.; Tan, B.; Cooper, A. I., Rapid and Reversible Hydrogen Storage in Clathrate Hydrates using Emulsion-Templated Polymers. *Adv Mater.* 20 (2008) 2663-2666.

[256] Ma, H., Dai, L. L., Particle-Laden Emulsions in Encyclopedia of Surface and Colloid Science, Second Edition P. Somasundaran (Ed.), Taylor and Francis, 2010.

[257] Walker, E. M.; Frost, D. S.; Dai, L. L., Particle Self-Assembly in Oil-in-Ionic Liquid Pickering Emulsions. *J Colloid Interface Sci.* 363 (2011) 307-313.

[258] Bala Subramaniam, A.; Abkarian, M.; Mahadevan, L.; Stone, H. A., Colloid Science: Non-Spherical Bubbles. *Nature.* 438 (2005) 930-930.

[259] Subramaniam, A. B.; Mejean, C.; Abkarian, M.; Stone, H. A., Microstructure, Morphology, and Lifetime of Armored Bubbles Exposed to Surfactants. *Langmuir.* 22 (2006) 5986-5990.

[260] Danov, K. D.; Petsev, D. P.; Denkov, N. D.; Borwankar, R., Pair Interaction Energy between Deformable Drops and Bubbles. *J Chem Phys.* 99 (1993) 7179.

[261] Lee, M. N.; Chan, H. K.; Mohraz, A., Characteristics of Pickering Emulsion Gels Formed by Droplet Bridging. *Langmuir.* 28 (2012) 3085-3091.

[262] Villers, D.; Platten, J. K., Temperature Dependence of the Interfacial Tension between Water and Long-Chain Alcohols. *J Phys Chem.* 92 (1988) 4023-4024.

[263] Payal, R. S.; Balasubramanian, S., Orientational Ordering of Ionic Liquids Near a Charged Mica Surface. *Chemphyschem.* 13 (2012) 1764-1771.

[264] Dragoni, D.; Manini, N.; Ballone, P., Interfacial Layering of a Room-Temperature Ionic Liquid Thin Film on Mica: A Computational Investigation. *Chemphyschem.* 13 (2012) 1772-1780.

[265] Rogers, M. A.; Wright, A. J.; Marangoni, A. G., Nanostructuring Fiber Morphology and Solvent Inclusions in 12-Hydroxystearic Acid / Canola Oil Organogels. *Curr Opin Colloid Interface Sci.* 14 (2009) 33-42.

[266] Rogers, M.; Wright, A.; Marangoni, A., Engineering the Oil Binding Capacity and Crystallinity of Self-Assembled Fibrillar Networks of 12-Hydroxystearic Acid in Edible Oils. *Soft Matter.* 4 (2008) 1483-1490.

[267] Rogers, M. A.; Marangoni, A. G., Solvent-Modulated Nucleation and Crystallization Kinetics of 12-Hydroxystearic Acid: A Nonisothermal Approach. *Langmuir.* 25 (2009) 8556-8566.

[268] Eloundou, J. P.; Girard-Reydet, E.; Gérard, J.; Pascault, J., Calorimetric and Rheological Studies of 12-Hydroxystearic Acid / Digycidyl Ether of Bisphenol A Blends. *Polymer Bulletin.* 53 (2005) 367-375.

[269] Rogers, M. A.; Kim, J. H. J., Rheological Assessment of the Sol–gel Transition for Self-Assembling Low Molecular Weight Gelators. *Food Res Int.* 44 (2011) 1447-1451.

[270] Voss, B.; Bara, J.; Gin, D.; Noble, R., Physically Gelled Ionic Liquids: Solid Membrane Materials with Liquidlike CO2 Gas Transport. *Chem Mater.* 21 (2009) 3027-3029.

[271] Terech, P.; Furman, I.; Weiss, R. G., Structures of Organogels Based upon Cholesteryl 4-(2-Anthryloxy)Butanoate, a Highly Efficient Luminescing Gelator: Neutron and X-Ray Small-Angle Scattering Investigations. *J Phys Chem.* 99 (1995) 9558-9566.

[272] Terech, P., Weiss, R. G., Introduction in Molecular gels: Materials with Self-Assembled Fibrillar Networks P. Terech, R.G. Weiss (Eds.), Springer, Dordrecht, 2006, p. 978.

[273] Zhu, G.; Dordick, J. S., Solvent Effect on Organogel Formation by Low Molecular Weight Molecules. *Chem Mater.* 18 (2006) 5988-5995.

[274] Lam, R.; Quaroni, L.; Pedersen, T.; Rogers, M. A., A Molecular Insight into the Nature of Crystallographic Mismatches in Self-Assembled Fibrillar Networks Under Non-Isothermal Crystallization Conditions. *Soft Matter.* 6 (2010) 404-408.

[275] Wang, R.; Liu, X.; Xiong, J.; Li, J., Real-Time Observation of Fiber Network Formation in Molecular Organogel:Â€‰ Supersaturation-Dependent Microstructure and its Related Rheological Property. *J Phys Chem B.* 110 (2006) 7275-7280.

[276] Kubo, W.; Kambe, S.; Nakade, S.; Kitamura, T.; Hanabusa, K.; Wada, Y.; Yanagida, S., Photocurrent-Determining Processes in Quasi-Solid-State Dye-Sensitized Solar Cells using Ionic Gel Electrolytes. *J Phys Chem B.* 107 (2003) 4374-4381.

[277] Mohmeyer, N.; Kuang, D.; Wang, P.; Schmidt, H.; Zakeeruddin, S. M.; Gratzel, M., An Efficient Organogelator for Ionic Liquids to Prepare Stable Quasi-Solid-State Dye-Sensitized Solar Cells. *J Mater Chem.* 16 (2006) 2978-2983.

[278] Trewyn, B. G.; Whitman, C. M.; Lin, V. S. -., Morphological Control of Room-Temperature Ionic Liquid Templated Mesoporous Silica Nanoparticles for Controlled Release of Antibacterial Agents. *Nano Lett.* 4 (2004) 2139-2143.

[279] Le Bideau, J.; Viau, L.; Vioux, A., Ionogels, Ionic Liquid Based Hybrid Materials. *Chem Soc Rev.* 4 (2011) 907-925.

[280] Nusai, Y.; Koizumi, H.; Tachibana, M.; Tani, K.; Kiba, N., The Roles of 1-Alkyl 1-3 Methylimidazolium-Based Ionic Liquids as Mobile Phase Additives in Semi-Micro High-Performace Liquid Chromatography for Separation of Aromatic Amines. *Anal Chem : Indian J.* 10 (2011) 365-373.

[281] Wang, J.; Pei, Y.; Zhao, Y.; Hu, Z., Recovery of Amino Acids by Imidazolium Based Ionic Liquids from Aqueous Media. *Green Chem.* 7 (2005) 196-202.

[282] Andre, F.; Hapiot, P.; Lagrost, C., Dimerization of Ion Radicals in Ionic Liquids. an Example of Favourable "Coulombic" Solvation. *Phys Chem Chem Phys.* 12 (2010) 7506-7512.

[283] Dickinson, E.; Flint, F. O.; Hunt, J. A., Bridging Flocculation in Binary Protein Stabilized Emulsions. *Food Hydrocoll.* 3 (1989) 389-397.

[284] Dickinson, E.; Ritzoulis, C.; Povey, M. J. W., Stability of Emulsions Containing both Sodium Caseinate and Tween 20. *J Colloid Interface Sci.* 212 (1999) 466-473.

[285] Meller, A.; Gisler, T.; Weitz, D. A.; Stavans, J., Viscoelasticity of Depletion-Induced Gels in Emulsion-Polymer Systems. *Langmuir.* 15 (1999) 1918-1922.

[286] Xiao, C.; Wylie, J., Depletion Forces and Packing Models. *Phys Lett A.* 357 (2006) 245-248.

[287] Bechinger, C.; Rudhardt, D.; Leiderer, P.; Roth, R.; Dietrich, S., Understanding Depletion Forces Beyond Entropy. *Phys Rev Lett.* 83 (1999) 3960-3963.

[288] Gokmen, M. T.; Van Camp, W.; Colver, P. J.; Bon, S. A. F.; Du Prez, F. E., Fabrication of Porous Clickable⊙ Polymer Beads and Rods through Generation of High Internal Phase Emulsion (HIPE) Droplets in a Simple Microfluidic Device. *Macromolecules.* 42 (2009) 9289-9294.

[289] Lye, G. J.; Stuckey, D. C., Structure and Stability of Colloidal Liquid Aphrons. *Colloids Surf , A.* 131 (1998) 119-136.

[290] Benjamin, I., Molecular Structure and Dynamics at Liquid-Liquid Interfaces. *Annu Rev Phys Chem.* 48 (1997) 407-451.

[291] Hampe, M. J.; Essmann, U.; Berkowitz, M., Structural and Dynamical Properties of Liquid–liquid Interfaces: A Systematic Molecular Dynamics Study. *J Mol Liq.* 125 (2006) 187-196.

[292] Luo, M.; Dai, L. L., Molecular Dynamics Simulations of Surfactant and Nanoparticle Self-Assembly at Liquid–Liquid Interfaces. *J Phys Condens Matter.* 19 (2007) 375109.

[293] Wardle, K. E.; Henderson, D. J.; Rowley, R. L., Molecular Dynamics Simulation of Surfactant Effects on Ion Transport through a Liquid-Liquid Interface between Partially Miscible Liquids. *Fluid Phase Equilib.* 233 (2005) 96-102.

[294] Schweighofer, K. J.; Essmann, U.; Berkowitz, M., Simulation of Sodium Dodecyl Sulfate at the Water-Vapor and Water-Carbon Tetrachloride Interfaces at Low Surface Coverage. *J Phys Chem B.* 101 (1997) 3793-3799.

[295] Dominguez, H., Computer Simulations of Surfactant Mixtures at the Liquid/Liquid Interface. *J Phys Chem B.* 106 (2002) 5915-5924.

[296] Dominguez, H.; Berkowitz, M. L., Computer Simulations of Sodium Dodecyl Sulfate at Liquid/Liquid and Liquid/Vapor Interfaces. *J Phys Chem B.* 104 (2000) 5302-5308.

[297] Luo, M.; Mazyar, O. A.; Zhu, Q.; Vaughn, M. W.; Hase, W. L.; Dai, L. L., Molecular Dynamics Simulation of Nanoparticle Self-Assembly at a Liquid-Liquid Interface. *Langmuir.* 22 (2006) 6385-6390.

[298] Song, Y.; Luo, M.; Dai, L. L., Understanding Nanoparticle Diffusion and Exploring Interfacial Nanorheology using Molecular Dynamics Simulations. *Langmuir.* 26 (2010) 5-9.

[299] Hanke, C. G.; Price, S. L.; Lynden-Bell, R. M., Intermolecular Potentials for Simulations of Liquid Imidazolium Salts. *Mol Phys.* 99 (2001) 801-809.

[300] de Andrade, J.; Boes, E. S.; Stassen, H., A Force Field for Liquid State Simulations on Room Temperature Molten Salts: 1-Ethyl-3-Methylimidazolium Tetrachloroaluminate. *J Phys Chem B.* 106 (2002) 3546-3548.

[301] de Andrade, J.; Boes, E. S.; Stassen, H., Computational Study of Room Temperature Molten Salts Composed by 1-Alkyl-3-Methylimidazolium CationsForce-Field Proposal and Validation. *J Phys Chem B.* 106 (2002) 13344-13351.

[302] Shah, J. K.; Brennecke, J. F.; Maginn, E., Thermodynamic Properties of the Ionic Liquid 1-*n*-Butyl-3-Methylimidazolium Hexafluorophosphate from Monte Carlo Simulations. *Green chem.* 4 (2002) 112-118.

[303] Morrow, T. I.; Maginn, E. J., Molecular Dynamics Study of the Ionic Liquid 1-*n*-Butyl-3-Methylimidazolium Hexafluorophosphate. *J Phys Chem B.* 106 (2002) 12807-12813.

[304] Margulis, C. J.; Stern, H. A.; Berne, B. J., Computer Simulation of a "Green Chemistry" Room-Temperature Ionic Solvent. *J Phys Chem B.* 106 (2002) 12017-12021.

[305] Liu, Z.; Wu, X.; Wang, W., A Novel United-Atom Force Field for Imidazolium-Based Ionic Liquids. *Phys Chem Chem Phys.* 8 (2006) 1096-1104.

[306] Liu, Z.; Huang, S.; Wang, W., A Refined Force Field for Molecular Simulation of Imidazolium-Based Ionic Liquids. *J Phys Chem B.* 108 (2004) 12978-12989.

[307] Chaumont, A.; Wipff, G., Solvation of "Big" Spherical Solutes in Room Temperature Ionic Liquids and their Aqueous Interface: A Molecular Dynamics Simulation Study. *J Mol Liq.* 131 (2007) 36-47.

[308] Chaumont, A.; Wipff, G., Strontium Nitrate Extraction to Ionic Liquids by a Crown Ether: A Molecular Dynamics Study of Aqueous Interfaces with C4mim+- Vs C8mim+-Based Ionic Liquids. *J Phys Chem B.* 114 (2010) 13773-13785.

[309] Chevrot, G.; Schurhammer, R.; Wipff, G., Surfactant Behavior of "Ellipsoidal" Dicarbollide Anions: A Molecular Dynamics Study. *J Phys Chem B.* 110 (2006) 9488-9498.

[310] Heggen, B.; Zhao, W.; Leroy, F.; Dammers, A. J.; Muller-Plathe, F., Interfacial Properties of an Ionic Liquid by Molecular Dynamics. *J Phys Chem B.* 114 (2010) 6954-6961.

[311] Zhao, W.; Leroy, F.; Balasubramanian, S.; Muller-Plathe, F., Shear Viscosity of the Ionic Liquid 1-*n*-Butyl 3-Methylimidazolium Hexafluorophosphate [Bmim][PF6] Computed by Reverse Nonequilibrium Molecular Dynamics. *J Phys Chem B.* 112 (2008) 8129-8133.

[312] Bhargava, B. L.; Balasubramanian, S., Layering at an Ionic Liquid−Vapor Interface: A Molecular Dynamics Simulation Study of [Bmim][PF6]. *J Am Chem Soc.* 128 (2006) 10073-10078.

[313] Sarangi, S. S.; Reddy, S. K.; Balasubramanian, S., Low Frequency Vibrational Modes of Room Temperature Ionic Liquids. *J Phys Chem B.* 115 (2011) 1874-1880.

[314] Nakashima, T.; Kawai, T., Quantum Dots-Ionic Liquid Hybrids: Efficient Extraction of Cationic CdTe Nanocrystals into an Ionic Liquid. *Chem Commun.* (2005) 1643-1645.

[315] Atkin, R.; Warr, G., Structure in Confined Room-Temperature Ionic Liquids. *J Phys Chem C.* 111 (2007) 5162-5168.

[316] Fedorov, M. V.; Lynden-Bell, R., Probing the Neutral Graphene-Ionic Liquid Interface: Insights from Molecular Dynamics Simulations. *Phys Chem Chem Phys.* 14 (2012) 2552-2556.

[317] Pinilla, C.; Del Popolo, M. G.; Lynden-Bell, R.; Kohanoff, J., Structure and Dynamics of a Confined Ionic Liquid. Topics of Relevance to Dye-Sensitized Solar Cells. *J Phys Chem B.* 109 (2005) 17922-17927.

[318] Nordström, J.; Aguilera, L.; Matic, A., Effect of Lithium Salt on the Stability of Dispersions of Fumed Silica in the Ionic Liquid BMImBF4. *Langmuir.* 28 (2012) 4080-4085.

[319] Berendsen, H. J. C.; Van der Spoel, D.; Vandrunen, R., Gromacs: A Message-Passing Parallel Molecular Dynamics Implementation. *Comput Phys Commun.* 91 (1995) 43-56.

[320] Lindahl, E.; Hess, B.; Van der Spoel, D., GROMACS 3.0: A Package for Molecular Simulation and Trajectory Analysis. *J Mol Model.* 7 (2001) 306-317.

[321] Van der Spoel, D.; Lindahl, E.; Hess, B.; Groenhof, G.; Mark, A. E.; Berendsen, H. J. C., GROMACS: Fast, Flexible, and Free. *J Comput Chem.* 26 (2005) 1701-1718.

[322] Humphrey, W.; Dalke, A.; Schulten, K., VMD: Visual Molecular Dynamics. *J Mol Graph.* 14 (1996) 33-38.

[323] Berendsen, H. J. C.; Grigera, J. R.; Straatsma, T. P., The Missing Term in Effective Pair Potentials. *J Phys Chem.* 91 (1987) 6269-6271.

[324] Mazyar, O. A.; Hase, W. L., Dynamics and Kinetics of Heat Transfer at the Interface of Model Diamond {111} Nanosurfaces. *J Phys Chem A.* 110 (2006) 526-536.

[325] Jorgensen, W. L.; Maxwell, D. S.; Tirado-Rives, J., Development and Testing of the OPLS all-Atom Force Field on Conformational Energetics and Properties of Organic Liquids. *J Am Chem Soc.* 118 (1996) 11225-11236.

[326] Bhargava, B. L.; Balasubramanian, S., Insights into the Structure and Dynamics of a Room-Temperature Ionic Liquid: Ab Initio Molecular Dynamics Simulation Studies of 1-N-Butyl-3-Methylimidazolium Hexafluorophosphate ([Bmim][PF6]) and the [Bmim][PF6] CO2 Mixture. *J Phys Chem B.* 111 (2007) 4477-4487.

[327] Yaws, C. L., Knovel, Yaws' Handbook of Thermodynamic and Physical Properties of Chemical Compounds, Knovel, Norwich, N.Y., 2003.

[328] Tokuda, H.; Hayamizu, K.; Ishii, K.; Susan, A. B. H.; Watanabe, M., Physicochemical Properties and Structures of Room Temperature Ionic Liquids. 1. Variation of Anionic Species. *J Phys Chem B.* 108 (2004) 16593-16600.

[329] Jacquemin, J.; Husson, P.; Padua, A. A. H.; Majer, V., Density and Viscosity of several Pure and Water-Saturated Ionic Liquids. *Green Chem.* 8 (2006) 172-180.

[330] Sloutskin, E.; Ocko, B. M.; Tamam, L.; Kuzmenko, I.; Gog, T.; Deutsch, M., Surface Layering in Ionic Liquids: An X-Ray Reflectivity Study. *J Am Chem Soc.* 127 (2005) 7796-7804.

[331] Law, G.; Watson, P. R., Surface Tension Measurements of *N*-Alkylimidazolium Ionic Liquids. *Langmuir.* 17 (2001) 6138-6141.

[332] Naval Research Laboratory Center for Computational Materials Science. **The A (Low) Quartz Structure**. Updated: 2007, 2011. URL: http://cst-www.nrl.navy.mil/lattice/struk/sio2a.html.

[333] Momma, K.; Izumi, F., VESTA: A Three-dimensional Visualization System for Electronic and Structural Analysis. *J Appl Crystallogr.* 41 (2008) 653-658.

[334] Accelrys Inc. (San Diego CA), Weblab Viewer Pro 3.7. .

[335] Wensink, E. J. W.; Hoffmann, A. C.; Apol, M. E. F.; Berendsen, H. J. C., Properties of Adsorbed Water Layers and the Effect of Adsorbed Layers on Interparticle Forces by Liquid Bridging. *Langmuir.* 16 (2000) 7392-7400.

[336] Hub, J. S.; de Groot, B. L.; Van der Spoel, D., G_wham - A Free Weighted Histogram Analysis Implementation Including Robust Error and Autocorrelation Estimates. *J Chem Theory Comput.* 6 (2010) 3713-3720.

[337] Kumar, S.; Bouzida, D.; Swendsen, R. H.; Kollman, P. A.; Rosenberg, J. M., The Weighted Histogram Analysis Method for Free-Energy Calculations on Biomolecules. I. the Method. *J Comput Chem.* 13 (1992) 1011-1021.

[338] Lui, M. Y.; Crowhurst, L.; Hallett, J. P.; Hunt, P. A.; Niedermeyer, H.; Welton, T., Salts Dissolved in Salts: Ionic Liquid Mixtures. *Chem Sci.* 2 (2011) 1491-1496.

[339] Crowhurst, L.; Mawdsley, P. R.; Perez-Arlandis, J.; Salter, P. A.; Welton, T., Solvent-Solute Interactions in Ionic Liquids. *Phys Chem Chem Phys.* 5 (2003) 2790-2794.

[340] B. Widom; J. S. Rowlinson, New Model for the Study of Liquid–Vapor Phase Transitions. *J Chem Phys.* 52 (1970) 1670.

[341] González-Melchor, M.; Bresme, F.; Alejandre, J., Molecular Dynamics Simulations of the Surface Tension of Ionic Liquids. *J Chem Phys.* 122 (2005) 104710.

[342] Linert, W., Bridge, M., Ohtaki, H., 2.46 - Solvation in Comprehensive Coordination Chemistry II J.A. McCleverty, T.J. Meyer (Eds.), Pergamon, Oxford, 2003, p. 597.

[343] Russo, D.; Hura, G.; Head-Gordon, T., Hydration Dynamics Near a Model Protein Surface. *Biophys J.* 86 (2004) 1852-1862.

[344] Zhang, L.; Wang, L.; Kao, Y.; Qiu, W.; Yang, Y.; Okobiah, O.; Zhong, D., Mapping Hydration Dynamics Around a Protein Surface. *Proc Natl Acad Sci U S A.* 104 (2007) 18461-18466.

[345] Andrievsky, G. V.; Klochkov, V. K.; Bordyuh, A. B.; Dovbeshko, G. I., Comparative Analysis of Two Aqueous-Colloidal Solutions of C60 Fullerene with Help of FTIR Reflectance and UV–Vis Spectroscopy. *Chem Phys Lett.* 364 (2002) 8-17.

[346] Storm, D. A.; Sheu, E. Y., Characterization of Colloidal Asphaltenic Particles in Heavy Oil. *Fuel.* 74 (1995) 1140-1145.

[347] Perkin, S.; Crowhurst, L.; Niedermeyer, H.; Welton, T.; Smith, A.; Gosvami, N., Self-Assembly in the Electrical Double Layer of Ionic Liquids. *Chem Commun.* 47 (2011) 6572-6574.

[348] Simon, P.; Gogotsi, Y., Materials for Electrochemical Capacitors. *Nat Mater.* 7 (2008) 845-854.

[349] Ballone, P.; Del Pópolo, M. G.; Bovio, S.; Podestà, A.; Milani, P.; Manini, N., Nano-Indentation of a Room-Temperature Ionic Liquid Film on Silica: A Computational Experiment. *Phys Chem Chem Phys.* 14 (2012) 2475-2482.

[350] Bovio, S.; Podestà, A.; Milani, P.; Ballone, P.; Del Pópolo, M. G., Nanometric Ionic-Liquid Films on Silica: A joint Experimental and Computational Study. *J Phys Condens Matter.* 21 (2009) 424118.

[351] Shimizu, K.; Pensado, A.; Malfreyt, P.; Pádua, A. A. H.; Canongia Lopes, J. N., 2D Or Not 2D: Structural and Charge Ordering at the Solid-Liquid Interface of the 1-(2-Hydroxyethyl)-3-Methylimidazolium Tetrafluoroborate Ionic Liquid. *Faraday Discuss.* 154 (2011) 155-169.

[352] Nishikawa, K.; Ooi, T., Tertiary Structure of Proteins. II. Freedom of Dihedral Angles and Energy Calculation. *J Phys Soc Japan.* 32 (1972) 1338-1347.

[353] Levitt, M., A Simplified Representation of Protein Conformations for Rapid Simulation of Protein Folding. *J Mol Biol.* 104 (1976) 59-107.

[354] Maiorov, V. N.; Crippen, G. M., Significance of Root-Mean-Square Deviation in Comparing Three-Dimensional Structures of Globular Proteins. *J Mol Biol.* 235 (1994) 625.

[355] Einstein, A., Über Die Von Der Molekularkinetischen Theorie Der Wärme Geforderte Bewegung Von in Ruhenden Flüssigkeiten Suspendierten Teilchen. *Annalen der Physik.* 322 (1905) 549-560.

[356] Paterson, A. R., A First Course in Fluid Dynamics, Cambridge University Press, Cambridge [Cambridgeshire], 1983.

[357] Ramshaw, J. D., Elements of Computational Fluid Dynamics, Imperial College Press, Hackensack, NJ, 2011.

[358] Iannelli, J., Characteristics Finite Element Methods in Computational Fluid Dynamics, Springer, New York, 2006.

[359] Taha, T.; Cui, Z. F., CFD Modelling of Slug Flow Inside Square Capillaries. *Chem Eng Sci.* 61 (2006) 665-675.

[360] Edward D. Wilkes; Scott D. Phillips; Osman A. Basaran, Computational and Experimental Analysis of Dynamics of Drop Formation. *Phys Fluids.* 11 (1999) 3577-3598.

[361] D. F. Zhang; H. A. Stone, Drop Formation in Viscous Flows at a Vertical Capillary Tube. *Phys Fluids.* 9 (1997) 2234-2242.

[362] Ghajar, M.; Hashemabadi, S., CFD Simulation of Capillary Condensation during Freeze Drying of Porous Material. *Chem Eng Technol.* 34 (2011) 1136-1142.

[363] van Baten, J. M.; Krishna, R., CFD Simulations of Mass Transfer from Taylor Bubbles Rising in Circular Capillaries. *Chem Eng Sci.* 59 (2004) 2535-2545.

[364] Chen, Y.; Wu, L.; Zhang, C., Emulsion Droplet Formation in Coflowing Liquid Streams. *Phys Rev E.* 87 (2013) 013002.

[365] Asadi, S., A Model of Nanodroplet Impact. *Adv Appl Sci Res.* 3 (2012) 649-655.

[366] Hirt, C. W.; Nichols, B. D., Volume of Fluid (VOF) Method for the Dynamics of Free Boundaries. *J Comp Phys.* 39 (1981) 201-225.

[367] Brackbill, J. U.; Kothe, D. B.; Zemach, C., A Continuum Method for Modeling Surface Tension. *J Comp Phys.* 100 (1992) 335-354.

[368] Teh, S.; Lin, R.; Hung, L.; Lee, A. P., Droplet Microfluidics. *Lab Chip.* 8 (2008) 198-220.

[369] Casadevall i Solvas, X.; deMello, A., Droplet Microfluidics: Recent Developments and Future Applications. *Chem Commun.* 47 (2011) 1936-1942.

[370] Baret, J., Surfactants in Droplet-Based Microfluidics. *Lab Chip.* 12 (2012) 422-433.

[371] Seemann, R.; Brinkmann, M.; Pfohl, T.; Herminghaus, S., Droplet Based Microfluidics. *Rep Prog Phys.* 75 (2012) 016601.

[372] Nisisako, T.; Torii, T.; Takahashi, T.; Takizawa, Y., Synthesis of Monodisperse Bicolored Janus Particles with Electrical Anisotropy using a Microfluidic Co-Flow System. *Adv Mater.* 18 (2006) 1152-1152.

[373] Nie, Z.; Park, J. I.; Li, W.; Bon, S. A. F.; Kumacheva, E., An "Inside-Out" Microfluidic Approach to Monodisperse Emulsions Stabilized by Solid Particles. *J Am Chem Soc.* 130 (2008) 16508-16508.

[374] Chen, Q.; Whitmer, J. K.; Jiang, S.; Bae, S. C.; Luijten, E.; Granick, S., Supracolloidal Reaction Kinetics of Janus Spheres. *Science.* 331 (2011) 199-202.

[375] Navia, P.; Troncoso, J.; Romani, L., Excess Magnitudes for Ionic Liquid Binary Mixtures with a Common Ion. *J Chem Eng Data.* 52 (2007) 1369-1374.

[376] Annat, G.; Forsyth, M.; MacFarlane, D. R., Ionic Liquid Mixtures - Variations in Physical Properties and their Origins in Molecular Structure. *J Phys Chem B.* 116 (2012) 8251-8258.

[377] Jablonski, P.; Müller-Blecking, A.; Borchard, W., A Method to Determine Mixing Enthalpies by DSC. *J Therm Anal Calorim.* 74 (2003) 779-787.

[378] Jiang, Y.; Xia, H.; Guo, C.; Mahmood, I.; Liu, H., Enzymatic Hydrolysis of Penicillin in Mixed Ionic Liquids/Water Two-Phase System. *Biotechnol Prog.* 23 (2007) 829-835.

[379] Tominaga, K., An Environmentally Friendly Hydroformylation using Carbon Dioxide as a Reactant Catalyzed by Immobilized Ru-Complex in Ionic Liquids. *Catal Today.* 115 (2006) 70-72.

[380] Chauvin, Y.; Olivier, H.; Wyrvalski, C. N.; Simon, L. C.; de Souza, R. F., Oligomerization Ofn-Butenes Catalyzed by Nickel Complexes Dissolved in Organochloroaluminate Ionic Liquids. *J Catal.* 165 (1997) 275-278.

[381] Bai, Y.; Cao, Y.; Zhang, J.; Wang, M.; Li, R.; Wang, P.; Zakeeruddin, S. M.; Grätzel, M., High-Performance Dye-Sensitized Solar Cells Based on Solvent-Free Electrolytes Produced from Eutectic Melts. *Nat Mater.* 7 (2008) 626-630.

[382] Wang, P.; Zakeeruddin, S. M.; Humphry-Baker, R.; GrÃ¤tzel, M., A Binary Ionic Liquid Electrolyte to Achieve 7% Power Conversion Efficiencies in Dye-Sensitized Solar Cells. *Chem Mater.* 16 (2004) 2694-2696.

[383] Lane, G. H.; Best, A. S.; MacFarlane, D. R.; Hollenkamp, A. F.; Forsyth, M., An Azo-Spiro Mixed Ionic Liquid Electrolyte for Lithium Metal– LiFePO4 Batteries. *J Electrochem Soc.* 157 (2010) A876-A884.

[384] Lin, Z.; Wragg, D. S.; Warren, J. E.; Morris, R. E., Anion Control in the Ionothermal Synthesis of Coordination Polymers. *J Am Chem Soc.* 129 (2007) 10334-10335.

[385] Long, J.; Guo, B.; Li, X.; Jiang, Y.; Wang, F.; Tsang, S. C.; Wang, L.; Yu, K. M. K., One Step Catalytic Conversion of Cellulose to Sustainable Chemicals Utilizing Cooperative Ionic Liquid Pairs. *Green Chem.* 13 (2011) 2334-2338.

[386] Lu, J.; Yan, F.; Texter, J., Advanced Applications of Ionic Liquids in Polymer Science. *Prog Polym Sci.* 34 (2009) 431-448.

[387] Torimoto, T.; Tsuda, T.; Okazaki, K.; Kuwabata, S., New Frontiers in Materials Science Opened by Ionic Liquids. *Adv Mater.* 22 (2010) 1196-1221.

[388] Ueki, T.; Watanabe, M., Macromolecules in Ionic Liquids: Progress, Challenges, and Opportunities. *Macromolecules.* 41 (2008) 3739-3749.

[389] Yoo, B.; Afzal, W.; Prausnitz, J. M., Effect of Water on the Densities and Viscosities of some Ionic Liquids Containing a Phosphonium Cation
. *Z Phys Chem.* 227 (2013) 157-165.

[390] Abdallah, D.; Weiss, R., Organogels and Low Molecular Mass Organic Gelators. *Adv Mater.* 12 (2000) 1237-1237.

[391] George, M.; Weiss, R. G., Molecular Organogels. Soft Matter Comprised of Low-Molecular-Mass Organic Gelators and Organic Liquids. *Acc Chem Res.* 39 (2006) 489-497.

[392] Pal, A.; Ghosh, Y. K.; Bhattacharya, S., Molecular Mechanism of Physical Gelation of Hydrocarbons by Fatty Acid Amides of Natural Amino Acids. *Tetrahedron.* 63 (2007) 7334-7348.

[393] Luo, X.; Liu, B.; Liang, Y., Self-Assembled Organogels Formed by Mono-Chain L-Alanine Derivatives. *Chem Commun.* (2001) 1556-1557.

[394] Abdallah, D.; Weiss, R., N-Alkanes Gel N-Alkanes (and Many Other Organic Liquids). *Langmuir.* 16 (2000) 352-355.

[395] Trivedi, D.; Ballabh, A.; Dastidar, P., An Easy to Prepare Organic Salt as a Low Molecular Mass Organic Gelator Capable of Selective Gelation of Oil from Oil/Water Mixtures. *Chem Mater.* 15 (2003) 3971-3973.

[396] Khoo, T.; Howlett, P. C.; Tsagouria, M.; MacFarlane, D. R.; Forsyth, M., The Potential for Ionic Liquid Electrolytes to Stabilise the Magnesium Interface for Magnesium/Air Batteries. *Electrochim Acta.* 58 (2011) 583-588.

[397] Khoo, T.; Somers, A.; Torriero, A. A. J.; MacFarlane, D. R.; Howlett, P. C.; Forsyth, M., Discharge Behaviour and Interfacial Properties of a Magnesium Battery Incorporating Trihexyl(Tetradecyl)Phosphonium Based Ionic Liquid Electrolytes. *Electrochim Acta.* 87 (2013) 701-708.

[398] Prausnitz, J. M., Lichtenthaler, R. N., de Azevedo, E. G., Molecular Thermodynamics of Fluid-Phase Equilibria, Prentice-Hall PTR, Upper Saddle River, N.J., 1999.

[399] Das, M.; Zhang, H.; Kumacheva, E., Microgels: Old Materials with New Applications. *Annu Rev Mater Res.* 36 (2006) 117-142.

[400] Pelton, R., Temperature-Sensitive Aqueous Microgels. *Adv Colloid Interface Sci.* 85 (2000) 1-33.

[401] Saunders, B. R.; Laajam, N.; Daly, E.; Teow, S.; Hu, X.; Stepto, R., Microgels: From Responsive Polymer Colloids to Biomaterials. *Adv Colloid Interface Sci.* 147-148 (2009) 251-262.

[402] Thorne, J. B.; Vine, G. J.; Snowden, M. J., Microgel Applications and Commercial Considerations. *Colloid Polym Sci.* 289 (2011) 625-646.

[403] Morris, G. E.; Vincent, B.; Snowden, M. J., Adsorption of Lead Ions Onto N-Isopropylacrylamide and Acrylic Acid Copolymer Microgels. *J Colloid Interface Sci.* 190 (1997) 198-205.

[404] Mulqueen, M., Huibers, P. D. T., Measuring Equilibrium Surface Tensions in Handbook of Applied Surface and Colloid Chemistry K. Holmberg (Ed.), John Wiley & sons, West Sussex, 2002, p. 201.

[405] du Noüy, P. L., A New Apparatus for Measuring Surface Tension. *J Gen Physiol.* 1 (1919) 521-524.

[406] Vonnegut, B., Rotating Bubble Method for the Determination of Surface and Interfacial Tensions. *Rev Sci Instrum.* 13 (1942) 6-9.

[407] Rowlinson, J. S., Widom, B., Molecular Theory of Capillarity, Clarendon Press, Oxford, Oxfordshire, 1982.

[408] Gibbs, J. W., On the Equilibrium of Heterogeneous Substances, The Academy, New Haven, 1874.

[409] Young, T., An Essay on the Cohesion of Fluids. *Philos Trans R Soc London.* 95 (1805) 65-87.

[410] Moody, M. P.; Attard, P., Monte Carlo Simulation Methodology of the Ghost Interface Theory for the Planar Surface Tension. *J Chem Phys.* 120 (2004) 1892-1904.

[411] Guy J. Gloor; George Jackson; Felipe J. Blas; Enrique de Miguel, Test-Area Simulation Method for the Direct Determination of the Interfacial Tension of Systems with Continuous Or Discontinuous Potentials. *J Chem Phys.* 123 (2005) 134703.

[412] Singh, J.; Kofke, D.; Errington, J., Surface Tension and Vapor-Liquid Phase Coexistence of the Square-Well Fluid. *J Chem Phys.* 119 (2003) 3405-3412.

[413] Kirkwood, J. G.; Buff, F. P., The Statistical Mechanical Theory of Surface Tension. *J Chem Phys.* 17 (1949) 338.

[414] Case, D. A.; Darden, T. E.; Cheatham III, T. E.; Simmerling, C. L.; Wang, J.; Duke, R. E.; Luo, R.; Walker, R. C.; Zhang, W.; Merz, K. M.; Roberts, B.; Hayik, S.; Roitberg, A.; Seabra, G.; Swails, J.; Gotz, A. W.; Kolossvary, I.; Wong, K. F.; Paesani, F.; Vanicek, J.; Wolf, R. M.; Liu, J.; Wu, X.; Brozell, S. R.; Steinbrecher, T.; Gohlke, H.; Cai, Q.; Ye, X.; Wang, J.; Hsieh, M. -.; Cui, G.; Roe, D. R.; Mathews, D. H.; Seetin, M. G.; Salomon-Ferrer, R.; Sagui, C.; Babin, V.; Luchko, T.; Gusarov, s.; Kovalenko, A.; Kollman, P. A., Amber 12. *University of California, San Francisco.* (2012) .

[415] Brooks, B. R.; Brooks III, C. L.; Mackerell, A. D.; Nilsson, L.; Petrella, R. J.; Roux, B.; Won, Y.; Archontis, G.; Bartels, C.; Boresch, S.; Caflisch, A.; Caves, L.; Cui, Q.; Dinner, A. R.; Feig, M.; Fischer, S.; Gao, J.; Hodoscek, M.; Im, K.; Kuczera, K.; Lazaridis, T.; Ma, J.; Ovchinnikov, V.; Paci, e.; Pastor, R. W.; Post, C. B.; Pu, J. Z.; Schaefer, M.; Tidor, B.; Venable, R. M.; Woodcock, H. L.; Wu, X.; Yang, W.; York, D. M.; Karplus, M., CHARMM: The Biomolecular Simulation Program. *J Comp Chem.* 30 (2009) 1545-1615.

[416] Kharlamov, G. V.; Onischuk, A. A.; Vosel, S. V.; Purtov, P. A., Molecular Dynamics Calculations of Small Drops Surface Tension. *Colloids Surf, A.* 379 (2011) 10-13.

[417] D'Auria, R.; Tobias, D. J., Relation between Surface Tension and Ion Adsorption at the Air-Water Interface: A Molecular Dynamics Simulation Study. *J Phys Chem A.* 113 (2009) 7286-7293.

[418] Hou, H. Y.; Chen, G.; Chen, G. L.; Shao, Y. L., A Molecular Dynamics Simulation on Surface Tension of Liquid Ni and Cu. *Comput Mater Sci.* 46 (2009) 516-519.

[419] Pohorille, A.; Wilson, M. A., Viewpoint 9 — Molecular Structure of Aqueous Interfaces. *J Mol Struct THEOCHEM.* 284 (1993) 271-298.

[420] Blokhuis, E. M.; Bedeaux, D., Pressure Tensor of a Spherical Interface. *J Chem Phys.* 97 (1992) 3576-3586.

[421] Paredes, X.; Fernández, J.; Pádua, A. A. H.; Malfreyt, P.; Malberg, F.; Kirchner, B.; Pensado, A. S., Using Molecular Simulation to Understand the Structure of [C2C1im]+-Alkylsulfate Ionic Liquids: Bulk and Liquid-Vapor Interfaces. *J Phys Chem B.* 116 (2012) 14159-14170.

[422] Werth, S.; Lishchuk, S.; Horsch, M.; Hasse, H., The Influence of the Liquid Slab Thickness on the Planar Vapor–Liquid Interfacial Tension. *Physica A.* 392 (2013) 2359.

[423] Wilson, M. A.; Pohorille, A.; Pratt, L. R., Molecular Dynamics of the Water Liquid-Vapor Interface. *J Phys Chem.* 91 (1987) 4873-4878.

[424] Ilan Benjamin, Theoretical Study of the Water/1,2-Dichloroethane Interface: Structure, Dynamics, and Conformational Equilibria at the Liquid–Liquid Interface. *J Chem Phys.* 97 (1992) 1432-1445.

[425] Linse, P., Monte Carlo Simulation of Liquid–liquid Benzene–water Interface. *J Chem Phys.* 86 (1987) 4177.

[426] Dolgikh, A. V.; Dorofeev, D. L.; Zon, B. A., Tolman's Nonlinearity of Capillary Waves. *Phys Rev E.* 67 (2003) 056311.

[427] Ismail, A. E.; Grest, G. S.; Stevens, M. J., Capillary Waves at the Liquid-Vapor Interface and the Surface Tension of Water. *J Chem Phys.* 125 (2006) 014702.

[428] Sides, S. W.; Grest, G. S.; Lacasse, M. D., Capillary Waves at Liquid-Vapor Interfaces: A Molecular Dynamics Simulation. *Phys Rev E.* 60 (1999) 6708-6713.

[429] Lacasse, M.; Grest, G.; Levine, A., Capillary-Wave and Chain-Length Effects at Polymer/Polymer Interfaces. *Phys Rev Lett.* 80 (1998) 309-312.

[430] Korochkova, E.; Boltachev, G.; Baidakov, V., Effect of Long-Range Interactions on the Surface Tension. *Russ J Phys Chem.* 80 (2006) 445-448.

[431] Bo Shi; Shashank Sinha; Vijay K. Dhir, Molecular Dynamics Simulation of the Density and Surface Tension of Water by Particle-Particle Particle-Mesh Method. *J Chem Phys.* 124 (2006) 204715.

[432] Blokhuis, E. M.; Bedeaux, D.; Holcomb, C. D.; Zollweg, J. A., Tail Corrections to the Surface Tension of a Lennard-Jones Liquid-Vapour Interface. *Mol Phys.* 85 (1995) 665-669.

[433] Buff, F. P.; Lovett, R. A.; Stillinger, F. H. J., Interfacial Density Profile for Fluids in the Critical Region. *Phys Rev Lett.* 15 (1965) 621-623.

[434] Croxton, C. A., Statistical Mechanics of the Liquid Surface, J. Wiley, Chichester [Eng.], 1980.

[435] Weeks, J. D., Structure and Thermodynamics of the Liquid–vapor Interface. *J Chem Phys.* 67 (1977) 3106.

[436] Vink, R. L. C.; Horbach, J.; Binder, K., Capillary Waves in a Colloid-Polymer Interface. *J Chem Phys.* 122 (2005) 134905.

[437] Hess, B.; Bekker, H.; Berendsen, H. J. C.; Fraaije, J. G. E. M., LINCS: A Linear Constraint Solver for Molecular Simulations. *J Comp Chem.* 18 (1997) 1463-1472.

[438] Hess, B., P-LINCS: A Parallel Linear Constraint Solver for Molecular Simulation. *J Chem Theory Comp.* 4 (2007) 116-122.

[439] Zeppieri, S.; Rodriguez, J.; Lopez de Ramos, A. L., Interfacial Tension of Alkane + Water Systems. *J Chem Eng Data.* 46 (2001) 1086-1088.

[440] Schofield, P., The Statistical Theory of Surface Tension. *Chem Phys Lett.* 62 (1979) 413-415.

[441] Bresme, F.; Chacón, E.; Tarazona, P., Molecular Dynamics Investigation of the Intrinsic Structure of Water-Fluid Interfaces Via the Intrinsic Sampling Method. *Phys Chem Chem Phys.* 10 (2008) 4704-4715.

[442] Bresme, F.; Chacón, E.; Tarazona, P.; Tay, K., Intrinsic Structure of Hydrophobic Surfaces: The Oil-Water Interface. *Phys Rev Lett.* 101 (2008) 056102-056102.

[443] Lebowitz, J. L.; Percus, J. K., Thermodynamic Properties of Small Systems. *Phys Rev.* 124 (1961) 1673-1681.

APPENDIX A

HUMIDITY-INDUCED GELATION OF AN IONIC LIQUID MIXTURE

Introduction

As discussed in Chapter 2, ILs are often called "designer solvents." This high "designability" is due to the binary nature of ILs - the presence of two species instead of one provides more degrees of freedom over which optimize a solvent for the desired application. It follows, therefore, that their flexibility can be further enhanced by adding more ionic species, effectively creating mixtures of ILs. Already, many IL mixtures have been designed for reaction media [378-380], solar cells [381, 382], batteries [383], and the self-assembly of metal-organic frameworks [384]. Mixtures can even be used to integrate processing steps. For example, by mixing a solvating IL with a catalytic IL, cellulose can be dissolved and dehydrogenated in one step at mild conditions with extremely high conversions [385]. Further reading on IL mixtures can be found in an excellent review by Niedermeyer et al. [214] . In this letter, we will focus on a mixture of two ILs: 1-butyl-3-methylimidazolium hexafluorophosphate ([BMIM][PF_6]) and trihexyltetradecylphosphonium bis(2,4,4-trimethylpentyl)phosphinate ([P_{66614}][Phos]).

Mixing behavior between ILs is usually close to ideal (i.e. negligible excess properties of mixing [214]), though there are some notable deviations. These include melting point depression and changes in packing configurations in some IL mixtures [376]. To our knowledge, immiscibility has only been reported in conjunction with large phosphonium-based ILs [215, 216, 376]. The unique mixing behavior we will discuss in this letter is the reversible gel formation in the mixture of the two ILs mentioned above. IL-based gels are valuable in that they can provide the attractive IL capabilities in applications where liquids are not well-suited (i.e. membranes) [279, 386-388]. Usually, gelation of an IL requires the addition of a gelator such as 12-hydroxystearic acid [201,

270] or a polymer [386]. However, the IL mixture discussed in this report only requires the addition of small amounts of water to form a gel. The advantage here is that water can be easily removed, due to the non-volatility of the ILs, thus allowing the gelling processes to be completely reversible.

Methodology

IL mixtures were prepared by placing specified masses of [BMIM][PF_6] (Aldrich, 97%) and [P_{66614}][Phos] (Aldrich, 95%) in a single vial and agitating via sonication (Sonics VibraCell 500W). These mixtures were then allowed to absorb water from the atmosphere, which is when gelling ensued. Differential interface contrast (DIC) images of the gel samples on glass slides were taken using a laser scanning confocal microscope (Leica SP5). Images of gel growth were obtained by observing the IL mixture on an open slide (no coverslip) so as to allow for the absorption of atmospheric water. Rheological measurements were taken at a strain rate of 0.1% using a TA instruments AR-G2 rheometer at ambient conditions. Differential scanning calorimetry measurements were taken using a TA DSC Q20, equilibrating the sample at 0^{o}C followed by a scan from -20^{o}C to 50^{o}C. All drying procedures were performed in a vacuum oven (Isotemp 281A) or water bath at 50^{o}C.

Results and Discussion

Control experiments performed under vacuum experienced no observable gelation, highlighting the importance of this small addition of water. It should be noted that this effect is rather unusual since each of these ILs exhibits lowered viscosity with increased water content [127, 389]. Figure A.1 shows gel growth over time in a mixture of 0.9233 g of [BMIM][PF_6] and 1.0767 g of [P_{66614}][Phos]. It should be noted that

although the ILs were vigorously mixed, they did not immediately form a homogenous phase. These ILs exhibit somewhat transient miscibility, with $[P_{66614}][Phos]$ initially forming droplets in $[BMIM][PF_6]$ (See Section 3.3.5). For this reason, the mixture initially appears opaque. The droplets disappear within a few hours as the ILs diffuse into one another and in the absence of water the mixture assumes a clear appearance. Due to the highly viscous nature of this IL mixture, the growth rate was on the order of hours. Within two hours, the beginning of gel growth could be seen at the bottom of the vial, as indicated by the slightly lighter spot at the bottom of the vial. The top portion of the mixture also formed a gel (opaque region at the top of the vial) and both growths continued to expand until meeting at 25 hours. At this point, the entire mixture assumed an opaque appearance due to gelling. Differences in water content were likely responsible for the two-phase appearance at 25 hours (since the top layer was directly exposed to the atmosphere), but both layers were gels. The resulting materials appeared viscoelastic and formed peaks in response to manipulation with a spatula.

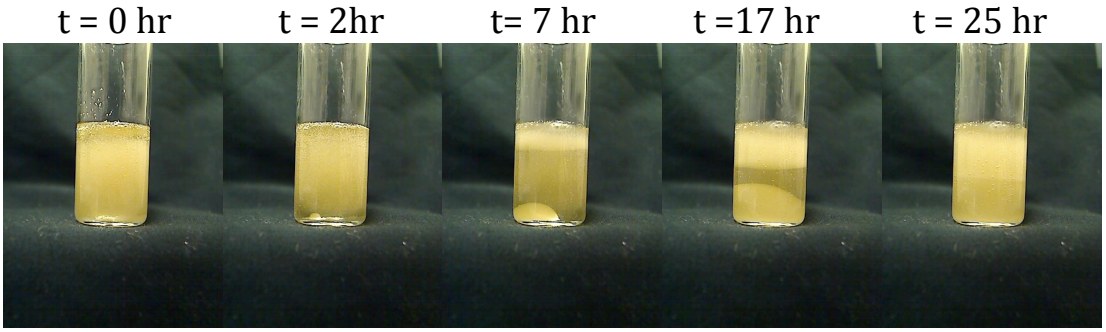

Figure A.1 Time evolution of gel growth (opaque regions) in a mixture of $[BMIM][PF_6]$ and $[P_{66614}][Phos]$.

Microscopically, gel growth occurred via two steps. Figure A.2 shows differential interface contrast (DIC) images of the IL mixture over time. In the first few minutes,

small fractal structures grew outwards from central points until they made contact with other growths. These structures were very fine and appear as dark regions in Figure A.2. In later stages, these contact surfaces served as "grain boundaries" separating individual microstructures. After 1000s, we began to see the appearance of larger fibril structures, which are characteristic of gel morphology [273]. As these larger structures grew, the smaller fractal growths began to disappear, indicating that they may have been incorporated into the fibrils. It should be noted, however, that some of these smaller fractal structures were convectively transported away from the growing fibrils during observation. Thus, the two steps of growth are (1) the formation of small fractal structures and (2) their disappearance with the simultaneous growth of larger fibrils. The first structure grew much more quickly than the second. These self-assembled structures provided the gel with an opaque appearance and viscoelastic nature.

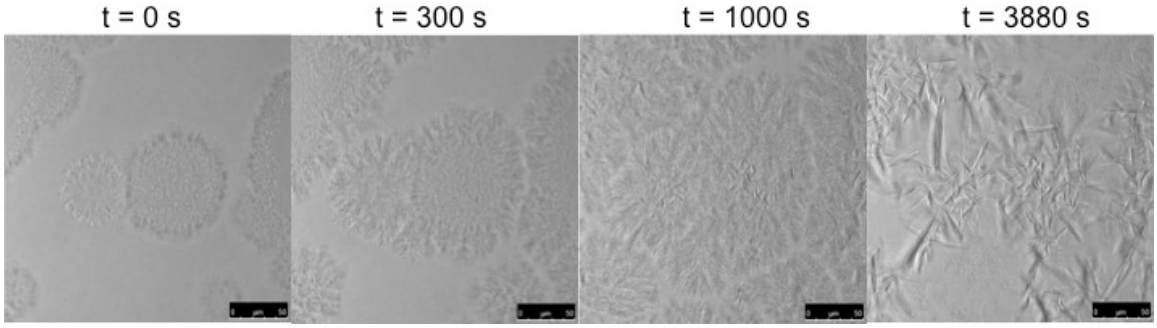

Figure A.2 Differential interface contrast images of gel growth in the IL mixture over time. At t = 0, the gel growth is represented by the darker regions in the center and sides of the image.

Phase behavior of this gelling system was quantified by measuring the water uptake of various mixtures of [BMIM][PF_6] and [P_{66614}][Phos] and observing whether or not a gel was formed in each mixture. These results are shown in Figure A.3. Here, only the mass/mole fractions of water and [BMIM][PF_6] and shown with the implication that

the balance of each system was composed of $[P_{66614}][Phos]$. Phosphonium-rich mixtures absorbed the most water from the atmosphere, but did not exhibit consistent gelation behavior. As the fraction of $[BMIM][PF_6]$ increased, water uptake decreased significantly and gel formation became consistently observable. Mixtures with $[BMIM][PF_6]$ mole fractions between 0.34 and 0.74 gelled upon absorbing water, as marked in the phase diagrams. Systems with mole fractions between 0.48 and 0.55 formed homogenous gels, whereas systems on the extremes of the gelling region often exhibited multiple gel phases, like the one seen in Figure A.1, likely due to premature phase separation in the IL mixture. Both mole and mass fractions of water decreased with $[BMIM][PF_6]$ content, suggesting that water primarily interacted with $[P_{66614}][Phos]$. However, the mass of water was relatively low, indicating that the gel was primarily composed of ILs. It should also be noted that even at miximum water saturation, no gelation was observed in either of the pure ILs.

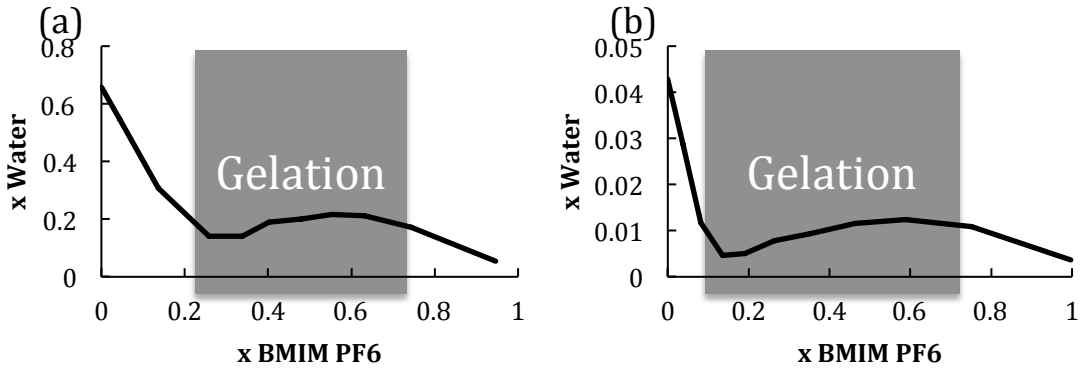

Figure A.3 Water uptake of the IL mixture in terms of (a) mole fraction and (b) mass fraction with respect to $[BMIM][PF_6]$ content (balance is $[P_{66614}][Phos]$). The gray region indicates mixtures in which gel formation occurred.

To demonstrate the difference between gelling and non-gelling mixtures of these ILs, we extracted rheological properties of four mixtures. Gelling mixtures contained [BMIM][PF_6] at mole fractions of 0.6 and 0.7 and non-gelling mixtures contained [BMIM][PF_6] at mole fractions of 0.1 and 0.2. Rheological measurements of storage/elastic modulus (G') and loss/viscous modulus (G'') and are plotted in Figure A.4 with respect to angular frequency. Upon gelation, the loss and storage moduli both increased by several orders of magnitude due to increased resistance to flow. Also, both G' and G'' of the gelled mixtures had similar values for the frequency range used, indicating that the gel was a viscoelastic material. Thus, we were able to see that the microstructures seen in Figure A.2 had a significant effect on the rheological properties of this IL mixture.

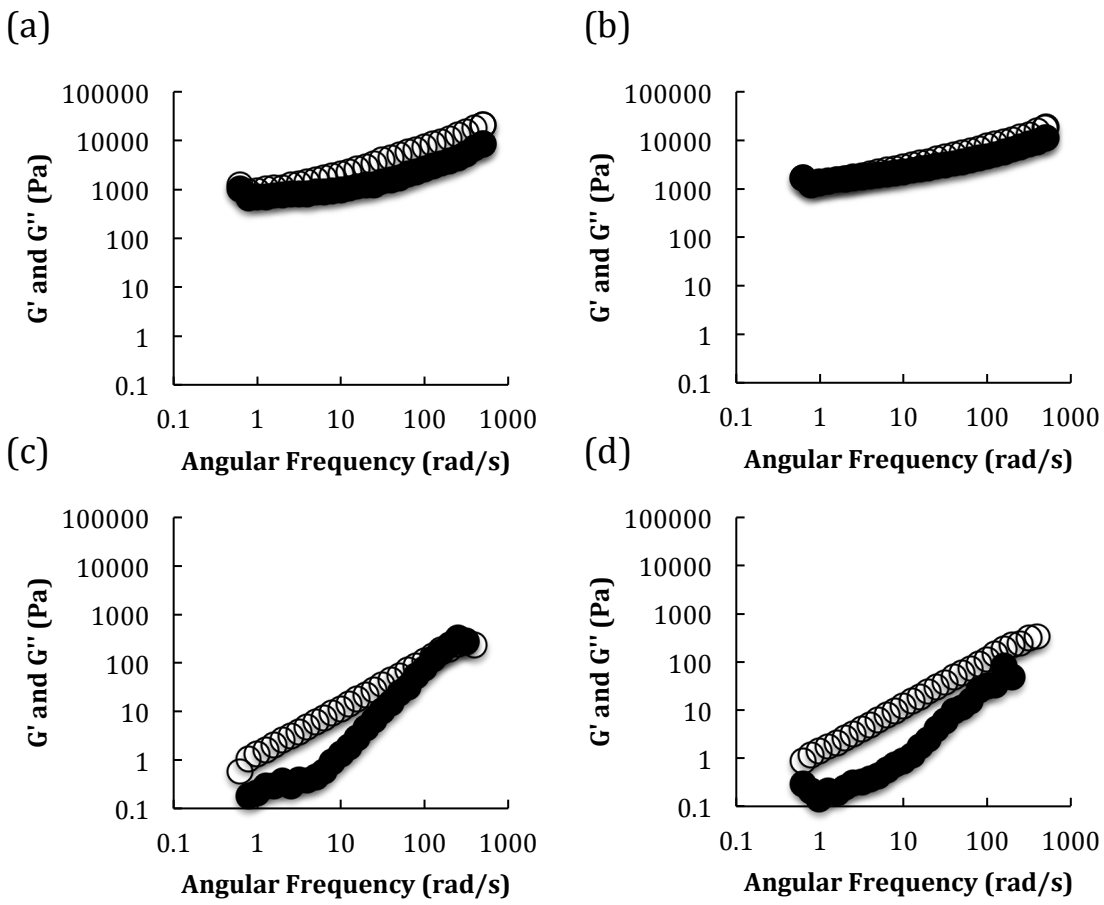

Figure A.4 Measurements of storage modulus (G', filled circles) and loss modulus (G'', open circles) of [BMIM][PF_6]/[P_{66614}][Phos] mixtures with [BMIM][PF_6] mole fractions of (a) 0.6, (b) 0.7, (c) 0.1, and (d) 0.2. In accordance with **Figure A.1**, samples measured in (a) and (b) were gels whereas those in (c) and (d) were liquids.

Gelation is a macroscopic manifestation of a molecular self-assembly phenomenon [390-392]. It occurs when the gelator molecules self-assemble into large networks that "trap" the continuous phase. The driving forces behind this self-assembly process are non-covalent interactions such as hydrogen bonding, $\pi - \pi$ interactions, and electrostatic interactions [266, 279, 392, 393]. The question was which species in our system served as gelators, self-assembling into large networks? Generally, gelator species

are large organic molecules with functional groups capable of forming large networks. Some examples include 12-Hydroxystearic acid [266, 267], fatty acid amides [392], and long (24-36 carbons) n-alkanes [394]. Generally, they gelator is only present in very small amounts (i.e. $\leq$ 5wt%) [390], so in terms of mass, water could be considered the gelator in this system. It is evident, however, that the water molecules would need to combine with other species in the system to form a sufficiently large self-assembled network. Since the molecular size and carbon chain length of [BMIM][PF_6] were relatively small, it seemed unlikely that this IL played a primary role as a gelator. In fact, [BMIM][PF_6] and similar ILs are often seen in the continuous phase of IL-based gels [201, 270, 395]. [P_{66614}][Phos] was very much like an organogelator, with H-bond capable function groups in the midst of long carbon chains. In fact, other [P_{66614}]-based ILs have been shown to form gels in the absence of additional gelator molecules [396, 397]. FTIR spectra show that a distinct O-H stretch at 3681 cm^{-1} in a [P66614][Phos]/water mixture shifted down to 3650 cm-1 upon addition of [BMIM][PF_6] (See Figure A.5). This suggests that hydrogen bonds in the [P66614][Phos]/water mixture (i.e. P-O-H) were weakened upon interacting with [BMIM][PF_6] and perhaps forming new hydrogen bonds such as P-O-H-F or P-O-H-C. Furthermore, imidazolium-based ILs are known to increase ordering in Phosphonium-based ILs due to the formation of extra H-bonds, decreasing entropy [216]. For these reasons, we propose that [P_{66614}][Phos] played the primary role in forming the self-assembled networks that gelled the system. This does not imply, however, that [BMIM][PF_6] was absent from self-assembled gel structure. We prepared an array of IL mixtures like those of Figure 3 with [BMIM][PF_6] replaced by [BMIM][BF_4] and [BMIM] bis(trifluoromethylsulfonyl)imide and found that

no gels were formed. Therefore, [BMIM][PF_6] was necessary for gel formation, which indicates that [P_{66614}][Phos] was not the only species incorporated into the self-assembled network. [BMIM][PF_6] possesses effective H-bond sites[235] and, along with water, provided the necessary interactions for the molecular self-assembly of the gelling network in this system.

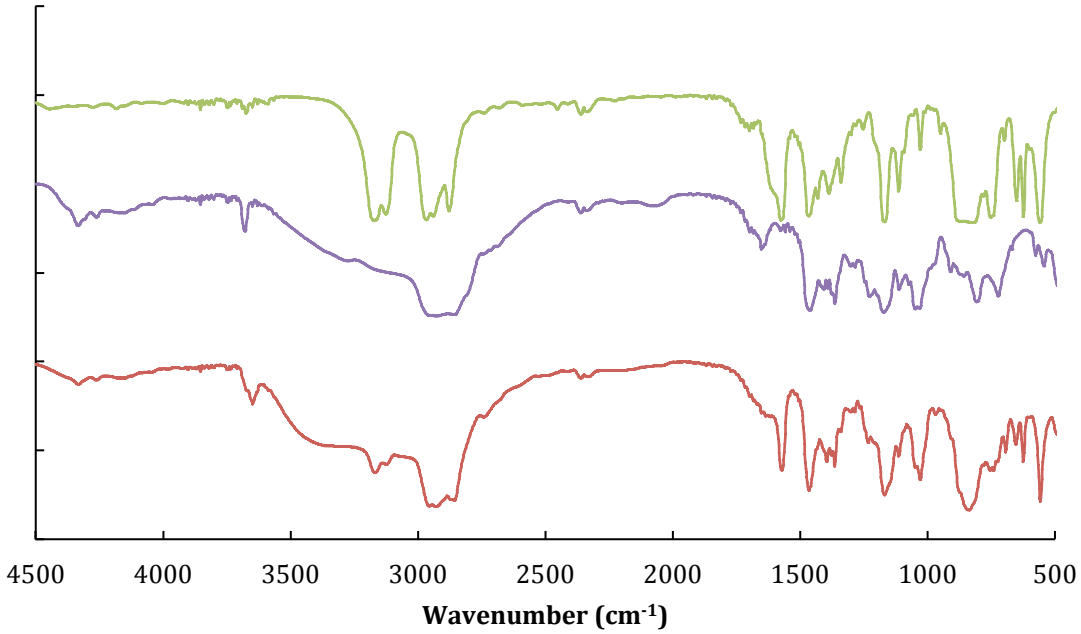

Figure A.5 FTIR spectra of [BMIM][PF_6] (green), [P_{66614}][Phos] (purple), and their gelled mixture (red).

Given that gelation took place only when water was present, we hypothesized that if water was removed, the mixture would again assume a liquid state. Water was removed either by heating in a vacuum oven. In all cases, the mixture assumed a liquid state identical to that before gelation. This process (See Figure A.6) was repeated multiple times, indicating that the gelation of this IL mixture was highly reversible and could be controlled by simply changing the water content. Herein, the advantageous non-volatility of ILs is highlighted as it facilitates this process, allowing only water to be removed.

Furthermore, since most gels use polymers or small organic molecules as gelators, the fact that the gelator (water) can be removed is rather unique. This phenomenon opens up new potential applications for an environmentally (i.e. humidity) responsive gel.

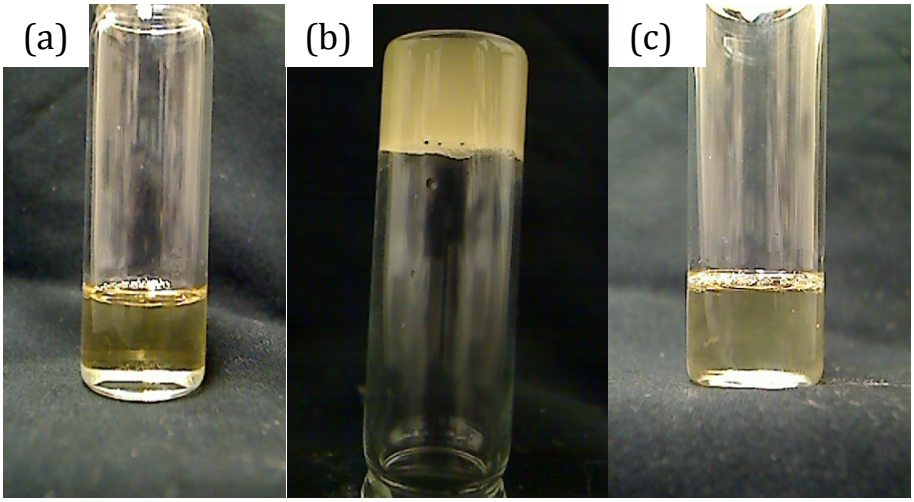

Figure A.6 Macroscopic views of the IL mixture (a) after initial mixing, (b) after gelation, and (c) after drying.

It should be noted that while the visually observable properties of the gel and liquid were restored upon adding or removing water, reversibility was not perfect. Figure A.7 shows representative differential scanning calorimetry (DSC) scans from 0 ^{o}C to 50 ^{o}C of (A) a gel formed directly from the IL mixture at room temperature, (B) a gel that had been dried to form a liquid state, then allowed to gel again, and (C) a gel formed directly from the IL mixture at -20^{o}C. Gel A exhibited two valleys at approximately 22 ^{o}C and 30 ^{o}C, which were integrated to give heats of melting of 1.5 kJ/mol and 2.0 kJ/mol, respectively. Gel B gave a single valley at 31^{o}C with a heat of melting of 1.1 kJ/mol. Therefore, gel B melted at a higher temperature, but required less energy to do so. Since these heats of melting were in the range of physical bonds [398], the data

suggest that gel B contained fewer physical bonds than gel A. Interestingly the valley of gel B exhibited high overlap with second valley of gel A. This suggests the two gels underwent similar transitions at approximately 31^{o}C. Figure A.2 shows that there were two types of structures that formed during gel growth: small fractal structures and large fibrils. We hypothesized that the two valleys of the gel A corresponded to the melting of these two types of structures. To test this hypothesis, we prepared a mixture of the two ILs and immediately placed it in the freezer at -20^{o}C (gel C). This caused the mixture to gel rapidly while forming only small fractal structures (left image of Figure A.7), in contrast to the large fibrils formed in Gel B (right image in Figure A.7). Figure A.7 shows that the DSC scan of gel C yielded a single valley that showed strong overlap with the first valley of the gel A. These results support our hypothesis that the two valleys seen in gel A were due to the melting of the two different self-assembled structures seen in Figure A.2 and Figure A.7. These results also suggest that while the rheological and visual properties of the gel could be restored through various drying and humidifying cycles, the internal structure was not always the same, as emphasized in the microscopic images of Figure A.7. Particularly, the large fibril structures became dominant over time (and drying cycles), repressing the reoccurrence of the small fractal structures. This may be due do the very slow chemical reaction between [BMIM][PF_6] and water [125], which would change the chemical composition of the gel and perhaps hinder self-assembly of the small fractal structures. Theoretical work on the molecular mechanisms behind this phenomenon is underway.

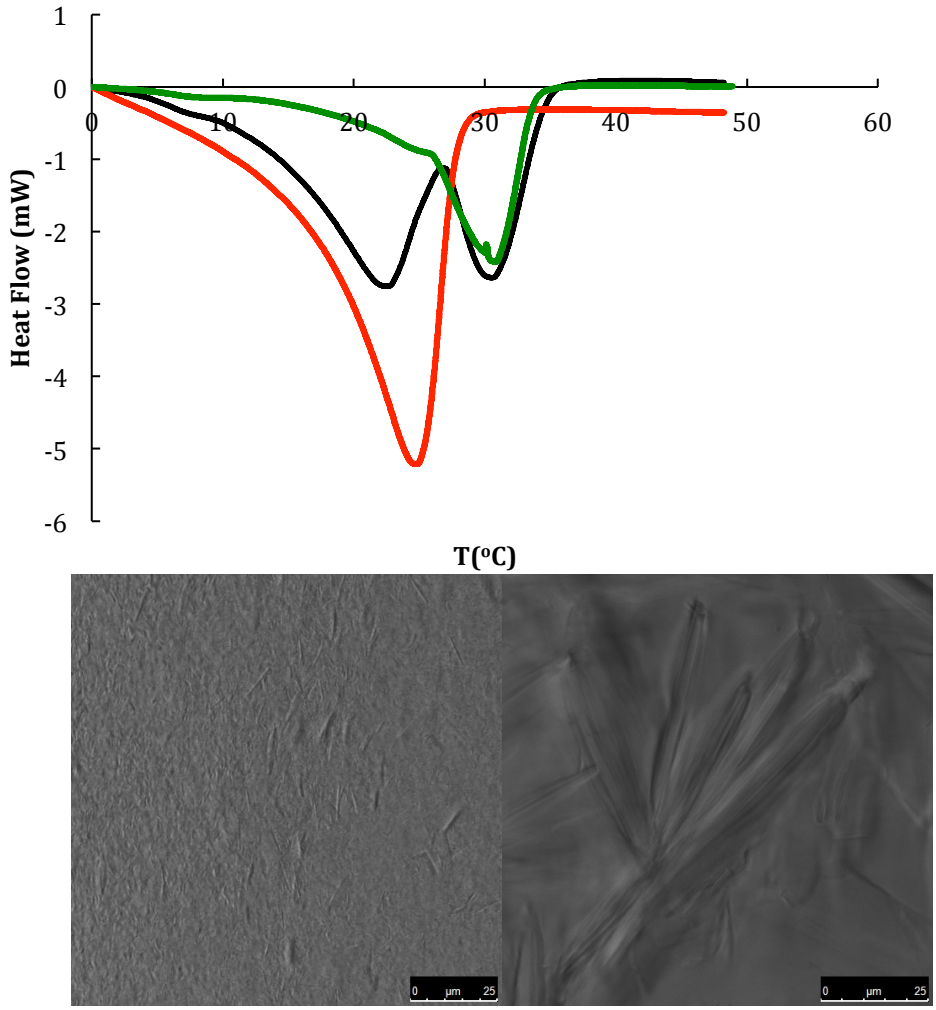

Figure A.7 DSC scans of an IL mixture allowed to gel at ambient conditions (black), and IL mixture that was gelled, dried, and re-gelled (green) and an IL mixture that was gelled at -20°C (red) to ensure that only the small-fractal structures were formed. DIC images of the self-assembled gel morphologies for the frozen gel and re-gelled gel are shown in the bottom left and bottom right images, respectively. Darker regions represent fibril formation. Scale bars represent 25 microns.

This gelling behavior may have many useful applications. In metal-air batteries, phosphonium-based IL electrolytes can form a stabilizing gel passivation layer at the air contact [396, 397]. With respect to colloids, the area of microgels has received increasing attention due to excitement over applications such as drug delivery, enhanced oil recovery, biomaterials, and water treatment [399-402]. A particularly attractive feature of

many microgels is their environmental responsiveness ("smart" particles), in which the individual particles react to changes in temperature, pH, or ionic strength [399-402]. We endeavored to create microgels by dispersing the IL mixture in water. Given that the gelation process was rather slow, we hypothesized that the IL droplets would absorb water and form individual microgels with the added flexibility that the microgels could be collected again into a single entity upon heating, whereupon the microgels would become liquid droplets an coalesce. As an initial test, we found that in the presence of excess water, the gel did not break down until 38^{o}C. Therefore, heating above this temperature was necessary. We added approximately 0.1 g of the IL mixture to 1 mL of water and agitated the system using sonication (Sonics VibraCell 500W). The resulting colloidal suspension is shown in Figure A.8a. Over a period of one month, this suspension did not settle and the liquid retained its opaque appearance. Microscopically, (inset of Figure A.8) the microgels ranged in size from 1-10 μm in diameter and usually, though not always, exhibited spherical shapes. Upon heating, the suspension quickly destabilized and Figure A.8b shows the two large gels that formed after cooling. These gels were removed and dried and thus forced back to a liquid state. Therefore, we have shown that this IL mixture can be used to create microgels and also that their formation is easily reversible. Such behavior may be useful in applications where microgels are used for removing species from a bulk phase [400, 403], because they can be collected and removed with relative ease.

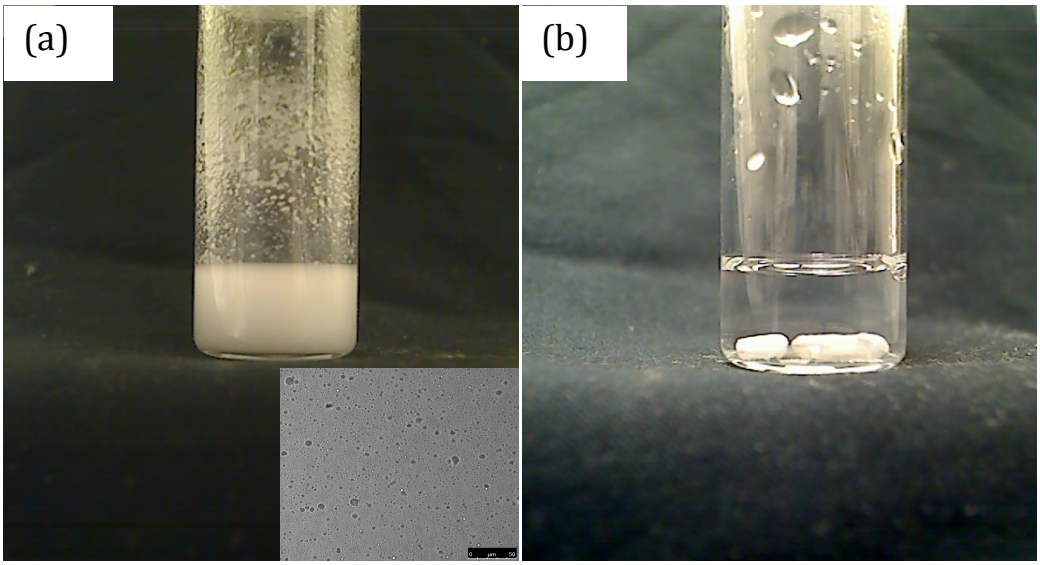

Figure A.8 Macroscopic views of (a) a dispersion of microgels (shown microscopically in the inset as a DIC image) formed from the IL mixture and (b) its destabilization upon heating.

Conclusion

We have reported the unique gelation behavior of a mixture of [BMIM][PF_6] and [P_{66614}][Phos] which forms a gel upon contact with finite amounts water. Gelation occurred over a matter of minutes to hours (depending on water exposure) through the formation of microscopic fractal structures that matured into long fibrils. Gelation only occurred when mole fractions of [BMIM][PF_6] were between 0.28 and 0.76, whereupon the elastic and storage moduli of the mixture increased by 1-2 orders of magnitude. Interestingly, the mixture resumed a liquid state upon drying, whereupon a gel could be formed again by addition of water. This reversibility was exploited in the creation of microgels that could be dispersed in water, then coalesced upon heating and drying. Gel formation was sensitive to the choice of anion, suggesting that hydrogen bond formation between the anion and water species played an important role in the gelation process.

APPENDIX B

COMPARISON ON THE CAPILLARY WAVE METHOD AND PRESSURE TENSOR ROUTE FOR CALCULATION OF INTERFACIAL TENSION IN MOLECULAR DYNAMICS SIMULATIONS

Introduction

The importance of surface tension is ubiquitous in natural and industrial processes. One simple example is that surface tension is responsible for the spherical shape of liquid droplets and bubbles. Thermodynamically, it is a measure of the free energy required to create a unit area of the specific surface or interface. Surface tension is of fundamental importance as it determines stability and capillary behavior biphasic systems such as emulsion, bubbles, and foams as well as microfluidic devices [186, 187], and self-assembly processes [23, 65]. Measuring surface tension quantity can be accomplished with goneometers, tensiometers, and spinning drop techniques [404-406]. These methods provide accurate determination of surface tension, which is imperative in applications where biphasic systems occur. Furthermore, surface tension plays a key role in describing unique capillary phenomena such as capillary waves, [407] marangoni flow [177, 408], and wetting behavior [409]. Surface tension-dependent phenomena such as these can also be investigated computationally, where a molecular view of the interface can be obtained.

Accurate and precise calculation of surface tension is becoming increasingly important in molecular models, particularly as they are used to examine nano-scale capillary phenomena. Molecular dynamics (MD) simulations provide a unique tool for such studies, allowing for a molecular-resolution view of the interface and its dynamics [128, 247, 248, 292, 293, 297, 298]. Surface tension is also a useful quantity for evaluating the adequacy of molecule-specific force fields [223] and the mechanisms behind particle-interface interactions [19, 27, 247, 248]. Theoretically, surface tension can be calculated at every time step of the simulation, but time-averaging is generally

necessary to obtain reliable results. However, these calculations can be problematic in some systems due to high fluctuation between time steps. In this report, we will discuss some of systems and how alternative methods can be used to calculate surface tension with reasonable precision.

Multiple methods have been used to calculate surface tension in both molecular dynamics (MD) and Monte Carlo (MC) simulations. Some methods base their calculation on the change in surface free energy caused by a change in surface area [410, 411]. Other methods are applied to MC simulations and base their calculations on density-distribution or on pressures calculated from volume perturbations [412]. However, the primary method for calculating surface tension in MD and MC simulations remains the Kirkwood-Buff method (also known as the pressure tensor route), which is based on the difference between the pressures normal and tangent to the interface [413]. Common MD simulation packages offer the pressure tensor method as part of their internal analysis tools[319-321, 414, 415], and new computational methods for calculating interfacial tension are often evaluated by checking their results against the pressure tensor route. However, the pressure tensor route method has some limitations, as will be discussed below.

The advantage of the pressure tensor route lies in its straightforward implementation, requiring extraction of the xx, yy, and zz components of the pressure tensor, which is often already calculated as part of the MD algorithm. In a standard MD simulation, the difference in pressure tensor components can be averaged over time to give surface tension values that often show good agreement with experimental values [223, 292, 298, 341, 416-418]. However, due to the necessarily small scale of MD

systems, pressure fluctuates widely during a simulation and there have been concerns about how the fluctuation affects the precision the surface tension calculation using the pressure tensor route [419, 420]. Indeed, surface tension calculations using this method have reported significant variation: 10% in ionic liquid [421] and Lennard-Jones fluid surface tensions [422], 17% in water surface tension [423], 57% in water/1,2-dichloroethane interfacial tension [424], and 80% in water/benzene interfacial tension [425]. Furthermore, the accuracy of this method becomes questionable for systems of lower interfacial tension, where the assumption of a flat interface tends to break down [426-429]. Efforts to improve the reliability of these calculations have so far focused on accounting for the effects of long-range molecular interactions [430]. Since most simulations only evaluate interaction potentials within a certain cut-off distance, including a tail correction in the pressure tensor method may give interfacial tensions closer to experimental results [431, 432]. However, these corrections can only be used for systems in which both phases are made up of the same components (i.e. liquid-vapor interfaces), and do not lessen the magnitude of the fluctuations in pressure.

In contrast, the capillary wave technique not only accounts for but also takes advantage of fluctuations in the interface. This technique is based on the capillary wave theory proposed by Buff et al. in 1965 [433]. According to this theory, capillary waves that travel across an interface must do work against interfacial tension as they distort the surface. Therefore, the magnitude of these fluctuations of the interface can be related to interfacial tension [433]. If surface fluctuations can be measured, then, they can be used to calculate interfacial tension [407, 434, 435]. In this way, interfacial tension can be calculated in MD simulations without direct use of the widely-varying pressure tensor.

Since the method relies simply on the position of molecules in the system rather than on any dynamic effects, it is reasonable to assume that the method would also work for MC simulations. Indeed, capillary wave theory has been shown to agree with the results of MC simulations when the surface has been adequately defined [436]. Our hypothesis was that by using this method, calculation of surface tension and interfacial tension would yield higher-precision results compared to those obtained with the pressure tensor route.

This paper compares the pressure tensor and capillary wave methods for systems involving water, hexane, and an ionic liquid (IL), 1-butyl-3-methylimidazolium hexafluorophosphate ([BMIM][PF_6]). The ionic liquid is examined because, unlike many force fields that are optimized for density, the [BMIM][PF_6] force field has been specifically optimized for interfacial properties such as interfacial tension [223]. Both liquid-vapor and liquid-liquid interfaces are examined.

Methodology

The pressure tensor method of calculating interfacial tension relates the tension to the difference between the pressure normal to and tangential to the surface. In a planar interface, where the plane is normal to the z direction, this becomes

$$\gamma = -\frac{1}{n}\left(\frac{p_x + p_y}{2} - p_z\right)L_z \tag{B.1}$$

where γ is interfacial tension, p_x, p_y, and p_z are components of the pressure tensor, L_z is the height of the simulated box and n is the number of interfaces [413]. This method assumes a flat interface parallel to the xy plane. In this study, the interfacial tension was calculated for each interface using GROMACS 4.5 analysis tools, which utilize the

pressure tensor method. Interfacial tension was calculated at each 10 ps of the simulation run. These values were then averaged over each nanosecond.

Much of the fluctuation of an interface is due to capillary waves at the interface, and the amplitude of this fluctuation is related to the interfacial tension. Capillary wave method takes advantage of this fluctuation over time to calculate the interfacial tension. When the effects of gravity are neglected, as they are in most molecular simulations, this relationship is described by

$$\gamma = \frac{k_B T}{2\pi\sigma^2} \ln\left(\frac{L}{l}\right) \tag{B.2}$$

where k_B is the Boltzmann constant, T is the absolute temperature, σ is the fluctuation of the interface from its equilibrium position, L is the length of the box in the x or y direction, and l is molecular diameter[419, 424]. In this study, l was taken as an average molecule diameter across all species in a particular system.

Determination of Interface Fluctuation

A weakness of the capillary wave method is the need to define the interface in space in order to determine its fluctuation [419]. There is no general consensus on how to define the interface in a way that is consistent across different systems, so this process can be somewhat arbitrary [248, 292]. One way to define the interface is to fit the simulation results to a density profile such as the error function density profile [424]:

$$\rho(z) = \frac{1}{2}(\rho_A + \rho_B) - \frac{1}{2}(\rho_A - \rho_B)\mathrm{erf}\left(\frac{z - \langle h \rangle}{\sqrt{2}\sigma}\right) \tag{B.3}$$

where ρ_A and ρ_B are the bulk densities of each phase and $\langle h \rangle$ is the average z position of the interface. This profile can be fit to the simulation results using an iterative method,

and the resulting σ can then be used in Equation B.2. Interfaces are often fit to a hyperbolic tangent profile. However, profiles based on the error function give calculated interfacial tensions in better agreement with the pressure tensor method[427, 428]. In this study, each interface was analyzed using the error function profile. This was done by taking the average density profile over one nanosecond of simulation time and fitting it to Equation B.3.

An interface can also be defined by the z coordinated of individual molecules [424]. In this method, the simulation box is divided into *N* columns parallel to the *z* axis. The *z* position of the interface (*h*) is then calculated for each column using the equation

$$h = \frac{1}{2}[\max(z_A) + \min(z_B)] \tag{B.4}$$

where $\max(z_A)$ is the largest *z* coordinate of any molecule in the *A* phase and $\min(z_B)$ is the smallest *z* coordinate of any molecule in the *B* phase. The *A* phase is below the interface and the *B* phase is above it. This *h* is instantaneous. The standard deviation of *h* between the columns in then taken as σ. A weakness of this approach is that it cannot be used for single component liquid-vapor interfaces. In this study, therefore, only the liquid-liquid interfaces were analyzed in this way. This study split each simulation box into a 10x10 grid ($N = 100$). Each box contained two interfaces at different *z* coordinates. To distinguish between them, z_{est}, a rough estimate of the *z* position of each interface was chosen by observation. Only molecules within a 2 nm of this position were considered part of the interface. If a particular column did not include molecules of both phases that column was not considered in calculating σ, and z_{est} was adjusted to minimize these exclusions. The instantaneous surface tension was then calculated for every 10 ps of the

simulation using Equation B.2 and the average taken over each nanosecond, as with the pressure tensor method.

Computational Details

All MD simulations were performed using the GROMACS 4.5 package[319-321]. The initial simulation box for each of the smaller systems was approximately 5.5 x 5.0 x 11.0 nm^3. The initial simulation box for the larger IL/water system was approximately 12.5 x 12.0 x 21.0 nm^3. Periodic boundary conditions (PBC) were applied in all three directions for each simulated box.

Water was described with the extended simple point charge (SPC/E) model [323] and hexane by the optimized intermolecular potentials for liquid simulations (OPLS) united atom force field[228]. The force field for the IL was an all-atom force field developed by Lopes, et al. [221, 222] and modified by Bhargava and Balasubramanian [223, 326] for more accurate interfacial behavior. For this force field, all H-bonds were constrained by the LINCS algorithm [437, 438].

After the initial boxes were generated, 1,000 energy minimization steps were performed using the steepest descent method. Initial atomic velocities were generated with a Maxwellian distribution at an absolute temperature of 300 K. Newton's equation of motion was integrated using the leap-frog algorithm with a time step of 0.002 ps. All simulations were carried out under the NPT ensemble (except for liquid-vapor systems, which used the NVT ensemble) using the Berendsen-thermostat [231] to maintain temperature at 300K and pressure at 1 bar by coupling the system to an external bath. The Particle-Mesh Ewald (PME) method was used to account for long-range electrostatic

interactions. The cut off distance for Lennard-Jones forces was chosen as r = 1.2 nm to match the cut-off used by the developers of the IL force field [223, 326].

Liquid-liquid interfaces were created placing an equilibrated box of one liquid (water, hexane, or IL) next to an equilibrated box of another liquid. These initial boxes were then simulated for four parallel runs of 20 ns each, except for the large IL/water system, which underwent four parallel runs of 15 ns. After the simulations were complete, interfacial tensions were evaluated for each system using both the pressure tensor and the capillary wave methods. Details of each simulation are shown in Table B.1.

Table B.1 Composition and parallel run details of the interfacial simulations examined in this study.

System	[BMIM]	[PF_6]	Hexane	Water	Runs
A (Hexane)	0	0	728	0	4
B (IL)	400	400	0	0	4
C (Hexane/Water)	0	0	541	4491	4
D (IL/Hexane)	400	400	652	0	4
E (IL/Water)	400	400	0	4483	4
F (IL/Water)	3200	3200	0	35375	3

Results and Discussion

To illustrate the behavior of surface tension throughout a simulation using the pressure tensor route, we generated individuals charts of the calculated surface tension values. Individuals charts provide a statistical view of data recorded over time, indicating the time-average as well as the limits within which data falls under normal conditions. The upper and lower control limits (UCL and LCL, respectively) were calculated using Equations B.5 and B.6 and provided an idea of the degree of variation throughout the simulation. In these equations, $\bar{x}$ represents the average value and $\overline{MR}$ represents the

average moving range of measurements. These charts plot surface tension calculations from the last 5 ns of representative simulations (by which time equilibration had been achieved). Figure B.1a plots pressure tensor route surface tension calculations for a hexane/vacuum system, and Figure B.1b reports the calculations for an IL/water system. For the hexane-vacuum system, an average interfacial tension of 17.2 mN/m was calculated, which agrees fairly well with the experimental value of 18.4 mN/m [327]. However, the IL/water system gave an average value of 2.7 mN/m, whereas the experimentally measured value is 10.06 mN/m [166]. Unfortunately, for both systems, the calculated interfacial tension varied wildly throughout the simulation. The upper and lower control limits for the hexane simulation were 299.1 mN/m and -264.1 mN/m, respectively, indicating that that the calculated interfacial tension could vary more than two orders of magnitude above or below the average value, even into physically impossible negative values. Variation was even higher in the IL/water system, which gave upper and lower control limits of 529.5 mN/m and -524.0 mN/m, respectively. This high variation may have been caused by the inherently lower interfacial tension of this system as well as the use of pressure coupling. Regardless, the variation in both systems is quite high and demonstrates that the pressure tensor method of calculating interfacial tension lacks precision. A closer look at the liquid interfaces gives us an idea of how to improve this precision.

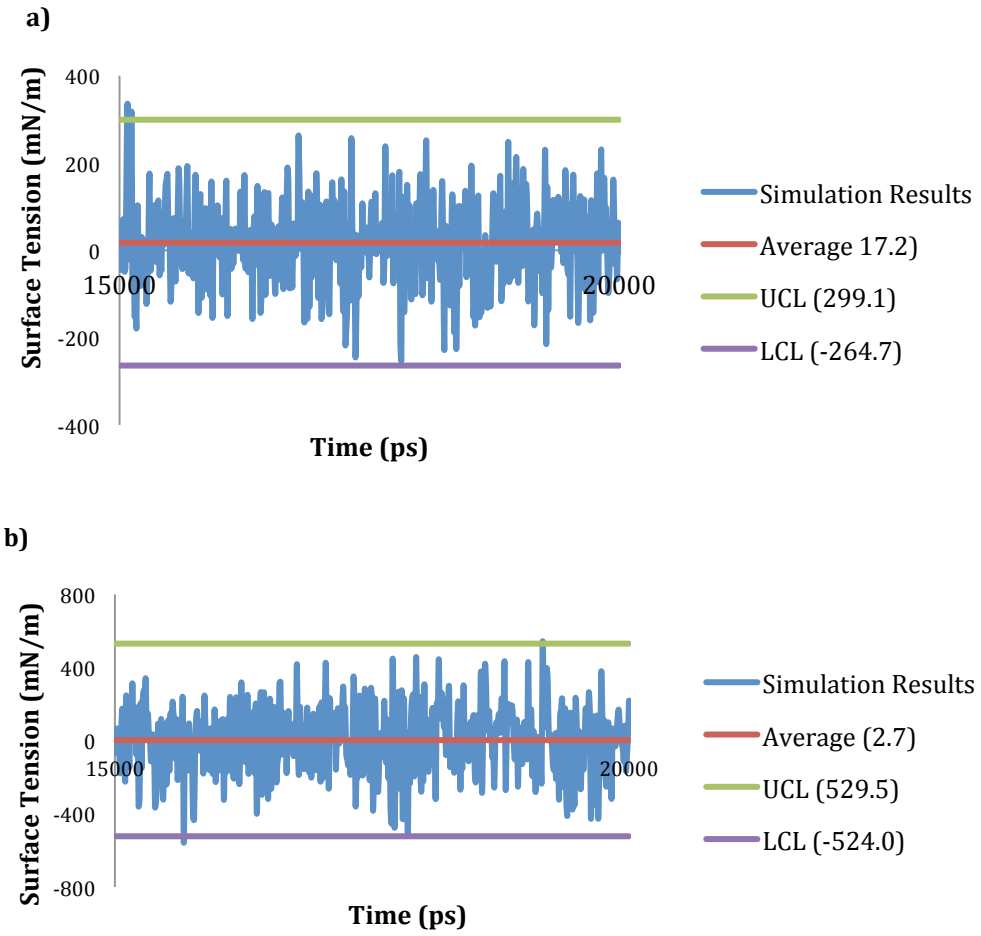

Figure B.1 Control charts for the interfacial tension of the (a) hexane liquid/vapor and (b) IL/water interfaces calculated using the pressure tensor method.

$$UCL = \bar{x} + 2.66\overline{MR} \tag{B.5}$$

$$LCL = \bar{x} - 2.66\overline{MR} \tag{B.6}$$

Figure B.2 shows the interfaces for the three liquid-liquid systems studied. The interfaces are represented by snapshots of the MD simulation and by bicubic interpolations of the simulated liquid-liquid interfaces. The interfaces are clearly not flat,

but instead exhibit peaks and valleys that change with time. This may explain the lack of precision of the pressure tensor method, which assumes a flat surface. In fact, the unevenness of the interface is directly connected to the interfacial tension. Capillary wave theory predicts that interfaces with lower interfacial tension will be rougher than interfaces with higher interfacial tension [407, 434]. According to this theory, a lower interfacial tension means that less work is required to increase the area of the interface. This suggests that, the lower the interfacial tension, the greater the amplitude of the capillary waves that ripple across the interface. The three simulations shown in Figure B.2 support capillary wave theory in this regard. The interpolations of the interfaces show that the IL/water and IL/hexane interfaces are relatively rough compared to the hexane/water interface, with higher peaks and lower valleys. This corresponds to the experimental interfacial tension of each system, which is many times higher for the hexane/water system than for the other two systems (IL/water: 10 mN/m [166]; IL/hexane: 13 mN/m [166]; water/hexane: 50 mN/m [439]). If fluctuations of the interface account for the imprecision of the pressure tensor method, the capillary wave method might be expected to be more precise since it accounts for these fluctuations and in fact depends on them to calculate interfacial tension.

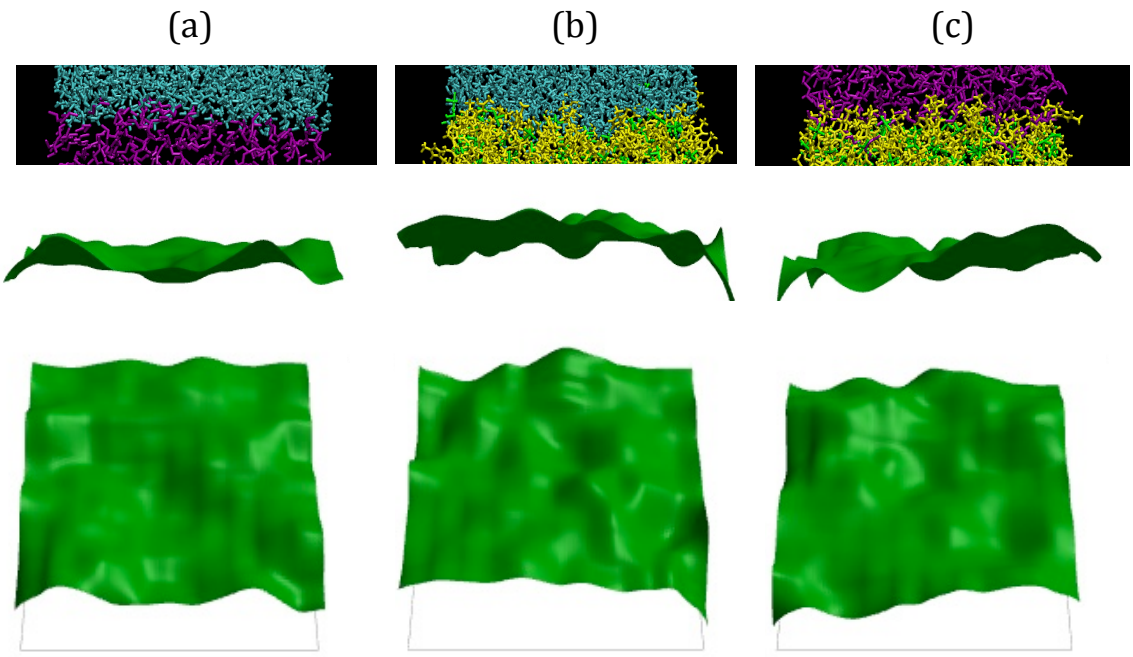

Figure B.2 MD snapshots (top) and bicubic interpolations (middle and bottom) of (a) water/hexane; (b), IL/water and (c) IL/hexane interfaces.

As discussed previously, the interface must first be defined in space before the capillary wave method can be used to calculate interfacial tension. In order to do this for each system studied, Equation B.3 was first fit to interfacial density profiles using nonlinear regression to determine values for $<h>$ and σ. Two examples of this fit can be seen in Figure B.3. These results seem promising because the error function density profile reasonably describes the density profiles of both liquid-vapor and liquid-liquid systems. This density profile might then provide a consistent definition of different interfaces in different systems that can be used to calculate interfacial tension.

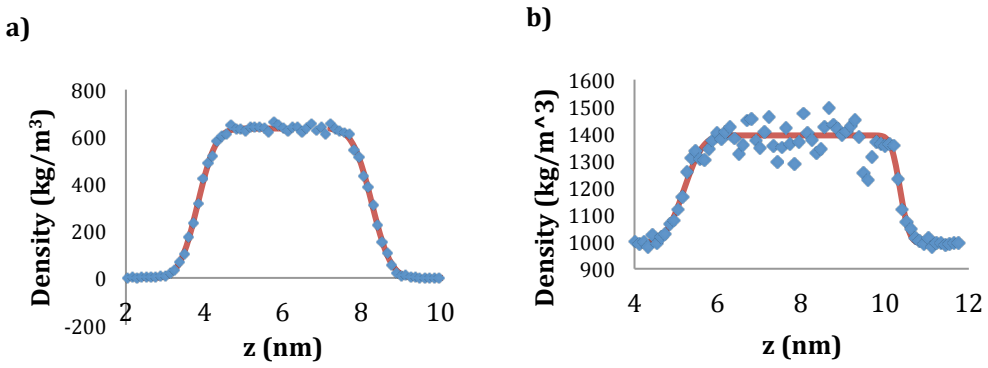

Figure B.3 Sample density profile for a) hexane liquid-vapor and b) water/IL liquid-liquid systems. Simulation results are illustrated as points whereas the error function fits are illustrated as solid red lines.

Interfacial tensions were calculated for five interfaces: hexane/vacuum, IL/vacuum, IL/water, IL/hexane, and hexane/water. For each interface, interfacial tension was calculated using both the pressure tensor method and the capillary wave method with the error function density profile used to find σ. Again, the error function density profile was used in an attempt to define the interface in a way which is objective and consistent across any interface, whether liquid-vapor or liquid-liquid. Interfacial tension was calculated over the last 15 ns of each simulation run and averaged over each nanosecond as described in the methodology section. Then, four parallel runs were combined to find an average value at each nanosecond. These results are shown in Figure B.4. The error bars at each nanosecond represent the standard deviation of the interfacial tension between the four parallel runs.

For three of the five systems, the capillary wave method clearly shows improved precision over the pressure tensor method. The smaller error bars in Figure B.4 indicate that the method is more precise from run to run, while the tension values also remain

more consistent over time, indicating increased precision within any given run. However, Figure B.4 does not show the capillary wave method to be obviously more precise for the IL/hexane system, and for the hexane/water system the capillary wave method appears to be less precise than the pressure tensor method. For those two systems, the capillary wave method also predicts a much higher interfacial tension than the pressure tensor method.

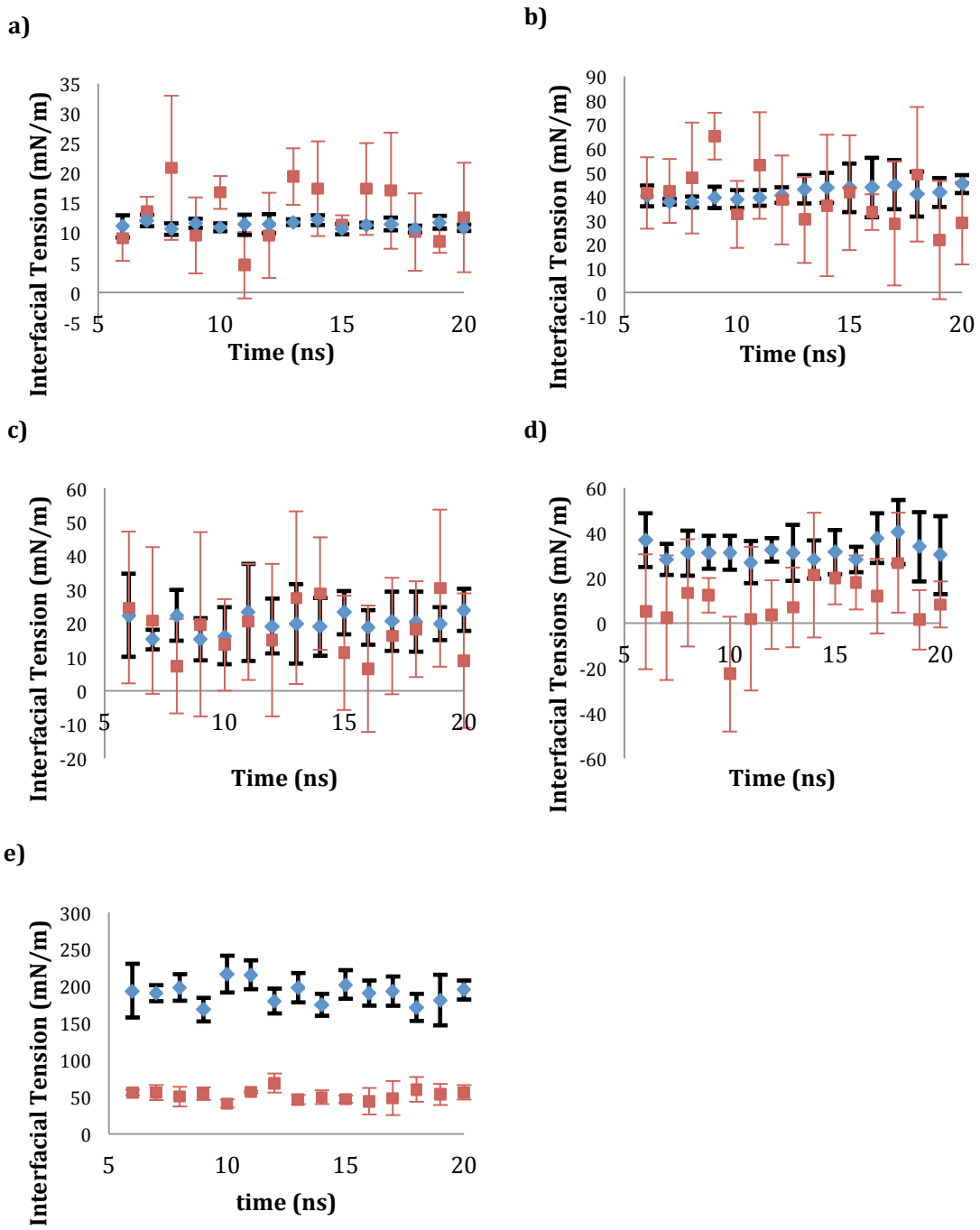

Figure B.4 Comparison of the pressure tensor route and the capillary wave method in the calculation of surface/interfacial tensions for (a) hexane/vacuum, (b) IL/vacuum, (c) IL/water, (d) IL/hexane and (e) hexane/water interfaces. Capillary wave method results are shown as blue diamonds with bold black error bars while pressure tensor route results are shown as red squares with thin red error bars.

However, in terms of percent deviation, the capillary wave method was superior. Figure B.5 shows how the variation in surface tension calculation as a percent of the calculated value for each simulation. Even with the high overestimation of the hexane/water system, the capillary wave method produced enhanced precision, reducing variation by an average of 66%. Benjamin has also reported increased precision using the capillary wave method in a water/1,2-dichloroethane system [424]. Even the hexane/vacuum system, where the pressure tensor route gave its lowest variation, the capillary wave method improved upon the precision significantly. Pressure tensor route variations ranged from 20% in the hexane/water system to 220% in the IL/hexane system. It should be noted that these variations were not a direct result of the large pressure fluctuations inherent in small systems (see Figure 1) since they were calculated from parallel run averages.

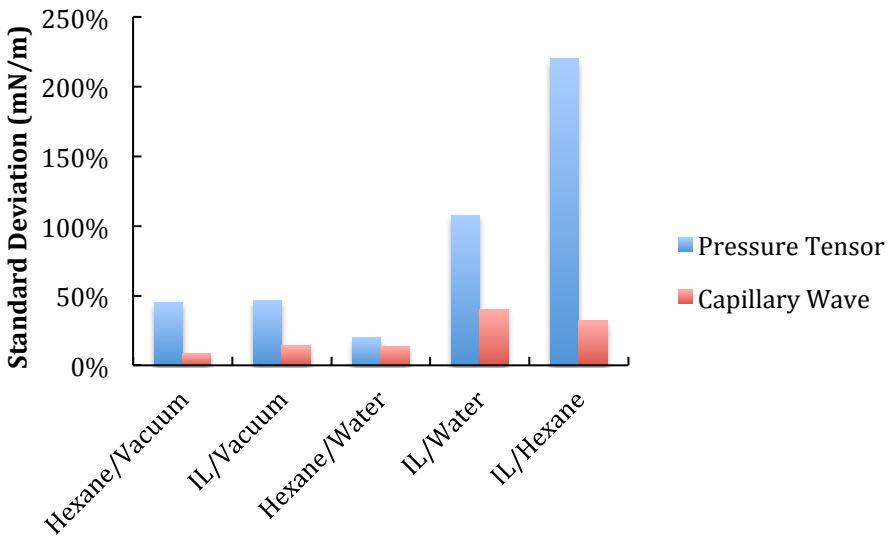

Figure B.5 Comparison of average percent variation in surface tension calculations.

To evaluate the accuracy of these methods, the average interfacial tension calculated by each method was compared to experimental values. This is shown in Table B.2, along with the average standard deviation of each method (the average of the error bars in Figure 4). For the two liquid/vacuum systems, the pressure tensor method appears to be somewhat more accurate for hexane while the capillary wave method is somewhat more accurate for IL. However, both methods agreed within error.

Liquid-liquid interfacial tensions were more erratic and less accurate for both calculation methods. This is understandable, since the liquid-liquid systems include many more molecular interactions at the interface. This should exaggerate errors caused by cut-off effects. The capillary wave method is still produces smaller standard deviation than the pressure tensor method for the IL/water and IL/hexane systems. However, the capillary wave method is less accurate for all three systems. While the two methods agree within error for the IL/water system, for the other two systems the capillary wave method drastically overstates the interfacial tension. The method is particularly inaccurate for the hexane/water system, which also produces a large standard deviation compared to the pressure tensor method. These results are curious since the two methods have been shown to be mathematically equivalent [440] and should not produce such wildly divergent answers.

Table B.2 Comparison of tensions calculated from the simulation with experiment.

		Pressure Tensor Method		Capillary Wave Method	
System	*Experimental Interfacial Tension (mN/m)*	*Interfacial Tension (mN/m)*	*% Difference from Experiment*	*Interfacial Tension (mN/m)*	*% Difference from Experiment*
Hexane/Vacuum	18.4[327]	13.2 ± 5.98	28.3%	11.3 ± .959	38.6%
IL/Vacuum	42.3[330, 331]	39.3 ± 5.87	7.1%	41.3 ± 5.78	2.4%
IL/Water	10.0[166]	17.8 ± 19.4	78%	20 ± 8.05	100%
IL/Hexane	13.4[166]	8.73 ± 19.2	34.8%	32 ± 10.2	139%
Hexane/Water	50.0[439]	52.7 ± 10.6	5.4%	191 ± 20	282%

The IL force field was optimized for surface tension using the pressure tensor route [223] while no such optimization was performed for the hexane force field. This means the hexane force field might not adequately describe the intermolecular forces that affect capillary waves at the interface, which might explain why the capillary wave method produces better results with the IL systems than with the hexane systems. Weaknesses in molecular force fields could explain the poor accuracy of the capillary wave method in general. Molecular force fields are optimized to successfully simulate experiment properties such as density or boiling point[228]. The pressure tensor method calculates interfacial tension directly from molecular interactions through calculation of the virial [413] while the capillary wave method is less direct, quantifying the *effect* of these interactions on fluctuations at the interface[407, 434]. It is possible that the molecular force fields used in this study generate realistic pressure tensors but not realistic capillary wave behavior at the interface. However, we hypothesized that the problem comes instead from the definition of the interface through the error function density profile.

To test this hypothesis, the position of the interface was calculated using Equation B.4 and the actual position of molecules. The standard deviation in the z-position of the interface, σ, was determined as described in the methodology section and used to calculate interfacial tension. The results are shown in Figure B.6 and Table B.3. These results show dramatic improvement for all three liquid-liquid systems. Figure B.6 shows that the capillary wave method, with the interface defined by Equation B.4, is much more precise than either the pressure tensor method or the capillary wave method using Equation B.3 to define the interface. Table B.3 shows that the capillary wave method agrees in accuracy with the pressure tensor method for all three systems.

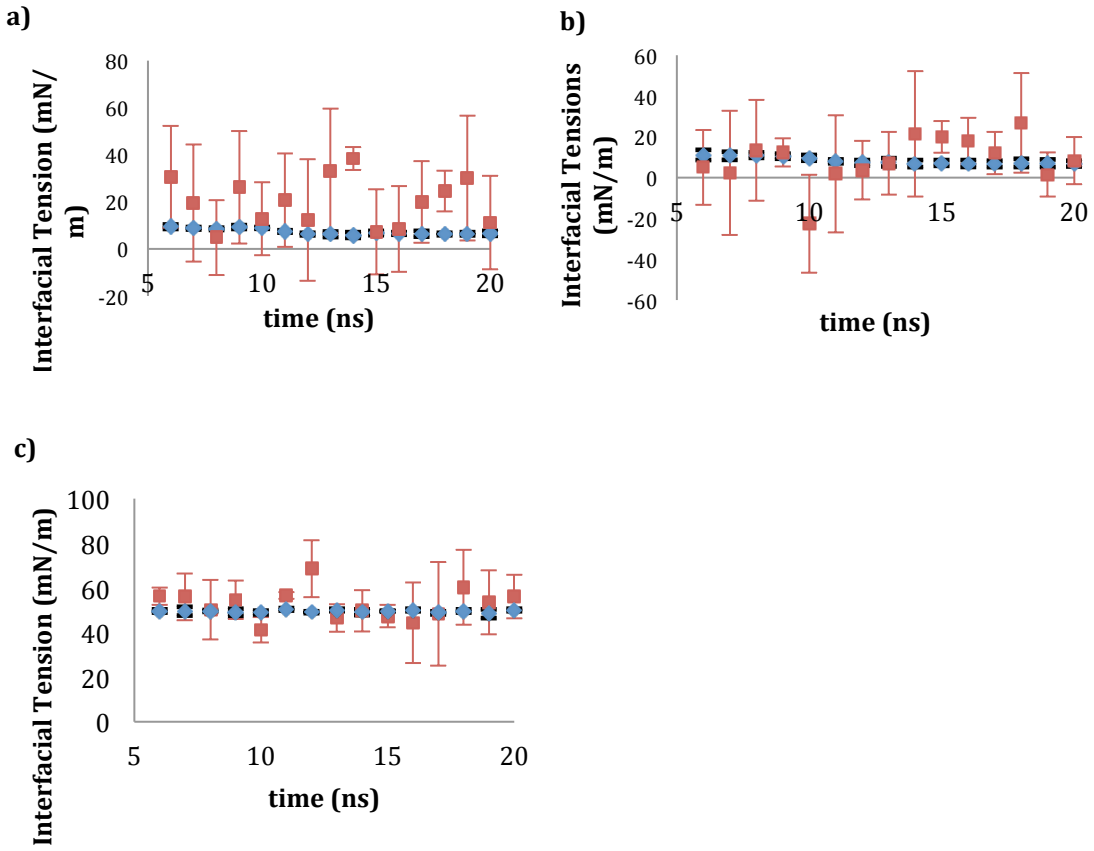

Figure B.6 Comparison of the pressure tensor route and the capillary wave method in the calculation of surface/interfacial tensions for (a) IL/water, (b) IL/hexane and (d) hexane/water interfaces. For the capillary wave method, Equation B.4 is used to define the interface rather than Equation B.1. Pressure tensor method results are shown as red squares with thin red error bars. Capillary wave method results are shown as blue diamonds with bold black error bars, though for many points the error bar is too small to see and can be assumed to be contained within the point marker.

Table B.3 Results of surface tension calculations employing the capillary wave method in conjunction with Equation B.4.

		Capillary Wave Method	
System	*Experimental Interfacial Tension (mN/m)*	*Interfacial Tension (mN/m)*	*% Difference from Experiment*
IL/Water	10	7.3 ± 0.78	27%
IL/Hexane	13.39	8.23 ± 1.6	38.5%
Hexane/Water	50	49.5 ± 0.9	1.0%

These results support our hypothesis that fitting Equation B.3 to the density profile of the simulated box did not adequately define the interface for the purposes of the capillary wave method. The results also support previous work that has argued that such methods (fitting the density profile) ignore the structural details of the interface and consequently provide limited information [441, 442]. Studies in which accurate capillary wave calculations of the hexane/water interfacial tension were reported have generally used more sophisticated methods [441]. This study reinforces the need to sufficiently define the interface before calculating interfacial tensions using the capillary wave method.

In the final stage of this study, we set out to investigate how the precision and accuracy of these methods were affected by system size. Given that calculated error decreases with O(1/n) in MD simulations [443], we expected both methods to improve with larger system sizes (n is the number of atoms). A large water/IL interface was simulated and analyzed using both methods. For the capillary wave method, the error function density profile was used to define the interface. Figure B.7 shows the results of 3 parallel runs of an IL/water system eight times larger than the previous systems (see

Table B.1). We observed a similar trend to that of the smaller systems: the capillary wave method produced smaller variations and more time-stable results. The 8x increase in system size allowed for enhancements in precision for both methods: 38% for the pressure tensor route and 45% for the capillary wave method. The average variations for the pressure tensor route and the capillary wave method were 12.0 mN/m and 4.4 mN/m, respectively. Thus the capillary wave method still produced a 63% improvement in precision. The increase in precision was greater for the capillary wave method than for the pressure tensor route, which may indicate that the error function density profile describes the interface better as the system gets larger and various cut-off effects are reduced. In terms of accuracy, both methods yielded values closer to the experimental measurements. The pressure tensor route yielded 12.8 mN/m and the capillary wave method yielded 13.4 mN/m. Therefore, larger system size not only decreased variation in the calculations, but also accuracy, and equally so for both methods.

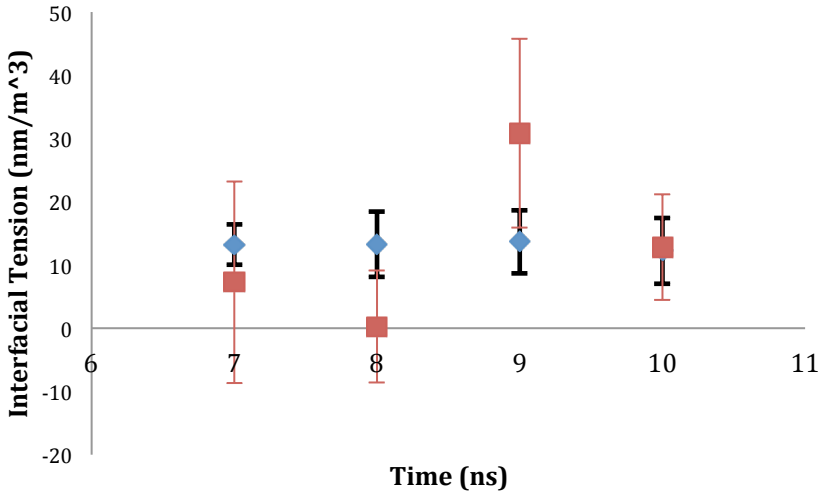

Figure B.7 Comparison of surface tension calculations on an IL/water system eight times larger than the previous simulations. Capillary wave method results are shown as blue

diamonds with bold error bars while pressure tensor route results are shown as red squares with thin error bars.

Conclusion

We have studied the calculation of surface and interfacial tension for a variety of liquid-vapor and liquid-liquid interfaces using MD simulations. Because of the inherently small scale of MD systems, large pressure fluctuations can cause calculations of surface tension using the pressure tensor route can be imprecise. The capillary wave method exhibited improved precision and stability throughout all of the simulated systems of this study. In implementing this method, the interface was defined by fitting an error function to the density profile. However, full mapping of the interface from coordinate files produced enhanced accuracy. Upon increasing the system size, both methods exhibited higher precision, although the capillary wave method was still more reliable.

APPENDIX C

DATA ANALYSIS MACROS

ImageJ Macros

This section consists of six macros entitled "Get DSD," "Open File List," Measure Deformities," Measure Bridges," "Continue," "Test Fill Droplets" and three functions entitled "TraceDroplets," "FillDroplets," and "GetParticleArea." In order to be functional, these must be placed in the StartupMacros.txt file in the "macros" folder of the ImageJ directory. Macros with a [#] notation in their name may be accessed via a hotkey (the # in the brackets). Within each macro, comments are preceded by the "//" notation.

To measure interfacial lifetimes as in Section 3.3.1, the "Measure Deformities" macro was used. Upon invoking this macro (from the ImageJ menu: Plugins > Macros > Measure Deformities), the user was asked for a text file containing the directories of the images to be analyzed. This file contained one directory per line and was contained in the same folder as the images. The macro then measured the area occupied by the lines of the lined paper in each of the images. These areas were copied from the "Summary" box into MS Excel for analysis. The "Open File List" macro was an alternative method of measuring the deformations, allowing the user to manually measure the interface in each image. After the user completed a measurement, the hotkey "a" was pressed (invoking the "Continue" macro) to proceed to the next image.

Bridged structures were analyzed using the "Measure Bridges" macro followed by the "Get DSD" macro. The purpose of the first macro is to use the DIC and confocal images to isolate the bridged droplets in a binary image (droplets are black, background is white). These binary images were saved in a folder entitled "Binaries," which was created within the directory by the macro. Again, the user was asked for a text file listing

the directories of the images to be analyzed. As with the "Measure Deformities" macro, this file resided the same folder as the images and contained only one directory per line. However, this macro read two images in each iteration - the confocal image followed by the DIC image. Therefore, the file with the list of image directories was organized accordingly. The user was allowed three pauses in which make any corrections that would interfere with droplet size distribution calculations. Each pause was terminated by pressing the "a" hotkey. In the first pause, the user erased any non-bridging particles from the confocal image. In the second pause, the user adjusted the contrast of the image so that the particles fully appeared when the confocal image was converted to binary format. The third pause allowed the user to use the ImageJ drawing tools to be sure that all bridged droplets were outlined correctly. In this stage, the user could press the "2" hotkey (invoking the "Test Fill Droplets" macro) to briefly preview how the macro would fill the droplet outlines. Finally, the final binary image was saved to the binaries directory for analysis with "Get DSD."

The "Get DSD" macro measured the areas of all of the droplets in all of the images to be analyzed, allowing for droplet size distributions to be generated. "Get DSD" read a list file where each line contained and image directory and the numerical zoom of that image as reported by the confocal microscope, separated by a space. This macro did not allow for any user input beyond the selection of the list file and output the areas measured for each droplet of each image into the "Summary" box. These data were copied to MS Excel for analysis.

Begin Macros

```
macro "Get DSD"
{
	var pathfile, filestring, i;
	pathfile=File.openDialog("Choose the file with the list of images to process:");
	filestring=File.openAsString(pathfile);
	imagefiles=split(filestring, "\n");

	var path=File.directory;

	//generate a list of all droplets and their areas
	for(i = 0; i < imagefiles.length; i++)
	{
		var imagedata = split(imagefiles[i]," "); //split into filename and zoom
		var DICTitle = imagedata[0]; //File name
		open(path + DICTitle);
		run("Set Scale...", "distance=" + 2.08*imagedata[1] + " known=1 pixel=1
unit=micron");
		run("Analyze Particles...", "size=25-Infinity circularity=0.00-1.00
show=Nothing display");
		selectWindow(DICTitle);
		close();
	}
}

macro "Open File List"
{
	var pathfile, filestring, i;
	pathfile=File.openDialog("Choose the file with the list of images to process:");
	filestring=File.openAsString(pathfile);
	imagefiles=split(filestring, "\n");

	var path=File.directory;


	for(i = 0; i < imagefiles.length; i++)
	{
		var Title = imagefiles[i]; //File name
		open(path + Title);

		bCont = 0;//Wait for user to take measurement
		while(bCont == 0){
		}

		close();
	}
```

```
}

macro "Measure Deformities"
{

	var pathfile, filestring, i;
	pathfile=File.openDialog("Choose the file with the list of images to process:");
	filestring=File.openAsString(pathfile);
	imagefiles=split(filestring, "\n");

	var path=File.directory;


	for(i = 0; i < imagefiles.length; i++)
	{

		var Title = imagefiles[i]; //File name
		open(path + Title);


	runMacro("/Users/denzilfrost/Desktop/ImageJ/macros/LabThreshold.ijm");
		run("Make Binary");
		run("Analyze Particles...", "size=0-Infinity circularity=0.00-1.00
summarize");

		selectWindow(Title);
		close();
	}
}
macro "Measure Bridges [1]"
{
	var pathfile, filestring, i;
	pathfile=File.openDialog("Choose the file with the list of images to process:");
	filestring=File.openAsString(pathfile);
	imagefiles=split(filestring, "\n");

	var path=File.directory;

	if (File.exists(path + "Binaries") == 0)
	{
		File.makeDirectory(path + "Binaries");//create folder for binary files
	}
	var savePath = path + "Binaries/";

	for(i = 0; i < imagefiles.length; i = i +2)
```

```
	{
		var ConfTitle = imagefiles[i];
		var DICTitle = imagefiles[i+1];

		open(path + ConfTitle);
		open(path + DICTitle);
		selectWindow(ConfTitle);

		brushWidth = 50;
		bCont = 0;//Wait for user to edit confocal image
		while(bCont == 0){
		}

		run("Color Balance...");

		bCont = 0;//Wait for user to edit confocal image
		while(bCont == 0){
		}
		brushWidth = 5;

		GetParticleArea();

		//Save Conf binary
		selectWindow(ConfTitle);
		saveAs("Tiff", savePath + ConfTitle);

		selectWindow(DICTitle);

		TraceDroplets();

		bCont = 0;//Wait for user to edit binary image
		while(bCont == 0){
		}

		//close overlay image
		selectWindow(DICTitle + "-overlay");
		close();

		FillDroplets();

		//Isolate droplets by subtracting particles from confocal image
		imageCalculator("Subtract", DICTitle, ConfTitle);
		run("Watershed");
		run("Analyze Particles...", "size=100-Infinity circularity=0.00-1.00
show=Masks summarize");
```

```
                wait(2000);
                close();

                //Save DIC binary files and close all windows
                saveAs("Tiff", savePath + DICTitle);
                close();
                selectWindow(ConfTitle);
                close();
        }
}

macro "Continue [a]" {bCont=1;}

function TraceDroplets()
{
        //create a second image for the overlay
        title = getTitle();
        x = getWidth;
        y = getHeight;
        overlay_title = title + "-overlay";
        run("Copy");
        newImage(overlay_title, "RGB White", x, y,1);
        run("Paste");
        selectWindow(title);

        //Trace Droplet edges
        run("Find Edges");
        run("Make Binary");
        run("Despeckle");
        run("Close-");
        run("Dilate");
        run("Dilate");
        run("Dilate");
        run("Skeletonize");
        run("Dilate");

        //Add overlay of original image so any tracing mistakes can be manually
corrected
        run("Add Image...", "image=" + overlay_title + " x=0 y=0 opacity=75");
}

macro "Test Fill Droplets [2]"
{
        run("Fill Holes");
        wait(1000);
```

```
	run("Undo");
}

function FillDroplets()
{
	//remove overlay image
	run("Remove Overlay");

	//Fill in droplets so their area can be measured
	run("Fill Holes");

	//get rid of "hair" from misread edges
	run("Erode");
	run("Erode");
	run("Dilate");
}

function GetParticleArea()
{
	run("Make Binary");
	run("Analyze Particles...", "size=0-Infinity circularity=0.00-1.00 show=Masks
summarize");
	wait(1000);
	close();
}
```

MD Simulation Data Analysis

These C++ algorithms were used to quickly analyze data from multiple parallel runs. These files were compiled using the command in the xTerm command line: g++ DataAnalSpecFile.cpp DensityDataFile.cpp DensityProfile.cpp EnergyDataFile.cpp -o DataAnalSpecFile. The program was then executed from xTerm using the command: ./DataAnalSpecFile. This program guided the user through several stages of input, including the specification of files to be analyzed. Two types of Gromacs output files could be analyzed: energy.xvg files from the g_energy command and density.xvg files from the g_density command. Multiple files of the same type could be entered and the program calculated corresponding averages and standard deviations of the data in these files. This feature was useful for compiling data from parallel runs.

"ColumnCalculator.cpp" was a stand-alone program that read many types of data files (.xvg suffix) from Gromacs and calculated the average and standard deviation of each column of data. This program was compiled in the same way as the one in the previous paragraph. Its primary use was to quickly obtain time averages from Gromacs output files.

The last section of code in this section is the bicubic interpolator used to generate the plots of the interfaces shown in Appendix B. This code is a collection of VBA macros used in an MS Excel file. The .gro file of an interfacial run was copied directly to a sheet of this excel file and the atoms of each phase were ordered by their proximity to the interface via MS Excel's sorting functions. For systems with two phases, the coordinates for each phases were separated by two empty rows, allowing the program to detect that where the coordinates for the second phase began. MS Excel generated the plots seen in

Appendix B using the surface plot function. This function, required a matrix input with the x and y dimensions on the top and right side, respectively. The coordinates from the gro file were copied to the Excel sheet starting at row 2 with the x, y, and z coordinates placed in columns E, F, and G, respectively. The x coordinates for the matrix were written from cell K3 onward to the right. The y coordinates were written starting at cell J4 and down. Upon executing the "FillMatrix" subroutine, the user was asked to specify how many coordinates to examine for each phase (effectively, how many atoms close to the interface). Values from 200-500 usually provided good results (i.e. no zero values in the matrix). "FillMatrix" then wrote a matrix of interfacial coordinates within the x and y values specified. "Bicubic" could then be executed, which re-wrote the values of this matrix with 10 interpolated points in between. This final matrix was written below the first and could be plotted to give figures like the ones seen in Appendix B.

DataAnalSpecFile.cpp

```
// Driver File for Data analysis

#include <iostream>
#include <string>
#include <fstream>
#include <cmath>
#include <iomanip>
#include "EnergyDataFile.h"
#include "DensityDataFile.h"
using namespace std;

bool FileExists(string filename);
void AddEnergyDataFile(string filename);
void AddDensityDataFile(string filename);
void StoreData(string label, double dataitem);
void SelectAndStoreData(int idata);
double calcStdev(vector<double> values, double avg);
```

```
vector<string> labels;
vector<double> data;
vector<double> stdevs;
vector<EnergyDataFile> energies;
vector<DensityDataFile> densities;

int main()
{
    int i, entry;
    bool bcontinue(true);
    ofstream results("Results.txt");

    //read energy and density files
    //string energyfiles[] = {"energy.xvg", "P1energy.xvg",
"P2energy.xvg", "P3energy.xvg"};
    //string densityfiles[] = {"density.xvg",
"P1density.xvg", "P2density.xvg", "P3density.xvg"};
    string szEntry;

    cout << "Enter a file name or 0 to continue" << endl;
    while(bcontinue)
    {
     cin >> szEntry;
     if(szEntry == "0")
     {
          bcontinue = false;
     }
     else
     {
          if(szEntry.find("energy") != string::npos &&
FileExists(szEntry))//energy file
          {
               AddEnergyDataFile(szEntry);
               cout << "energy file read" << endl;
          }
          if(szEntry.find("density") != string::npos &&
FileExists(szEntry))//density file
          {
               AddDensityDataFile(szEntry);
               cout << "density file read" << endl;
          }
     }
    }

    //orient the use on how to ask for data
```

```
    cout << "Enter the number indicating the data you wish
to collect,or enter 0 to print and exit" << endl;
    cout << "1 - Average Potential energy" << endl;
    cout << "2 - Average Temperature" << endl;
    cout << "3 - Average Pressure" << endl;
    cout << "4 - Average Density" << endl;
    cout << "5 - Average Surface Tension" << endl;
    cout << "6 - Interfacial width by one solvent" << endl;
    cout << "7 - Interfacial width by two solvents" <<
endl;
    cout << "8 - Mole fraction of a solute in a bulk
region" << endl;
    cout << "9 - Mole fraction of a solute in an interface
defined by one solvent" << endl;
    cout << "10 - Mole fraction of a solute in an interface
defined by two solvents" << endl;

    bcontinue = true;
    while(bcontinue)
    {
     cin >> entry;
     if(entry == 0)
          bcontinue = false;
     else
          SelectAndStoreData(entry);
    }

    //Print Data
    results << left << setw(60) << "Data" << setw(15) <<
"Average" << setw(15) << "StDev" << endl;
    for(i = 0; i < data.size(); i++)
    {
     results << left << setprecision(5) << setw(60) <<
labels[i] << setw(15)  << data[i] << setw(15) << stdevs[i]
<< endl;
    }
    results.close();
    return 0;
}

bool FileExists(string filename)
{
    ifstream file(filename.c_str());
    return file;
}
```

```
void AddEnergyDataFile(string filename)
{
    energies.resize(energies.size() + 1);
    energies[energies.size()-1] = EnergyDataFile(filename);
}

void AddDensityDataFile(string filename)
{
    densities.resize(densities.size() + 1);
    densities[densities.size()-1] =
DensityDataFile(filename);
}

void StoreData(string label, double dataitem, double stdev)
{
    labels.resize(labels.size() + 1);
    data.resize(data.size() + 1);
    stdevs.resize(stdevs.size() + 1);

    labels[labels.size() -1] = label;
    data[data.size() -1] = dataitem;
    stdevs[stdevs.size() -1] = stdev;
}

void SelectAndStoreData(int idata)
{
    vector<double> values;
    int i;
    string label, szSolvent1, szSolvent2, szSolute;
    double sum(0), avg, stdev;
    label = szSolvent1 = szSolvent2 = szSolute = "";

    for(i = 0; i < densities.size(); i++)
    {
     values.resize(values.size() + 1);
     switch(idata)
     {
          case 1:
               label = "Average Potential Energy (kJ/mol)";
               values[i] = energies[i].getPotential();
               break;
          case 2:
               label = "Average Temperature (K)";
               values[i] = energies[i].getT();
```

```
                    break;
               case 3:
                    label = "Average Pressure (bar)";
                    values[i] = energies[i].getP();
                    break;
               case 4:
                    label = "Average Density (kg/m^3)";
                    values[i] = energies[i].getrho();
                    break;
               case 5:
                    label = "Average Interfacial Tension
(mN/m)";
                    values[i] = energies[i].getgamma();
                    break;
               case 6:
                    if(label == "")
                    {
                         cout << "Enter the name of the species
by which you wish to define the interface (90%-10% rule)"
<< endl;
                         cout << "Options are:" << endl;
                         densities[0].PrintProfileNames();
                         cin >> szSolvent1;
                         label = "Interfacial Width Defined by "
+ szSolvent1 + "(nm)";
                    }
                    values[i] =
densities[i].getInterfacialWidth(szSolvent1);
                    break;
               case 7:
                    if(label == "")
                    {
                         cout << "Enter the names of the 2
species by which you wish to define the interface (90%-90%
rule)" << endl;
                         cout << "Options are:" << endl;
                         densities[0].PrintProfileNames();
                         cin >> szSolvent1 >> szSolvent2;
                         label = "Interfacial Width Defined by "
+ szSolvent1 + " and " + szSolvent2 + "(nm)";

                    }
                    values[i] =
densities[i].getInterfacialWidth(szSolvent1, szSolvent2);
                    break;
```

```
          case 8:
               if(label == "")
               {
                    cout << "Enter the names of the bulk
region and solute species to consider" << endl;
                    cin >> szSolvent1 >> szSolute;
                    label = "Mole fraction of " + szSolute
+ " in " + szSolvent1 + " region";
               }
               values[i] =
densities[i].getBulkMoleFraction(szSolvent1, szSolute);
               break;
          case 9:
               if(label == "")
               {
                    cout << "Enter the names of the
interface basis and solute species to consider" << endl;
                    cin >> szSolvent1 >> szSolute;
                    label = "Mole fraction of " + szSolute
+ " in interface defined by " + szSolvent1;
               }
               values[i] =
densities[i].getInterfaceMoleFraction(szSolute,
szSolvent1);
               break;
          case 10:
               if(label == "")
               {
                    cout << "Enter the names of the 2
solvents to define the interface and the solute to
consider" << endl;
                    cin >> szSolvent1 >> szSolvent2 >>
szSolute;
                    label = "Mole fraction of " + szSolute
+ " in interface defined by " + szSolvent1 + " and " +
szSolvent2;

               }
               values[i] =
densities[i].getInterfaceMoleFraction(szSolute, szSolvent1,
szSolvent2);
               break;
          default:
               return;
               break;
```

```
     }
     sum += values[i];
    }

    //calculate average and stdev
    avg = sum/double(values.size());
    stdev = calcStdev(values, avg);
    StoreData(label, avg, stdev);
}

double calcStdev(vector<double> values, double avg)
{
    int i;
    double stdev, sum(0);

    for(i = 0; i < values.size(); i++)
    {
     sum += pow(values[i] - avg, 2);
    }
    sum = sum/double(values.size());
    stdev = sqrt(sum);
    return stdev;
}
```

DensityDataFile.h

```
/* Header file for DensityFileData class
Represents data from density.xvg and allows easy access to
important parameters
Filename: DensityDataFile.h*/

#include <string>
#include <vector>
#include <iostream>
#include "DensityProfile.h"
using namespace std;

class DensityDataFile
{
    public:
     //constructors
     DensityDataFile();
     DensityDataFile(string FileName);
```

```
     //accessor methods
     double getcount();
     double getmaxz();
     double getInterfacialWidth(string ProfileName);
     double getInterfacialWidth(string Profile1Name, string
Profile2Name);
     double getBulkMoleFraction(string bulk, string
solute);//for bulk
     double getInterfaceMoleFraction(string solute, string
InterfaceBasis);//for interface defined by one solvent
     double getInterfaceMoleFraction(string solute, string
solvent1, string solvent2);//for interface defined by two
solvents (90%-90% rule)

     //Helper Methods
     void PrintProfile(string ProfileName);
     void PrintProfileNames();
    private:
     double count;
     double maxz;
     void ReadDataFile(string FileName);
     void CombineProfiles(string Profile1, string Profile2,
string NewProfileName);
     vector<DensityProfile> Profiles;
     vector<double> GetDoubleData(string row);
     string ExtractNameFromLine(string line);
     bool ProfileExists(string ProfileName);
     DensityProfile GetProfile(string ProfileName);
     double getMoleFraction(string solute, double zstart,
double zend);
};
```

DensityDataFile.cpp

```
//Analyzes density.xvg and assigns species to individual
density profiles
//Filename: DensityDataFile.cpp

#include "DensityDataFile.h"
#include <fstream>

DensityDataFile::DensityDataFile()
{
```

```
    //ReadDataFile("density.xvg");
    count = 0;
}

DensityDataFile::DensityDataFile(string FileName)
{
    ReadDataFile(FileName);
    count = 0;
}

void DensityDataFile::ReadDataFile(string FileName)
{
    //Open Data Files
    ifstream densityfile(FileName.c_str());

    //locals
    string line, first3;
    vector<double> currData, z;
    vector<string> names;
    int i;
    bool IsName = false;
    if (densityfile.is_open())
    {
     while (densityfile.good())
     {
          //read a line of the file
          getline (densityfile,line);

          //collect names of profiles
          if(line.length() > 3)
          {
               first3 = line.substr(0,3);
               if(first3 == "@ s")
               {
                    //add space for another name
                    Profiles.resize(Profiles.size() + 1);
                    Profiles[Profiles.size() -1] =
DensityProfile(ExtractNameFromLine(line));
               }
          }

          //only get data rows
          if (line[0] != '#' && line[0] != '@' && line !=
"")
          {
```

```
                currData = GetDoubleData(line);
                count++;

                //add z points
                for(i = 0; i < Profiles.size(); i++)
                {
                     Profiles[i].Addz(currData[0]);
                     maxz = currData[0];
                }

                //add rho points
                for(i = 1; i < currData.size(); i++)
                {
                     Profiles[i-1].Addrho(currData[i]);
                }

           }
      }
    }

    CombineProfiles("BMI","PF6","BMIMPF6");
    CombineProfiles("ETA","NO3","EAN");

    for(i = 0; i < Profiles.size(); i++)
    {
     Profiles[i].RunCalcs();
    }

    //Close Data File
    densityfile.close();
}

void DensityDataFile::CombineProfiles(string Profile1,
string Profile2, string NewProfileName)
{

    if(ProfileExists(Profile1) && ProfileExists(Profile2))
    {
     //add another profile
     Profiles.resize(Profiles.size() + 1);
     Profiles[Profiles.size()-1] =
DensityProfile(NewProfileName, GetProfile(Profile1),
GetProfile(Profile2));
     Profiles[Profiles.size()-1].RunCalcs();
    }
```

```
    else
    {
     if (!ProfileExists(Profile1))
     {
          cout << "Could not find profile named " <<
Profile1 << endl;
     }

     if (!ProfileExists(Profile2))
     {
          cout << "Could not find profile named " <<
Profile2 << endl;
     }
    }
}

vector<double> DensityDataFile::GetDoubleData(string row)
{
    //takes a text line of data and returns a vector of
doubles
    vector<string> data;
    vector<double> numdata;
    int i;
    bool IsNewEntry;
    char currChar;

    IsNewEntry = true;
    //split the columns into vector elements
    for (i = 0; i <= row.length(); i++)
    {
     currChar = row[i];
     if(currChar == ' ')
     {
          IsNewEntry = true;
     }
     else
     {
          if(IsNewEntry)
          {
               data.resize(data.size() + 1);
          }
          data[data.size() - 1] += currChar;
          IsNewEntry = false;
     }
    }
```

```
    //resize the number data vector to hold everything it
needs
    numdata.resize(data.size());

    //convert to double
    for (i = 0; i < data.size(); i++)
    {
     numdata[i] = atof(data[i].c_str());
    }

    return numdata;
}

string DensityDataFile::ExtractNameFromLine(string line)
{
    int i;
    string name = "";
    bool IsName = false;

    //search for the text between the quotes
    for(i = 3; i < line.length(); i++)
    {
     if(line[i] == '\"')
     {
          if(IsName)
               IsName = false;
          else
               IsName = true;
     }

     if(IsName && line[i] != '\"')
          name += line[i];
    }
    return name;
}

void DensityDataFile::PrintProfile(string ProfileName)
{
    vector<double> z, rho;
    int i;

    for(i = 0; i < Profiles.size(); i++)
    {
     if(Profiles[i].getName() == ProfileName)
```

```
     {
          z = Profiles[i].getz();
          rho = Profiles[i].getrho();
     }
    }
    cout << ProfileName << " density profile" << endl;
    cout << "z          rho (kg/m^3)" << endl;

    for(i = 0; i < z.size(); i++)
    {
     cout << z[i] << "     " << rho[i] << endl;
    }
}

void DensityDataFile::PrintProfileNames()
{
    int i;
    for(i = 0; i < Profiles.size(); i++)
    {
     cout << Profiles[i].getName() << endl;
    }
}

bool DensityDataFile::ProfileExists(string ProfileName)
{
    int i;
    for(i = 0; i < Profiles.size(); i++)
    {
     if(Profiles[i].getName() == ProfileName)
          return true;
    }

    return false;
}

DensityProfile DensityDataFile::GetProfile(string
ProfileName)
{
    int i;
    for(i = 0; i < Profiles.size(); i++)
    {
     if(Profiles[i].getName() == ProfileName)
          return Profiles[i];
    }
}
```

```
double DensityDataFile::getInterfacialWidth(string
ProfileName)
{
    double z10a, z90a, z10d, z90d, width;
    DensityProfile currProfile;

    currProfile = GetProfile(ProfileName);
    z10a = currProfile.getz10a();
    z90a = currProfile.getz90a();
    z10d = currProfile.getz10d();
    z90d = currProfile.getz90d();

    //take into account periodic boundary conditions
    if(z90a < z10a)
    {
     z90a+= maxz + currProfile.getz()[1];//max plus
interval for periodic conditions
    }
    if(z10d < z90d)
    {
     z10d+=maxz + currProfile.getz()[1];//pbc as above
    }
    //cout << "z90a: " << z90a << " z10a: " << z10a <<
endl;
    //cout << "z10d: " << z10d << " z90d: " << z90d <<
endl;
    width = (z90a - z10a + z10d - z90d)/2;
    return width;
}

double DensityDataFile::getInterfacialWidth(string
Profile1Name, string Profile2Name)
{
    double z90a1, z90a2, z90d1, z90d2, width;
    DensityProfile profile1, profile2;

    profile1 = GetProfile(Profile1Name);
    profile2 = GetProfile(Profile2Name);
    z90d1 = profile1.getz90d();
    z90d2 = profile2.getz90d();
    z90a1 = profile1.getz90a();
    z90a2 = profile2.getz90a();

    //interfaces should be descending to ascending
```

```
    //so width = z90a - z90d

    //take care of pbc
    if(z90a1 < z90d2)
    {
     z90a1+= maxz + profile1.getz()[1];
    }
    if(z90a2 < z90d1)
    {
     z90a2+= maxz + profile1.getz()[1];
    }

    cout << "z90a1: " << z90a1 << " z90d2: " << z90d2 <<
endl;
    cout << "z90a2: " << z90a2 << " z90d1: " << z90d1 <<
endl;
    width = (z90a1-z90d2 + z90a2-z90d1)/2;
    return width;
}

double DensityDataFile::getBulkMoleFraction(string bulk,
string solute)
{
    //finds the mole fraction of solute in a bulk region
    DensityProfile bulkprofile;

    bulkprofile = GetProfile(bulk);
    return getMoleFraction(solute, bulkprofile.getz90a(),
bulkprofile.getz90d());
}

double DensityDataFile::getInterfaceMoleFraction(string
solute, string InterfaceBasis)
{
    //Finds the mole fraction of solute in the interfaces
    DensityProfile InterfaceProfile;
    double frac1, frac2, frac;

    InterfaceProfile = GetProfile(InterfaceBasis);
    frac1 = getMoleFraction(solute,
InterfaceProfile.getz10a(), InterfaceProfile.getz90a());
    frac2 = getMoleFraction(solute,
InterfaceProfile.getz90d(), InterfaceProfile.getz10d());

    frac = (frac1 + frac2)/2;
```

```
    return frac;
}

double DensityDataFile::getInterfaceMoleFraction(string
solute, string solvent1, string solvent2)
{
    DensityProfile solv1profile, solv2profile;
    double frac1, frac2, frac;

    solv1profile = GetProfile(solvent1);
    solv2profile = GetProfile(solvent2);

    frac1 = getMoleFraction(solute, solv1profile.getz90d(),
solv2profile.getz90a());
    frac2 = getMoleFraction(solute, solv2profile.getz90d(),
solv1profile.getz90a());

    frac = (frac1 + frac2)/2;
    return frac;
}

double DensityDataFile::getMoleFraction(string solute,
double zstart, double zend)
{
    //finds the mole fraction of a solute within a
specified region
    double totalmoles(0), solutemoles, molefraction,
currmoles;
    int i;

    //get total moles from all species
    for(i = 0; i < Profiles.size(); i++)
    {
     currmoles = Profiles[i].getMoles(zstart, zend);
     if(Profiles[i].getName() != "BMI" &&
Profiles[i].getName() != "PF6")
          totalmoles+= currmoles;

     if(Profiles[i].getName() == solute)
     {
          solutemoles = currmoles;
     }
    }
    molefraction = solutemoles/totalmoles;
    return molefraction;
```

```
}

double DensityDataFile::getcount()
{
    return count;
}

double DensityDataFile::getmaxz()
{
    return maxz;
}
```

DensityProfile.h

```
/* Header file for DensityProfile Class
Represents a density profile of a single species with
respect to z from density.xvg
Filename: DensityProfile.h*/

#include <string>
#include <vector>
using namespace std;

class DensityProfile
{
    public:
     //Constructors
     DensityProfile();
     DensityProfile(string szName);
     DensityProfile(string szName, DensityProfile profile1,
DensityProfile profile2);

     //mutator methods
     void Addz(double iz);
     void Addrho(double irho);

     //accessor methods
     double getbulkrho();
     double getrho90();
     double getrho10();
     string getName();
     double getz90a();
     double getz90d();
     double getz10a();
```

```
     double getz10d();
     vector<double> getz();
     vector<double> getrho();
     double getMW();
     double getMass(double zstart, double zend);
     double getMoles(double zstart, double zend);

     //helper methods
     void RunCalcs();
    private:
     double bulkrho;
     double rho90;
     double rho10;
     int astart;//index of z vector representing start of
increase in density profile to bulk value
     int aend;//""""" end of increase of density profile to
bulk value
     int dstart;//""""" start of decrease of density profile
to zero
     int dend;//""""" end of decrease of density profile to
zero
     string Name;
     double z90a;//z location of 90% bulk density on
ascending side
     double z90d;// """"" descending side
     double z10a;// """"" 10% bulk density of ascending side
     double z10d;// """"" descending side
     double zinterp(int ileft, int iright, double refrho);
     vector<double> z;
     vector<double> rho;
     void FindDensitySlopes();
     void rhocalcs();
     void zcalcs();
};
```

DensityProfile.cpp

```
/*Represents the density profile of a single species
Filename: DensityProfile.cpp*/

#include <iostream>
#include "DensityProfile.h"

DensityProfile::DensityProfile(string szName)
```

```
{
    Name = szName;
}

DensityProfile::DensityProfile()
{
    Name = "No Name";
}

DensityProfile::DensityProfile(string szName,
DensityProfile profile1, DensityProfile profile2)
{
    vector<double> rho2;
    int i;

    Name = szName;
    z = profile1.getz();
    rho = profile1.getrho();
    rho2 = profile2.getrho();

    //add densities
    for(i = 0; i < rho.size(); i++)
    {
     rho[i]+= rho2[i];
    }
}

void DensityProfile::RunCalcs()
{
    //cout << Name << ": Slope Calc" << endl;
    FindDensitySlopes();
    //cout << Name << ": rho Calc" << endl;
    rhocalcs();
    //cout << Name << ": z Calc" << endl;
    zcalcs();
}

void DensityProfile::zcalcs()
{
    //determines the values of z at which the density
reaches 90% or 10% of its bulk value (assigns values to z90
a and d, z10 a and d)

    int i, ileft(-1), iright(-1);
```

```
//initialize values
z90a = z90d = z10a = z10d = 0;

//determine ascending values
for(i = astart; i != aend; i++)
{
 if(z10a == 0)
 {
      if(rho[i] < rho10)
      {
           ileft = i;
      }
      else if(rho[i] > rho10 && ileft !=-1)
      {
           iright = i;

           //calculate z10a
           z10a = zinterp(ileft, iright, rho10);
           iright = ileft = -1;
      }
 }
 else if(z90a == 0)
 {
      if(rho[i] < rho90)
      {
           ileft = i;
      }
      else if(rho[i] > rho90 && ileft != -1)
      {
           iright = i;

           z90a = zinterp(ileft, iright, rho90);
           iright = ileft = -1;
      }
 }
 //account for pbc
 if(i == z.size() -1)
      i = -1;//restart loop
}

//determine descending values
for(i = dstart; i != dend; i++)
{
 if(z90d == 0)
 {
```

```
            if(rho[i] > rho90)
            {
                 ileft = i;
            }
            else if(rho[i] < rho90 && ileft !=-1)
            {
                 iright = i;

                 //calculate z90d
                 z90d = zinterp(ileft, iright, rho90);
                 iright = ileft = -1;
            }
       }
       else if(z10d == 0)
       {
            if(rho[i] > rho10)
            {
                 ileft = i;
            }
            else if(rho[i] < rho10 && ileft != -1)
            {
                 iright = i;

                 z10d = zinterp(ileft, iright, rho10);
                 iright = ileft = -1;
            }
       }

       if(i == rho.size() -1)
            i = -1;//reset to zero when loop starts again
     }
}

double DensityProfile::zinterp(int ileft, int iright,
double refrho)
{
     double ztemp;
     ztemp = (z[iright]-z[ileft])/(rho[iright]-
rho[ileft])*(refrho-rho[ileft]) + z[ileft];
     return ztemp;
}

void DensityProfile::rhocalcs()
{
     //determines the bulk density value and uses it to
```

```
determine rho10 and rho 90 (10% and 90% of bulk rho)
    int i, count(0);
    double sum(0);
    for(i = aend + 1; i != dstart; i++)
    {
     sum+= rho[i];
     if(i >= rho.size() -1)
          i = -1;//reset to zero when loop starts again
     count++;
    }

    bulkrho = sum/double(count);
    rho90 = bulkrho*0.9;
    rho10 = bulkrho*0.1;
}

void DensityProfile::FindDensitySlopes()
{
    //Determines values of astart, aend, dstart, dend
    //locals
    vector<double> drho;
    int i, imax(0), imin(0);
    double h(z[1]-z[0]);

    //create a vector of derivatives of rho
    drho.resize(rho.size());
    for(i = 0; i < rho.size(); i++)
    {

     //use CFD with 5-point span to calculate drho
     if(i < 2)
     {
          drho[i] = (rho[i+2]-rho[rho.size()-3 + i])/(4*h);
     }
     else if(i > rho.size()-3)
     {
          drho[i] = (rho[i + 2 - rho.size()] -
rho[i])/(4*h);
     }
     else
     {
          drho[i] = (rho[i+2]-rho[i-2])/(4*h);
     }

     //determine index of max drho
```

```
 if(drho[i] > drho[imax])
      imax = i;

 if(drho[i] < drho[imin])
      imin = i;
}

//find astart
i = imax;
do
{
 astart = i;
 i--;
 if(i < 0)
      i += drho.size(); //reset for periodicity
}while (drho[i] > 0);

//find aend
i = imax;
do
{
 aend = i;
 i++;
 if(i == drho.size())
      i = 0; //reset for periodicity
}while (drho[i] > 0);

//find dstart
i = imin;
do
{
 dstart = i;
 i--;
 if(i < 0)
      i += drho.size();
}while (drho[i] < 0);

//find dend
i = imin;
do
{
 dend = i;
 i++;
 if(i == drho.size())
      i = 0;
```

```
    }while (drho[i] < 0);
}

double DensityProfile::getMass(double zstart, double zend)
{
    //returns the mass/m^3 within region specified
    //this should only be used to calculate mole and mass
fractions
    //since this will cancel out the m^3 included

    int i;
    double mass(0);

    //loop through density profile to sum pertinent masses
    for(i = 0; i < rho.size(); i++)
    {
     if(zstart < zend)//don't need to worry about pbc
     {
          if(z[i] > zstart && z[i] < zend)
          {
               mass+= rho[i];
          }
     }
     else //need to take into account pbc
     {
          if(z[i] < zend || (i < z.size()-1 && z[i] >
zstart))
          {
               mass+= rho[i];
          }
     }

     //take care of boundaries
     if(i != 0 && i != rho.size()-1)
     {
          if(z[i] < zstart && z[i+1] > zstart)
          {
               mass+= rho[i]*(z[i+1]-zstart)/(z[i+1]-z[i]);
          }
          if(z[i] > zend && z[i-1] < zend)
          {
               mass+= rho[i]*(zend-z[i-1])/(z[i]-z[i-1]);
          }
     }
    }
```

```
    return mass;
}

double DensityProfile::getMoles(double zstart, double zend)
{
    double moles;
    moles = getMass(zstart, zend)/getMW();
    return moles;
}

double DensityProfile::getMW()
{
    if(Name == "BMI")
     return 0.1422451;
    else if(Name == "PF6")
     return 0.1449642;
    else if(Name == "SOL" || Name == "Water")
     return 0.01802;
    else if(Name == "HEX")
     return 0.0861754;
    else if(Name == "NA")
     return 0.02298977;
    else if(Name == "CL" || Name == "CL-")
     return 0.035453;
    else if(Name ==  "DNP")
     return 0.01201;//just carbon
    else if(Name ==  "BMIMPF6")
     return 0.2872093;
    else if(Name ==  "ETA")
     return 0.04611;
    else if(Name ==  "NO3")
     return 0.06201;
    else if(Name ==  "EAN")
     return 0.10812;
    else
     return 0;

}

void DensityProfile::Addz(double iz)
{
    z.resize(z.size() + 1);
    z[z.size() - 1] = iz;
}
```

```
void DensityProfile::Addrho(double irho)
{
    rho.resize(rho.size() + 1);
    rho[rho.size() - 1] = irho;
}

double DensityProfile::getbulkrho()
{
    return bulkrho;
}

double DensityProfile::getrho90()
{
    return rho90;
}

double DensityProfile::getrho10()
{
    return rho10;
}

string DensityProfile::getName()
{
    return Name;
}

double DensityProfile::getz90a()
{
    return z90a;
}

double DensityProfile::getz90d()
{
    return z90d;
}

double DensityProfile::getz10a()
{
    return z10a;
}

double DensityProfile::getz10d()
{
    return z10d;
}
```

```
vector<double> DensityProfile::getz()
{
    return z;
}

vector<double> DensityProfile::getrho()
{
    return rho;
}
```

EnergyDataFile.h

```
/* Header file for EnergyFileData class
Filename: EnergyDataFile.h*/

#include <string>
#include <vector>
using namespace std;

class EnergyDataFile
{
    public:
     //constructors
     EnergyDataFile();
     EnergyDataFile(string FileName);

     //accessor methods
     double getPotential() const;
     double getT() const;
     double getP() const;
     double getrho() const;
     double getgamma() const;
     double getcount() const;
    private:
     double count;
     double Potential;
     double T;
     double P;
     double rho;
     double gamma;
     void ReadDataFile(string FileName);
     vector<double> GetDoubleData(string row);
};
```

EnergyDataFile.cpp

```
//Analyzes energy.xvg.   Finds the average Potential
energy, T, P, and surface tension from the energy.xvg file.
//Filename: EnergyFileData.cpp

#include "EnergyDataFile.h"
#include <fstream>
#include <iostream>

EnergyDataFile::EnergyDataFile()
{
    ReadDataFile("energy.xvg");
}

EnergyDataFile::EnergyDataFile(string FileName)
{
    ReadDataFile(FileName);
}

void EnergyDataFile::ReadDataFile(string FileName)
{
    //Open Data Files
    ifstream energyfile(FileName.c_str());

    //locals
    string line;
    vector<double> currData, avg;
    int i;

    if (energyfile.is_open())
    {
     while (energyfile.good())
     {
          //read a line of the file
          getline (energyfile,line);

          //only get data files
          if (line[0] != '#' && line[0] != '@' && line !=
"")
          {
               currData = GetDoubleData(line);
               if (avg.size() == 0)
```

```
                    avg.resize(currData.size(),0);

                //store count in first element, don't need
time
                avg[0] = avg[0] + 1;

                //add values to total sum for averaging
later
                for (i = 1; i < currData.size(); i++)
                {
                    avg[i] = avg[i] + currData[i];
                }
            }
        }
        //average out total sums
        for (i = 1; i < avg.size(); i++)
        {
            avg[i] = avg[i]/avg[0];  //avg[0] contains the
count
        }

        //convert surface tension from bar*nm to mN/m
        avg[5] = avg[5]/20.0;

        count = avg[0];
        Potential = avg[1];
        T = avg[2];
        P = avg[3];
        rho = avg[4];
        gamma = avg[5];

        //Close Data Files
        energyfile.close();
    }
    else
    {
        cout << "Unable to open " << FileName << endl;
    }
}

double EnergyDataFile::getcount() const
{
    return count;
}
```

```
double EnergyDataFile::getPotential() const
{
    return Potential;
}

double EnergyDataFile::getT() const
{
    return T;
}

double EnergyDataFile::getP() const
{
    return P;
}

double EnergyDataFile::getrho() const
{
    return rho;
}

double EnergyDataFile::getgamma() const
{
    return gamma;
}

vector<double> EnergyDataFile::GetDoubleData(string row)
{
    //takes a text line of data and returns a vector of
doubles
    vector<string> data;
    vector<double> numdata;
    int i;
    bool IsNewEntry;
    char currChar;

    IsNewEntry = true;
    //split the colums into vector elements
    for (i = 0; i <= row.length(); i++)
    {
     currChar = row[i];
     if(currChar == ' ')
     {
          IsNewEntry = true;
     }
     else
```

```
     {
          if(IsNewEntry)
          {
               data.resize(data.size() + 1);
          }
          data[data.size() - 1] += currChar;
          IsNewEntry = false;
     }
    }

    //resize the number data vector to hold everything it
needs
    numdata.resize(data.size());

    //conver to double
    for (i = 0; i < data.size(); i++)
    {
     numdata[i] = atof(data[i].c_str());
    }

    return numdata;
}
```

ColumnCalculator.cpp

```
//Reads a data file and calculates the average and standard
deviation for each column of data

#include <iostream>
#include <string>
#include <fstream>
#include <cmath>
#include <vector>
using namespace std;

void ReadFile(string szFileName);
void DoCalculations();
void PrintResults(bool printnames);
bool IsLegendEntry(string line);
bool IsDoubleEntry(string line);
void AddColumnName(string line);
void AddDoubleData(string line);
vector< vector<double> > data;
vector<string> colnames;
```

```
vector<double> avgs;
vector<double> stdevs;

int main()
{
    string szFileName, printresults;
    bool bprint(false);
    cin >> szFileName;
    //cin >> printresults;

    //if(printresults == "y")
    bprint = true;//just always print the names

    ReadFile(szFileName);
    DoCalculations();
    PrintResults(bprint);
    return 0;
}

void ReadFile(string szFileName)
{
    string line;
    vector<double> currData;
    ifstream datafile(szFileName.c_str());
    if(datafile.is_open())
    {
     while(datafile.good())
     {
          getline(datafile,line);

          //add column name if this is a legend row
          if(IsLegendEntry(line))
               AddColumnName(line);
          else if(IsDoubleEntry(line))
               AddDoubleData(line); //read and add double
data

     }
    }
}

void DoCalculations()
{
    int i, j;
    vector<double> sums, sumsqs;
```

```
    //initialize global vectors
    avgs.resize(data[0].size());
    stdevs.resize(data[0].size());

    //initialize local vectors
    sums.resize(data[0].size());
    sumsqs.resize(data[0].size());
    for(j = 0; j < data[0].size(); j++)
    {
     sums[j] = 0;
     sumsqs[j] = 0;
    }

    //calc averages
    for(i = 0; i < data.size(); i++)//i is for rows
    {
     for(j = 0; j < data[0].size(); j++)//j is for columns
     {
          sums[j] += data[i][j];
     }
    }

    for(j = 0; j < data[0].size(); j++)
     avgs[j] = sums[j]/double(data.size());

    //calc stdevs
    for(i = 0; i < data.size(); i++)//i is for rows
    {
     for(j = 0; j < data[0].size(); j++)//j is for columns
     {
          sumsqs[j] += pow(data[i][j]-avgs[j],2);
     }
    }

    for(j = 0; j < data[0].size(); j++)
     stdevs[j] = sqrt(sumsqs[j]/double(data.size()));
}

void PrintResults(bool printnames)
{
    int j;
    if(printnames)
    {
     for(j = 0; j < data[0].size(); j++)
```

```
     {
          cout << colnames[j] << " = " << avgs[j] << " +/-
" << stdevs[j] << endl;
     }
     //cout << endl;
    }
    //for(j = 0; j < data[0].size(); j++)
    //{
    //    cout << avgs[j] << " " << stdevs[j] << " ";
    //}
    //cout << endl;
}

bool IsLegendEntry(string line)
{
    string first3;
    if(line.length() > 3)
    {
     first3 = line.substr(0,3);
     if(first3 == "@ s")
          return true;
    }
    return false;
}

bool IsDoubleEntry(string line)
{
    if (line[0] == '#' || line[0] == '@' || line == "")
     return false;
    return true;
}

void AddColumnName(string line)
{
    int i;
    string name = "";
    bool IsName = false;

    //make first column the x axis (t or z)
    if(colnames.size() == 0)
    {
     colnames.resize(colnames.size() + 1);
     colnames[0] = "xtz";
    }
```

```
    //search for the text between the quotes
    for(i = 3; i < line.length(); i++)
    {
     if(line[i] == '\"')
     {
          if(IsName)
               IsName = false;//this is an end quotation
          else
               IsName = true;//this is a start quotation
     }
     if(IsName && line[i] != '\"')
          name += line[i];
    }
    colnames.resize(colnames.size() + 1);
    colnames[colnames.size()-1] = name;
}

void AddDoubleData(string line)
{
    vector<string> szItems;
    vector<double> Items;
    int i;
    bool IsNewEntry;
    char currChar;
    IsNewEntry = true;
    //split the columns into vector elements
    for(i = 0; i <= line.length(); i++)
    {
     currChar = line[i];
     if(currChar == ' '  || currChar == '\t')
     {
          IsNewEntry = true;
     }
     else
     {
          if(IsNewEntry)
               szItems.resize(szItems.size() + 1);
          szItems[szItems.size()-1] += currChar;
          IsNewEntry = false;
     }
    }

    //resize the Items vector to hold everything the
szItems vector has
    Items.resize(szItems.size());
```

```
    //convert szitems to doubles
    for(i = 0; i < szItems.size(); i++)
    {
     Items[i] = atof(szItems[i].c_str());
    }

    //add row to data vector
    data.resize(data.size() + 1);
    data[data.size()-1] = Items;
}
```

Bicubic Interpolation VBA Macros

```
Sub FillMatrix()
Dim StartRow1 As Integer, StartCol As Integer, xCol As Integer, yCol As Integer, zCol As Integer, ScanLimit As Integer
Dim i As Long, j As Integer, x As Double, y As Double, k As Integer, dist1 As Double, dist2 As Double
Dim currX1 As Double, currY1 As Double, z1 As Double, z2 As Double, currDist1 As Double, StarRow2 As Integer, currDist2 As Double
Dim currX2 As Double, currY2 As Double, yinterval As Double, xinterval As Double, iz1 As Integer, iz2 As Integer

'Initiate Variables
StartRow1 = 3 'first row of matrix and 1st phase
StartCol = 10
xCol = 5
yCol = 6
zCol = 7
ScanLimit = InputBox("Please enter the total number of entries to scan")
xinterval = Cells(StartRow1 + 2, StartCol) - Cells(StartRow1 + 1, StartCol) / 2
yinterval = Cells(StartRow1, StartCol + 2) - Cells(StartRow1, StartCol + 1) / 2

'Determine StarRow for phase 2
i = 0
Do Until Cells(StartRow1 + i, zCol) = ""
   i = i + 1
Loop
StartRow2 = StartRow1 + i + 2

'fill in z values
i = 1
Do Until Cells(StartRow1 + i, StartCol) = ""
```

```
j = 1
Do Until Cells(StartRow1, StartCol + j) = ""
        x = Cells(StartRow1 + i, StartCol)
        y = Cells(StartRow1, StartCol + j)
        iz1 = 0
        iz2 = 0
        'dist1 = 1
        'dist2 = 1
        z1 = 0
        z2 = 0
        For k = 0 To ScanLimit
            'Phase 1
            currX1 = Cells(StartRow1 + k, xCol)
            currY1 = Cells(StartRow1 + k, yCol)
            'currDist1 = Sqr((currX1 - x) ^ 2 + (currY1 - y) ^ 2)
            If Abs(currX1 - x) <= xinterval And Abs(currY1 - y) <= yinterval Then
               'dist1 = currDist1
               z1 = z1 + Cells(StartRow1 + k, zCol)
               iz1 = iz1 + 1
            End If

            'Phase 2
            currX2 = Cells(StartRow2 + k, xCol)
            currY2 = Cells(StartRow2 + k, yCol)
            'currDist2 = Sqr((currX2 - x) ^ 2 + (currY2 - y) ^ 2)
            'If currDist2 < dist2 Then
            If Abs(currX2 - x) <= xinterval And Abs(currY2 - y) <= yinterval Then
               'dist2 = currDist2
               z2 = z2 + Cells(StartRow2 + k, zCol)
               iz2 = iz2 + 1
            End If
        Next k

        'Average out z's
        z1 = z1 / iz1
        z2 = z2 / iz2

        If iz1 = 0 Then 'could not find a molecule in phase one close enough
            Cells(StartRow1 + i, StartCol + j) = z2
        ElseIf iz2 = 0 Then 'could not find a molecule in phase two close enough
            Cells(StartRow1 + i, StartCol + j) = z1
        Else
            Cells(StartRow1 + i, StartCol + j) = (z1 + z2) / 2 'average of adjacent
interfacial atoms' z coordinates
        End If
```

```
      j = j + 1
   Loop
   i = i + 1
Loop
End Sub
Sub Bicubic()
Dim nPoints As Integer, i As Integer, j As Integer, BaseCol As Integer, BaseRow As Integer, StartRow As Integer
Dim k As Integer, DataPoint As Double, InterpInterval As Double, l As Integer, m As Integer
Dim P(1, 1) As Variant, Px(1, 1) As Variant, Py(1, 1) As Variant, Pxy(1, 1) As Variant, a(3, 3) As Variant
Dim iInterp As Integer, jinterp As Integer


'Specify base column and row (where the actual data starts)
BaseCol = 10
BaseRow = 3

'ask the user for the number of interpolated points desired
'nPoints = InputBox("Please enter the desired number of interpolated points")
nPoints = 10 'this gives a pretty smooth graph

'determine start row
i = 1
Do Until Cells(BaseRow + i, BaseCol) = ""
   i = i + 1
Loop
StartRow = BaseRow + i + 1 'row where we will being writing the interpolated value matrix

Call WriteInterpolatedCoordinates(BaseRow, BaseCol, StartRow, nPoints)

'Write interpolated data out by quadrants
i = BaseRow + 1 '1st quadrant P00
j = BaseCol + 1 '1st quadrant P00
'reading and writing from left to right while progressing downward
Do Until Cells(i + 1, j) = ""
   Do Until Cells(i, j + 1) = ""
      'Assign function data points
      P(0, 0) = Cells(i, j)
      P(0, 1) = Cells(i, j + 1)
      P(1, 0) = Cells(i + 1, j)
      P(1, 1) = Cells(i + 1, j + 1)
```

```
        'quadrant ref point should be the top left corner of the quadrant
        'Assign derivatives
        Call QuadrantxDerivatives(i, j, BaseCol, BaseRow, Px)
        Call QuadrantyDerivatives(i, j, BaseCol, BaseRow, Py)
        Call QuadrantxyDerivatives(i, j, BaseCol, BaseRow, Pxy)

        'calculate a coefficients
        Call CalculateCoefficients(P, Px, Py, Pxy, a)
        'Call PrintPandCoef(P, Px, Py, Pxy, a)

        'write out interpolated matrix for this quadrant
        InterpInterval = 1 / (nPoints + 1)
        For k = 0 To nPoints + 1
           For l = 0 To nPoints + 1
              iInterp = (StartRow) + (i - BaseRow) + nPoints * (i - BaseRow - 1) + k
              jinterp = (BaseCol) + (j - BaseCol) + nPoints * (j - BaseCol - 1) + l
              Cells(iInterp, jinterp) = f(k * InterpInterval, l * InterpInterval, a)
           Next l
        Next k
        j = j + 1
     Loop
     i = i + 1
     j = BaseCol + 1 '1st quadrant P00
Loop
End Sub
Function f(xnorm As Double, ynorm As Double, a As Variant) As Double
Dim i As Integer, j As Integer
f = 0
For i = 0 To 3
     For j = 0 To 3
        f = f + a(i, j) * xnorm ^ i * ynorm ^ j
     Next j
Next i
End Function
Sub PrintPandCoef(P As Variant, Px As Variant, Py As Variant, Pxy As Variant, a As
Variant)
'P values
     Cells(17, 10) = "P00"
     Cells(18, 10) = "P01"
     Cells(19, 10) = "P10"
     Cells(20, 10) = "P11"
     Cells(21, 10) = "Px00"
     Cells(22, 10) = "Px01"
     Cells(23, 10) = "Px10"
     Cells(24, 10) = "Px11"
```

```
    Cells(25, 10) = "Py00"
    Cells(26, 10) = "Py01"
    Cells(27, 10) = "Py10"
    Cells(28, 10) = "Py11"
    Cells(29, 10) = "Pxy00"
    Cells(30, 10) = "Pxy01"
    Cells(31, 10) = "Pxy10"
    Cells(32, 10) = "Pxy11"
    Cells(17, 11) = P(0, 0)
    Cells(18, 11) = P(0, 1)
    Cells(19, 11) = P(1, 0)
    Cells(20, 11) = P(1, 1)
    Cells(21, 11) = Px(0, 0)
    Cells(22, 11) = Px(0, 1)
    Cells(23, 11) = Px(1, 0)
    Cells(24, 11) = Px(1, 1)
    Cells(25, 11) = Py(0, 0)
    Cells(26, 11) = Py(0, 1)
    Cells(27, 11) = Py(1, 0)
    Cells(28, 11) = Py(1, 1)
    Cells(29, 11) = Pxy(0, 0)
    Cells(30, 11) = Pxy(0, 1)
    Cells(31, 11) = Pxy(1, 0)
    Cells(32, 11) = Pxy(1, 1)

'coefficient values ("a")
    Cells(17, 12) = "a00"
    Cells(18, 12) = "a01"
    Cells(19, 12) = "a02"
    Cells(20, 12) = "a03"
    Cells(21, 12) = "a10"
    Cells(22, 12) = "a11"
    Cells(23, 12) = "a12"
    Cells(24, 12) = "a13"
    Cells(25, 12) = "a20"
    Cells(26, 12) = "a21"
    Cells(27, 12) = "a22"
    Cells(28, 12) = "a23"
    Cells(29, 12) = "a30"
    Cells(30, 12) = "a31"
    Cells(31, 12) = "a32"
    Cells(32, 12) = "a33"
    Cells(17, 13) = a(0, 0)
    Cells(18, 13) = a(0, 1)
    Cells(19, 13) = a(0, 2)
```

```
   Cells(20, 13) = a(0, 3)
   Cells(21, 13) = a(1, 0)
   Cells(22, 13) = a(1, 1)
   Cells(23, 13) = a(1, 2)
   Cells(24, 13) = a(1, 3)
   Cells(25, 13) = a(2, 0)
   Cells(26, 13) = a(2, 1)
   Cells(27, 13) = a(2, 2)
   Cells(28, 13) = a(2, 3)
   Cells(29, 13) = a(3, 0)
   Cells(30, 13) = a(3, 1)
   Cells(31, 13) = a(3, 2)
   Cells(32, 13) = a(3, 3)
End Sub
Sub QuadrantxDerivatives(quadi As Integer, quadj As Integer, BaseCol As Integer,
BaseRow As Integer, ByRef Px As Variant)
Dim i As Integer, j As Integer, h As Double, quadRow As Integer, quadCol As Integer

For quadRow = 0 To 1
   For quadCol = 0 To 1
      i = quadi + quadRow
      j = quadj + quadCol
      'Find out which finite difference formula to use
      If Cells(i + 1, BaseCol) = "" Then
         'use backwards difference
         h = Cells(i, BaseCol) - Cells(i - 1, BaseCol)
         Px(quadRow, quadCol) = (Cells(i, j) - Cells(i - 1, j)) / h
      ElseIf i - 1 = BaseRow Then
         'use forward difference
         h = Cells(i + 1, BaseCol) - Cells(i, BaseCol)
         Px(quadRow, quadCol) = (Cells(i + 1, j) - Cells(i, j)) / h
      Else
         'use central difference
         h = Cells(i + 1, BaseCol) - Cells(i, BaseCol)
         Px(quadRow, quadCol) = (Cells(i + 1, j) - Cells(i - 1, j)) / (2 * h)
      End If
   Next quadCol
Next quadRow

End Sub
Sub QuadrantyDerivatives(quadi As Integer, quadj As Integer, BaseCol As Integer,
BaseRow As Integer, ByRef Py As Variant)
Dim i As Integer, j As Integer, h As Double, quadRow As Integer, quadCol As Integer

For quadRow = 0 To 1
```

```
   For quadCol = 0 To 1
      i = quadi + quadRow
      j = quadj + quadCol
      'Find out which finite difference formula to use
      If Cells(BaseRow, j + 1) = "" Then
         'use backwards difference
         h = Cells(BaseRow, j) - Cells(BaseRow, j - 1)
         Py(quadRow, quadCol) = (Cells(i, j) - Cells(i, j - 1)) / h
      ElseIf j - 1 = BaseCol Then
         'use forward difference
         h = Cells(BaseRow, j + 1) - Cells(BaseRow, j)
         Py(quadRow, quadCol) = (Cells(i, j + 1) - Cells(i, j)) / h
      Else
         'use central difference
         h = Cells(BaseRow, j + 1) - Cells(BaseRow, j)
         Py(quadRow, quadCol) = (Cells(i, j + 1) - Cells(i, j - 1)) / (2 * h)
      End If
   Next quadCol
Next quadRow

End Sub
Sub QuadrantxyDerivatives(quadi As Integer, quadj As Integer, BaseCol As Integer,
BaseRow As Integer, ByRef Pxy As Variant)
Dim i As Integer, j As Integer, h As Double, k As Double, quadRow As Integer, quadCol
As Integer

For quadRow = 0 To 1
   For quadCol = 0 To 1
      i = quadi + quadRow
      j = quadj + quadCol
      'Find out which finite difference formula to use
      If i - 1 = BaseRow And j - 1 = BaseCol Then 'top left corner
         'use xForwardDiff and yForwardDiff
         h = Cells(i + 1, BaseCol) - Cells(i, BaseCol)
         k = Cells(BaseRow, j + 1) - Cells(BaseRow, j)
         Pxy(quadRow, quadCol) = (Cells(i + 1, j + 1) - Cells(i, j + 1) - Cells(i + 1, j) +
Cells(i, j)) / (h * k)
      ElseIf i - 1 = BaseRow And Cells(BaseRow, j + 1) = "" Then 'top right corner
        'use xFFD and y BFD
        h = Cells(i + 1, BaseCol) - Cells(i, BaseCol)
        k = Cells(BaseRow, j) - Cells(BaseRow, j - 1)
        Pxy(quadRow, quadCol) = (Cells(i + 1, j) - Cells(i, j) - Cells(i + 1, j - 1) + Cells(i,
j - 1)) / (h * k)
      ElseIf Cells(i + 1, BaseCol) = "" And j - 1 = BaseCol Then  'bottom left corner
         'use xBFD and y FFD
```

```
            h = Cells(i, BaseCol) - Cells(i - 1, BaseCol)
            k = Cells(BaseRow, j + 1) - Cells(BaseRow, j)
            Pxy(quadRow, quadCol) = (Cells(i, j + 1) - Cells(i - 1, j + 1) - Cells(i, j) + Cells(i
- 1, j)) / (h * k)
        ElseIf Cells(i + 1, BaseCol) = "" And Cells(BaseRow, j + 1) = "" Then 'bottom right
corner
            'use xBFD and yBFD
            h = Cells(i, BaseCol) - Cells(i - 1, BaseCol)
            k = Cells(BaseRow, j) - Cells(BaseRow, j - 1)
            Pxy(quadRow, quadCol) = (Cells(i, j) - Cells(i - 1, j) - Cells(i, j - 1) + Cells(i - 1, j
- 1)) / (h * k)
        ElseIf i - 1 = BaseRow Then 'top side, not a corner
            'use xFFD and yCFD
            h = Cells(i + 1, BaseCol) - Cells(i, BaseCol)
            k = Cells(BaseRow, j) - Cells(BaseRow, j - 1)
            Pxy(quadRow, quadCol) = (Cells(i + 1, j + 1) - Cells(i, j + 1) - Cells(i + 1, j - 1) +
Cells(i, j - 1)) / (2 * h * k)
        ElseIf j - 1 = BaseCol Then 'left side
            'use xCFD and yFFD
            h = Cells(i + 1, BaseCol) - Cells(i, BaseCol)
            k = Cells(BaseRow, j + 1) - Cells(BaseRow, j)
            Pxy(quadRow, quadCol) = (Cells(i + 1, j + 1) - Cells(i - 1, j + 1) - Cells(i + 1, j) +
Cells(i - 1, j)) / (2 * h * k)
        ElseIf Cells(BaseRow, j + 1) = "" Then 'right side
            'use xCFD and yBFD
            h = Cells(i + 1, BaseCol) - Cells(i, BaseCol)
            k = Cells(BaseRow, j) - Cells(BaseRow, j - 1)
            Pxy(quadRow, quadCol) = (Cells(i + 1, j) - Cells(i - 1, j) - Cells(i + 1, j - 1) +
Cells(i - 1, j - 1)) / (2 * h * k)
        ElseIf Cells(i + 1, BaseCol) = "" Then 'bottom side
            'use xBFD and yCFD
            h = Cells(i, BaseCol) - Cells(i - 1, BaseCol)
            k = Cells(BaseRow, j) - Cells(BaseRow, j - 1)
            Pxy(quadRow, quadCol) = (Cells(i, j + 1) - Cells(i - 1, j + 1) - Cells(i, j - 1) +
Cells(i - 1, j - 1)) / (2 * h * k)
        Else
            'use xCFD and yCFD
            h = Cells(i, BaseCol) - Cells(i - 1, BaseCol)
            k = Cells(BaseRow, j) - Cells(BaseRow, j - 1)
            Pxy(quadRow, quadCol) = (Cells(i + 1, j + 1) - Cells(i - 1, j + 1) - Cells(i + 1, j -
1) + Cells(i - 1, j - 1)) / (4 * h * k)
        End If
    Next quadCol
Next quadRow
```

```
End Sub
Sub CalculateCoefficients(P As Variant, Px As Variant, Py As Variant, Pxy As Variant, ByRef a As Variant)
'solution to the system of 16 unknowns and 16 equations
a(0, 0) = P(0, 0)
a(0, 1) = Py(0, 0)
a(1, 0) = Px(0, 0)
a(1, 1) = Pxy(0, 0)
a(0, 2) = 3 * P(0, 1) - Py(0, 1) - 2 * a(0, 1) - 3 * a(0, 0)
a(0, 3) = -2 * P(0, 1) + Py(0, 1) + a(0, 1) + 2 * a(0, 0)
a(2, 0) = 3 * P(1, 0) - Px(1, 0) - 2 * a(1, 0) - 3 * a(0, 0)
a(3, 0) = -2 * P(1, 0) + Px(1, 0) + a(1, 0) + 2 * a(0, 0)
a(1, 2) = 3 * Px(0, 1) - Pxy(0, 1) - 3 * a(1, 0) - 2 * a(1, 1)
a(1, 3) = -2 * Px(0, 1) + Pxy(0, 1) + 2 * a(1, 0) + a(1, 1)
a(2, 1) = 3 * Py(1, 0) - Pxy(1, 0) - 3 * a(0, 1) - 2 * a(1, 1)
a(3, 1) = -2 * Py(1, 0) + Pxy(1, 0) + 2 * a(0, 1) + a(1, 1)
a(3, 2) = -6 * P(1, 1) + 3 * Px(1, 1) + 2 * Py(1, 1) - Pxy(1, 1) + 6 * a(0, 0) + 4 * a(0, 1) + 2 * a(0, 2) + 3 * a(1, 0) + 2 * a(1, 1) + a(1, 2) - 3 * a(3, 0) - 2 * a(3, 1)
a(3, 3) = 4 * P(1, 1) - 2 * Px(1, 1) - 2 * Py(1, 1) + Pxy(1, 1) - 4 * a(0, 0) - 2 * a(0, 1) + 2 * a(0, 3) - 2 * a(1, 0) - a(1, 1) + a(1, 3) + 2 * a(3, 0) + a(3, 1)
a(2, 3) = -2 * P(1, 1) + Py(1, 1) + 2 * a(0, 0) + a(0, 1) - a(0, 3) + 2 * a(1, 0) + a(1, 1) - a(1, 3) + 2 * a(2, 0) + a(2, 1) + 2 * a(3, 0) + a(3, 1) - a(3, 3)
a(2, 2) = 3 * P(1, 1) - Py(1, 1) - 3 * a(0, 0) - 2 * a(0, 1) - a(0, 2) - 3 * a(1, 0) - 2 * a(1, 1) - a(1, 2) - 3 * a(2, 0) - 2 * a(2, 1) - 3 * a(3, 0) - 2 * a(3, 1) - a(3, 2)
End Sub
Sub WriteInterpolatedCoordinates(BaseRow As Integer, BaseCol As Integer, StartRow As Integer, nPoints As Integer)
Dim i As Integer, j As Integer, k As Integer, DataCoordinate As Double, InterpInterval As Double

'Write out x and y values based on the number of interpolated points
'write x points
i = 1
j = 1
Do Until Cells(BaseRow + i + 1, BaseCol) = ""
   'Determine data point and interpolation interval
   DataCoordinate = Cells(BaseRow + i, BaseCol)
   InterpInterval = (Cells(BaseRow + i + 1, BaseCol) - DataCoordinate) / (nPoints + 1)

   'write data point
   Cells(StartRow + j, BaseCol) = DataCoordinate
   j = j + 1

   'write interpolated point
   For k = 1 To nPoints
```

```
        Cells(StartRow + j, BaseCol) = DataCoordinate + InterpInterval * k
        j = j + 1
    Next k
    i = i + 1
Loop
Cells(StartRow + j, BaseCol) = Cells(BaseRow + i, BaseCol) 'get last data point

'write y points
i = 1
j = 1
Do Until Cells(BaseRow, BaseCol + i + 1) = ""
    'Determine data point and interpolation interval
    DataPoint = Cells(BaseRow, BaseCol + i)
    InterpInterval = (Cells(BaseRow, BaseCol + i + 1) - DataPoint) / (nPoints + 1)

    'write data point
    Cells(StartRow, BaseCol + j) = DataPoint
    j = j + 1

    'write interpolated point
    For k = 1 To nPoints
        Cells(StartRow, BaseCol + j) = DataPoint + InterpInterval * k
        j = j + 1
    Next k
    i = i + 1
Loop
Cells(StartRow, BaseCol + j) = Cells(BaseRow, BaseCol + i) 'get last data point
End Sub
```

MD Simulation Scripts

BASH scripts were often used to save time and eliminate human error in the preparation of MD run files. These were particularly useful when combining simulation boxes to form an interface or managing 26 and more run files for a PMF calculation. Scripts for the latter application mostly dealt with file naming and compilation of run files. Combining simulation boxes was more complicated, however, and the script is included here. To execute this script, the notation used was ./CombineBoxes Box1.gro Box2.gro 0.5. Intuitively, Box1.gro and Box2.gro were the boxes to be combined and the number denoted the width by which these boxes would be separated. Sometimes a few repetitions were needed to avoid overlap between the molecules of the two boxes.

Combine Boxes

```
FirstBox=$1
SecondBox=$2
dist=$3
LenFirst=`tail -n 1 $FirstBox|awk '{print $3}'`
LenSecond=`tail -n 1 $SecondBox|awk '{print $3}'`
FirstZ=`echo "scale=4; $LenFirst/2+$dist/2"|bc`
SecondZ=`echo "scale=4; $LenSecond/2 + $dist/2"|bc`
FirstAtoms=`head -n 2 $FirstBox|tail -n 1`
SecondAtoms=`head -n 2 $SecondBox|tail -n 1`
TotalLen=`echo "scale=4; $dist + $LenFirst + $LenSecond + $dist"|bc`
TotalAtoms=`echo "$FirstAtoms + $SecondAtoms"|bc`
FirstHeadLines=`echo "$FirstAtoms + 2"|bc`
SecondHeadLines=`echo "$SecondAtoms + 2"|bc`
x=`tail -n 1 $FirstBox|cut -d' ' -f4`
y=`tail -n 1 $FirstBox|cut -d' ' -f7`

use gromacs-4.5.3
editconf_mpi -f $FirstBox -o upperbox.gro -center 0 0 $FirstZ
editconf_mpi -f $SecondBox -o lowerbox.gro -center 0 0 "-$SecondZ"
echo "Whole Box for Interface" > wholebox.gro
echo "$TotalAtoms" >> wholebox.gro
```

```
head -n $FirstHeadLines upperbox.gro >temp
tail -n $FirstAtoms temp >> wholebox.gro
head -n $SecondHeadLines lowerbox.gro > temp
tail -n $SecondAtoms temp >> wholebox.gro
echo "   $x   $y   $TotalLen" >> wholebox.gro
genconf_mpi -f wholebox.gro -o wholebox.gro -renumber
editconf_mpi -f wholebox.gro -o wholebox.gro -c
rm temp
```

BIOGRAPHICAL SKETCH

Education

Aug 2013	PhD in Chemical Engineering, Arizona State University (ASU) GPA: 4.17/4.00
Aug 2012	MSE in Chemical Engineering, ASU
Apr 2010	BS in Chemical Engineering, Brigham Young University (BYU) GPA: 3.81/4.00

Publications

1. **Frost, D. S.**; Kroeger, N. J.; Robledo, M.; Dai, L. L. "Humidity-Induced Gelation of an Ionic Liquid Mixture" (Submitted)

2. **Frost, D. S.**; Machas, M.; Perea, B.; Dai, L. L. "Non-Convective Mixing of Miscible Ionic Liquids" (Submitted)

3. **Frost, D. S.**; Nofen, E. M.; Dai, L. L. "Self-Assembly at Ionic Liquid-Based Interfaces: A Combined Experimental and Computational Study" (Submitted)

4. Nickerson, S.; **Frost, D. S.**; Phelan, H.; Dai, L. L. "Comparison of the Capillary Wave Method and Pressure Tensor Route for Calculation of Interfacial Tension in Molecular Dynamics Simulations" (Submitted)

5. **Frost, D. S.**; Ngan, M.; Dai, L. L. "Spontaneous Transport of Microparticles Across Liquid-Liquid Interfaces" (Submitted)

6. **Frost, D. S.**; Machas, M.; Dai, L. L. "Molecular Dynamics Studies on the Adaptability of an Ionic Liquid in the Extraction of Solid Nanoparticles" *Langmuir* (2012), *28*, 13924.

7. Zou, J.; **Frost, D. S.**, Dai, L. L. "Effects of Gelator 12-Hydroxystearic Acid (12-HSA) on Ionic Liquid Based Pickering Emulsions" *Colloids and Surfaces A* (2012), *414*, 477.

8. **Frost, D. S.**; Schoepf, J.; Nofen, E. M.; Dai, L. L. "Understanding Bridging in Ionic Liquid-Based Pickering Emulsions" *J. Colloid and Interface Science* (2012), *383*, 103.

9. **Frost, D. S.**; Dai, L. L "Molecular Dynamics Simulations of Charged nanoparticle Self-Assembly at Ionic Liquid Based Interfaces" *J. Chemical Physics* (2012), *136*, 084706. (Selected for Publication in the Virtual Journal of Biological Physics Research)

10. **Frost, D. S.**; Dai, L. L. "Molecular Dynamics Simulations of Nanoparticle Self-Assembly at Ionic Liquid-Water and Ionic-Liquid-Oil Interfaces" *Langmuir* (2011), *27*, 11339.

11. Walker, E; **Frost, D. S.**; Dai, L. L. "Particle Self-assembly in Oil-in-Ionic Liquid Pickering Emulsions" *J. Colloid and Interface Science* (2011), *363*, 307.

Meeting Presentations

1. **Frost, D. S.**; Machas, M.; Dai, L. L. "Molecular Dynamics Simulations of Nanoparticle Self-Assembly at Ionic Liquid-Based Interfaces" *American Chemical Society National Meeting*, **New Orleans, LA**, April 2013

2. **Frost, D. S.**; Ma, H.; Shoepf, J. J.; Nofen, E. M.; Dai, L. L. "Ionic Liquid-Based Pickering Emulsions: Particle Self-Assembly and Extraction Phenomena" *Emulsification: Modeling, Technologies, and Applications*, **Lyon, France**, November 2012

3. **Frost, D. S.**; Shoepf, J. J.; Nofen, E. M.; Dai, L. L. "Understanding Droplet Bridging in Ionic Liquid-Based Pickering Emulsions" *American Institute of Chemical Engineering Annual Meeting*, **Pittsburgh, PA**, November 2012

4. **Frost, D. S.**; Walker, E. M.; Shoepf, J. J.; Ma, H.; Dai, L. L. "Particle Self-Assembly at Ionic Liquid-Based Interfaces" *Achievement Rewards for College Scientists Awards Ceremony*, **Phoenix, AZ**, May 2012

5. **Frost, D. S.**; Walker, E. M.; Shoepf, J. J.; Ma, H.; Dai, L. L. "Particle Self-Assembly at Ionic Liquid-Based Interfaces" *ASU Graduate Student Appreciation Day*, **Tempe, AZ**, March 2012

6. **Frost, D. S.**; Dai, L. L. "Molecular dynamics simulations of nanoparticle self assembly at ionic liquid-based interfaces" *American Chemical Society National Meeting*, **San Diego, CA**, March 2012

7. **Frost, D. S.**; Walker, E. M.; Shoepf, J. J.; Ma, H.; Dai, L. L. "Particle Self-Assembly at Ionic Liquid-Based Interfaces" *Gordon Research Conference on Colloidal, Macromolecular, & Polyelectrolyte Solutions*, **Ventura, CA**, February 2012

8. **Frost, D. S.**; Dai, L. L. "Molecular Dynamics Simulations of Nanoparticle Self-Assembly at Ionic Liquid-Based Interfaces" *American Institute of Chemical Engineering Annual Meeting*, **Minneapolis, MN**, October 2011

9. **Frost, D. S.**; Dai, L. L. "Molecular Dynamics Simulations of Nanoparticle Self-Assembly at Ionic Liquid-Based Interfaces" *Adaptive Intelligent Materials and Systems (AIMS) Center Open House*, **Tempe, AZ**, October 2011

10. **Frost, D. S.**; Dai, L. L. "Molecular Dynamics Simulations of Nanoparticle Self-Assembly at Ionic Liquid-Based Interfaces" *ASU/IBM Meet Watson Event*, **Tempe, AZ**, September 2011

11. **Frost, D. S.**; Dai, L. L. "Ionic Liquid-Based Pickering Emulsions, The New Frontier" *Science Foundation Arizona Graduate Summit*, **Flagstaff, AZ**, May 2011

Academic Honors

2012 - present	National Science Foundation (NSF) Graduate Fellow
2012 - 2013	Achievement Rewards for College Scientists (ARCS) Scholar
2010 - 2012	Science Foundation of Arizona Graduate Fellow
2012	NASA Graduate Fellow
2012	Six Sigma Greenbelt/Blackbelt
2011	Outstanding Chemical Engineering Teaching Assistant (ASU)
2010	Don B. Olsen Mentorship Award
2008-2010	BYU Half-Tuition Scholarship
2008-2010	SMART Grant Award
2007-2008	BYU Full-Tuition Scholarship
2004-2005	BYU Half-Tuition Scholarship